FATIGUE FRACTURE INTERACTION MECHANISMS IN CORTICAL BONE

---

by

Lloyd Fletcher

School of Mechanical Engineering

Faculty of Engineering, Computer and Mathematical Sciences

A thesis submitted in fulfilment of the

requirements for the degree of

Doctor of Philosophy

at

The University of Adelaide

August 2015

Abstract

The skeletal system accumulates microscale fatigue damage with everyday use. Bone has the ability to repair fatigue damage; however, the effectiveness of the repair mechanism can deteriorate with age and disease leading to an accumulation of damage. An increase in fatigue microdamage with age is thought to contribute to the occurrence of fragility fractures in the elderly. However, the mechanisms that are responsible for the interaction of fatigue damage and the fracture resistance of bone are not well understood. Therefore this thesis aims to analyse the mechanisms of interaction between accumulated fatigue damage and the fracture resistance of cortical bone (i.e. fatigue fracture interaction mechanisms). This aim is achieved by the application of engineering fracture mechanics theory to investigate the effects of accumulated fatigue damage on the fracture resistance of cortical bone.

This thesis consists of two main components: 1) experimental studies and 2) numerical modelling. The experimental component is separated into three separate experiments, each designed to analyse the effects of fatigue damage on the fracture resistance of cortical bone. The first experiment analysed the effects of tensile fatigue damage on the longitudinal fracture resistance of cortical bone; the second experiment analysed the effects of tensile fatigue damage on the longitudinal and transverse fracture resistance of cortical bone; and the third experiment analysed the effects of tensile and compressive fatigue damage on the transverse fracture resistance of cortical bone. The general methodology used for these experiments included splitting specimens into control and damaged groups then *ex-vivo* fatigue loading the damaged group specimens. All specimens were then fracture resistance tested and the fracture behaviour of the control and damaged groups was compared. The results of these experiments were used to propose conceptual models of fatigue fracture interaction. In general the results showed that fatigue microdamage in the form of linear microcracks is detrimental to the fracture resistance of cortical bone.

The second component of this thesis was the numerical modelling of the toughening mechanisms in cortical bone and their contribution to the overall fracture resistance behaviour. The specific mechanisms that were modelled include: uncracked ligament bridging, crack deflection and microcracking. The results from the numerical modelling were then combined with the experimental data to develop a model of toughening behaviour in bone.

Overall, the results of this thesis show that fatigue microdamage is detrimental to the fracture resistance of cortical bone. In addition to this, microstructural changes with age or disease may exacerbate the detrimental effects of fatigue microdamage on the fracture resistance of cortical bone. Therefore the results of this thesis suggest that fatigue microdamage may be a contributing factor to clinical fractures.

Declaration

I certify that this work contains no material which has been accepted for the award of any other degree or diploma in my name, in any university or other tertiary institution and, to the best of my knowledge and belief contains no material previously published or written by another person , except where due reference has been made in text. In addition, I certify that no part of this work will, in the future, be used in a submission in my name, for any other degree or diploma in any university or other tertiary institution without the prior approval of the University of Adelaide and where applicable, any partner institution responsible for the joint award of this degree.

I give consent to this copy of my thesis when deposited in the University Library, being made available for loan and photocopying, subject to the provisions of the Copyright Act 1968.

The author acknowledges that copyright of published works contained within this thesis resides with the copyright holder(s) of those works.

I also give permission for the digital version of my thesis to be made available on the web, via the University's digital research repository, the Library Search and also through web search engines, unless permission has been granted by the University to restrict access for a period of time.

……

Lloyd Fletcher

Acknowledgements

I would like to express my sincere gratitude to everyone who supported me as I worked on this thesis including my supervisors, family and friends.

Firstly, I would like to thank my principal supervisor John Codrington, whose unique style of supervision suited me perfectly. Thank you for always being available as a sounding board for new ideas and helping me to crystallise my sometimes scattered thought processes into useful concepts and models. I will miss being asked ‘Have you finished your thesis yet?’ every day when walking down the corridor but it will be satisfying to put a completed copy of this document on your desk and reply ‘Yes’.

I would also like to thank my supervisor Ian Parkinson for being the voice of biological reason when John and I would get carried away with an engineering concept. Without you this work may have lost some of its relevance to biological and clinical applications. And thanks to Chris Leigh for all your help procuring laboratory supplies.

To my parents, sister, grandpa and parents in law for the weekly family dinners which always involved much merriment and alcohol. These dinners allowed me relax and just enjoy being with the people I love most. I would like to especially thank my parents for supporting me through my undergraduate study and for always supporting me in all my endeavours.

To my friends for making me realise that I had a life outside of research work. Thanks to all of my friends at archery for giving me somewhere to escape to. Thank you to Brendan for always being available to chat about the latest developments in our favourite card game. And thank you to Ashton, Emily, Campbell and Kira for sharing our weekly roleplaying game session. With special thanks to Ashton for sharing your love and insight into the world of game design.

To all of the students I have had the pleasure to teach while I completed this work. Being able to share my knowledge with you and learn from you in turn brought me great joy. Teaching is an essential part of gaining knowledge, for what use is knowledge if it is not shared?

Most importantly I would like to thank my beautiful wife, Sarah. You are the most loving person in my life. Thank you for being understanding and providing a supportive shoulder to lean on after a tough day at work. Without you I would not be the person I am today and I would not have pursued a research career that allowed me to apply my engineering knowledge to a medical application.

Thank you all, your support and encouragement made this work possible.

Table of Contents

Chapter 1: Introduction

1 Introduction

1.1 Background

The fracture (or more correctly “failure”) of bone, as seen from an engineering perspective has three main contributing factors, the external loading, the bone macrostructure, and the bone tissue material properties. Loading is applied to a bone by muscle action through connecting tissues, such as tendons. The bulk geometry (or macrostructure) of the bone determines how the loading is transmitted through it and the stresses generated from this loading. Bone tissue material properties characterise the mechanical behaviour of bone tissue independent of its bulk geometry. This includes various properties that describe how resistant the material is to deformation and how resistant it is to failure. The dominant failure mode in bone is by crack growth (Behiri and Bonfield, 1984; Nalla et al., 2004a; Norman et al., 1995a). Crack growth in bone can occur from a single traumatic loading event (referred to as fracture in clinical literature). In addition, low level repeated loading (known as fatigue in engineering), can cause the accumulation of microscale cracks (Frost, 1960; O’Brien et al., 2003; Schaffler et al., 1995; Zioupos et al., 1996). It is thought that fatigue microcracks play an important role in the age related decrease in bone toughness which leads to clinical failures such as stress and fragility failures. The general goal of this research is therefore to better understand bone tissue material behaviour, specifically with regard to the fatigue and fracture behaviour and interactions between these two failure mechanisms.

The mechanical behaviour of any material is inherently linked to its physical structure and the base components that form the material. Bone is a hierarchical composite with unique material characteristics from the macro (whole bone level) to the nano level (base components of the composite) (see Figure 1.1).

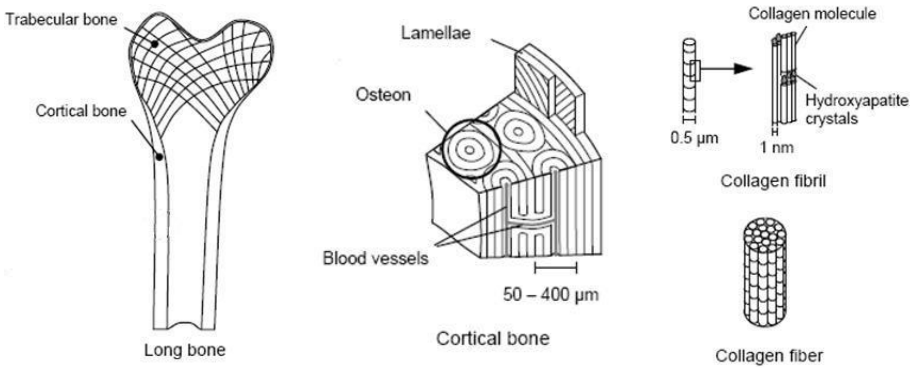

(a) Macrostructure (b) Microstructure (c) Nanostructure

Figure 1.1: Schematic representation of hierarchical structure of cortical bone (figure adapted from Rho et al. (1998)).

The three main phases of the bone composite include: the protein or organic phase (primarily collagen type I); the mineral or inorganic phase (calcium hydroxyapatite); and water (Rho et al., 1998). At the macro scale (Figure 1.1 (a)), a typical long bone, such as the femur, consists of two distinct types of bone. These are the solid cortical bone that makes up the main shaft and the 'sponge like' trabecular bone in the proximal and distal ends of the bone (which are also covered by a thin layer of cortical bone) (Tortora and Derrickson, 2008). At the microscale (Figure 1.1 (b)) the cross section of the cortical bone consists of laminated sheets of bone material known as lamellae. These lamellae form in rings around the whole shaft of the bone and in much smaller concentric circles within the bone shaft, known as osteons, through which blood vessels pass. The lamellae and osteons are orientated parallel to the long axis of the bone ±10-20° (Martin and Burr, 1989). At the nanoscale (Figure 1.1 (c)), each of these lamellae sheets are made from collagen fibrils tightly packed together. The fibrils consist of long collagen protein chains with flat and 'plate like' calcium hydroxyapatite crystals placed in and around them (Rho et al., 1998).

The failure processes in bone are dependent on the hierarchical structure of the tissue as well as the arrangement of the constituent phases. Cracks in the bone tissue initiate at the nano scale and grow to microscale lengths. They then interact with features of the microstructure, such as lamellae boundaries or osteons, which can cause cracks to deflect, branch, or even arrest (O'Brien et al., 2005a; Poundarik et al., 2012; Vashishth, 2007a). Understanding of these crack growth toughening mechanisms is important for understanding fracture in bone and the factors that alter the overall toughening behaviour such as fatigue microdamage.

Fatigue microdamage is an important contributor to the overall fracture behaviour of cortical bone. Fatigue microdamage is caused by repetitive loading of the skeletal system due to everyday activities (Burr et al., 1985). Normally fatigue damage is repaired by cellular action *in-vivo*; however, this process has been shown to be inhibited with aging leading to an accumulation of damage with age (Diab et al., 2006; Schaffler et al., 1995; Zioupos, 2001a). Thus, the accumulation of fatigue damage is thought to be a contributing factor to the age related decrease in the toughness of human bone (Diab and Vashishth, 2005; Norman et al., 1998; Parsamian and Norman, 2001). Fatigue damage is also linked to the occurrence of clinical fractures such as fragility fractures in the elderly and stress fractures in the young. Fragility fractures are thought to be the result of reduced bone quality while stress fractures are normally the result of a sharp increase in physical activity. Both of these clinical fractures are thought to be due to an accumulation of fatigue damage. For fragility fractures the accumulation of fatigue damage is caused by

degradation of bones' material properties. For stress fractures, it is the increased magnitude and/or frequency of that loading which causes an increase in fatigue damage. While fatigue damage has been implicated as a factor in both of these types of clinical fractures, the microscale mechanisms that cause the fatigue induced damage to contribute to the overall final fracture are not well understood. To further understand the mechanisms of failure in bone and the mechanisms that cause fatigue damage to interact with the failure processes in bone, an engineering analysis technique such as fracture mechanics can be applied.

As crack growth is the dominant failure mechanism in bone, current research has focused on the use of fracture mechanics to understand these failure processes (Granke et al., 2015; Zimmermann et al., 2011). Fracture mechanics is an engineering technique that accounts for flaws and defects in a material to predict strength via resistance to crack growth. The most commonly used prediction parameter is the Stress Intensity Factor (SIF), which describes the severity of the stresses at a crack tip due to the applied loading and geometry of the crack (Anderson, 2005). The SIF is then compared to a critical value known as the fracture toughness. If the SIF for a particular crack is higher than the fracture toughness, that crack will grow and cause eventual failure of the material. Another fracture prediction parameter is the J-Integral. The J-Integral is a strain energy based measure that can also account for non-linear material effects (unlike the stress intensity factor). The J-Integral is therefore more appropriate for use with bone material as it exhibits non-linear fracture mechanisms such as plasticity, microcracking and other non-linear fracture toughening mechanisms (Yang et al., 2006a; Yan et al., 2007).

For a composite material such as bone a single value fracture toughness measure is not sufficient to capture the full crack growth resistance behaviour. The reason for this is that the fracture toughness of bone rises with increasing crack length (Koester et al., 2008; Vashishth, 2004). The resistance of a material to crack growth as a function of crack length is known as the fracture resistance curve and for cortical bone the fracture resistance curve increases with increasing crack length. This increasing fracture resistance in bone is caused by the presence of various toughening mechanisms acting on the crack as it propagates, such as microcracking, ligament bridging and crack deflection (Vashishth, 2004; Zimmermann et al., 2011). Each of these mechanisms increases the apparent toughness of cortical bone by either shielding the crack from the applied load or by altering the stress field around the crack tip. Thus, experimental and modelling techniques used in fracture mechanics can be applied to cortical bone to provide further insight into the contributions of fatigue microdamage to the overall fracture resistance behaviour and the toughening mechanisms that cause this behaviour.

The overall purpose of this project is to combine the use of engineering fatigue and fracture theory to investigate the effects of accumulated fatigue damage on the fracture resistance of cortical bone. This project will limit its scope to analysis of bone tissue material properties. Specifically, this will include the microscale behaviour of fatigue damage and how this interacts with the crack growth mechanisms in cortical bone. This project will involve experimental analysis of *ex-vivo* induced fatigue microdamage on the rising fracture resistance curve and the toughening mechanisms that cause this behaviour. From the experimental data, conceptual models will be developed to describe the effects of the fatigue damage on the fracture toughening mechanisms. These conceptual models and the toughening mechanisms responsible for them will then be analysed using the computer modelling techniques known as Finite Element Analysis (FEA). Overall, the combination of experimental and numerical fracture mechanics will provide insight into the effects of fatigue microdamage on the fracture resistance of cortical bone and the mechanisms that cause this interaction. The results of this work will have important implications for the understanding of the material level mechanisms that are responsible for clinical fractures such as fragility and stress fractures, which are linked to the occurrence of fatigue damage in bone.

1.2 Motivation

While this project will focus on the material level (microscale) behaviour of fatigue and crack growth in bone, the overall motivation of this work is to increase the understanding of clinical failures related to fatigue loading. There are two main types of failure observed in bone that are directly related to fatigue and fatigue damage accumulation. These are: 'stress' fractures and 'fragility' fractures (Burr, 1997). Stress fractures are common in military recruits and athletes who subject their skeletal structure to intensive periods of repetitive loading (Giladi et al., 1991; Iwamoto and Takeda, 2003). Stress fractures are caused by the growth and coalescence of fatigue cracks. They normally occur due to a sharp increase in physical activity that does not allow enough time for the body to repair or adapt to the new loading (Forwood and Burr, 1993; Taylor and Kuiper, 2001). Unlike stress fractures, fragility fractures can occur due to everyday loading, such as walking. Fragility fractures are the result of weakened bone material and structure, which makes it susceptible to failure (Danova et al., 2003; Diab et al., 2006). One factor thought to play a significant role in fragility fractures is the accumulation of fatigue microdamage (Norman et al., 1998; Vashishth, 2007a; Zioupos, 2001a). This can occur if the body's natural ability to repair fatigue damage is hindered by age or disease (Lee et al., 2012; Schwartz and Sellmeyer, 2007; Zioupos, 2001b). The purpose of this project is to improve the understanding of the underlying fracture mechanisms related to the clinical fatigue failures

described above. This is achieved by applying engineering fracture analysis techniques to understand the material properties of bone. Further understanding of bone tissue material properties will also allow clinicians to develop new methodologies to identify those at risk of fracture and reduce the incidence rates of stress and fragility fractures.

1.3 Aims and Objectives

Global Aim: Analyse and develop conceptual models of the effects of accumulated fatigue damage on the fracture resistance and crack growth toughening mechanisms in cortical bone.

Specific Objectives:

1) Develop experimental techniques that combine fatigue damage accumulation and fracture mechanics testing methods *ex-vivo*, including:
   a) Fracture specimen configurations that allow for both fatigue and fracture testing
   b) Methods for assessing the fatigue damage before fracture testing
   c) Optical methods for analysing the interaction of fatigue damage with the crack path toughening mechanisms
2) Conduct experiments to cause the accumulation of fatigue damage *ex-vivo* before subsequent fracture resistance testing, including:
   a) Conduct *ex-vivo* fatigue loading to cause the accumulation of fatigue microdamage
   b) Use control and fatigued specimens for fracture resistance tests and compare the results of these groups based on the fracture resistance curve and the fracture toughening mechanisms
   c) Compare large and small scale crack growth in both the longitudinal and transverse crack growth directions
   d) Analyse the effects of different types of fatigue damage (tensile diffuse damage and compressive microcracks) on the transverse fracture behaviour of cortical bone
3) Develop conceptual models of fatigue fracture interaction from the experimental data, including models for analysing:
   a) The effects of and difference between fatigue induced damage and microdamage formed during crack growth in bone
   b) The effect of fatigue induced damage on the fracture resistance curve and the crack path toughening mechanisms

4) Analyse the toughening mechanisms in cortical bone using Finite Element Analysis (FEA), including finite element models for:
   a) Analysing the assumption of using the standard equations used to process the fracture resistance data for the non-standard specimen configurations developed as part of the first objective
   b) Isolate and explicitly model the microscale toughening mechanisms in bone including: microcracking, ligament bridging and crack deflection
5) Combine the results of the experimental and finite element modelling work to propose models of fracture behaviour in bone and the effect that fatigue induced damage has on normal fracture behaviour

1.4 Scope

The scope of this project will be limited to the material level mechanisms responsible for fracture in cortical bone in the absence of the normal biological repair mechanisms. Fatigue damage in bone can be repaired by cellular action through a process known as remodelling. The timescale for bone to begin the remodelling process is generally in the order of weeks (Burr et al., 1990, 1985; Milgrom et al., 1985). In contrast to this, fatigue damage occurs directly during the loading event and accumulates with each ongoing load cycle (Mori and Burr, 1993). In the case of aged or diseased bone, the repair mechanism can be inhibited leading to an even larger timescale for repair to occur (Burr, 2003, 1993; Schaffler, 2003). This can lead to increased accumulation of fatigue damage due to normal loading, such as walking (Diab et al., 2006; Diab and Vashishth, 2007; Taylor and Lee, 2003). While remodelling and repair is an important process in the aetiology of fatigue failure of bone; the relative timescale of the repair process allows for the crack growth mechanisms (i.e. material properties) to be separated from the repair mechanism. Thus, the scope of this project is limited to the analysis of crack growth mechanisms in cortical bone without including the effects of bone repair.

1.5 Outline of Thesis

The following is an outline of all experiments and modelling conducted as part of this research. The first chapter begins by detailing engineering fatigue and fracture theory along with a literature review of the application of both of these theories to cortical bone. The literature review concludes with identified knowledge gaps and how the aims and objectives of this project intend to address these knowledge gaps.

Following the literature review the experimental work is presented in three separate chapters with each experimental study separated based on the methodology used and the specific project objective that the experiment addresses. The first experimental study

used a circular notched compact tension or ‘C(T)’ fracture specimen configuration with a tensile fatigue method used to generate microdamage ahead of the circular notch. The C(T) configuration allows for the analysis of large scale crack growth (crack growth greater than 1mm) in the longitudinal direction (crack growth parallel to the long axis of a bone). The first experiment will address the objective of analysing the effects of fatigue damage on the large scale longitudinal fracture resistance behaviour of cortical bone. The second experimental study uses a uniform 3 point bend specimen for fatigue testing, which is subsequently notched to create a Single Edge Notched Bend or SEN(B) specimen for fracture resistance testing. The use of a SEN(B) fracture specimen allows for analysis of small scale crack growth (crack growth less than 1mm) and analysis of the longitudinal and traverse (parallel and perpendicular to the long axis of the bone respectively) fracture resistance of cortical bone. The second experiment relates to the objective of analysing the effects of fatigue induced damage on the transverse and longitudinal fracture behaviour of small scale crack growth. The third experimental study uses a circular notched SEN(B) specimen for both the bending fatigue and fracture testing in both the longitudinal and transverse crack growth directions. The third experiment addresses the objective of analysing the effects of both tensile diffuse damage and compressive microcracks on the fracture resistance of cortical bone. Each of the experimental chapters describes the specific methodology used in the experiment, the results of the experiment and discussion of the results leading to the development of conceptual models of fatigue fracture interaction.

The experimental chapters are then followed by two chapters detailing the finite element models used in this work. The first finite element modelling chapter details the analysis of the circular notched fracture specimen configuration used in the first and third experiments. The purpose of this analysis is to verify that the assumption of using the standard equations for non-conventional geometry does not alter the statistical comparisons given in the first and third experiments. The second finite element modelling study analyses the main toughening mechanisms present in cortical bone including: microcracking, ligament bridging and crack deflection. The results of the individual finite element models for each of these toughening mechanisms are then used to analyse the relative contribution of each mechanism to the overall fracture resistance behaviour of cortical bone. The results from each of the toughening mechanism finite element models are also compared to the experiments presented in this thesis to provide further insight into the conceptual models proposed by the experimental results.

The overall findings of the experimental and finite element modelling work of this project are synthesised and discussed as part of the last section of the final finite element modelling chapter. This is followed by the conclusion, which summarises the main findings of all work presented in this thesis and the significance that the results of this research has for future research.

Chapter 2: Literature Review

2 Literature Review

The following literature review is divided into several sections: the first section describes the biomechanical properties of bone that can be derived from monotonic tests. The next three sections discuss engineering fatigue theory, the accumulation of fatigue damage in cortical bone and the application of fatigue theory to cortical bone. Sections five and six discuss fracture mechanics theory and the application of this theory to cortical bone, respectively. In section seven the existing knowledge on the effects of accumulated fatigue damage on the fracture behaviour (also referred to as fatigue fracture interaction) of cortical bone is discussed. This chapter is then concluded by summarising the knowledge gaps identified in the literature review and how the global aim and specific objectives will address these gaps.

2.1 Monotonic Properties of Cortical Bone

Before discussing the fatigue and fracture behaviour of cortical bone it is useful to understand the material properties of bone that can be derived from a monotonic tensile or compressive test. Due to the composite structure of cortical bone it has directionally dependent elastic properties; that is, cortical bone is orthotropic. Typically, if a cortical bone sample is taken from a long bone such as the femur or tibia, a specimen orientated parallel to the long axis of the bone (approximately parallel to the osteon direction) will have a higher elastic modulus than either the circumferential or radial directions. Note that specimens orientated parallel to the long axis are termed 'longitudinal' while the radial and circumferential directions show similar elastic properties and are often grouped together and termed 'transverse'. The typical tensile elastic properties of bone are outlined in Table 2.1 below for both human and bovine bone.

Table 2.1: Summary of typical tensile elastic properties of secondary human and bovine bone in both the longitudinal and transverse directions. Data presented as mean ± standard deviation. The values presented as the transverse direction relate to the circumferential direction. Values taken from Reilly and Burstein (1975).

	Human		**Bovine**	
Property	**Longitudinal**	**Transverse**	**Longitudinal**	**Transverse**
Elastic Modulus (GPa)	17.7±3.6	12.8±3.0	23.1±3.2	10.4±1.6
Yield Stress (MPa)	114±7.1	-	141±12	-
Failure Stress (MPa)	133±15.6	53±10.7	150±11	54±5.8

Cortical bone also has different material properties (i.e. monotonic properties) when loaded in compression or when loaded in tension. The main difference between the compressive and tensile properties is the yield and fracture strengths (Cezayirlioglu et al., 1985), with the yield and fracture strengths being much higher in compression. The reason for this is that under compressive loading, bone fails via a shear based mechanism causing it to break at an angle to the primary axis of loading (see for example the images in Caler and Carter (1989)). This is caused by the sliding of lamellar sheets at the angle of maximum resolved shear stress. Conversely, under tensile loading bone fails by the breakage of collagen fibres and osteon pull out (Hiller et al., 2003). Note that the compressive elastic modulus in the longitudinal and transverse directions for bovine cortical bone are similar to those shown in Table 2.1.

Another factor that affects the elastic behaviour of bone is the microstructural arrangement of the osteons. When bone is initially formed it is termed primary bone and it has an irregular pattern of primary osteons (Enlow, 1962). As ageing occurs in human bone the primary bone is replaced by secondary osteons through a process known as remodelling. This leads to a more porous and less dense microstructure with different mechanical properties to primary bone (Diab and Vashishth, 2007; Hoc et al., 2006; Nalla et al., 2006). The process of remodelling is also linked to the repair of damage formed *in-vivo* and this is discussed further in section 2.3.2. The data presented in Table 2.1 is for secondary osteonal bone in both humans and bovine.

While the properties of bone derived from a monotonic tensile test are useful in terms of understanding the bulk material behaviour; they do not capture the underlying failure mechanisms in the material due to crack growth or the effects of more complicated loading patterns such as cyclic fatigue. The engineering theory for fatigue and fracture analysis and the applications of these theories to bone will be discussed in the following sections.

2.2 Fracture Properties of Cortical Bone

2.2.1 Engineering Fracture Mechanics Theory

As the dominant failure mode in bone is crack growth, the most appropriate theoretical framework through which to analyse this failure mechanism is fracture mechanics. Fracture mechanics is used to investigate and predict how and if a material will fail by assuming the presence of cracks or crack like defects and flaws. The foundation of fracture mechanics stems from the theoretical stress singularity (infinite stresses) that occurs at the tip of a sharp crack. The severity of the singularity is dependent on several factors including the geometry of the crack (and local structure) and remote loading conditions. Around the crack tip, an area of plastic deformation is usually formed to

alleviate the theoretically infinite stresses. However, if the zone is small then just outside of the crack tip the material behaves in accordance with the linear elastic fracture theory, commonly known as Linear Elastic Fracture Mechanics (LEFM) (Anderson, 2005).

There are three different loading modes that can be applied to a crack. The three different loading modes are termed mode I, mode II and mode III. Mode I loading is the result of a tensile opening applied to the crack face; mode II is caused by shear loading on the crack faces; and mode III loading is caused by out of plane forces and is also known as the tearing mode. Each of these loading modes is shown schematically in Figure 2.1. It is also possible for fracture to occur in a material due to a combination of loading modes known as mixed mode loading.

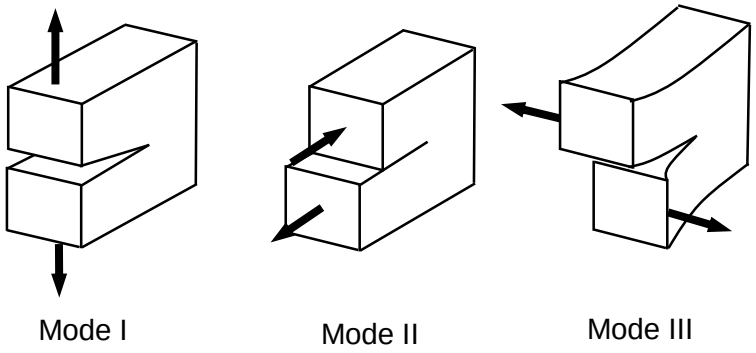

Figure 2.1: Loading modes that can be applied to a crack.

There are several parameters used to characterise the initiation of crack growth (including stable and unstable crack propagation). The main two alternative parameters are the strain energy release rate ‘G’ and stress intensity factor ‘K’. Critical values for these quantities are measured experimentally and are referred to as the fracture toughness of the material (Janssen et al., 2004). If the strain energy release rate or stress intensity factor for a given crack (due to the applied loading) is above this critical value, then the crack will grow and can result in failure of the structure. The most commonly used method of measuring the fracture toughness and predicting fracture of a material is the stress intensity factor.

The stress intensity factor ‘K’ directly describes the stress field that surrounds a crack tip and the severity of the stress singularity that occurs at a sharp crack tip. The stress field near the crack tip is expressed as a power series expansion using polar coordinates centred on the crack tip (see Figure 2.2). The power series expression for the stress field about the crack tip is often simplified to only include the first term as follows:

$$\sigma_{xx} = \frac{K_I}{\sqrt{2\pi r}} cos\left(\frac{\theta}{2}\right)\left[1 - sin\left(\frac{\theta}{2}\right) sin\left(\frac{3\theta}{2}\right)\right] \quad (2.1)$$

$$\sigma_{yy} = \frac{K_I}{\sqrt{2\pi r}} cos\left(\frac{\theta}{2}\right)\left[1 + sin\left(\frac{\theta}{2}\right) sin\left(\frac{3\theta}{2}\right)\right] \quad (2.2)$$

$$\tau_{xy} = \frac{K_I}{\sqrt{2\pi r}} cos\left(\frac{\theta}{2}\right) sin\left(\frac{\theta}{2}\right) cos\left(\frac{3\theta}{2}\right) \quad (2.3)$$

$$\sigma_{zz} = 0\ (Plane\ Stress)\ or\ \upsilon(\sigma_{xx} + \sigma_{yy})\ (Plane\ Strain) \quad (2.4)$$

$$\tau_{xz}, \tau_{yz} = 0 \quad (2.5)$$

where the stress components 'σ_{xx}', 'σ_{yy}', 'σ_{zz}', 'τ_{xz}' and 'τ_{yz}' are defined in Figure 2.2. 'K_I' is the mode I stress intensity factor, 'r' is the radial distance of the stress element from the crack tip and 'θ' is the angular location of the stress element as defined in Figure 2.2.

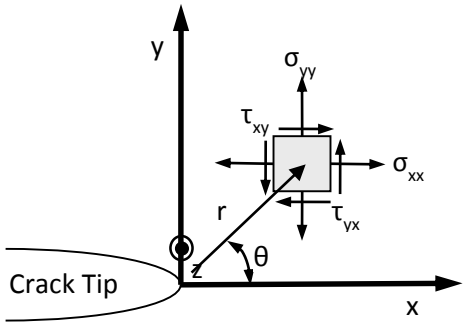

Figure 2.2: Crack tip coordinate system definition for equations 2.1 to 2.5, note that the positive z axis is defined coming out of the page.

This assumption is made as the first term of the power series shows that the stress is inversely proportional to the square root of the distance from the crack tip ($\sigma \propto 1/\sqrt{r}$). Therefore, near the crack tip ($r \to 0$), this term is dominant and completely describes the local stress and displacement fields. At the crack tip ($r = 0$) the first term of the equation approaches infinity, giving the stress singularity. The stress intensity factor (denoted as 'K') is the coefficient of this singular term: $\sigma \propto K_I/\sqrt{r}$ with the subscript denoting the loading mode as shown in Figure 2.1. The magnitude of the stress intensity factor describes the severity of the stress singularity at the crack tip.

For a given material there will be a critical value of the stress intensity factor known as the fracture toughness. If the applied stress intensity factor for a given crack equals or exceeds this critical value then crack growth will occur. The theoretical formulation of the stress intensity factor assumes an infinitely sharp crack with linear elastic deformation. Real materials plastically deform at the crack tip forming an area known as the process zone. If the plastic zone is small compared to the overall specimen or structure then the stress intensity factor describes the stress field just outside this process zone.

Experimentally the fracture toughness of a material is determined by loading notched specimens of a specific geometry. There are two common types of specimen geometry; the Compact Tension or C(T) specimen and the Single Edge Notched Bend SEN(B) specimen. To determine a single fracture initiation toughness value a specimen is monotonically loaded in displacement control while measuring the force. The displacement is increased until crack growth starts, which is shown by either a sudden drop in load for unstable crack growth or a steady non-linearity in the load-displacement curve for stable crack growth. From this load-displacement curve a critical loading is determined using the procedures detailed in a fracture testing standard such as ASTM E1820 (2011). This critical load and the specimen geometry are then used along with the specifications for the relevant specimen configuration to determine if the test was valid so that the fracture initiation toughness can be calculated. Further details for fracture toughness testing are outlined in ASTM standard E1820 (2011).

Fibre composite materials with directionally dependent properties show unique fracture toughness behaviour depending on the orientation of the crack with respect to the fibres in the composite material. This is especially evident in fibre composites where the fracture toughness is significantly higher when the crack is orientated such that it is transverse to the fibre direction as opposed to breaking along the fibre direction (Chong et al., 2007; Jacobsen and Sørensen, 2001; Pegoretti et al., 1996; Sinclair et al., 2004). The reason for this is that in a fibre composite sheet the fibres have high strength along their tensile axis. Therefore, a crack travelling transverse to the fibres must break the fibres or leave the fibres remaining in the crack wake supporting load that would otherwise propagate the crack. In contrast to this, when the crack is propagating in parallel to the fibres the crack can propagate along the weak interface between the fibres and the matrix (Pegoretti et al., 1996). For crack growth parallel to the fibre direction the fibres do not need to be broken and the toughness is significantly lower than transverse crack growth. These fracture toughening mechanisms in fibre composites lead to significant non-linear behaviour which cannot be fully accounted for using LEFM.

For materials with significant non-linear behaviour or materials with large plastic zones; the use of the stress intensity factor and LEFM is not suitable. Thus, another method has been developed to characterise the toughness of non-linear materials known as the J-integral (or non-linear strain energy release rate). The advantage of the J-integral method is that it can be used in situations where there is a larger amount of plasticity at the crack tip. The J-integral is an energy measure that considers the amount of energy consumed during crack growth, per unit crack area formed. The J-integral 'J' was first derived by Rice (Rice, 1968):

$$\Pi = \int_A W\, dA - \int_\Gamma T_i u_i\, ds \tag{2.6}$$

$$J = -\frac{d\Pi}{dA} = \int_\Gamma \left(W\, dy - T_i \frac{\partial u_i}{\partial x} ds \right) \tag{2.7}$$

by considering the potential energy 'π' of a two dimensional cracked body along a contour denoted 'Γ' with surface tractions T_i. Where 'W' is the strain energy density and 'u_i' is the displacement vector. The parameters for these equations are shown diagrammatically in Figure 2.3. For the linear elastic case the stress intensity factor 'K' and the J-integral 'J' are related using:

$$J = G = \frac{K^2}{E'} \tag{2.8}$$

For the purely linear elastic case the J-integral 'J' is equivalent to the strain energy release rate, G, with E' = E/(1-v^2) for plane stress and E' = E for plane strain.

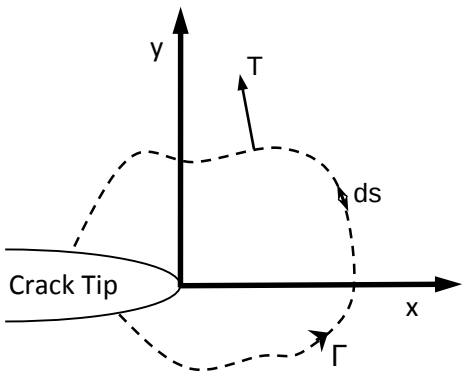

Figure 2.3: Representation of crack tip and coordinate system with the parameters defined as in equations 2.6 and 2.7. The closed contour path encircling the crack tip is denoted as Γ while the traction vectors along the path are denoted as T.

Experimentally, the J-integral is measured in a similar manner to the stress intensity factor based fracture toughness. However, the J-integral calculation includes an energy term based on the plastic area under the load-displacement curve for the test. The equations used to experimentally determine the J-integral fracture toughness are:

$$J = J_{el} + J_{pl} \tag{2.9}$$

$$J_{el} = \frac{K^2}{E'} \tag{2.10}$$

$$J_{pl} = \frac{\eta A_{pl}}{Bb} \tag{2.11}$$

where 'K' is the stress intensity factor and E' is defined as in equation 2.8. In equation 2.11, 'B' is the specimen thickness; 'b' is the uncracked ligament length; 'A_{pl}' is the plastic area under the load displacement curve and 'η' is factor dependent on the specimen configuration defined in ASTM standard E1820.

Experimental fracture mechanics is inherently destructive as it requires that a crack is grown in the material being analysed whereas finite element modelling allows for non-destructive analysis of cracks in a component. Therefore, it is beneficial to apply the theory of fracture mechanics to numerical modelling techniques such as Finite Element Analysis (FEA). A further advantage of FEA is that a model can be parametrised and solved for various characteristics of the crack geometry without having to conduct a prohibitive number of experimental tests. Early work on application of FEA in fracture mechanics focused on deriving the solutions for static stress intensity factors for various common crack geometries (Byskov, 1970; Tracey, 1971). More recent applications of FEA to fracture mechanics include the analysis of complex three dimensional crack geometries and the modelling of crack paths and propagation (Liu et al., 2012; Roe and Siegmund, 2003; Ural et al., 2011; Xu and Yuan, 2009).

2.2.2 Fracture Analysis of Cortical Bone

Initial work on the fracture testing of bone focused on the use of single value fracture toughness tests using LEFM. As cortical bone is an orthotropic material it shows distinctly different crack growth behaviour and fracture behaviour in the longitudinal and transverse directions. Typical fracture toughness values for bovine cortical bone range from

3.2MPa√m in the longitudinal direction to 6.5MPa√m in the transverse direction (Behiri and Bonfield, 1989). While a single fracture initiation toughness value can be instructive in terms of crack initiation in a material, it does not account for stable crack growth following initiation. To account for stable crack growth the fracture toughness must be considered as a function of crack length, known as the fracture resistance curve.

For brittle materials a single fracture toughness value is adequate to describe its behaviour as following crack initiation the crack continues to grow in an unstable manner. However, for ductile materials and for composite materials like bone there is a significant portion of stable crack growth and the full fracture resistance curve needs to be considered. Bone tends to increase its resistance to crack growth as a crack propagates through the material (Malik et al., 2003; Nalla et al., 2004b). This behaviour can be described by the use of a fracture resistance curve that shows the variation of the fracture toughness with increasing crack growth as shown in Figure 2.4. A material that increases its resistance to crack growth as the crack propagates through it is said to have a rising resistance curve (Anderson, 2005).

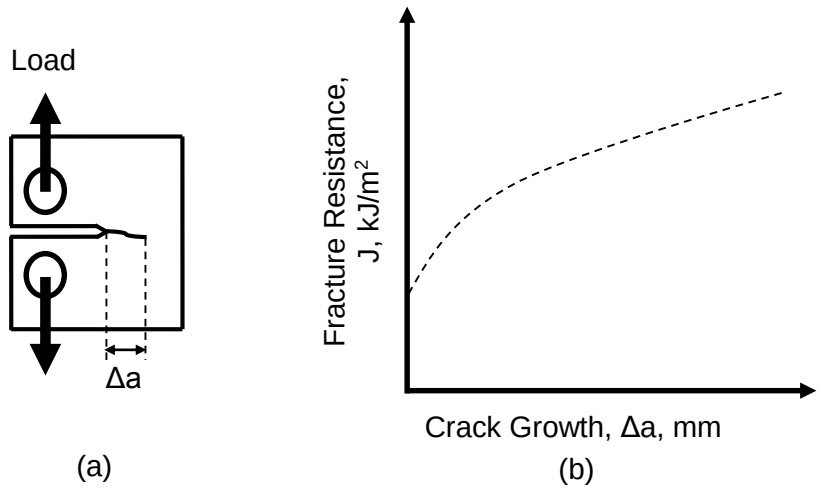

Figure 2.4: (a) Compact tension fracture specimen showing points of applied load and crack extension measurement Δa. (b) Rising fracture resistance curve behaviour typical of cortical bone.

There have been several toughening mechanisms proposed for bone that lead to its rising resistance curve behaviour. A summary of the relevant knowledge in relation to the toughening of cortical bone is given by Ritchie et al. (2009) in which they describe the toughening mechanisms in bone. These include: crack deflection, uncracked ligament bridging and microcracking. Each of these toughening mechanisms acts to shield the crack tip from the applied loading or absorbs energy that would otherwise be used to propagate the crack. Figure 2.5 shows a schematic of these toughening mechanisms. Note that all of these toughening mechanisms are present in bone for cracks growing in

both the longitudinal and transverse orientations with respect to the long axis of the bone (Nalla et al., 2004b; Vashishth et al., 2003). For cracks growing in the transverse direction (breaking across collagen fibres), it has been shown that crack deflection is more prevalent when compared to the longitudinal direction (splitting the collagen fibres) (Koester et al., 2008).

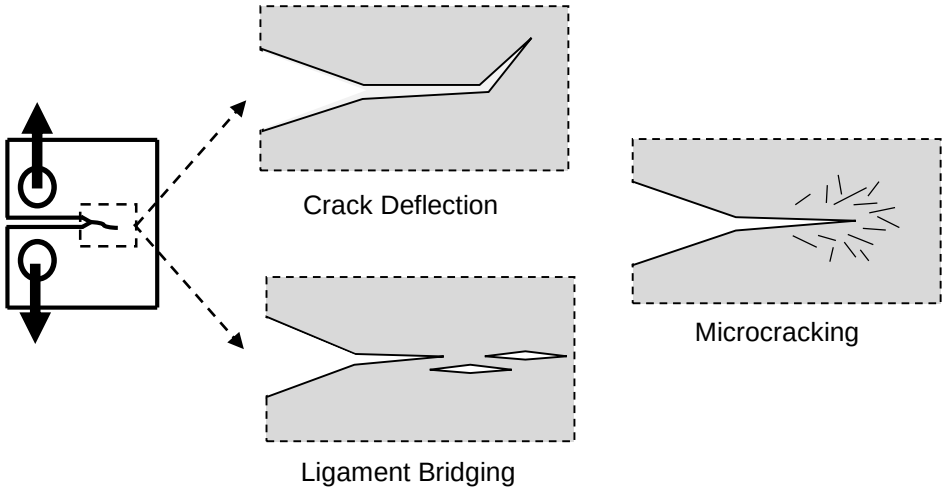

Figure 2.5: Representation of the crack path toughening mechanisms present in bone.

The toughening mechanisms shown in Figure 2.5 to significant non-linear fracture behaviour in bone and thus the use of LEFM is limited in its application to bone (Yang et al., 2006a, 2006b). In addition to these toughening mechanisms, cortical bone also undergoes irreversible plastic deformation in the form of fibril sliding and microdamage formation that leads to non-linearity (Yang et al., 2006a; Yan et al., 2007). To account for this non-linear behaviour it is necessary to apply Elastic Plastic Fracture Mechanics (EPFM) in the form of the J-integral (Yang et al., 2006b). The J-integral includes a more complete analysis of the fracture behaviour of cortical bone as it includes both linear elastic effects (similar to the SIF) and a plastic non-linear term that accounts for plastic phenomena such as microdamage formation and plastic slip of collagen fibres. As yet this technique has not been applied to the analysis of the effects of fatigue induced damage on the fracture resistance of cortical bone. It is likely that the application of the J-integral to fatigue fracture interaction will provide further insight into the effects of fatigue induced damage on both the linear and non-linear components of the J-integral fracture resistance of bone. It can be hypothesised that fatigue induced damage will interact with the plastic behaviour (i.e. collagen slip and microdamage formation during crack growth) of cortical bone and may have a more significant effect on the plastic (non-linear) component of the J-integral.

While most of the fracture mechanics work in relation to cortical bone has focused on experiments there are also a limited number of works that have used FEA analysis to analyse the fracture behaviour of cortical bone. Thus far, finite element analysis techniques have been used to analyse the effects of age and porosity on the SIF based resistance curve of cortical bone (Tang and Vashishth, 2011; Ural and Vashishth, 2006). Other finite element modelling studies have analysed the growth of microcracks in the cortical bone microstructure (Donaldson et al., 2014; Jonvaux et al., 2012; Mischinski and Ural, 2013, 2011). Some studies have focused on recreating the overall fracture resistance curve for cortical bone tests specimens using FEA (An et al., 2011; Ural and Vashishth, 2007, 2006). However, these studies did not analyse the individual contributions of the various toughening mechanisms in cortical bone (i.e. ligament bridging, deflection and microcracking) and collapsed all of these mechanisms into a single fracture law. Therefore, not only have the individual contributions of toughening mechanisms such as ligament bridging, crack deflection and microcracking not been analysed for cortical bone, but there is no analysis of mechanisms of fatigue fracture interaction using FEA.

2.3 Fatigue Properties of Cortical Bone

2.3.1 Engineering Fatigue Theory

The most common approach to analysing the fatigue behaviour of a material is the stress-life approach. This is a stochastic approach by which many (ideally defect free) samples are cycled at different stress ranges to obtain the number of cycles to failure. The resulting data is then presented as a Basquin (1910) power law expression; typically a function of the applied stress range as given by:

$$\frac{\Delta\sigma}{2} = \sigma_f'\left(N_f\right)^b \tag{2.12}$$

In this expression, the applied stress range is: $\Delta\sigma = \sigma_{max} - \sigma_{min}$ with $\Delta\sigma/2$ being the applied stress amplitude, and the number of cycles to failure is, N_f. The constants σ_f' and b are unique to the material being analysed (Suresh, 1998). In this equation it is also common to substitute the applied stress range with an applied strain range. A typical stress-life curve is shown in Figure 2.6. This curve shows that as the stress range is increased the number of cycles to failure will decrease up to the point of monotonic failure.

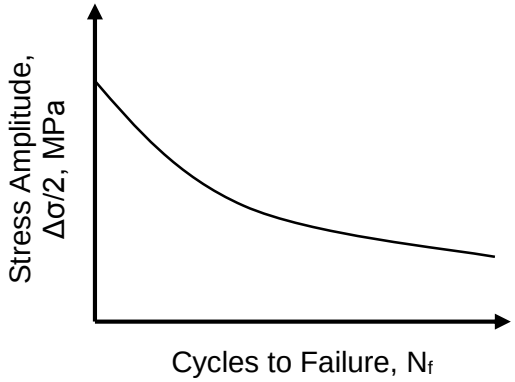

Figure 2.6: Schematic representation of the stress-life fatigue curve for typical engineering materials.

The stress-life fatigue behaviour of a material can be analysed using various loading controls with typical fatigue tests being conducted under load or strain control. The most common loading regimes for uniaxial tests are: tensile-tensile, compression-compression and fully reversed loading. For both fully tensile and fully compressive loading the specimen is loaded to a specified maximum stress value and then unloaded based on the loading ratio $R = \sigma_{min}/\sigma_{max.}$ The loading ratio for full tension or compression is often set at R = 0.1 or 10% of the maximum loading value. In contrast to this, fully reversed loading cycles a specimen between a specified maximum tensile and maximum compressive stress. The loading ratio used for fully reversed loading is R = -1 and the loading ratio R= 1 is given for monotonic loading. It is also possible to analyse the fatigue behaviour of a material in either bending or torsional loading. Torsional loading allows the analysis of (almost) pure shear loading and can also be combined with axial loading to analyse mixed mode fatigue. Bending fatigue is normally conducted using either three or four point bending, which creates a tensile stress on one surface of the beam and compressive stress on the opposing stress on the opposing surface with zero axial normal stress at the neutral axis. Apart from the loading ratio and loading mode there are other parameters that affect the fatigue life of a given material, described below.

Other factors affecting the fatigue life of a material include: test temperature, surface finish and loading frequency. The first factor, material temperature, can have a significant effect on the fatigue life of a material especially for polymers, which have relatively low melting points (Hertzberg et al., 1975; Radon and Culver, 1975; Sauer and Richardson, 1980). However, this effect can also be observed in some metals, which become more brittle with decreasing temperature, such as low and medium carbon steels (Ritchie, 1999; Rosenfield and Shetty, 1983). In general, decreasing temperature causes a material to

become more brittle and decreases fatigue life. The second factor, surface finish, affects the fatigue life of a material as a rough surface finish creates more regions of stress concentration that can initiate fatigue cracks leading to fatigue failure in less cycles than a smoother surface finish (Bayoumi and Abdellatif, 1995; Itoga et al., 2003).

The third factor, loading frequency, is coupled to another material behaviour known as creep. Creep is the behaviour of a material in response to a given load over time. That is, if a constant load is applied to a material the measured displacement will increase exponentially over time through creep processes. In contrast to this, fatigue is the response of a material to a given number of loading cycles independent of the time the specimen is held at a given loading. For some materials it is difficult to determine if there is a truly cyclic damage processes or if the damage process in the material is time dependent. For metals there is a truly cyclic fatigue process that is linked to shear slip and dislocation motion. If the material is failing via cyclic processes then increasing test frequency will have minimal effect on the number of cycles to failure. For polymeric materials test frequency is important as polymers store some of the energy during cycling as heat (Hertzberg et al., 1975; Sauer and Richardson, 1980). This leads to a phenomenon known as stress softening. If the polymer is cycled at high frequencies (>10Hz) this can lead to a large accumulation of heat that can cause the polymer to partially melt and fail (Radon and Culver, 1975; Sauer and Richardson, 1980). Depending on the composition, composite materials can show a cyclically dependent fatigue process that leads to the accumulation of microscale damage. Specifically, this takes the form of debonding and delamination in fibre composites with a polymeric matrix.

There are various material level mechanisms by which damage accumulates during fatigue loading. For a typical metal, fatigue damage forms due to plastic slip and movement of dislocations in the metallic lattice. The accumulation of these dislocations leads to an accumulation of plastic strain and eventual cracking along the shear slip planes (Lankford and Kusenberger, 1973; Miller, 1993; Tanaka and Mura, 1981). In composite materials the damage mechanism is variable based on the constituent phases of the composite. For general plastic/fibre composites (e.g. carbon fibre or fibre glass) plastic slip of polymer chains eventually causes delamination and debonding along the weak interfaces between the different phases of the composite (Harris et al., 1975; Mizutani et al., 2000). Cortical bone shares some similar characteristics with fibre composites and hence it has some similar damage mechanisms, such as the formation of microscale damage (Diab and Vashishth, 2007; Schaffler et al., 1995; Zioupos, 2001a).

During the fatigue cycling process a material accumulates damage until eventual failure. The accumulation of damage leads to various changes in apparent material properties from those measured at the start of the test. Note that the microscale material properties of the fatigue specimen do not change throughout the fatigue test however, the accumulation damage or discontinuities throughout the specimen causes the 'apparent' material properties for the bulk specimen to change. The most common material characteristic to measure the accumulation of damage during a fatigue test is the elastic modulus or the specimen stiffness for polymeric materials and composite materials such as bone (Diab and Vashishth, 2005; Zioupos et al., 2001). Note that other material characteristics such as the apparent yield stress and apparent work to fracture do change during the fatigue life of a material. However, the measurement of stiffness during a fatigue test is non-destructive and can be measured at set intervals during the test without having to interrupt the test. The stiffness loss curve for a particular specimen can be determined by analysing the linear region of the load displacement waveform at each cycle and curve fitting a line to this region with the slope of the line giving the specimen stiffness.

More recent approaches to the analysis of fatigue in materials have focused on applying the analytical techniques of fracture mechanics to analyse the mechanisms of fatigue in different materials. For the purpose of fatigue analysis the crack growth processes in a material can be divided into three main stages: stage I, nucleation and development of microscale cracks; stage II, stable macrocrack growth and stage III, unstable crack growth and catastrophic failure. The most common form of fracture mechanics based fatigue is the Paris Law, which analyses stable macroscopic crack growth due to cyclic loading (i.e. stage II crack growth) (Paris et al., 1961). The Paris Law characterises the crack growth rate with respect to the number of cycles in terms of the stress intensity factor. As the purpose of this research project is to analyse the effect of microscale damage (i.e. stage I fatigue processes) on the fracture behaviour of cortical bone, fracture mechanics approaches to fatigue (such as Paris Law fatigue crack growth) will not be considered.

2.3.2 Fatigue Damage Accumulation and Repair *in-vivo*

The skeletal system of the human body naturally accumulates fatigue damage with use (Burr, 2003; Martin, 2003; Schaffler et al., 1995; Zioupos, 2001a). The first evidence of this was given by Frost (1960) who developed an experimental method for staining human rib bones in basic fuchsin to identify damage using an optical microscope. Frost showed that human rib bones had a natural population of microcracks that could be attributed to the cyclic loading due to breathing. Subsequently it was shown that other bones, such as the femur and tibia, also have an inherent amount of microdamage due to fatigue (Schaffler et al., 1995).

There are two main types of damage present in the bone microstructure; microcracks and diffuse damage. Microcracks are classified based on their length relative to the diameter of an osteon structure (200-300μm), short microcracks appear between lamellar sheets and are 100-200μm in length. Long microcracks are classified as being >300μm and interact with osteon boundaries that can act to arrest their growth (Vashishth, 2007a). Unlike microcracks, diffuse damage is large areas of sub-microscale cracks that are approximately 1-3μm. Analysis of bone has found that microdamage can be induced *ex-vivo* by fatigue cycling and that different loading modes produce different types of fatigue damage (Caler and Carter, 1989; O'Brien et al., 2003; Zioupos et al., 1996).

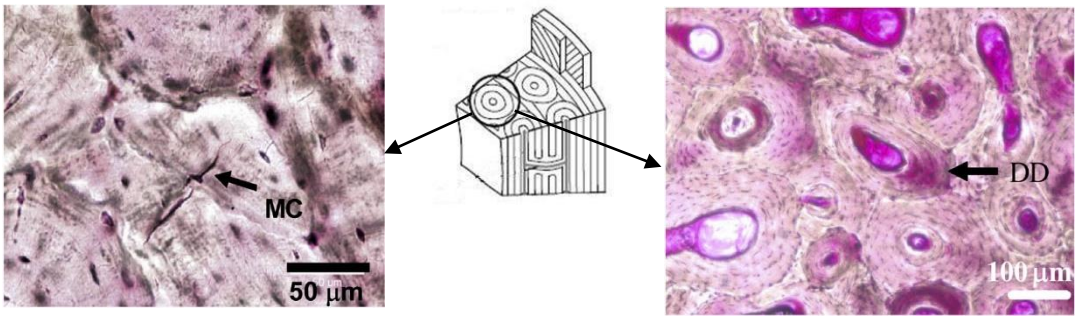

(a) Microcrack (MC) (b) Diffuse Damage (DD)

Figure 2.7: (a) Optical micrograph of a micro crack and (b) a zone of diffuse damage in cortical bone. Figure adapted from Vashishth (2007a).

Bone tissue is unique when compared to engineering materials in that it has the capability to repair accumulated fatigue damage. This repair process can be subdivided into two main categories: modelling and remodelling (Frost, 1969). Bone modelling is the process by which bone tissue is added or removed from the external or internal surface of the bone leading to changes in geometrical cross section (i.e. changes in bone macrostructure). In contrast to this, remodelling occurs in existing bone leading to microstructural changes. In particular, bone remodelling is thought to occur as a targeted mechanism of resorption (via osteoclasts) and formation (via osteoblasts) whereby a region of damaged material is removed and replaced with a secondary osteon structure. This is function of a group of cells, including osteoblasts and osteoclasts, known as a basic multicellular unit (Bruce Martin and Burr, 1982; Burr, 2003; Burr et al., 1985; Martin, 1992; Mori and Burr, 1993). An experiment by Mori and Burr (1993) using a canine model showed significant remodelling activity beginning 8 days after fatigue loading, but not immediately after loading. In this same study it was shown that the microcracks generated due to the fatigue loading occurred directly during the loading event.

The timescale for full repair of fatigue damage in cortical bone is in the order of weeks, while the fatigue damage is accumulated during the application of loading (e.g. over a few hours of intense exercise). In a study involving military recruits by Milgrom et al. (1985), 33% of stress fractures were found to occur within the first two weeks of military training. In another study using a rabbit model of stress fracture, Burr et al. (1990) found that within three weeks 72% of test subjects had developed a stress fracture. Note that these studies used bone scintigraphy to detect the presence of a stress fracture. This method detects the cellular activity present when bone is healing; however, it does not detect the fracture itself (Finestone and Milgrom, 2012).

For fragility fractures it has been shown that remodelling rates can be significantly decreased with ageing and disease and this leads to an accumulation of microdamage, which can cause failure (Diab et al., 2006; Mohsin et al., 2006; O'Brien et al., 2005a; Schaffler et al., 1995). Thus, the study of fatigue failure in cortical bone also needs to consider processes by which the damage accumulates in the material and eventually causes failure. As the damage is accumulated during a loading event with the repair process taking place in a number of weeks the damage accumulation process can be partially decoupled from the repair process. This allows for the analysis of the fatigue behaviour of bone using *ex-vivo* testing and engineering fatigue theory.

2.3.3 Fatigue Testing of Cortical Bone

Stress-life fatigue theory has been extensively applied to bone *ex-vivo* including testing under many different loading modes, such as tension (Caler and Carter, 1989; Zioupos et al., 2001), compression (Taylor et al., 1999), and torsion (Turner et al., 2001; Vashishth et al., 2001). Some of the first researchers to extensively analyse large sample sets of stress-life fatigue data for cortical bone include Carter and colleagues (Carter et al., 1976; Carter and Caler, 1985; Carter and Hayes, 1977, 1976). Carter and Caler (1985) analysed creep fatigue interaction in cortical bone. This work attempted to determine if the time to failure (creep) or the number of cycles to failure (fatigue) is an important parameter for predicting failure of bone. Note that time dependent and cycle dependent failure processes are important to consider in for many materials as cyclical failure processes can be extremely different to time dependent failure (such as dislocation build up in metals). After considering an extensive sample size Carter and Caler (1985) showed that in tension, above a stress range of 60 MPa creep (time dependent) effects were dominant, while below this stress range cyclic fatigue was dominant. They also showed that for compressive loading a cyclic mechanism was more dominant, while in tension a creep or time dependent mechanism was more dominant. Other experiments by Carter also investigated parameters that affect the fatigue life of bone including temperature, density

and microstructure (Carter et al., 1976; Carter and Hayes, 1976). This work showed that increasing test temperature from 21°C to 45°C caused a significant decrease in the fatigue life of the specimens. It was also shown that specimens with a higher density showed an increased fatigue life. Similarly, a secondary osteonal microstructure exhibited a decreased fatigue life due to the porous microstructure.

The initial work on the stress-life fatigue of cortical bone has been extended by many researchers to include an analysis of the types of damage that are associated with various fatigue loading modes (Diab et al., 2006; George and Vashishth, 2005; O'Brien et al., 2003; Taylor et al., 2003). In tension bone tends to form diffuse damage, which is characteristic of a time (creep) dependent mechanism. From the areas of diffuse damage microcracks initiate perpendicular to the loading direction, eventually causing failure of the specimen (Boyce et al., 1998; George and Vashishth, 2005). In compressive fatigue tests, microcracks form parallel to the loading direction with a length of 100-200μm (Fleck and Eifler, 2003; O'Brien et al., 2003; Taylor et al., 1999). These compressive microcracks are formed due to shear slip. Finally, torsional loading causes a fatigue mechanism that is time dependent with microcracks that are >300μm in length that interact with the osteon boundaries in bone (Taylor et al., 2003). Despite the large amount of data available for the stress-life fatigue of bone in various loading modes; the data still shows significant inter study variability making it difficult to make comparisons between data from different studies (Taylor, 1998; Taylor et al., 1999). This issue was partly resolved by Taylor (1998) who proposed a 'stressed volume' or 'Weibull' approach to resolve scatter in fatigue data. Essentially this approach is based on the assumption that a given volume will fail at its weakest point or where the worst defect exists. It is also assumed that the distribution of defects in a material is not dependent on the volume size. Thus, a larger volume is more likely to have a critical defect and will fail before a smaller volume. It follows that the relatively small test specimens will fail after a much larger number of cycles compared to a whole bone due to the number of critical defects being lower.

The use of the stress-life fatigue approach in cortical bone allows for the analysis of the number of cycles to failure. However, it does not provide any information on the mechanisms by which fatigue cracks grow and cause eventual failure of the material. To analyse the material level mechanisms of crack growth the use of fracture mechanics theory is required. Normally this analysis would be conducted using a Paris Law fatigue approach to analyse the mechanisms of crack growth in the material (Nalla et al., 2005; Shelton et al., 2003). For the purpose of this project however, the Paris Law fatigue approach is not suitable as only the microscale fatigue crack accumulation will be analysed with relation to the fracture resistance behaviour of cortical bone.

2.4 Fatigue Fracture Interaction

The accumulation of fatigue damage *in-vivo* is thought to contribute to the occurrence of clinical failures such a fragility fracture in the elderly and stress fractures in the young (Burr et al., 1997, 1990; Diab et al., 2006). Thus, there has been considerable interest in the effects of fatigue damage on the fracture behaviour of bone due to its contribution to clinical failures. The interaction of fatigue damage with the fracture behaviour of bone is termed fatigue fracture interaction. It is thought that the increase in microdamage with age is a significant contributor to the prevalence of fragility fractures (Diab et al., 2006; Schaffler et al., 1995; Vashishth, 2007a). However, there is disagreement in published work on the mechanisms by which fatigue damage affects fracture behaviour in cortical bone. Some of the proposed mechanisms postulate that microdamage formation during dominant crack growth as well as the presence of existing fatigue damage is beneficial due to stress redistribution and activation of other toughening mechanisms. Other proposed mechanisms suggest that microdamage formation leads to a decrease in toughness and a deterioration of mechanical properties with age. It is not currently clear under which circumstances microdamage is beneficial or detrimental to the fracture behaviour of bone.

There are several detrimental effects of microdamage accumulation that have been shown by previous studies. The most obvious is the analysis of aged bone that shows significantly decreased toughness, which can be partly attributed to the presence of fatigue damage (Schaffler et al., 1995; Zioupos et al., 1996; Zioupos and Currey, 1998). A number of previous fatigue fracture interaction studies have taken aged bone and determined the level of microdamage that was present *in-vivo* before mechanical testing to determine its strength (Norman et al., 1998; Yeni et al., 1997; Yeni and Norman, 2000). These studies typically show a reduction in strength and fracture toughness with age and microdamage accumulation. However, as the body ages the properties of the bone constituents (i.e. of the collagen and mineral) also deteriorate (Paschalis et al., 2004; Vashishth, 2007b; Wang et al., 2002; Zimmermann et al., 2011). This makes it difficult to discern the true role of the microdamage. Other studies have induced fatigue damage *ex-vivo* by cycling specimens at constant load amplitude (Martin et al., 1997; Parsamian and Norman, 2001; Yeni and Fyhrie, 2002). Several works show that after the development of microdamage in bone the strength and fracture toughness decreases. Although, Martin et al. (1997) showed that after considerable stiffness loss due to fatigue damage in equine bone there was a non-significant effect on the strength. This is despite the prevalence of stress fractures in race horses.

While there are detrimental effects of microdamage there are also benefits in terms of the toughening behaviour of cortical bone. In a study by Parsamian and Norman (2001), the authors propose that there is an initial increase in fracture toughness due to the presence of diffuse damage in bone, although after this the fracture toughness drops rapidly with increased damage. The results of Parsamian and Norman (2001) are limited by their small sample size with no replicates performed at each given amount of damage. Further, Parsamian and Norman (2001) did not compare their damaged specimens to a control (i.e. not damaged) group. Therefore it is possible that the results of Parsamian and Norman (2001) are only representative of noise in the data with no effect of diffuse damage on the overall fracture behaviour. Thus, considerable further work is required to understand the effects of diffuse damage on the fracture behaviour of cortical bone. A more recent work has led to the suggestion that the formation of microcracks during crack growth contributes to the toughening of cortical bone and its rising resistance curve behaviour (Zimmermann et al., 2011). Specifically it is has been suggested that the microcracks formed during crack growth may provide initiation sites for the crack growth toughening mechanisms, such as ligament bridging and crack deflection (Koester et al., 2011; Zimmermann et al., 2011). Note that no direct evidence is provided for this proposed mechanism and it is not clear if fatigue induced microcracks interact with or alter this behaviour in any way. Despite this suggestion the effect of fatigue induced damage on the normal fracture resistance behaviour of cortical bone has not been investigated. While there are some studies that have used experimental fracture mechanics to analyse the effects of fatigue induced damage on the fracture behaviour of bone there are no studies that use finite element modelling techniques to analyse this behaviour.

The main limitation of previous published work investigating the effect of microdamage on the fracture behaviour of bone is that it has used a standard fracture toughness test based on LEFM (Norman et al., 1998; Parsamian and Norman, 2001; Yeni and Fyhrie, 2002; Yeni and Norman, 2000). As mentioned previously the fracture resistance of bone increases as a crack grows, due to its inherent toughening mechanisms. It is possible that the presence of fatigue induced microdamage interacts with the toughening mechanisms in cortical bone and alters the normal fracture resistance behaviour. As the amount of fatigue induced microdamage increases with age in humans it is possible that the interaction of fatigue damage with the fracture toughening mechanisms partially explains the degradation in toughness with age. Furthermore, the LEFM approach has the limitation that it is unable to fully account for non-reversible plastic deformation such as microdamage formation and plastic slip between collagen fibrils. Therefore the use of a J-integral based resistance curve method can provide new insights into the effects of toughening due to the presence of microdamage.

Table 2.2 summarises previous studies directly related to the aim of this thesis. This summary clearly shows that there are minimal studies analysing the effects of fatigue damage on the fracture behaviour of cortical bone. Several previous studies have analysed the effects of aging on fracture toughness but they have not isolated the effects of fatigue damage. In addition to this, many of the studies have only used LEFM which cannot fully account for non-linear fracture mechanisms in cortical bone. Thus, there is a need to apply non-linear fracture resistance theory (i.e. J-integral) to gain further understanding of the mechanisms of fatigue fracture interaction in cortical bone. This will also provide further understanding of the contribution of fatigue microdamage to failure mechanisms in aged bone.

Table 2.2: Summary of previous work applying fracture mechanics theory to analyse failure mechanisms in cortical bone.

Authors	Year	Species	Specimen Type[1]	Test Type	Test Condition	Results
Vashishth et al.	1997	Human / Bovine	C(T), L	K_R	None	N/A
Norman et al.	1998	Human	C(T), L	G_{IC}	Age[2]	$G_{IC}\downarrow$ as microdamage ↑
Parsamian and Norman	2001	Human	C(T), L	K_{IC}	Ex-vivo Fatigue	Ambiguous
Yeni and Fyhrie	2002	Bovine	SEN(B), T	K_{IC}	Ex-vivo Fatigue	$K_{IC}\downarrow$ as microdamage ↑
Nalla et al.	2004	Human	C(T). L	K_R	Age	K_0, $K_R\downarrow$ as age ↑
Diab and Vashishth	2005	Bovine	SEN(B) T	K_{IC}	Ex-vivo Fatigue	$K_{IC}\downarrow$ as microdamage ↑
Koester et al.	2008	Human	SEN(B), T	J_R	None	N/A
Koester et al.	2011	Human	SEN(B), L/T	J_R	Age	J_0, $J_R\downarrow$ as age ↑

[1] C(T): compact tension specimen, SEN(B): singled edge notched bend specimen, L: longitudinal orientation, T: transverse orientation, [2] Fatigue damage density and microcrack length was measured and correlated with fracture toughness in this study.

2.5 Summary of Literature Gaps

From the preceding literature review the following research gaps can be identified:

1. It is not clear under what circumstances fatigue induced microdamage or microdamage that forms during dominant crack growth are beneficial or detrimental to the fracture resistance behaviour of bone

2. The mechanisms of fatigue fracture interaction are not well understood and there are no conceptual models explaining the effects of fatigue induced damage on the fracture resistance of cortical bone
3. Current experimental work on fatigue fracture interaction is limited by:
    - Use of a single value toughness measurement that does not consider the effects of microdamage on the full fracture resistance curve
    - Use of Linear Elastic Fracture Mechanics (LEFM), which cannot fully account for the non-linear fracture behaviour in bone, such as plasticity and microdamage formation
4. There is no numerical or finite element modelling of fatigue fracture interaction in cortical bone

The aim of the research presented in this thesis is to analyse the effects of fatigue induced microdamage on the fracture resistance behaviour of cortical bone. This research will use combined experiments and numerical modelling to propose mechanisms of fatigue fracture interaction that explain the conditions under which fatigue induced microdamage has no effect on the fracture behaviour or when it has a positive and/or negative effect. The experiments will analyse full resistance curves for cortical bone based on the J-integral as this will fully describe non-linear and plastic effects that result from the interaction of fatigue induced microdamage with new damage that is formed during crack growth. Further analysis will be conducted using crack path imaging in combination with the fracture resistance curve results to provide further evidence for the fatigue fracture interaction mechanisms proposed in this thesis. The fracture mechanisms discussed as part of the experimental work will then be parametrically analysed utilising finite element analysis techniques. The use of finite element modelling will allow each for each of the major toughening mechanisms in cortical bone (i.e. ligament bridging, crack deflection and microcracking) to be decoupled such that their individual contribution to the overall toughening behaviour can be under

Chapter 3: Experiment 1

Longitudinal Fatigue Fracture Interaction in Cortical Bone

Statement of Authorship: Experiment 1

Title of Paper	Effects of fatigue induced damage on the longitudinal fracture resistance of cortical bone
Publication Status	Published
Publication Details	Fletcher, L., Codrington, J., Parkinson, I., 2014. Effects of fatigue induced damage on the longitudinal fracture resistance of cortical bone. J. Mater. Sci. Mater. Med. 25, 1661–1670. doi:10.1007/s10856-014-5213-5 Note: Introduction has been altered to be more coherent with the overall thesis, data presentation method has also been updated

Principal Author

Name of Principal Author (Candidate)	Lloyd Fletcher		
Contribution to the Paper	Formulated overall experimental design. Conducted all experimental work and data analysis. Drafted first version of the manuscript and edited manuscript. Submitted final copy of the manuscript and managed response to peer review.		
Overall percentage (%)	80		
Signature		Date	

Co-Author Contributions

By signing the Statement of Authorship, each author certifies that:

i. the candidate's stated contribution to the publication is accurate (as detailed above);
ii. permission is granted for the candidate in include the publication in the thesis; and
iii. the sum of all co-author contributions is equal to 100% less the candidate's stated contribution.

Name of Co-Author	John Codrington		
Contribution to the Paper	Contributed to development of the work, proof read manuscript and contributed to the discussion of results.		
Signature		Date	

Name of Co-Author	Ian Parkinson		
Contribution to the Paper	Contributed to development of the work, proof read manuscript and contributed to the discussion of results.		
Signature		Date	

3 Experiment 1: Longitudinal fatigue fracture interaction in cortical bone

This experiment has been published as a journal article entitled 'Effects of fatigue induced damage on the longitudinal fracture resistance of cortical bone' (Fletcher et al., 2014).

3.1 Introduction

The purpose of the experimental component of this research is to analyse the effects of fatigue induced damage on the fracture resistance of cortical bone. For this type of experiment the test specimens are split into equal groups of control and fatigue damaged specimens. The damaged group specimens then undergo cyclic loading to induce the formation of fatigue damage while the control specimens remain undamaged (apart from any damage due to machining or that was present *in-vivo*). Both the control and damaged specimens are then fracture tested and the fracture behaviour is compared between both groups. There have been several previous studies that have used a similar experimental approach however, these studies were limited by the application of a linear elastic fracture analysis that only considered the fracture initiation toughness and not the full fracture resistance curve (Parsamian and Norman, 2001; Yeni and Fyhrie, 2002). The following introduction will analyse the results and limitations of two key previous fatigue fracture interaction studies (Parsamian and Norman, 2001; Yeni and Fyhrie, 2002). The limitations and findings of these previous studies will then be used to justify the methodology for the present experimental work.

A similar experiment to the present study of this chapter was conducted by Parsamian and Norman (2001). This study used compact tension fracture specimens which were cyclically loaded before fracture toughness testing using a linear elastic fracture approach. The main findings of this study showed that there may be a toughening effect of diffuse damage in cortical bone. However, the results of Parsamian and Norman (2001) need to be considered with some caution as they did not include a control group to compare with their fatigue damaged specimens and they did not have multiple specimens which accumulated the same amount of fatigue damage (i.e. no replicates). Parsamian and Norman (2001) proposed that the fracture initiation toughness is a fourth order polynomial function of the diffuse damage density; that is, a small amount diffuse damage provides an initial increase in the fracture toughness while increasing the amount of diffuse damage causes a decrease in the fracture initiation toughness. It is difficult to provide evidence for this type of finding as there were no replicates performed at each of the diffuse damage

levels and there was no control group to compare the result of the damaged group with. Therefore, as no replicates were performed and a small sample size was used the observed fourth order polynomial shape may not actually be a trend in the data and could be a result of scatter. Further to this the study by Parsamian and Norman (2001) did not analyse the crack path in their samples and the relationship of the crack path with the fatigue induced damage.

A study by Yeni and Fyhrie (2002) also analysed the effects of fatigue damage on the fracture behaviour of cortical bone. This study used four point bending fatigue of uniform specimens before notching and fracture testing in a three point bending configuration. The study by Yeni and Fyhrie analysed the fracture initiation toughness using a linear elastic fracture approach and showed that the accumulation of fatigue microdamage caused a significant decrease in the fracture initiation toughness of cortical bone for their fatigue damaged group when compared to a control group. This study also showed that the load-displacement curve for the damaged group was similar to the control group but it was shifted by a small amount in the positive direction of the displacement axis (x axis) and by a larger amount in the negative direction of the load axis (y axis). The translation along the load axis leads to a decrease in the critical fracture load and hence the fracture initiation toughness in the presence of fatigue microdamage.

Apart from the work of Parsamian and Norman (2001) and by Yeni and Fyhrie (2002) there has been minimal further work on the effects of fatigue microdamage on the fracture behaviour of cortical bone. However, there has been significant increase in the knowledge of the fracture behaviour of 'normal' cortical bone, this includes: the use of a fracture resistance curves and the use of a non-linear fracture approach (such as the J-integral). As mentioned previously the studies by both Parsamian and Norman (2001) and Yeni and Fyhrie (2002) used a linear elastic fracture approach. This type of fracture model has been shown to not fully account for the non-linear fracture processes in cortical bone including the plastic slip of collagen fibrils and the formation of microdamage during crack growth (Yang et al., 2006a; Yan et al., 2007).

The studies by Parsamian and Norman (2001) and by Yeni and Fyhrie (2002) only analysed the fracture initiation toughness of cortical bone in the presence of fatigue damage and did not consider the effects on the full fracture resistance curve. Fatigue microdamage has been shown to be detrimental to the fracture initiation toughness of cortical bone it is highly likely that it alters the crack propagation behaviour and resistance curve of the material. Also, the translation of the load-displacement curve proposed by Yeni and Fyhrie suggests that the resistance curve will be altered in the presence of fatigue microdamage. Furthermore, it is not known how fatigue induced microdamage

effects the ability of bone to form new microdamage during crack propagation and how fatigue induced damage effects the fracture toughening mechanisms in bone such as crack deflection and ligament bridging. Therefore it is reasoned that applying a non-linear fracture model such as the J-integral will provide increased understanding of the effects of fatigue damage on the fracture behaviour of cortical bone. Combining a non-linear fracture model, such as the J-integral, with a fracture resistance curve approach will allow for the interaction of the fatigue induced damage with the crack path toughening behaviour to be analysed. Combining non-linear fracture resistance testing with optical analysis of the interaction of the crack path with the fatigue induced damage will lead to the elucidation of the material level mechanisms of fatigue fracture interaction in cortical bone.

The aim of this first experimental study is to use a non-linear fracture resistance (J-integral) approach to characterise the effects of fatigue induced microdamage on the fracture behaviour of cortical bone. This will include an analysis of the fracture resistance curves for control and fatigue damaged bovine compact tension fracture specimens as well as comparison of the elastic and plastic components of the J-integral. The crack paths will also be analysed using fluorescence microscopy to determine the effects of microdamage on the toughening mechanisms such as ligament bridges and crack deflection. The fracture resistance curves and crack path image results will then combined to propose mechanisms of fatigue fracture interaction in cortical bone. The scope of this chapter will be limited to the longitudinal or splitting mode of fracture in bovine cortical bone due to the restrictions of the compact tension specimen configuration. *In-vivo* bone fracture is a complex process where a crack path may progress with both longitudinal and transverse propagation due to the composite microstructure and multi-directional loading. Understanding of the effects of fatigue induced microdamage on the longitudinal fracture mode of cortical bone is the first step in gaining a complete understanding of fatigue fracture interaction mechanisms in cortical bone.

3.2 Materials and Method

3.2.1 Specimen Preparation

The femur of a single bovine animal (approximate age 12-18 months) was obtained fresh from a meat wholesaler, immediately wrapped in PBS (Phosphate Buffered Saline) soaked gauze and stored at -20°C until machining. The specimens were sectioned along their length using a band saw into 30 mm slices. Each segment was then cut into four pieces by cutting through the diameter of the segment at a 45° angle to the frontal plane of the bone then taking cuts at 90° about the circumference of the bone segment from the initial cut. These segments were then wet machined to the final compact tension specimen shape as shown in Figure 3.1 using a low speed diamond saw. The holes were machined

in the specimen using a custom made jig and a cordless drill. The initial starter notch was aligned in the longitudinal direction (parallel to the long axis of the bone and approximately the same direction as the collagen fibre orientation). The nominal characteristic dimensions of the specimens (based on ASTM standard E1820 (2011)) were: initial crack length a = 4mm, thickness B = 2 mm and W = 12 mm. Refer to Figure 3.1 for a diagram of a machined compact tension specimen showing its orientation and the characteristic dimensions ‘a’ and ‘W’.

A total of 20 compact tension specimens were machined from the bovine femur used in this study. Each specimen had a circular based starter notch drilled using a 2mm drill bit and custom made jig. It was assumed that the non-standard circular notch geometry would not alter the comparison of fracture resistance results as it was consistent between control and damaged groups. This assumption is verified using finite element modelling techniques later in Chapter 6. After machining each specimen is then wet polished using increasingly fine grades of silicon carbide paper followed by a final polish using 0.5µm aluminium oxide slurry. After polishing the specimens were wrapped in gauze soaked in PBS and stored in individual airtight containers at -20°C until testing. The specimens were allocated to the control or fatigue damaged group using a stratified random sampling technique to ensure the specimens from different segments along the length or positions around the circumference of the bone were evenly distributed between groups. Each group was assigned a total of 10 specimens.

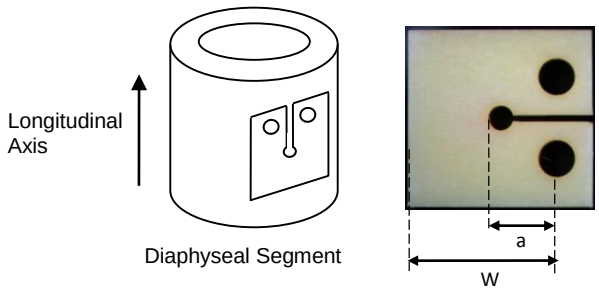

Figure 3.1: (a) Orientation of the compact tension specimens used in this study with respect to the longitudinal axis of the bone. (b) Compact tension specimen showing the characteristic dimensions ‘a’ and ‘W’.

3.2.2 Mechanical Testing Overview

The mechanical testing for this study consisted of two stages 1) cyclic loading to generate fatigue microdamage ahead of the notch without initiating a main fracture and 2) non-linear fracture resistance tests to grow a dominant crack through the fatigue damaged bone. Figure 3.2 schematically outlines the general methodology for this study.

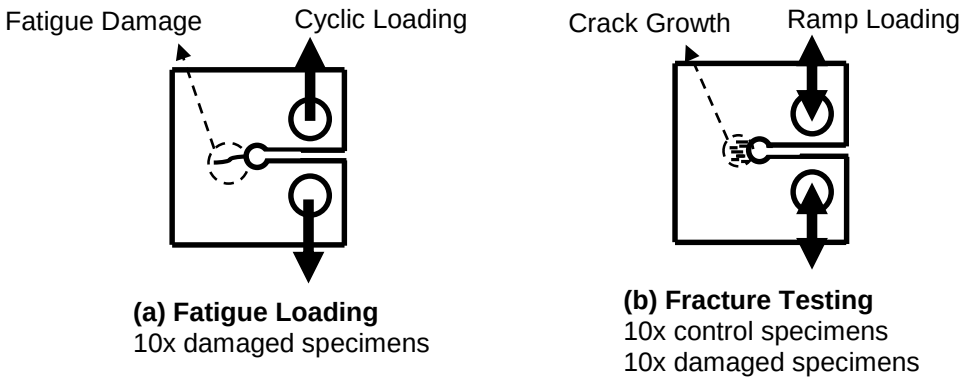

Figure 3.2: Overview of the experimental methodology. (a) Fatigue testing of the damaged group to induce the formation fatigue induced microcracks and (b) fracture testing of both the control and damaged groups (b).

3.2.3 Fatigue Damage Testing

All specimens were submerged in a solution of PBS and 0.001 M Calcein prior to any mechanical testing to label any damage that was already present in the specimen. The specimens were immersed in the stain overnight (14 hours) at 4˚C. The specimens were then imaged using a fluorescent microscope (Leica DM6600) at a magnification of 100x under blue light excitation (I3 filter cube, λ = 450-490 nm). Images were taken in a grid pattern ahead of the circular notch that consisted of 3x2 images to give a total imaged area of approximately 4mm x 2mm in size (as shown in Figure 3.3).

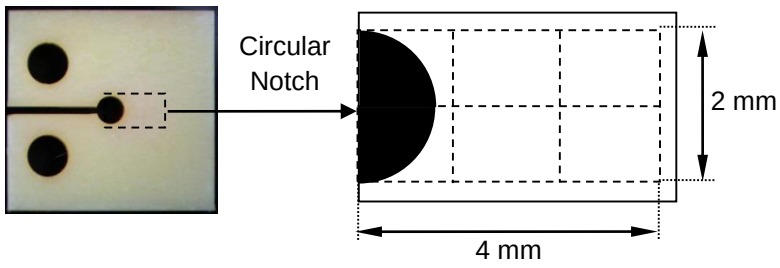

Figure 3.3: Schematic of the grid pattern imaging area used for microdamage detection.

The specimens allocated to the damaged group were then fatigued using a Test Resources 800LE4 screw driven mechanical test machine. All mechanical testing was conducted at room temperature (nominally 22°C) with the specimens fully immersed in a bath of PBS. The fatigue tests were conducted in load control using a sine waveform with a frequency of 2Hz and a load ratio $R = P_{min}/P_{max} = 0.1$ (where 'P' is the magnitude of applied load). The applied load was measured using a ±400N load cell and the load line displacement was measured *via* a ±1mm Linear Variable Displacement Transducer (LVDT) from the machine crosshead.

The monotonic failure load of the circular notched specimens was measured to be 92.8±5.2N (mean± standard deviation (SD)) with a sample size of nine specimens. All specimens were fatigued at a maximum load of P_{max} = 55N, which is approximately 60% of the monotonic failure load. The fatigue tests were stopped after the specimen had experienced a 5% stiffness loss or 40000 cycles had elapsed (whichever occurred first). Note that these limits were chosen based on the results of pilot testing which showed that macrocracks would nucleate from the microdamage after this point in the loading protocol with complete failure occurring at approximately 10% stiffness loss. The specimen stiffness was monitored *in-situ* at intervals of 500 cycles using the output from the load cell and LVDT. The specimen was then removed from the machine, immersed in fluorochrome stain, and imaged using the protocol described above to detect any fatigue damage. If microcracks were detected then the fatigue test was stopped. If no microcracks were present the fatigue test was continued in blocks of an additional 20000 cycles until the specimen had undergone a further 5% stiffness loss or microcracks were observed via fluorescent microscopy. It should be emphasised that the fatigue loading was only stopped once fatigue damage was observed optically. Note that the control specimens for each damaged group were removed from the freezer, thawed and held at room temperature for the maximum fatigue test time for each damaged group.

3.2.4 Fracture Resistance Testing

The fracture resistance curve was obtained for each specimen in terms of the J-integral, 'J', as a function of crack extension, 'Δa', using the unloading compliance method. The J-integral fracture resistance curve tests were conducted using the same test machine and sensors described in the fatigue testing protocol. Specimens were partially wrapped in PBS soaked gauze during fracture resistance testing and continuously hydrated using an eye dropper. The fracture resistance tests were conducted in displacement control with a ramping rate of 0.015mm/s (Fletcher et al., 2012). The compliance of the machine load line was determined using aluminium calibration specimens (compact tension) of similar stiffness to the bone specimens. The displacement values measured during the bone tests were then corrected based on the machine compliance. Prior to testing, the starter notch of each specimen was sharpened by sliding a flat scalpel blade over the base of the circular notch tip.

In addition to the compliance based crack length measurements, a stereo zoom microscope and an attached digital camera (Amscope SM-1TNZ) was mounted in the test frame to measure the crack length optically. To increase the contrast of the crack image the surface of the specimen ahead of the crack tip was shaded using a graphite pencil. An image was taken during each unloading portion of the test to correct the specimen

compliance based measurement of the crack length. The J-integral resistance curve was calculated according to procedures outlined in ASTM Standard E1820 using the following relationships:

$$J = J_{el} + J_{pl} \tag{3.1}$$

$$J_{el} = \frac{K^2}{E} \tag{3.2}$$

$$J_{pl} = \frac{\eta A_{pl}}{Bb} \tag{3.3}$$

In equation 3.1 the J integral is separated into two components: the elastic component (equation 3.2) and the plastic component (equation 3.3). In equation 3.2 'K' is the stress intensity factor and 'E' is the elastic modulus. For these calculations the elastic modulus was taken as 11 GPa for bovine bone in the fibre splitting (radial or circumferential) direction (Reilly and Burstein, 1975). In equation 3.3 'A_{pl}' is the incremental plastic area under the load displacement curve, 'B' is the specimen thickness, 'b' is the uncracked ligament length and η = 2+0.522 b/W (ASTM Standard E1820, 2011). The elastic component of the J-integral accounts for the linear fracture behaviour of bone while the plastic component accounts for non-linear behaviour such as plasticity and microdamage formation during crack propagation.

Following the fracture tests the specimens were again immersed in the Calcein solution to mark the crack path using the same immersion time and stain concentration for the fatigue damage detection (14 hrs in 0.001 M). This allowed for confirmation of the final crack length with the *in-situ* stereo microscope images as well as allowing visualization of toughening mechanisms along the crack path. All data processing and statistical analysis was performed using custom Matlab programs (Mathworks, Version R2012b).

3.3 Results

3.3.1 Fatigue Damage Detection

All damaged specimens showed evidence of microdamage around the circular notch following fatigue testing. A custom program was developed in Matlab (Mathworks, Version R2012b) to process the image data and assess the microdamage for each of the specimens. The primary form of damage observed in this study was linear microcracks.

For all specimens the microcrack density and the average microcrack length were determined (a typical imaged specimen is shown in Figure 3.4). The damage density was taken as the number of cracks observed in the imaged area divided by the imaged area (imaged area is shown in Figure 3.3).

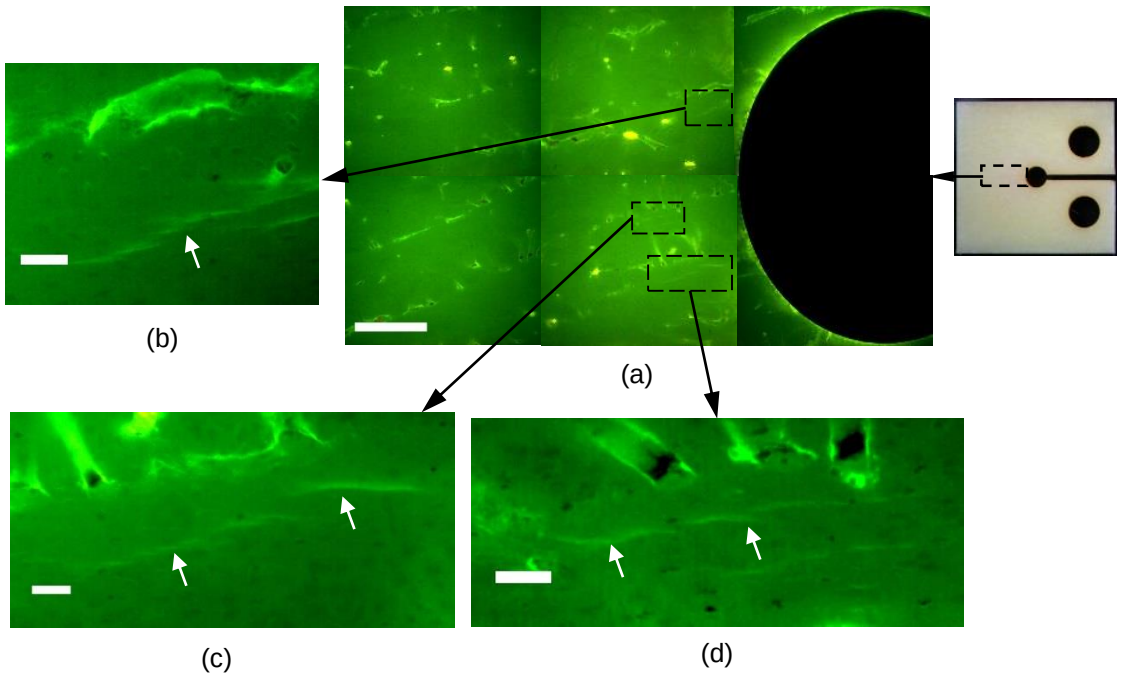

Figure 3.4: (a) Grid pattern fluorescent microscope imaging of a damaged specimen (scale bar: 500µm). Magnified views of damaged regions are shown in insets (b), (c) and (d) (scale bars: 50µm). White arrows indicate areas of fatigue damage.

The average crack density for the control specimens was 0.099±0.010 cracks/mm^2 (mean±standard deviation), for the damaged specimens it was 1.89±0.65 cracks/mm^2. Note that the crack density for the control group is representative of the 'background' level of fatigue damage present in the specimens prior to fatigue loading. This crack density for the damaged specimens is towards the upper bound of damage observed *in-vivo* and is representative of damage densities observed in the elderly who are more susceptible to fragility fractures (Schaffler et al., 1995). The average microcrack length for the control specimens was 85±12µm. The average microcrack length for the damaged specimens was 96±16µm. The damage zone size was also assessed for each specimen; this was defined as the distance from the edge of the circular notch parallel to the starter notch (nominal direction of crack growth in the resistance curve tests) to the furthest microcrack. The damage zone size was 0.99±0.25mm. This is of interest as any interaction between the existing damage and the main fracture is likely to occur within this range of the starter notch. Figure 3.4 shows the fatigue damage observed on a typical specimen following cyclic loading.

3.3.2 Fracture Resistance Curve Data

The resistance curve data and all statistical analysis were processed using custom Matlab programs (Mathworks, Version R2012b). Resistance curves for all specimens within the control group are shown in Figure 3.5 (a). The curves were obtained using a power law fit to the data for each individual specimen. The correlation coefficients, or 'r^2' value, ranged from 0.67 to 0.97 for both the control and damaged groups (note that an individual curve with scatter is shown in Figure 6.10). It can be seen in Figure 3.5 that the fracture behaviour of all specimens within the group is relatively consistent .The same was observed for the damaged group. The control and damaged group curves are compared in Figure 3.5 (b), using the scatter bands for the overall fit to the group data. This comparison shows that the damaged group has decreased toughening behaviour and the decrease in toughness is most significant near the starter notch ($0 < \Delta a < 1$mm).

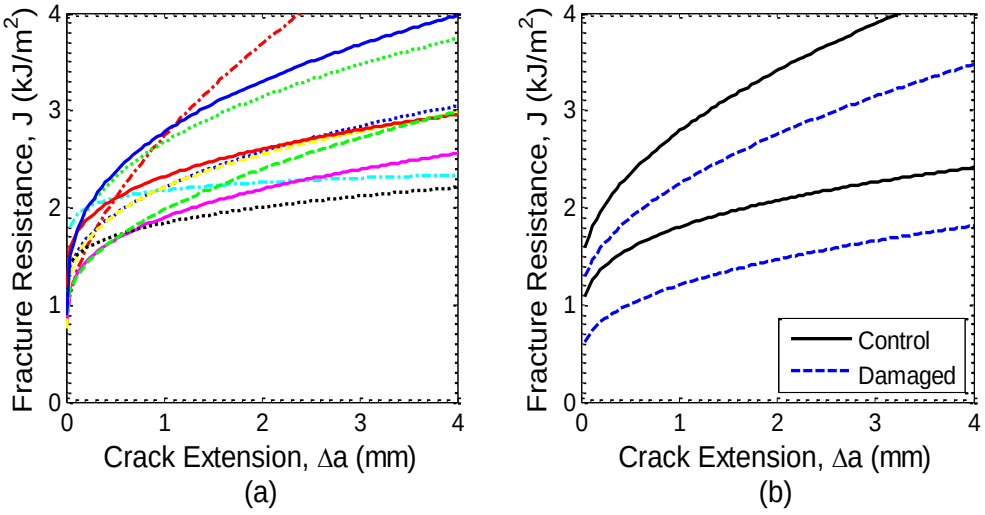

Figure 3.5: (a) All fracture resistance curves for the control group and (b) comparison of the fracture resistance curves for the control and damaged group using upper and lower scatter bands.

Note that the method of presenting the resistance curve data was chosen as it more accurately represented the shape of the fracture resistance data. Specifically, the resistance curves tend to have less scatter near the initiation point ($\Delta a = 0$) and then increased scatter as the crack grows. The reason for this behaviour is that the initial point on the resistance curve is dependent on the local material resistance which in turn is dependent on where the crack initiates in the microstructure. This behaviour is relatively consistent between specimens. Therefore the scatter near the initiation point is reduced compared to the overall resistance curves. The rest of the resistance curve after the initiation point is dependent on both the local material resistance and toughening mechanisms that form along the crack path. Both of these characteristics are dependent on the microstructural features that are encountered by the crack as it grows. As each

crack follows a unique path through the microstructure there is a unique combination of toughening mechanisms. Therefore the scatter would be expected to increase for the overall resistance curve as the crack grows due to the unique combination of toughening mechanisms.

The scatter bands for the resistance curve data were calculated by taking the set of all (Δa,J) points from each resistance curve. This set of points point was then broken into a thousand discrete steps based on increments in crack extension. The minimum and maximum data point was taken for each discrete step in crack length and the sets of minimum and maximum points were then fitted with power law curves. The proportion of data points within the scatter bands was calculated, if the proportion of data points within the bands was greater than 95% the scatter bounds were accepted. If the proportion of data points within the scatter bands was lower than 95% the number of discrete steps in crack length was decreased and the process continued iteratively until 95% or more of the data points were within the bounds.

The overall resistance curve was further broken down into the elastic and plastic components (as described in equations 1-3). The curves for the elastic and plastic components of the J-integral are shown in Figure 3.6 (a) and (b) respectively. The elastic component of the J-integral accounts for the local crack tip stress field in terms of the stress intensity factor. The plastic component of the J-integral accounts for energy absorbed during crack propagation due to plasticity and microcracking. Analysis of the elastic component of the J-integral shows that the damaged group has significantly reduced linear toughening behaviour. The damaged group has a reduced plastic component within the damage zone (a < 1mm) and approaches a similar value to the control group as the crack extends away from the damage zone.

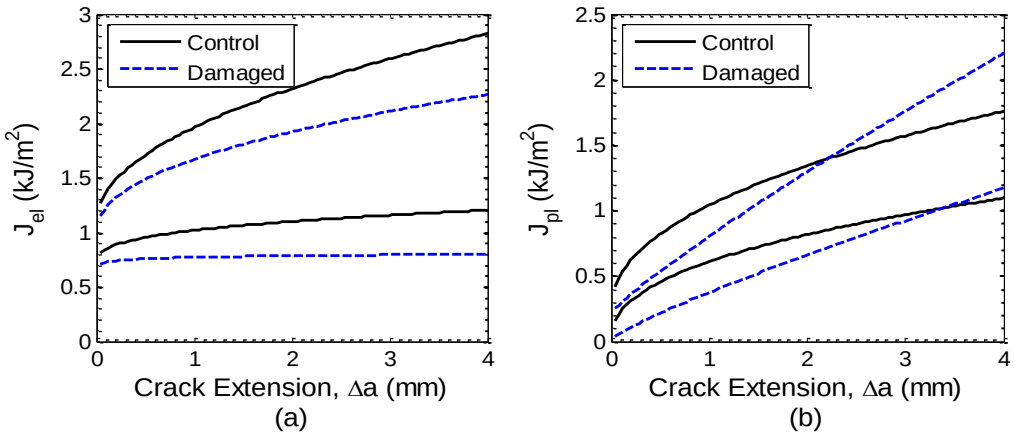

Figure 3.6: Scatter bands for: (a) the elastic component of the J-integral resistance curve for the control and damaged groups and (b) the plastic component of the J-integral resistance curve for the control and damaged groups.

The following table (Table 3.1) compares the J-integral resistance curve data for the control and damaged groups. The resistance curve was analysed based on three parameters: J_0 the fracture initiation toughness taken as the value of the resistance curve as $\Delta a \rightarrow 0$ and dJ/da the slope of the resistance curve at the point a_Q (as defined in ASTM Standard E1820 (2011)). Note that the value of a_Q was extremely consistent between specimens, for the control group a_Q = 0.23±0.004mm and for the damaged group a_Q = 0.22±0.006mm. Both J_0 and dJ/da are single value parameters that are used to characterise the behaviour of a non-linear fracture resistance curve. The value of dJ/da is included here so that the results are comparable to tests conducted using ASTM standard E1820 and previous work conducted on the fracture resistance of bone (Barth et al., 2010; Koester et al., 2011). All data was tested for normality using the Shapiro-Wilk test, all $p > 0.05$, therefore the data was assumed to be normal. T-tests were then conducted between the control and damaged group for each parameter measured in Table 1 with significance level 'α' of 0.05. The results of this study show that fatigue induced microdamage significantly decreases the fracture initiation toughness 'J_0' ($p = 0.031$) and causes no significant difference for the growth toughness 'dJ/da' at the point a_Q ($p = 0.16$).

Table 3.1: Fracture resistance curve data for the control and damaged groups including average toughening rate 'dJ/da' within ($\Delta a < 1$mm) and outside ($\Delta a > 1$mm) the damage zone. All data is presented as mean±standard deviation. The p values for the t-tests between the control and damaged group are also included with '*' denoting a significant test.

	J_0 (kJ/m^2)	**dJ/da, a_Q, ((kJ/m^2)/mm)**	**dJ/da, Δa<1mm, ((kJ/m^2)/mm)**	**dJ/da, Δa>1mm, ((kJ/m^2)/mm)**
Control	1.23±0.21	1.18±0.49	1.55±0.58	0.25±0.30
Damaged	0.96±0.29	0.85±0.38	1.07±0.26	0.11±0.38
T-test (p value)	0.031*	0.16	0.030*	0.27

As mentioned previously analysis of the fluorescent microscopy images revealed that the damage zone extended ~1mm from the edge of the circular notch. To analyse the effect of how the fracture resistance changes within and outside of the fatigue damage zone, the data within the range $0 < \Delta a < 1$mm ('near' region) was assessed and compared to the growth outside of this region ('far' region). Table 3.1 shows a comparison of the slope of the resistance curves (average toughening rate) over the first 1 mm and final sections of crack growth. This data shows that there is significant difference in the average toughening rate in the damage zone for the damaged group ($p = 0.030$). Outside of this damage zone both groups decrease in toughening rate when compared to inside the damaged zone and show no significant difference in toughening rate ($p = 0.27$).

3.3.3 Crack Path Imaging and Damage Interaction

The following figures show crack path images for both the control (Figure 3.7) and damaged (Figure 3.8) groups. The control specimen shows toughening behaviour that is typical in cortical bone including crack deflection (Figure 3.7 (d)) and uncracked ligament bridging (Figure 3.7 (c) and (d)). The damaged specimen (Figure 3.8) shows fatigue induced damage marked by white lines, which indicates that the majority of microcracks formed during fatigue did not directly interact with the main fracture.

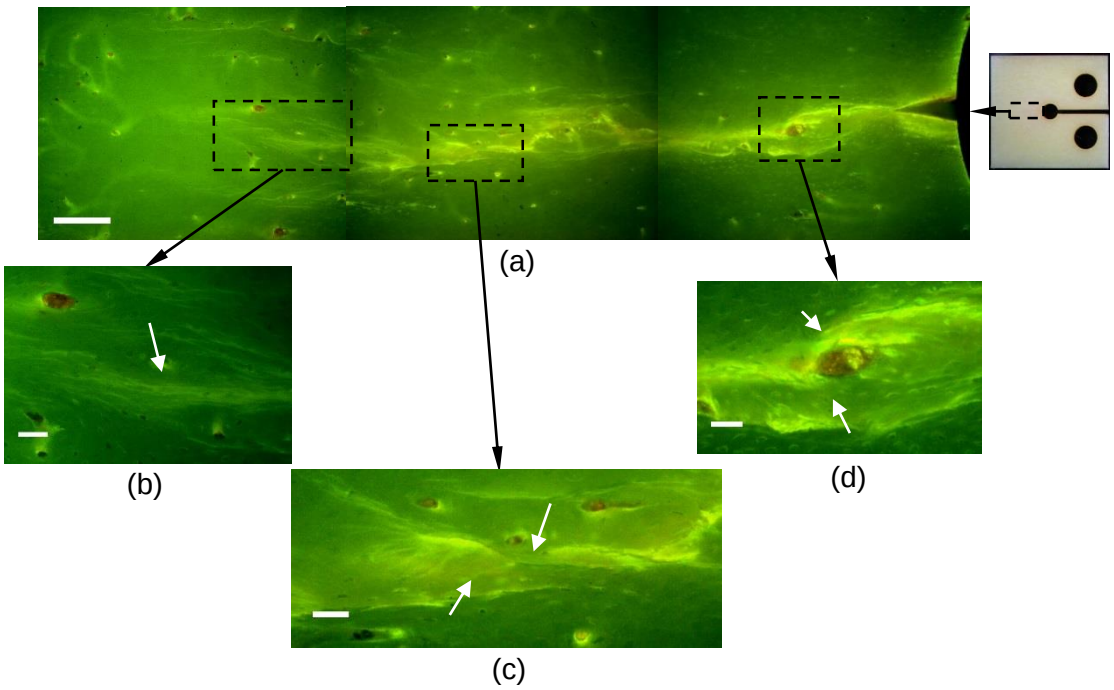

Figure 3.7: (a) Crack path of a typical control specimen showing various toughening mechanisms along the crack path: (b) microcracking ahead of the tip of the main crack, (c) several ligament bridges and (d) deflection and ligament bridge formation. Scale bar for (a) is 250µm and for (b)-(d) 50µm.

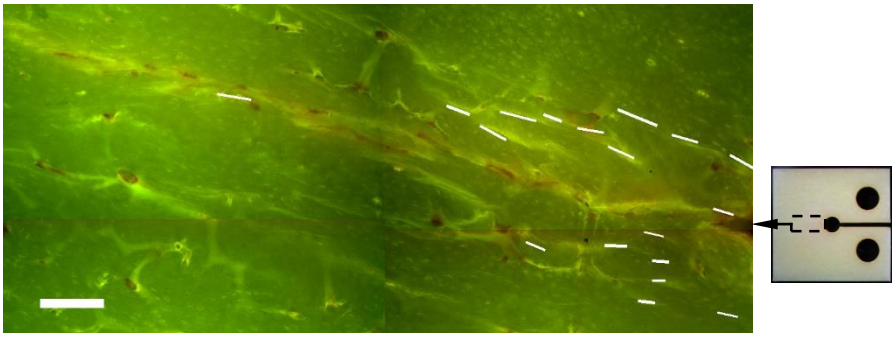

Figure 3.8: Typical damaged specimen following resistance curve testing. The approximate location of the fatigue induced microcracks are marked using white lines. Scale bar in the bottom left hand corner is 250µm.

Further analysis of the crack path images was undertaken on all specimens to characterise the presence of ligament bridges along the crack length. A ligament bridge was defined as a region of material in the crack wake that remained uncracked. Ligament bridges are thought to be the primary cause of toughening behaviour in bone (Nalla et al., 2004b). Both groups showed similar total numbers of ligament bridges along the crack path. The control group had an average of 5.3±1.2 bridges/specimen while the damaged group had an average of 5.0+1.1 bridges/specimen. However, the damaged group had a reduced occurrence of ligament bridges within the damage zone (average of 1.4±0.7 bridges/specimen) compared to outside the damage zone (average of 3.3±0.8 bridges/specimen). The control specimens exhibited similar numbers of ligament bridges within (average of 2.7±1.3 bridges/specimen) and outside of the near notch ($\Delta a<1mm$) region (average of 2.6±1.2 bridges/specimen). Further to this it was observed that five of the ten control specimens formed large ligament bridges (width > 50 μm) within near the starter notch while none of the fatigued specimens formed large ligament bridges near the starter notch.

3.4 Discussion

The results of this study are consistent with previous findings showing a decrease in fracture toughness of bone due to the presence of microcracks (Diab and Vashishth, 2005; Norman et al., 1998). The percentage decrease in fracture initiation toughness for this study is ~20% which agrees with the previous results (Diab and Vashishth, 2005; Norman et al., 1998). This reduction in toughness is expected due to the accumulation of damage in the region in which the crack initiates acting to weaken the material structure. Bone derives some of its toughening behaviour due to the dissipation of energy from the formation of microcracks in the process zone of the main propagating crack (Vashishth et al., 2003). If damage has already formed, this decreases the ability of bone to form further damage and dissipate energy, thus leading to a decrease in fracture initiation toughness. This is due to the weak interfaces in the microstructure already having formed microdamage due to fatigue loading and therefore during crack growth it is difficult for new damage to form. Analysis of the plastic component of the J-integral provides further evidence for this as the damaged group shows a significant reduction in the plastic component (related to fibril plasticity and microdamage formation) within the damage zone ($\Delta a < 1mm$). This mechanism is similar to the damage saturation mechanism proposed by Diab and Vashishth (2005).

Further analysis was undertaken to assess the average toughening rate within the damage zone ($\Delta a < 1mm$) and outside the damage zone ($\Delta a > 1mm$). This was used to characterise the effects of damage on the toughening behaviour of bone. The average toughening rate within the zone of microdamage shows that the growth toughness is decreased by the presence of fatigue induced microcracks. In contrast to this, the average toughening rate outside the damaged region for both the control and damaged specimens is similar. The toughening rate of bone due to microcracking is highly dependent on the position and location of damage with respect to the main fracture.

There are three main mechanisms by which microcracks can affect the crack propagation behaviour of bone, these include: 1) microcracks located in the vicinity of the main propagating fracture, but not linking with the main crack path; 2) microcracks linking with the main crack path and aligned with the main fracture; and 3) microcracks linking with the crack path but misaligned or offset with the main fracture. The net effect of fatigue induced microcracks on the toughening behaviour is the summation of these three mechanisms. Each of these cases is outlined schematically in Figure 3.9. The most prevalent in the current experiments is the first case where the damage is located in the vicinity of the main crack but is not linking (see Figure 3.8). Despite this mechanism being more prevalent, it is not clear which mechanism has the most significant effect on the overall fracture resistance. Furthermore, non-linking microcracks may also affect the local stress field providing either a net shielding or concentration at the main crack tip, which will influence the stress intensity factor (i.e. the J_{el} component). Note that the interaction of non-linking microcracks can be analysed using finite element modelling; this will be discussed in chapter 7.

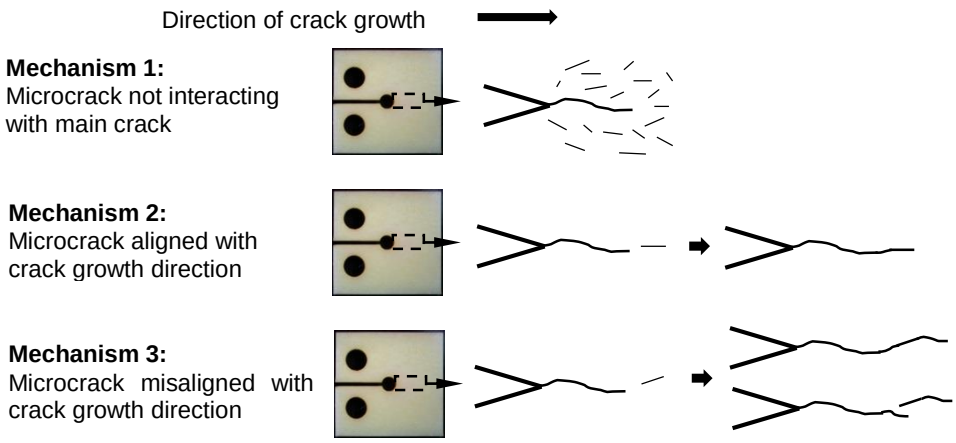

Figure 3.9: Representation of the three mechanisms of fatigue fracture interaction. Mechanism 1: microcracks in the vicinity of the main crack but not linking. Mechanism 2: microcracks linking with the main crack and aligned with the optimal direction of crack propagation. Mechanism 3: microcracks linking with the main crack and misaligned with the optimal direction of crack growth leading to crack deflection or ligament bridging.

For the first case, if there are microcracks located in the vicinity of the propagating fracture but not along its path these will act to reduce the ability of bone to form new damage and dissipate energy leading to a reduction in the rate of toughening. This is due to the weak interfaces in the microstructure already having formed damage which increases the energy required to form new damage or propagate the existing damage. A similar mechanism has previously been shown in the growth of fatigue microcracks where cracks have initiated at weak areas in the microstructure and arrested at microstructural boundaries requiring a higher driving force to continue growing (O'Brien et al., 2005b). This is also the same mechanism that acts to reduce the fracture initiation toughness in the presence of microdamage. For the second case, if a microcrack is orientated in the direction of optimal driving force then this will allow the main crack to link with it and advance through the already broken material at a lower energy 'cost' leading to a reduced rate of toughening. For the third case, if the microcrack is misaligned or offset from the direction of crack propagation this can cause deflection and/or ligament bridging leading to an increased rate of toughening.

In the longitudinally orientated specimens tested in this study the microcracks were preferentially aligned in the same direction as the main crack (see Figure 3.7). Thus, when the main fracture encounters a microcrack on its path it is more likely to allow the main crack to link and advance through the already damaged material. As the fatigue induced microcracks are orientated in the direction of crack propagation any deflection caused by fatigue induced cracks will be minimal. The fatigue induced microcracks along the path will also act to reduce the ability of bone to dissipate energy by forming new damage. Thus, the overall effect is a reduction in the rate of toughening. In contrast to this when testing in the transverse direction, microcracks may not be orientated in the direction of crack growth due to the microcracks preferentially following the weak interfaces in the longitudinal direction. Therefore, when the main crack encounters a microcrack misaligned with the direction of crack propagation it can cause a large deflection from the optimal path of loading along the fibre direction of bone. It is likely that this will cause an overall increase in the rate of toughening due to the large deflection from the optimal loading path. Thus, it would be expected that in the transverse direction the third mechanism of fatigue fracture interaction would become more influential.

Bone derives its toughening behaviour from its composite structure. Crack growth in cortical bone follows the path of least resistance. That is, the crack will follow a path where there is sufficient local driving force to overcome the material resistance in a particular direction. Previous studies have shown that the formation of microdamage is highly dependent on the microstructure and hence the preferred planes or directions of failure of

cortical bone (Boyce et al., 1998; Fleck and Eifler, 2003; O'Brien et al., 2007). Microcracks will preferentially form at the weak interfaces in the microstructure, the fact that ligament bridging or crack deflection occurs at a similar location is likely due to the weak interface in the microstructure and may not be a consequence of fatigue induced microcracks. This is evident when comparing the toughening mechanisms between control and damaged specimens (see Figure 3.7 and Figure 3.8), the control and damaged specimens show similar numbers of ligament bridges along the whole crack path however, the damaged specimens form less ligament bridges within the damage zone. This would suggest that fatigue induced microcracks inhibit the formation of ligament bridges. Thus, the microcracks that form as a result of crack propagation (i.e. not fatigue induced damage) in bone provide toughening through energy dissipation and are responsible for the formation of ligament bridges and crack deflection. Whereas the effect of fatigue induced damage is to reduce the rate of toughening by reducing the ability of bone to dissipate energy through the formation of microdamage. Ultimately the toughening behaviour of bone is a direct consequence of the microstructure and the interaction of the main fracture with weak interfaces in the structure.

Further analysis of the elastic and plastic components of the J-integral showed that both components were reduced within the damaged group. For the elastic component the toughening rate is significantly reduced in the damaged group when compared to the control. A possible explanation for this is that the damaged group showed a decreased number of ligament bridges within the damage zone when compared to the control. Reduced ligament bridging at the start of the main crack for the damaged group would reduce the applied load required to propagate the main crack. This is because there would be less bridges to support the load applied to the crack thus, reducing the elastic component of the J-integral. The plastic component shows that within the damage zone the damaged specimens have reduced toughness ($\Delta a < 1mm$). As discussed previously this is due to the fatigue induced damage inhibiting the ability of bone to form new damage during crack propagation effectively reducing the ability of bone to plastically deform by forming microdamage. Outside the damaged zone the damaged group can form new damage during crack propagation and the plastic J-integral approaches a similar value to the control group.

3.5 Conclusion

This study demonstrates the influence of fatigue microdamage on the fracture behaviour of cortical bone. The accumulation of fatigue microcracks resulted in a decrease in fracture initiation toughness due to the decreased ability of bone to dissipate energy by forming

new microcracks. The results also show that fatigue induced microcracks lead to a decrease in the rate of toughening by three mechanisms of fatigue fracture interaction:

1. Microcracks in the vicinity of the main crack and not linking: this inhibits the ability of bone to form new microcracks during crack propagation reducing the plastic component of the J-integral
2. Microcracks aligned with the optimal direction of crack growth and linking with the main crack: this causes a decrease in toughening as the main crack can propagate through the broken section of material with less energy
3. Microcracks misaligned with the optimal direction of crack growth and linking with the main crack: this can cause the formation of a ligament bridge or allows the crack to deflect from the optimum path leading to an increase in toughness

The net effect of fatigue induced microcracks on the fracture toughening behaviour of bone is the summation of these three mechanisms. In this study, the majority of fatigue induced microcracks did not link with the main crack. Furthermore, fatigue induced microcracks reduce the formation of ligament bridges and lead to a significant decrease in the toughening behaviour of bone. Thus, the overall effect of fatigue induced microcracks is to reduce the fracture initiation toughness and growth toughness of cortical bone.

3.6 Limitations and Future Work

This study has several limitations including the use of bovine bone as an analogue for human bone and the use of relatively large initial crack lengths. While the microstructure of bovine bone is different to human bone (bovine bone tends to have a plexiform structure, while human bone is secondary osteonal (Lipson and Katz, 1984; Rho et al., 1998) the toughening mechanisms present along the crack path are the same (as shown Figure 3.7). Thus, it is expected that the absolute values for fracture resistance curves will be different between human and bovine bone however, the decrease in fracture initiation toughness and average toughening rate in the damage zone will still be present as the mechanisms of fatigue fracture interaction will be the same. Furthermore, the microcrack densities observed in the fatigue damaged specimens are similar to those observed in elderly individuals at risk of fractures (Schaffler et al., 1995).

It would also be desirable to test the effect of microdamage accumulation on the fracture resistance of cortical bone using a small scale fracture testing procedure. Cracks in the order of 1-2mm are closer to the size scale of failures observed *in-vivo* (Koester et al., 2008). At this smaller scale microcracks are closer to the size scale of the main propagating failure and are more likely to interact with the main fracture and effect

toughening behaviour. Another limitation of the present study is that only the longitudinal (parallel to the long axis of the bone) crack growth direction was tested. Fracture *in-vivo* is generally due to complex mixed mode loading with crack growth in both the transverse and longitudinal directions. Thus, the resultant fracture behaviour is the superposition of each fracture mode. Cortical bone shows significantly different fracture toughness in the transverse direction and toughening mechanisms such as crack deflection become more dominant (Behiri and Bonfield, 1989; Koester et al., 2011). Therefore it would be desirable to test the effects of fatigue damage on the transverse fracture resistance of cortical bone.

The purpose of the second experimental study (Chapter 4) will be to improve on and address some of the limitations of the first experimental study (Chapter 3). The limitations that will be addressed in the second study include: analysis of fatigue fracture interaction at small scales (Δa ~1mm) and in the transverse crack growth direction

.

Chapter 4: Experiment 2

Longitudinal and Transverse Fatigue Fracture Interaction in Cortical Bone

Statement of Authorship: Experiment 2

Title of Paper	Methods for assessing the effects of accumulated fatigue damage on the fracture resistance of cortical bone
Publication Status	Published
Publication Details	Fletcher, L.C., Codrington, J.D., Parkinson, I.H., 2015. Methods for assessing the effects of accumulated fatigue damage on the fracture resistance of cortical bone, in: Proceedings: The 8th Australasian Conference of Applied Mechanics. Presented at the 8th Australasian Conference of Applied Mechanics, Melbourne, Australia.

Principal Author

Name of Principal Author (Candidate)	Lloyd Fletcher		
Contribution to the Paper	Formulated overall experimental design. Conducted all experimental work and data analysis. Drafted first version of the manuscript and edited manuscript based on feedback from other authors. Submitted final version of the manuscript and presented paper at the conference.		
Overall percentage (%)	80		
Signature		Date	

Co-Author Contributions

By signing the Statement of Authorship, each author certifies that:

i. the candidate's stated contribution to the publication is accurate (as detailed above);
ii. permission is granted for the candidate in include the publication in the thesis; and
iii. the sum of all co-author contributions is equal to 100% less the candidate's stated contribution.

Name of Co-Author	John Codrington		
Contribution to the Paper	Contributed to overall experimental design, proof read manuscript and contributed to the discussion of results.		
Signature		Date	

Name of Co-Author	Ian Parkinson		
Contribution to the Paper	Contributed to overall experimental design, proof read manuscript and contributed to the discussion of results.		
Signature		Date	

4 Experiment 2: Longitudinal and transverse fatigue fracture interaction in cortical bone

This experimental work has been published as a conference paper in the proceedings of the 8th Australasian Conference of Applied Mechanics (Fletcher et al., 2015).

4.1 Introduction

The aim of the second experimental study was to investigate the effects of fatigue induced damage on the fracture behaviour of cortical bone at 1) small crack length scales (Δa ~ 1mm) and 2) different fracture orientations (i.e. longitudinal and transverse). Both small scale fracture and fracture orientation are important for *in-vivo* failure of cortical bone. Specifically, for *in-vivo* fatigue failures such as stress fractures small scale crack growth is extremely important as these failures are normally small in size (Burr et al., 1985; Spitz and Newberg, 2002). For more catastrophic failures, such as those from a single high magnitude loading event the resultant loading on the fracture is normally mixed mode and is not normally orientated completely aligned or perpendicular to the collagen fibres. However, it is important to understand the crack growth processes in bone for both primary orientations (i.e. longitudinal and transverse) as the more complex loading conditions can be analysed as a superposition of the primary orientations.

In order to test both small scale fracture behaviour and different fracture orientations a different fracture specimen configuration to the one used in the first experimental study is required (note that the C(T) configuration was used in the first study). The reason for this is that it is impractical to machine a C(T) fracture specimen with a small initial crack length (Δa = 1-2mm) as a compact tension specimen with a 2mm initial crack length has a characteristic dimension W = 4 mm, giving outer dimensions of 5x4.8mm. Secondly, when fracture testing in the transverse direction using a compact tension specimen, the crack will deflect to the fibre direction without the use of side grooves, which would be extremely impractical to manufacture on a specimen with W = 4 mm. In addition, machining side grooves suppresses the crack deflection toughening mechanism and is not representative of the true toughening behaviour of cortical bone. There are several recommended fracture specimen configurations that can be used for non-linear resistance curve testing (as per ASTM standard E1820). The standard compact tension specimen was utilised in the first study of Chapter 3. A similar configuration is the disc shaped compact tension specimen. This configuration can be immediately discounted for use in the current study as it suffers from the same limitations as the standard compact tension specimen.

Another alternative specimen configuration is the Single Edge Notched Bend specimen (SEN(B)). This specimen geometry allows for small initial crack lengths for relatively large beam specimens and can be used for transverse fracture testing. Specifically, the geometric configuration of the SEN(B) specimen allows for an initial crack length of a_0 = 2.25 mm, a characteristic dimension of W = 4.5mm (Note that for a SEN(B) specimen 'W' is the height), a length of 20 mm and a support span of S = 18mm, which is within the practical bounds of machining. This specimen geometry will allow for crack growth in the small scale region of Δa ~1mm. The SEN(B) specimen is also suitable for testing cortical bone in the transverse direction without the use of side grooves (Koester et al., 2008).

While the SEN(B) configuration has several advantages in terms of fracture resistance testing, the method of fatigue damaging the specimens also needs to be considered. One option for fatiguing a specimen of this geometry would involve machining the specimen without the notch and then using any of the following loading modes for fatigue testing: uniform tension, uniform compression or three/four point bending. Both uniform tension and compression testing require that the specimen is clamped at its ends. For a uniform beam specimen this would cause fatigue damage to concentrate near the clamps causing failure at this region. For this reason the three point bending fatigue approach is advantageous as the maximum stress and thus, the fatigue damage, will concentrate at the mid span of the beam.

There have been two previous studies that have used a bending fatigue approach followed by notching and fracture testing. These are the study by Yeni and Fyhrie (2002) and the study by Diab and Vashishth (2005). The methodology used in each study was similar in that a four point bending fatigue approach was used with a long slender bend specimen (slenderness ratio: length/width>10). Following fatigue testing these specimens were notched and fracture toughness tested. In both of these studies the fracture toughness was characterised using a single value for the fracture initiation toughness and using linear elastic fracture theory to determine the stress intensity factor. The advantage of a long slender beam geometry is that it allows for fatigue testing that is directly comparable to literature data (see for example: Boyce et al.(1998)). However, a long slender beam geometry is not suitable for fracture resistance testing as the small width of the beam does not allow enough uncracked ligament for any significant amount of crack growth. Further to this, both of the studies by Yeni and Fyhrie (2002) and Diab and Vashishth (2005) did not perform post fracture test analysis to determine the location of the fatigue damage relative to the crack path in the specimen. Therefore the studies by Yeni and Fyhrie (2002) and Diab and Vashishth (2005) could not give direct evidence for the mechanisms that caused the decrease in fracture toughness observed in both studies.

To further the knowledge of fatigue fracture interaction mechanisms in cortical bone It would be desirable to analyse the full fracture resistance curve for fatigue damaged specimens along with crack path analysis to determine the mechanisms of interaction between the fatigue damage and the main crack path. Therefore the purpose of this study is to investigate the mechanisms of fatigue fracture interaction in both the transverse and longitudinal direction using a small scale fracture approach. This study will use a SEN(B) fracture specimen configuration that will allow analysis of the non-linear fracture resistance curves in both the longitudinal and transverse crack growth directions. Further analysis of the crack paths in the longitudinal and transverse specimens will elucidate the role of the fatigue damage on the fracture behaviour of cortical bone.

4.2 Materials and Method

4.2.1 Specimen Preparation

Two bovine femurs (from different animals) were obtained fresh from a meat wholesaler (approximate age 12-18 months). The proximal and distal epiphyses of each femur were removed using a bandsaw before sectioning the shaft of the bone into two equal length segments. Each segment was then cut into four pieces by cutting through the diameter of the segment at a 45° angle to the frontal plane of the bone then taking cuts at 90° about the circumference of the bone segment from the initial cut. The final specimen shape was then wet machined using a low speed diamond saw (Model 660, South Bay Industries). The first femur was used to machine three point bending specimens with nominal dimensions: width ‘W’ = 4.5mm, thickness ‘B’ = 2.25mm and length ‘L’ = 20mm (as shown in Figure 4.1). These dimensions were chosen such that the specimen could be notched and fracture tested following fatigue loading. The dimensions conform to the requirements of the Single Edge Notch Bend (SEN(B)) fracture specimen geometry as detailed in ASTM E1820 (2011). The specimens from the first femur were cut such that once the specimen was notched for fracture testing the crack growth direction would be approximately parallel to the fibre direction or long axis of the bone (longitudinal direction).

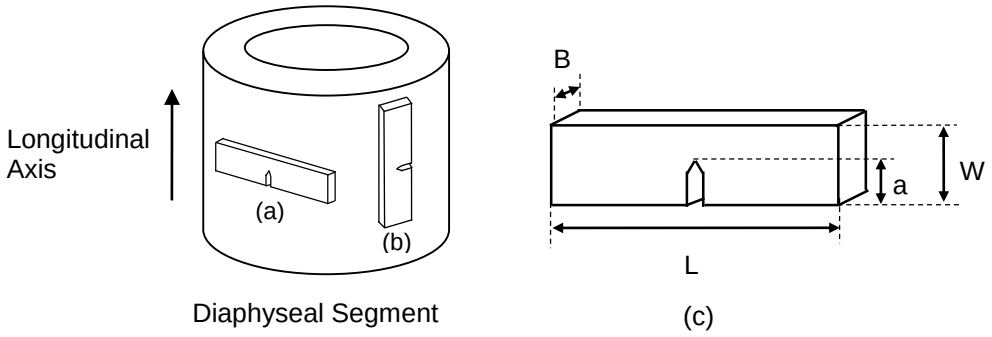

Figure 4.1: (a) Orientation of longitudinal and (b) transverse fracture specimens with respect to the long axis of the bone. (c) Specimen showing the characteristic dimensions.

A total of thirty two specimens were obtained from the first femur with ten being assigned to the control group and ten being assigned to the fatigue damaged group. Note that the remaining specimens from each femur (those not assigned to the control or damaged group) were used for monotonic pilot tests and pilot tests for the fatigue loading protocol. The second femur was used to cut three point bending specimens of the same nominal dimensions as those described above. However, the specimens were orientated such that once the specimen was notched for fracture testing the crack growth direction would be approximately perpendicular to fibre direction or long axis of the bone (transverse direction). A total of thirty two specimens were obtained from the second femur with ten being assigned to the control group and ten being assigned to the damaged group. All specimens were polished using increasingly fine grades of silicon carbide cloth to a 2µm surface finish before a final polish using a 0.5µm aluminium oxide slurry to aid in the fluorescence microscopy analysis of the fatigue damage and crack path following fracture testing. After machining, all specimens were stored in Phosphate Buffered Saline (PBS) soaked gauze at -20°C. All specimens were thawed and rehydrated overnight in a bath of PBS at 4°C before mechanical testing. Immediately prior to mechanical testing all specimens were stored in a bath of PBS at room temperature (nominally 22°C) for 2 hours.

4.2.2 Mechanical Testing Overview

The mechanical testing for this study consisted of two sequential parts: 1) cyclic loading to generate fatigue microdamage in the damaged group specimens of the longitudinal and transverse groups and 2) fracture resistance testing of both control and damaged specimens from the longitudinal and transverse groups. This is outlined schematically in Figure 4.2 below.

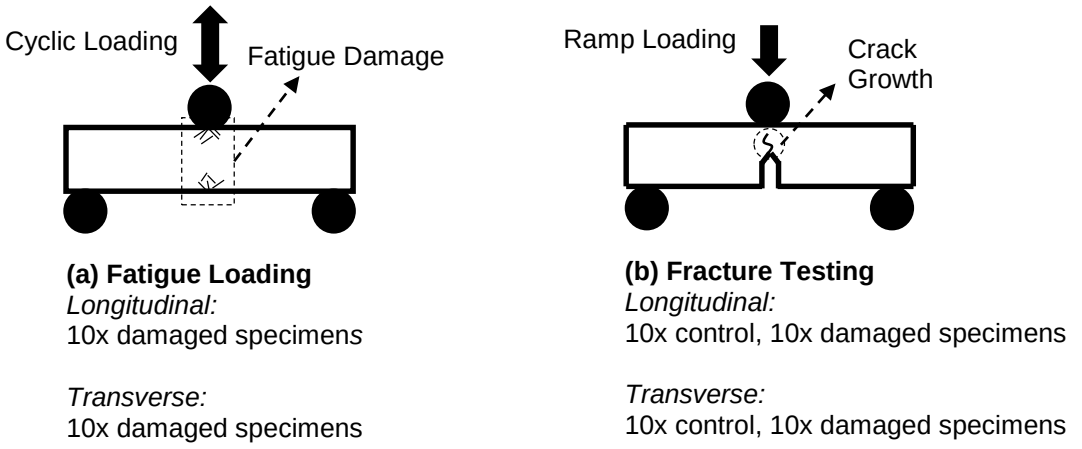

Figure 4.2: Outline of experimental methodology including: (a) fatigue loading to generate microdamage in the damaged specimen and (b) fracture testing of both control and damaged group specimens.

4.2.3 Fatigue Damage Detection and Fatigue Damaging Protocol

Prior to any mechanical testing all specimens were immersed in a fluorochrome stain (Calcein) and imaged to identify any existing damage due to the machining process. The specimens were immersed in a solution of PBS and 0.001M Calcein overnight (14 hours) at 4°C. All imaging of fatigue damage was performed using a Leica DM6600 fluorescence microscope with the specimen exposed to blue light at a magnification of 100x. The specimens were imaged in a 5x2 grid pattern (5.1x2.7mm images) from the tensile edge along the height of the specimen at its mid span. Following the fatigue testing protocol all specimens were again immersed in the calcein stain and the damaged specimens were subsequently imaged using the protocol described above. The crack path for all specimens was then imaged following the fracture resistance testing.

All specimens allocated to one of the damaged groups were fatigue loaded using a Test Resources 800LE4 screw driven materials testing machine. The output load was measured using a ±400N load cell and the load line displacement was measured using a ±1mm LVDT mounted against the cross head of the test machine actuator. The purpose of the cyclic loading was to cause fatigue damage to accumulate in the specimen without causing complete failure. The tests were continued until the specimens had undergone 5% stiffness loss (pilot testing showed that failure occurred at approximately 10% stiffness loss). All specimens were fatigue loaded in three point bending with a support span of 'S' = 18mm (the distance between the lower anvils) with a contact roller radius of 1mm. Each specimen was fatigued at a maximum load that would correspond to a maximum outer fibre stress at the mid span of 70MPa for the longitudinal specimens and 130MPa for the transverse specimens (this stress range was chosen based on pilot testing and represents a compromise between test time and physiological loading). Fatigue testing was conducted in load control using a sine waveform. The loading frequency was 2Hz with a constant loading ratio $R = P_{min}/P_{max} = 0.1$. All fatigue tests were conducted at room temperature (nominally 22°C) with the specimen submerged in a bath of PBS. Note that the control specimens for each damaged group were removed from the freezer, thawed and held at room temperature for the maximum fatigue test time for each damaged group.

4.2.4 Fracture Resistance Testing

Fracture resistance tests were conducted on the longitudinal and transverse specimens following the fatigue loading described above. The specimens were notched using a low speed diamond saw such that the initial crack length was $a_0 = 2.25$mm ($a/W = 0.5$) or greater (as specified in ASTM E1820). The notch was then sharpened using a flat bladed scalpel. The fracture resistance tests were conducted using the same mechanical test machine and sensors as described in the fatigue testing section above.

The fracture specimens were orientated in the three point bending fixture, such that the crack would grow towards the edge of the specimen that had undergone tensile loading during the fatigue protocol. The unloading compliance method was used to determine the J-integral fracture resistance, with corresponding crack length measurements made *in-situ* using a stereo microscope. For the purpose of processing the resistance curve data the crack length was inferred from the standard compliance equations. The initial crack length was corrected based on the optical crack length similar to the method used by Nalla et al. (2004a). The reason for this is that the crack paths in the transverse specimens include large amounts of deflection and *in-situ* methods of measurements of crack length can become unreliable. Conversely, the use of a compliance-based crack length is more consistent compared with optical methods and gives an indication of the crack length as the equivalent ideal (or straight) crack length. The longitudinal specimens show much straighter crack paths and can be processed using the *in-situ* crack length data. However, for the two groups to be compared similar methods of processing need to be used. The fracture resistance tests were conducted in displacement control with a constant ramping rate of 1mm/min. During the fracture resistance testing the specimens were kept hydrated by a gauze wick soaked in PBS with periodic hydration provided using an eye dropper. The J-integral was calculated at each unload step using the equations outlined in ASTM E1820 (2011) and discussed in Section 3.2.4. All data processing and statistical analysis was performed using custom Matlab programs (Mathworks, Version R2012b).

4.3 Results

4.3.1 Fatigue Damage Localisation

The fatigue damage images were analysed for both the longitudinal and transverse groups. Figure 4.3 shows typical fatigue damage patterns in both the longitudinal and transverse specimens. For the longitudinal specimens fatigue damage tended to form on the tensile edge of the specimen with long slender microcracks mostly aligned with the fibre direction of the bone, as shown in Figure 4.3 (a). For most of the longitudinal specimens, the damage formed on the compressive side (underneath the top anvil) was minimal compared to the fatigue damage formed on the tensile side. For the transverse group fatigue damage formed equally on both the tensile and compressive edges of the specimens. The compressive damage side of a typical transverse specimen (Figure 4.3 (c)) shows some damage from indentation of the top anvil with distinct microcracks radiating away from the anvil contact point. The tensile edge of the transverse specimens shows similar fatigue microdamage morphology to the longitudinal specimens. However, the orientation of the damage is less dependent on the fibre direction (see Figure 4.3 (a) and (c)).

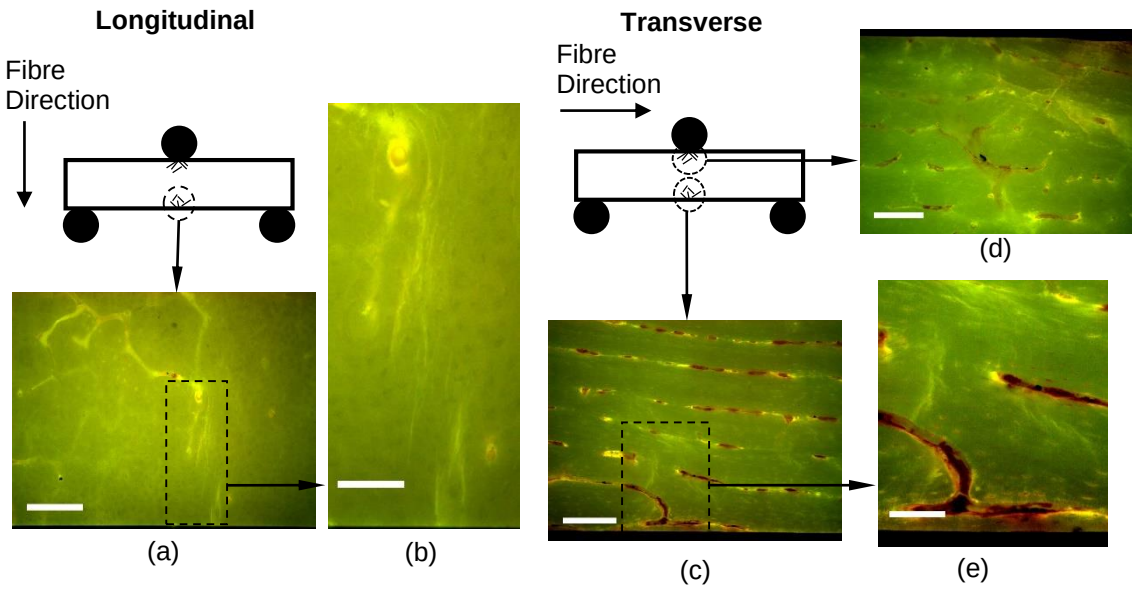

Figure 4.3: (a),(b) Fatigue damage images for a typical longitudinal specimen and (c) to (e) show fatigue damage in a transverse specimen. Note that the fatigue damage has concentrated at the top and bottom quarter of the specimen. Scale bars for (a), (c) and (d) are 250 µm and the close up insets (b) and (e) are 100µm.

The analysis of the fatigue damage patterns in Figure 4.3 shows that the fatigue for a uniform specimen concentrates at the outer edges of the specimen. Thus, the fatigue damage concentrates in a region far from central portion of the specimen that is used for crack growth in the fracture resistance tests. Therefore it is unlikely that the fatigue damage will directly interact with the crack path toughening behaviour.

4.3.2 Fracture Resistance Curves

Fracture resistance testing was performed on all specimens in the longitudinal and transverse groups. Table 4.1 details the fracture resistance data for all test groups. Normality was tested for each of the variables analysed in Table 4.1 using the Shapiro-Wilk test with normality being assumed for all variables with $p > 0.05$. T-tests were performed between the control and damaged group for both the fracture initiation toughness (initial value or y-intercept of the resistance curve) and growth toughness (slope of the resistance curve at a_Q). Note that for the longitudinal specimens, a_Q = 0.22±0.008mm and for the transverse, a_Q = 0.22±0.01mm, (mean±standard deviation). A statistical test for the variables given in Table 4.1 was considered significant if $p < 0.05/3$ or $p < 0.0167$, using the Bonferroni correction for multiple comparisons. No statistically significant differences were observed between any of the test groups. Note that while there is no significant difference between control and damaged groups within each specimen orientation, there is a significant difference between the results for the longitudinal and transverse fracture groups.

Table 4.1: Fracture resistance data for both longitudinal and transverse groups. Statistical comparisons are shown for the control and damaged groups as well as the longitudinal and transverse control groups. The data is presented as mean ± standard deviation with '*' denoting a significant test.

	Longitudinal		**Transverse**	
	J_0, (kJ/m^2)	**dJ/da, a_Q, ((kJ/m^2)/mm)**	**J_0, (kJ/m^2)**	**dJ/da, a_Q, ((kJ/m^2)/mm)**
Control	0.65±0.25	1.82±0.64	2.02±0.83	9.79±4.3
Damaged	0.63±0.27	1.51±0.48	2.20±0.77	10.6±4.6
T-test (p value) Control vs Damaged	0.89	0.58	0.91	0.73
T-test (p value) Long vs Trans	0.0004*	0.0002*		

Figure 4.4 shows all of the fitted resistance curves for both (a) the longitudinal and (b) the transverse control groups, this figure gives an indication of the overall variance in fracture resistance curves between specimens. The damaged specimens from each group showed a similar distribution of resistance curves. The correlation coefficients for the fitted resistance curves of all specimens ranged from 'r^2' = 0.87 to 0.99.

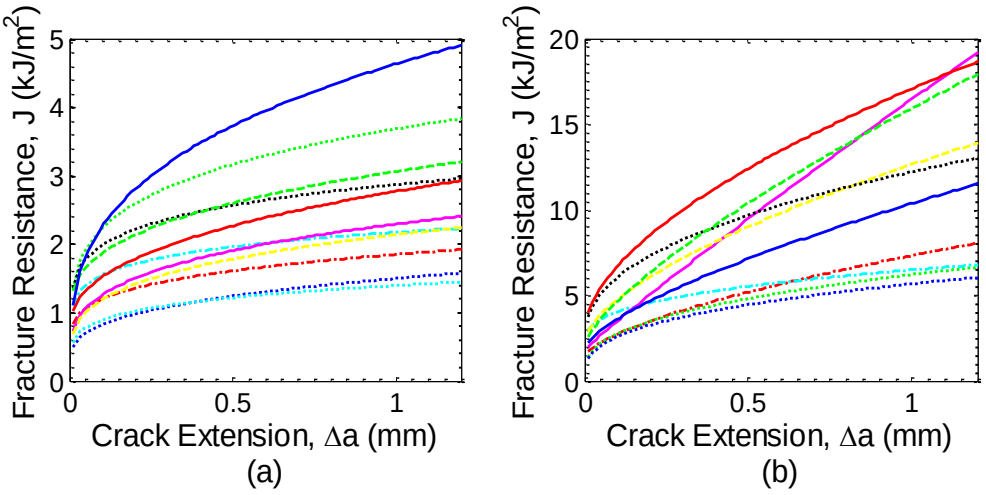

Figure 4.4: All fracture resistance curves for the control groups (a) longitudinal control and (b) transverse control specimens.

Figure 4.5 shows a comparison of the scatter bands for (a) the overall fracture resistance curves of the longitudinal groups and (b) the transverse groups. The numerical data presented in Table 4.1 is reflected in the analysis of the scatter bands for the overall fracture resistance curves. The scatter bounds for the curves shown in Figure 4.5 show significant overlap for both longitudinal and transverse groups indicating minimal difference between control and damaged specimen for each primary orientation.

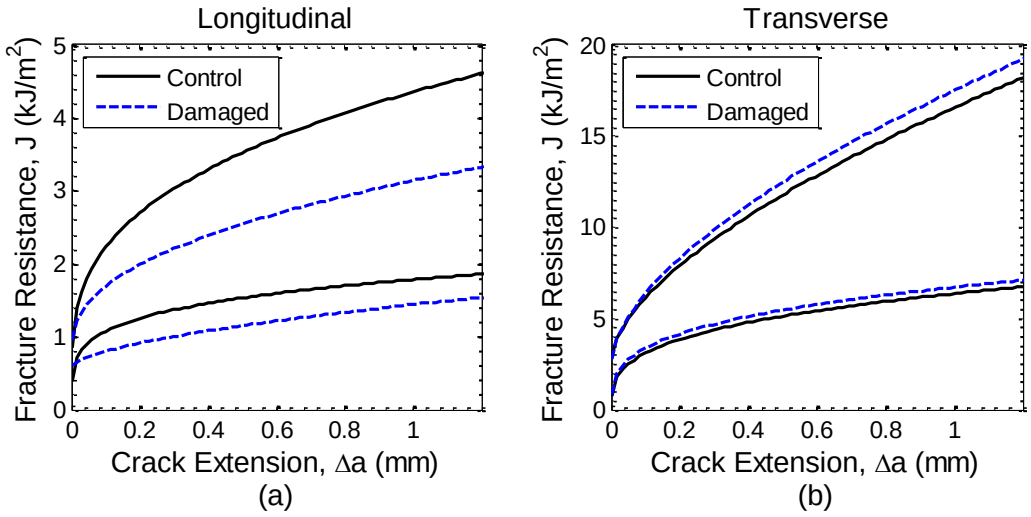

Figure 4.5: (a) Overall fracture resistance curves for the longitudinal and (b) transverse groups, the scatter bands for both the control and damaged group are shown in each case.

Figure 4.6 (a) compares the scatter bands for the elastic component of the J-integral for the longitudinal and (b) transverse groups. Figure 4.7 compares the plastic component of the J-integral for the longitudinal (a) and transverse (b) groups. The scatter bounds for the elastic and the plastic components of the J-integral are similar for the tensile and compressive damaged groups when compare to their respective control. Similar to the comparison of the overall fracture resistance curves the curves for the elastic and plastic components of the J-integral show minimal differences when comparing the damaged to control specimens.

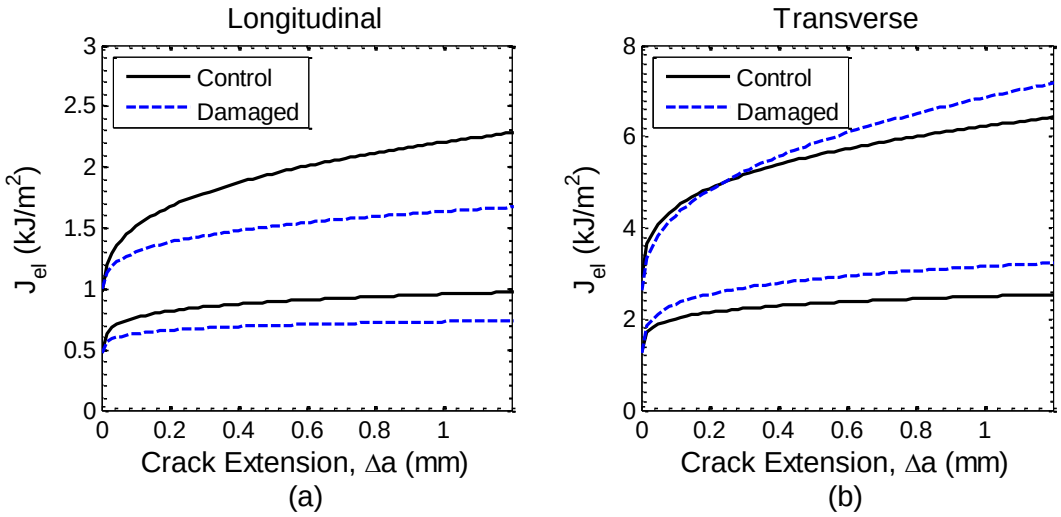

Figure 4.6: Comparison of scatter bands for the elastic component of the J-integral fracture resistance curve 'J_{el}'. (a) Shows the results for the longitudinal group and (b) shows the results for the transverse group.

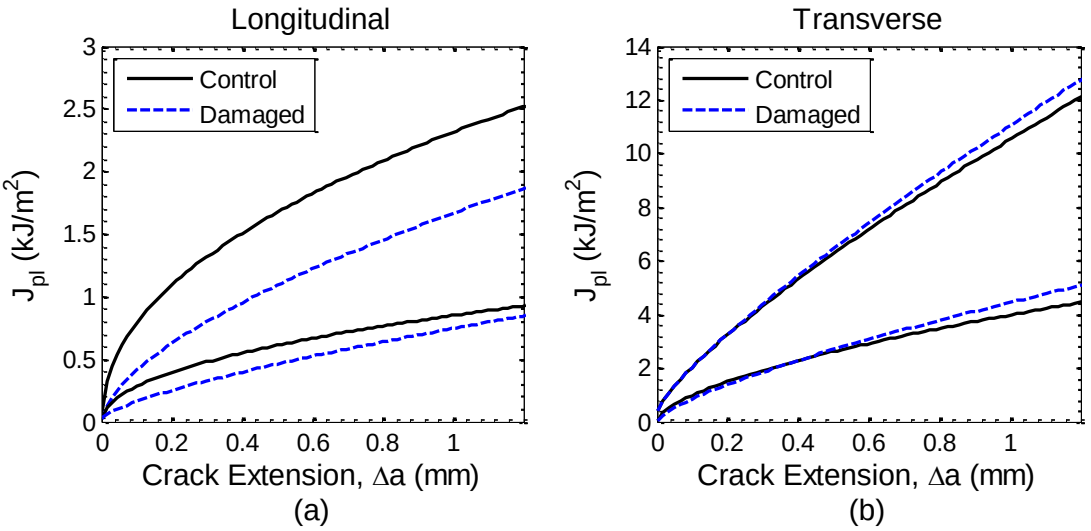

Figure 4.7: Comparison of scatter bands for the plastic component of the J-integral fracture resistance curve 'J_{pl}'. (a) Shows the results for the longitudinal group and (b) shows the results for the transverse group.

4.3.3 Crack Path Imaging

The fracture resistance curves showed no statistically significant differences between control and damaged specimens for both either longitudinal or the transverse specimens. Thus, it would be expected that the crack path toughening mechanisms for the control and damaged groups would be similar. While there were no differences between the control and fatigue damaged specimens there are significant differences in crack path toughening when comparing the longitudinal and transverse control groups. Analysis of the crack path toughening mechanisms for the longitudinal and transverse fracture specimens shows that the toughening behaviour is significantly dependent on collagen fibre orientation. Crack path images are shown for a typical longitudinally orientated specimen in Figure 4.8 and a typical transverse fracture specimen Figure 4.9. Note that the crack path for the longitudinal specimen is primarily aligned with the fibre direction. While the longitudinal specimen shows minimal crack deflection it does show a significant amount of uncracked ligament bridging, which can be seen in Figure 4.8 (b). In contrast to this the transverse fracture specimen shows significant amounts of crack deflection with the main crack path following a 'stair step' pattern though the 'brick like' microstructure in the bovine bone (Currey, 1960, 1959) (see Figure 4.9). Comparison of the crack path images with images of the fatigue damage showed that the fatigue induced damage did not interact with the main crack path directly.

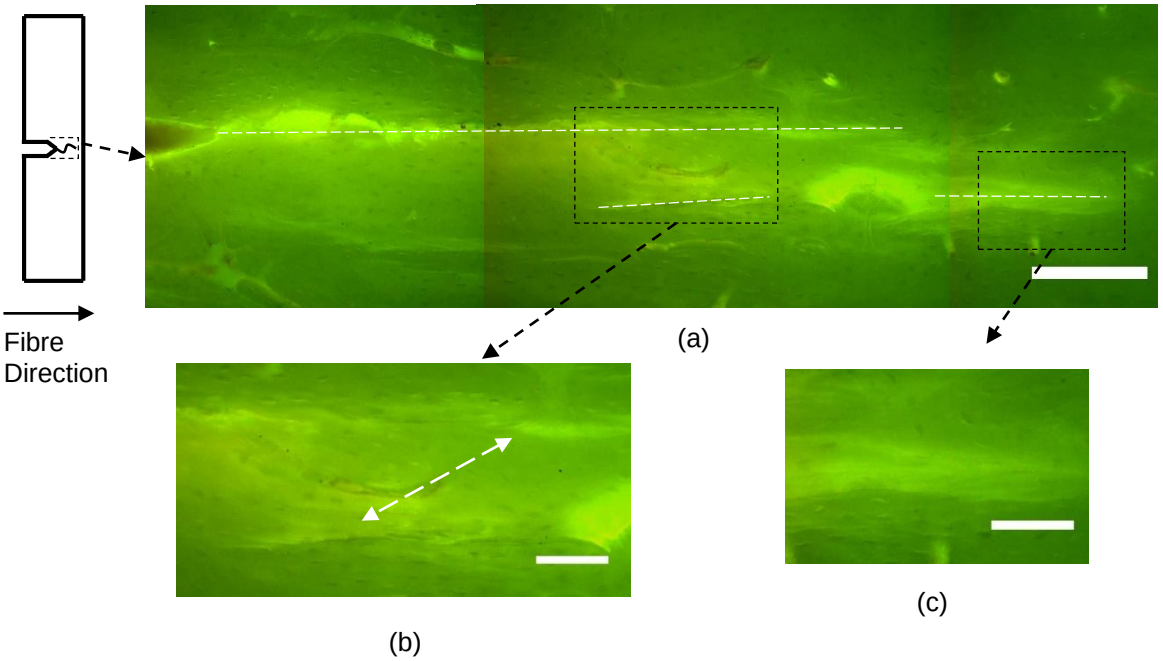

Figure 4.8: (a) Crack path for a longitudinal control specimen. (b) Close up view of an uncracked ligament bridge with the crack tips marked using white arrow heads. (c) Microdamage formation at the crack tip. The main crack path has been marked with a dashed white line to improve clarity. Scale bar for (a) is 250µm and scale bars for (b) and (c) are 100µm.

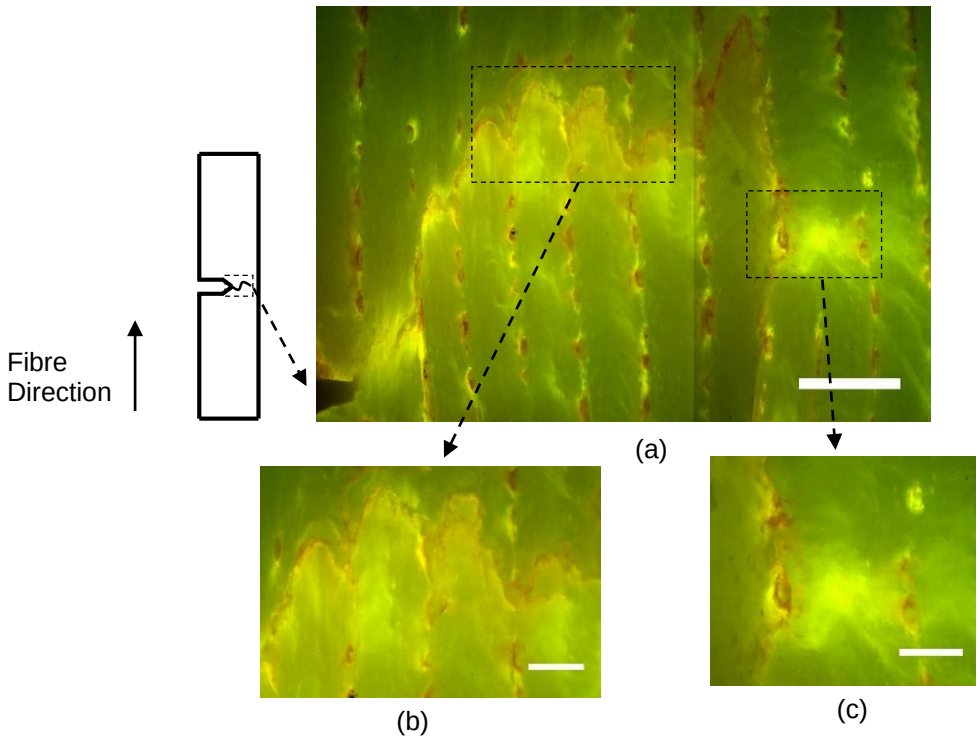

Figure 4.9: (a) Crack path for a typical transverse fracture specimen showing significant amounts of crack deflection. (b) Magnified view of stair step deflection region. (c) Crack tip microdamage. Scale bar for (a) is 250µm and scale bars for (b) and (c) are 100µm.

The crack path images (Figure 4.8 and Figure 4.9) show distinct patterns of staining. For both figures pools of lighter green stain indicate the presence of diffuse damage. From both of these figures it is clear that the stain is mainly localised near the crack path with the intensity reducing further from the main crack path. Also, near the crack path microcracks are marked with a light green stain and appear as more distinct breaks in the structure. For the transverse crack image the osteon structure are marked with a brown stain colour similar to the main crack path. This could be an indication that these regions have more mineral exposed for the stain to bind to.

It is also interesting to note that the microdamage formed during crack growth is similar to the induced fatigue microdamage (Figure 4.3) for both the longitudinal and transverse groups. Specifically, the longitudinal specimen forms microdamage during crack growth that takes the form of long slender microcracks orientated approximately parallel to the crack growth direction (approximately parallel to the fibre direction). Also for the longitudinal specimens the crack growth microdamage concentrates near the main crack path. For the transverse specimens the crack growth microdamage forms in a manner that is less dependent on the fibre orientation. The crack growth microdamage for the transverse specimens also forms at larger distances from the main crack path compared to the longitudinal specimens.

4.4 Discussion

4.4.1 Analysis of fatigue fracture Interaction

For both the longitudinal and transverse damaged group specimens the fatigue testing protocol was able to produce fatigue damage without causing failure of the specimen, this is shown in Figure 4.3. Both the longitudinal and transverse damaged groups showed fatigue damage concentrated along the outer edges of the specimen. Analysis of the fracture resistance curves showed no statistically significant difference between the fracture initiation toughness and growth toughness for these specimens (see Table 4.1). Further to this, the overall fracture resistance curves were very similar when comparing the control and damaged specimens from each group. This is evident when considering Figure 4.5, which shows significant overlap of the scatter bands for the resistance curves of the control and damaged specimens. This similarity in the fracture resistance curves is also evident for the elastic and plastic components of the J-integral for control and damaged specimens (see Figure 4.6 and Figure 4.7). Overall, there are no significant differences in the fracture resistance behaviour shown between the control and damaged specimens of each group.

This result is different to previous work where *ex-vivo* fatiguing produced a significant decrease in the fracture initiation toughness (Diab and Vashishth, 2005; Fletcher et al., 2014; Parsamian and Norman, 2001; Yeni and Fyhrie, 2002). A possible explanation for the results of the present study is seen when the fatigue damage for the uniform specimens is analysed with respect to the crack path of the fracture resistance test. The fatigue damage formed in the specimens in both the longitudinal and transverse groups concentrated towards the outer edges (outer quarters) of the specimen (see Figure 4.3). However, when the fracture resistance test is performed a notch is cut that has a depth of half the specimen width. A crack is then grown from this notch for the fracture resistance test. For the uniform specimen configuration the fatigue damage is occurring on the outer edges while the crack growth for the fracture test is occurring in the middle section of the specimen. As the fatigue damage is not located on the crack path for the fracture resistance test it is expected that no interaction of the fatigue damage with the crack path would be observed and there should be no significant difference in fracture resistance between the control and damaged groups as observed in this study. From these results, it can be seen that the uniform three point bending specimen that is notched following fatigue testing is not a suitable method for analysing fatigue fracture interaction mechanisms in cortical bone. This is because the crack growth for the fracture test does not occur in the fatigue damaged zone and hence there will be no interaction of the fatigue damage with the main crack path.

Previous studies by Yeni and Fyrhie (2002) and Diab and Vashishth (2005) did show a statistically significant difference in the fracture initiation toughness (single toughness value measured using LEFM) for uniform specimens that were notched following fatigue testing. There are a number of methodological differences in the study by Diab and Vashishth (2005) when compared to the present work that may account for the difference in results. These include: use of a non-standard long slender fracture specimen (compared to the standard SEN(B) geometry used in the present work) and the use of a four point bending fatigue method (compared to the three point bending method used in this study). The long slender specimen configuration used by Diab and Vashishth (2005) is non-standard and is only suitable for fracture initiation toughness tests not fracture resistance tests. For the present study the dimensions of the uniform specimens were chosen to conform to the requirements of the SEN(B) configuration for fracture resistance testing thus the specimens and had a low aspect ratio (short and wide). This configuration allows for an uncracked ligament of suitable length for stable crack growth and therefore the full resistance curve can be analysed. The choice of a long slender beam configuration in the study by Diab and Vashishth (2005) was to allow for fatigue damage accumulation in four point bending similar to other previous fatigue studies in bone (Boyce et al., 1998).

The use of a four point bending method with an inner span of half the outer span will lead to a relatively large fatigue damage zone within the inner span of the specimen. For the present study a three point bending method was chosen to concentrate the damage along the same axis as the initial notch.

A limitation of the study by Diab and Vashishth (2005) is that the localisation of the fatigue damage and the location of the fatigue damage relative to the crack path was not analysed. It is possible that the fatigue damage concentrated on the outer edges of the specimen similar to what was observed in the present study. This would cause the fatigue damage to not be located near the crack path and hence any interaction of the fatigue damage with the crack path is unlikely. Also, as a four point bending fatigue method was used by Diab and Vashishth (2005) the damage zone would be relatively large compared to the overall specimen dimensions. Thus, the decrease in fracture initiation toughness observed in the study by Diab and Vashishth (2005) is more likely due to the large area of fatigue damage leading to bulk changes in the specimens' material properties. That is, large fatigue damaged areas may change the overall stress field in the specimen and hence change the observed fracture toughness due to these changes rather than by a direct crack path interaction mechanism.

It is worth contrasting the four point bending fatigue method used by Diab and Vashishth (2005) with the three point bending fatigue method used in this study. Four and three point bending lead to significantly different stress profiles in the specimen undergoing fatigue loading and therefore the damage distribution would be expected to be different. The main difference between these two loading modes is that the three point bending fatigue method leads to the area of maximum stress being concentrated underneath the central anvil while four point bending distributes this area between the top two anvils. Therefore for a given stiffness loss as a result of fatigue loading the damage from three point bending will be concentrated on the edges of the specimen in the plane of the top anvil (as is shown in Figure 4.3). For a four point bending fatigue specimen the damage will be distributed over the larger area between the top anvils leading to a less dense damage distribution. However, as both configurations are under bending loading the beam neutral axis (i.e. the longitudinal centre line of the beam) will have zero axial stress. Hence as described above the damage will be minimal near the centre of the specimen and will not interact with the crack path for a fracture test.

4.4.2 Comparison of Longitudinal and Transverse Fracture Behaviour

While the analysis of fatigue fracture interaction was not possible in this study it was possible to gain some insight into the difference in fracture behaviour for the longitudinal and transverse groups. Analysing the fracture resistance data for the longitudinal

specimens shows that the transverse specimens have significantly higher fracture initiation toughness and significantly higher growth toughness (toughening rate/slope of the resistance curve). A comparison of the longitudinal control group to the transverse control group shows that the average fracture initiation toughness of the transverse control group was approximately three times higher than the longitudinal control group. The average growth toughness of the transverse control group was approximately five times higher than the longitudinal control group (see results in Table 4.1). Comparison of the overall fracture resistance curves (Figure 4.4 and Figure 4.5) also shows that the transverse specimens have higher initiation toughness and a higher rate of toughening.

The significant difference in fracture resistance curves between longitudinal and transverse fracture specimens can be attributed to microstructural effects and contrasting crack path toughening behaviour (as shown in Figure 4.8 and Figure 4.9). In the absence of any other toughening mechanisms (i.e. ligament bridging, crack deflection) the transverse crack growth direction will have a higher resistance to both crack initiation and growth. The reason for this is that for the crack to propagate it must break across the collagen fibres which requires a larger applied stress than splitting between the fibres. This material resistance effect is evident when contrasting the yield stress of cortical bone in the fibre breaking (150MPa) and fibre splitting direction (54MPa) (Reilly and Burstein, 1975).

A further difference in fracture resistance behaviour between the longitudinal and transverse specimens is evident when comparing the elastic and plastic components of the J-integral (Figure 4.6 and Figure 4.7 respectively). For both the elastic and plastic component of the J-integral the transverse specimens show a higher initiation point and higher rate of toughening when compared to the longitudinal specimens. The elastic component of the J-integral describes the applied loading and how this interacts with the local material resistance to crack growth. Transverse crack growth requires that the crack either break across the fibres (high local material resistance) or that the crack deflects along these fibres to a non-optimal orientation (reduced driving force). Whereas a longitudinal crack has lower local material resistance to crack growth as the crack can propagate along the weak interfaces in the microstructure (i.e. between lamellar sheets or collagen fibres). Hence, it would be expected that the transverse specimens would have a higher elastic component of the J-integral when compared to longitudinal specimens. The plastic component of the J-integral results from non-linear crack growth behaviour such as plasticity, microdamage formation and energy consumed by toughening mechanisms such as crack deflection and ligament bridge formation. At the end of the crack growth region the plastic component of the J-integral for the transverse group is

approximately ten times that of the longitudinal specimens. This suggests that plastic phenomena contribute significantly to the difference between overall resistance curves for the transverse and longitudinal specimens. For the transverse specimens it is possible that crack deflection consumes a significant amount of energy during crack growth and this could account for the significantly higher plastic component of J-integral. In addition to the differences in the elastic and plastic components of the J-integral the longitudinal and transverse specimens also show different crack growth microdamage and different crack path toughening mechanisms.

The crack growth microdamage for both the longitudinal and transverse specimens shows similar morphology to the fatigue damage induced in the damaged group specimens. For the longitudinal specimens the crack growth microdamage forms approximately parallel to the crack propagation direction (which is approximately parallel to the fibre orientation in the microstructure). This microdamage takes the form of long slender microcracks approximately parallel to the crack path. The reason both the fatigue microdamage and crack growth microdamage form in this manner is due to the orientation of the weak interfaces in the microstructure. Specifically, the applied stress is acting to split apart the weak interfaces between collagen fibres/lamellar sheets so that microdamage forms along these interfaces. For the transverse specimens the crack growth microdamage forms in patterns that are less dependent on the orientation of the lamellar sheet or the collagen fibre orientation. This is due to the applied stress being orientated along the collagen fibres. Where microdamage will form is a competition between the local material resistance and the direction of maximum resolved principal stress.

Apart from the material resistance to crack growth there is also a difference in the crack path toughening mechanisms for the longitudinal and transverse specimens. Comparison of the crack path images (Figure 4.8 and Figure 4.9) of a typical longitudinal and transverse fracture specimen from this study shows that the longitudinal specimen exhibits only a minimal amount of crack deflection with the main crack propagating along the fibre direction of the bone specimen. In contrast to this the transverse fracture specimen shows significant amounts of crack deflection and a ‘stair step’ pattern of crack growth following the ‘brick like’ microstructure of the bovine bone. The longitudinal specimen shows the formation of large ligament bridges along the crack path rather than the deflections observed in the transverse specimen. Analysis of the crack path images from this study shows that in the longitudinal fracture specimens ligament bridging is the more prevalent toughening mechanism while for the transverse fracture specimens crack deflection is the more prevalent toughening mechanism. The orientation dependence of fracture initiation toughness in cortical bone has been shown in previous fracture initiation

studies using bovine bone (Behiri and Bonfield, 1989) and fracture resistance studies in human bone (Zimmermann et al., 2011). It has also been shown previously that bovine cortical bone has a higher fracture initiation toughness than human cortical bone (see for example: Norman et al., 1995b; Vashishth et al., 1997 and Nalla et al., 2004a; Yeni and Norman, 2000). These previous studies and the results of the present study suggest that the fracture resistance of cortical bone is highly dependent on the crack growth direction and the overall microstructural arrangement of the base components of the cortical bone composite.

The fracture resistance behaviour of a material is highly dependent on its microstructure, therefore it would be expected that bovine and human bone would exhibit different toughening behaviour based on the differences in their microstructures. This effect is especially prevalent when considering the case of transverse crack growth for human and bovine bone. Comparing the microstructure of bovine and human bone shows that bovine bone has a 'brick like' microstructure (see Figure 4.9) while human bone exhibits a secondary osteonal structure (Nalla et al., 2006; Yeni and Norman, 2000). While the microstructures of human and bovine are different they both exhibit similar toughening mechanisms, such as microcracking, ligament bridging and crack deflection. As the mechanisms of fatigue fracture interaction proposed in this study are based on interaction with these mechanisms they would be similar but different in magnitude for human bone.

4.5 Conclusion

The aim of this experimental work was to investigate the effects of fatigue microdamage on the fracture resistance behaviour of cortical bone at a small relative scale and for both longitudinal and transverse crack growth. Unfortunately, the experimental results did not show any fatigue fracture interaction as the fatigue damage did not occur in the crack growth area for the fracture resistance tests. The results of this study suggest that the current methodology (fatiguing a uniform beam specimen before notching and conducting a fracture resistance test) is not a suitable method for investigating the effects of fatigue fracture interaction in cortical bone. However, the comparison of the longitudinal and transverse control fracture specimens did provide further insight into the differences in fracture resistance behaviour and crack path toughening mechanisms for these crack growth directions.

The current methodology (fatiguing a uniform beam specimen before notching) caused the fatigue damage to concentrate towards the outer edges of the uniform bend specimen. Therefore no fatigue damage formed in the centre half of the specimen where the crack growth for the fracture resistance test takes place. Thus, when the fracture resistance tests were performed no interaction between the crack path and fatigue induced damage

was observed in the stable crack growth portion of the test. The concentration of fatigue damage away from the crack growth zone of the fracture resistance test explains why there were no significant differences observed in the fracture resistance curves for the control or damaged groups. This indicates that uniform bending fatigue tests are not suitable for analysing the mechanisms of fatigue fracture interaction in cortical bone using a resistance curve approach.

Despite the limitations of this study the comparison of the longitudinal and transverse control specimens provided insight into the different fracture behaviour observed in each of these primary crack orientations. The fracture resistance curves for longitudinal and transverse specimens showed significant differences in fracture initiation, growth toughness and fracture toughening mechanisms. Comparison of the control specimens from both the longitudinal and transverse control groups shows that the 'brick like' microstructure of bovine bone leads to a 'stair step' like pattern of crack deflection in the transverse direction, which leads to significant toughening. The comparison between the longitudinal and transverse fracture specimens also shows that for longitudinal cracking, ligament bridging is the most prevalent mechanism while for transverse cracking, crack deflection is the most prevalent toughening mechanism.

4.6 Limitations and Future Work

The main limitation of this work is the concentration of fatigue damage away from the notch for the fracture resistance tests. Therefore in future experiments the SEN(B) fracture specimen geometry will need to be modified to concentrate the fatigue damage in the region ahead of the main notch for the fracture resistance tests. A second limitation of the present study is that it only analysed the scenario were the specimen was notched such that the crack in the fracture test was growing toward the edge that had accumulated tensile fatigue damage. Therefore for future experimental work it would be desirable to analyse the effects of both tensile and compressive fatigue damage on the fracture behaviour of cortical bone.

Chapter 5: Experiment 3

Fatigue Fracture Interaction in cortical Bone for Different Fatigue Damage Morphologies

5 Experiment 3: Fatigue fracture interaction in cortical bone for different fatigue damage morphologies

5.1 Introduction

The purpose of Experiment 3 was to analyse the effect of fatigue induced microdamage on the transverse fracture resistance of cortical bone using a small scale approach and analysing different fatigue damage morphologies. As discussed in Chapter 4 it is desirable to analyse the fracture resistance behaviour of cortical bone at relatively small scales (Δa ~ 1mm) to be relevant with respect to clinical fatigue failures. Further, at this length scale the propagating fracture is within an order of magnitude of the characteristic length of the fatigue induced damage. Hence, it is likely that for these relatively similar scales the fatigue induced microdamage will have a more pronounced effect on the fracture resistance behaviour of cortical bone. This experimental study also analysed the effect of different fatigue damage morphologies on the fracture resistance of cortical bone. The two main types of fatigue damage normally observed *in-vivo* are both diffuse damage and linear microcracks. For young bones the proportion of diffuse damage tends to be higher while for older individuals linear microcracks become more prevalent (Burr et al., 1998; Diab et al., 2006; Schaffler et al., 1995). Therefore investigation of the effects of diffuse damage on fracture resistance will have important implications for the analysis of stress fractures *in-vivo* while the analysis of linear microcracks will be more significant for fragility fractures.

Cortical bone shows two distinct morphologies of fatigue damage when loaded in either tension (diffuse damage nucleating linear microcracks) or compression (linear microcracks) parallel to the collagen fibre direction (Boyce et al., 1998). Each of these types of fatigue damage interacts differently with the cortical bone microstructure. Thus, it was expected that the different types of damage would interact differently with the fracture resistance of cortical bone. Under tensile loading cortical bone shows a diffuse type damage pattern that appears as large areas of stained bone under an optical microscope. When analysed under an electron microscope this area of damage appears as a web of small 1-3 μm cracks (Diab and Vashishth, 2007; Vashishth, 2007a). With continued loading these areas of diffuse damage nucleate distinct microcracks. Compressive loading produces microcracks in the bone microstructure of 100 to 300 μm length. These microcracks tend to form at the weak interfaces of the cortical bone microstructure such as between lamellar sheets. Fatigue microcracks will generally arrest

at microstructural barriers such as the cement line of an osteon (Diab and Vashishth, 2005; Lee et al., 2000; O'Brien et al., 2005b; Vashishth, 2007a; Zioupos, 2001a).

Diffuse damage and linear microcracks interact with the microstructure of cortical bone differently. Diffuse damage tends to form in areas that cross microstructural boundaries such as across the cement lines around osteons and across lamellar sheets. Microcracks tend to form in the weak interfaces of the microstructure such as between lamellar sheets. An area of diffuse damage is formed from many small cracks (~1-3 μm) that do not significantly interact with the microstructure of cortical bone (Boyce et al., 1998; Diab et al., 2006; Vashishth, 2007a; Zioupos and Currey, 1994). It is unlikely that diffuse damage will affect the fracture behaviour of cortical bone as it does not directly interact with microstructural features that are responsible for crack path toughening mechanisms (i.e. weak interfaces in the microstructure). However, tensile and compressive microcracks are on the order of 100 to 300 μm in length, which is within an order of magnitude of the total crack extension in a fracture resistance test ($\Delta a < 2$ mm). Therefore they are more likely to interact with the fracture behaviour of cortical bone. Further to this, microcracks tend to form at the weak interfaces in the cortical bone microstructure. These weak interfaces play a significant role in the overall fracture behaviour of cortical bone by contributing to toughening mechanisms such as microcracking, crack deflection and ligament bridging (Koester et al., 2008; R. . Nalla et al., 2005; Vashishth et al., 2003).

Apart from investigating different fatigue damage morphologies Experiment 3 also addressed some of the limitations of the second experimental study (Chapter 4). In the second experimental study a Single Edge Notch Bend SEN(B) configuration was chosen as it allowed for testing at small crack lengths (crack extension, $\Delta a \sim 1$mm) and it allowed for fracture testing transverse to the longitudinal axis of the bone. The second experimental study used a uniform beam configuration for fatigue damage accumulation before being notched and performing fracture resistance tests. This type of test methodology has significant limitations for investigating the mechanisms of fatigue fracture interaction in cortical bone. The reason for this is that fatigue damage of a uniform beam specimen tends to concentrate in the outer quarters of specimen while the fracture test is performed such that the crack grows in the middle half of the specimen. Hence there was no interaction of the fatigue damage with the crack path of the fracture test because the damage was not located near the crack path. As a consequence, no significant differences in fracture behaviour were observed between the control and fatigue damaged groups. Experiment 3 also aimed to develop a new methodology that would allow for the analysis of fatigue fracture interaction mechanisms in the transverse crack growth direction and at small crack lengths. For the purpose of developing a new

methodology it is desirable to use a Single Edge Notched Bend 'SEN(B)' specimen configuration as it allows for testing at small crack lengths and transverse fracture testing. However, it would not be possible to fatigue damage a standard notched SEN(B) specimen as the standard notch geometry would be too sharp leading to macrocrack initiation rather than the accumulation of a zone of fatigue damage ahead of the notch. To address this limitation it was decided that the standard notch geometry would be replaced by a blunt circular notch. This methodology was used in the first experimental study successfully with a circular notched Compact Tension specimen configuration.

The aim of this study was to investigate the mechanisms of fatigue fracture interaction in cortical bone, specifically analysing the transverse crack growth direction using a small scale fracture approach. This study also analysed the effects of both tensile and compressive fatigue damage on the fracture resistance behaviour in order to elucidate the role of different types of fatigue damage in the fracture behaviour of cortical bone. This study used a circular notched SEN(B) specimen configuration which will allow for the accumulation of fatigue damage around the blunt notch before sharpening. The notch was then sharpened using a scalpel blade and performing fracture resistance tests were performed. Comparison of the fatigue fracture interaction mechanisms for both diffuse damage and linear microcracks potentially provides new insight into their contribution to the aetiology of clinical failures such as stress and fragility fractures.

5.2 Materials and Method

The methodology for this study was based upon that of the previous two experimental works presented in Chapters 3 and 4. The protocols used for sectioning the specimens, imaging the fatigue damage/crack path and for the fatigue/fracture resistance testing were the same as in the previous experiments. The major difference in experimental method between this study and the second experimental study (Chapter 4) was the use of a circular notch with Single Edge Notch Bend SEN(B) specimen geometry.

5.2.1 Specimen Preparation

Two bovine femurs were obtained fresh from a meat wholesaler (approximate age 12-18 months). The proximal and distal epiphyses of each femur were removed using a bandsaw before sectioning the shaft of the bone into two equal length segments. Each segment was then cut into four pieces by cutting through the diameter of the segment at a 45° angle to the frontal plane of the bone then taking cuts at 90° about the circumference of the bone segment from the initial cut. The final specimen shape was then wet machined using a low speed diamond saw (Model 660, South Bay Industries). Specimens were stored at -20°C wrapped in gauze soaked in Phosphate Buffered Saline (PBS). Both

femurs were used to machine circular notched, Single Edge Notched Bend 'SEN(B)' specimens with nominal dimensions: width W = 4.5 mm, thickness B = 2.25 mm and length L = 20 mm (as shown in Figure 5.1). The circular notch was machined using a bench top mini-mill such that the initial crack length was a_0 = 2.25 mm (a/W = 0.5) or greater (as specified in ASTM E1820) with a circular notch diameter, d = 3 mm. It was assumed that the non-standard circular notch geometry would not alter the comparison of fracture resistance results as it was consistent between control and damaged groups. This assumption is verified using finite element modelling techniques in Chapter 6. Note that the mill was irrigated using a spray bottle of PBS to maintain specimen hydration and reduce degradation from heating. The specimens were orientated such that the notch was aligned with the radial direction of the long bone, with the crack growth direction from outer to inner fibre, as shown in Figure 5.1. This orientation causes the crack to grow transverse to the collagen fibre direction in cortical bone. All specimens were wet polished using increasingly fine grades of silicon carbide paper to aid in the imaging of fatigue induced damage and crack path analysis.

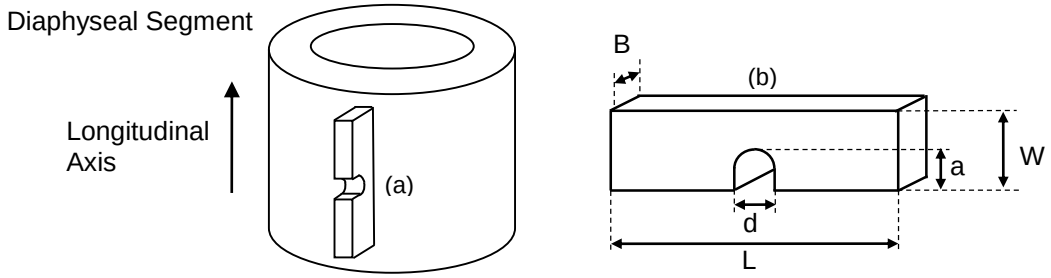

Figure 5.1: Circular notched Single Edged Notched Bend specimen configuration used in this study. (a) Orientation of the specimen with respect to the longitudinal axis of the bone and (b) characteristic dimensions of the specimen.

The first femur was used for the analysis of tensile fatigue damage on the fracture resistance of cortical bone. A total of forty seven specimens were obtained from the first femur. From these specimens eight were used for monotonic load pilot tests to establish the monotonic failure load of the specimens. A further five specimens were used to establish the fatigue testing protocol. The remaining thirty four specimens were assigned to either the tensile control or tensile damaged group using a stratified random sampling technique giving a total of seventeen specimens per test group. The second femur was used for the compressive fatigue damage and control groups.

A total of fifty three specimens were obtained from the second femur. From these specimens, eight were used for monotonic load pilot tests to establish the monotonic failure load of the specimens. A further five specimens were used to establish the fatigue testing protocol. The remaining forty specimens were assigned to either the control or

compressive damaged group using a stratified random sampling technique giving a total of twenty specimens per group. Note that a stratified random sampling technique was used to assign specimens to test groups to ensure that specimens from different locations of the bone were equally assigned to the test groups.

5.2.2 Mechanical Testing Overview

The mechanical testing for this study consisted of two sequential parts: 1) cyclic loading to generate fatigue microdamage in the damaged group specimens 2) fracture resistance testing of both control and damaged groups. The overall testing methodology is outlined schematically in Figure 5.2. The fracture resistance curves and crack path toughening mechanisms are then compared between the damaged and control groups for both the tensile and compressive damage groups.

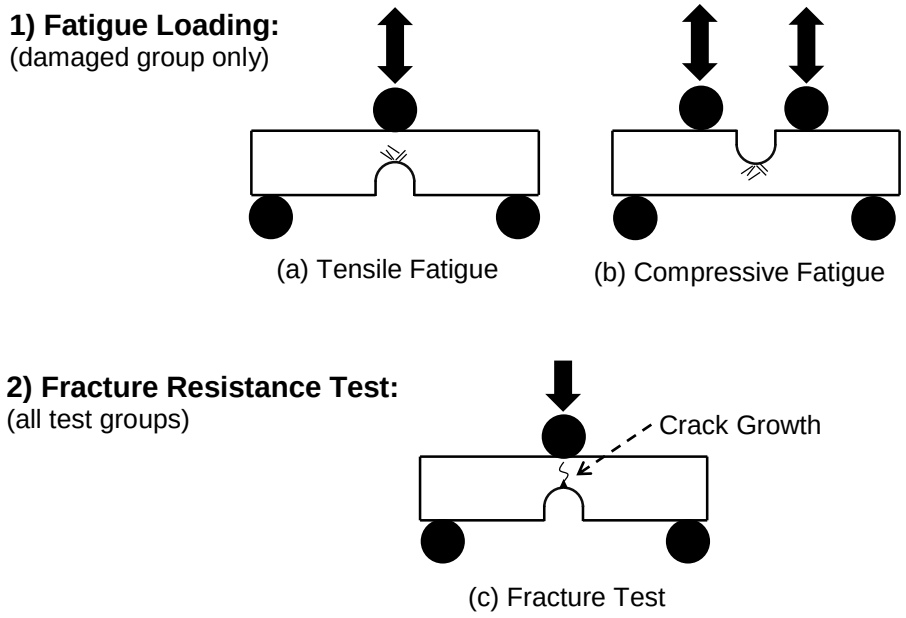

Figure 5.2: (a) Schematic of the testing protocol used for the tensile fatigue damage specimens and (b) the compressive fatigue damage specimens. (c) All specimens from both the damage and control groups underwent fracture resistance testing.

5.2.3 Fatigue Damage Testing

Prior to any mechanical testing all specimens were immersed in a fluorochrome stain (Calcein) to mark any existing damage due to the machining process. The specimens were immersed in a solution of PBS and 0.001M Calcein overnight (14 hours) at 4°C. All imaging of fatigue damage and crack path was performed using a Leica DM6600 fluorescence microscope with the specimen exposed blue light at a magnification of 100x. The specimens were imaged in a 2x3 grid pattern (2.70x4.05mm images) from the circular notch to the far edge of the specimen. Following the fatigue testing protocol all specimens

were again immersed in the calcein stain and the damaged specimens were subsequently imaged using the protocol described above. The crack path for all specimens was imaged after the fracture resistance testing to analyse the interaction of the fatigue damage with the crack path and various toughening mechanisms such as ligament bridging and crack deflection.

All specimens allocated to either the tensile or compressive damaged group were fatigue loaded using a Test Resources 800LE4 screw driven materials testing machine. Fatigue testing was conducted in load control using a sine waveform. The loading frequency was 2Hz with a constant loading ratio $R = P_{min}/P_{max} = 0.1$. The output load was measured using a ±400N load cell and the load line displacement was measured using a ±1mm LVDT mounted against the cross head of the test machine actuator. Specimens were thawed and rehydrated in a bath of PBS at room temperature for 2 hours prior to fatigue testing.

The purpose of the cyclic loading was to cause fatigue damage to accumulate in the specimen without causing complete failure. The fatigue loading for both the tensile and compressive specimens was continued until the specimens had undergone 5% stiffness loss (pilot testing showed that failure occurred at approximately 10% stiffness loss for both the tensile and compressive specimens). The tensile fatigue specimens were loaded in three point bending with a support span of S = 18mm and the circular notch underneath the central anvil as shown in Figure 5.2 (a). The compressive fatigue specimens were loaded in four point bending with an outer support span of S_o = 18mm and an inner support span of S_i = 7mm. The anvil roller radius for all testing was r = 1mm. The circular notch was aligned between the central span of the upper anvils as shown in Figure 5.2 (b). For the tensile damage specimens, fatigue pilot testing showed that a nominal maximum stress of 170MPa at the base of the notch would produce fatigue damage in a reasonable test time (10,000 – 100,000 cycles) (note that this stress value was calculated using the equation for stress in a beam under three point bending ignoring the stress concentration effect of the notch). Note that this number of fatigue cycles is representative of an in-vivo study on stress fracture in rabbits (Burr et al., 1990) in which most animals suffered a stress fracture after 100,800 cycles. For the compressive specimens fatigue pilot testing showed that a nominal maximum stress of 144MPa at the circular notch produced fatigue damage in a reasonable test time. All fatigue tests were conducted at room temperature (nominally 22°C) with the specimen fully submerged in a bath of PBS. Note that the control specimens for each damaged group were removed from the freezer, thawed and held at room temperature for the maximum fatigue test time for each damaged group.

5.2.4 Fracture Resistance Testing

Fracture resistance tests were conducted on all specimens following the fatigue loading protocol. The base of the circular notch was sharpened using a flat bladed scalpel. The fracture resistance tests were conducted using the same mechanical test machine and sensors as described in the fatigue testing section above. The unloading compliance method was used to determine the J-integral fracture resistance in accordance with ASTM E1820 (2011), with corresponding crack length measurements made *in-situ* using a stereo zoom microscope (Amscope SM-1TNZ) For the purpose of processing the resistance curve data the crack length was inferred from the compliance equations outlined in ASTM E1820. The initial crack length was corrected based on the optical crack length similar to the method used by Nalla et al. (2004a) (see further detail in Chapter 4). The fracture resistance tests were conducted in displacement control with a constant ramping rate of 1 mm/min. During the fracture resistance testing the specimens were kept hydrated by a gauze wick soaked in PBS with periodic hydration provided using an eye dropper. The J-integral was calculated at each unload step using the equations outline in ASTM E1820 (2011). All data processing and statistical analysis was performed using custom Matlab programs (Mathworks, Version R2012b).

5.3 Results

5.3.1 Fatigue Damage Imaging

The fatigue protocol and specimen configuration used in this study successfully caused the accumulation of fatigue damage in both the tensile and compressive group specimens. Figure 5.3 shows a fatigue damage pattern observed in a tensile fatigue specimen. This specimen shows diffuse damage radiating out from the circular notch as shown in Figure 5.3 (c). The edge of the specimen opposite the circular notch (under compressive bending stress) shows the formation of distinct microcracks directly under the top anvil. The damage formation under the top anvil is probably due to a combination of the indentation effect of the top anvil and the compressive bending stress in the specimen. The specimen shown in Figure 5.4 exhibits compressive type damage with distinct microcracks in the bone concentrated near the circular notch. The far edge of the specimen, underneath the circular notch (under tensile bending stress) shows patterns of diffuse damage similar to the tensile specimens shown in Figure 5.3.

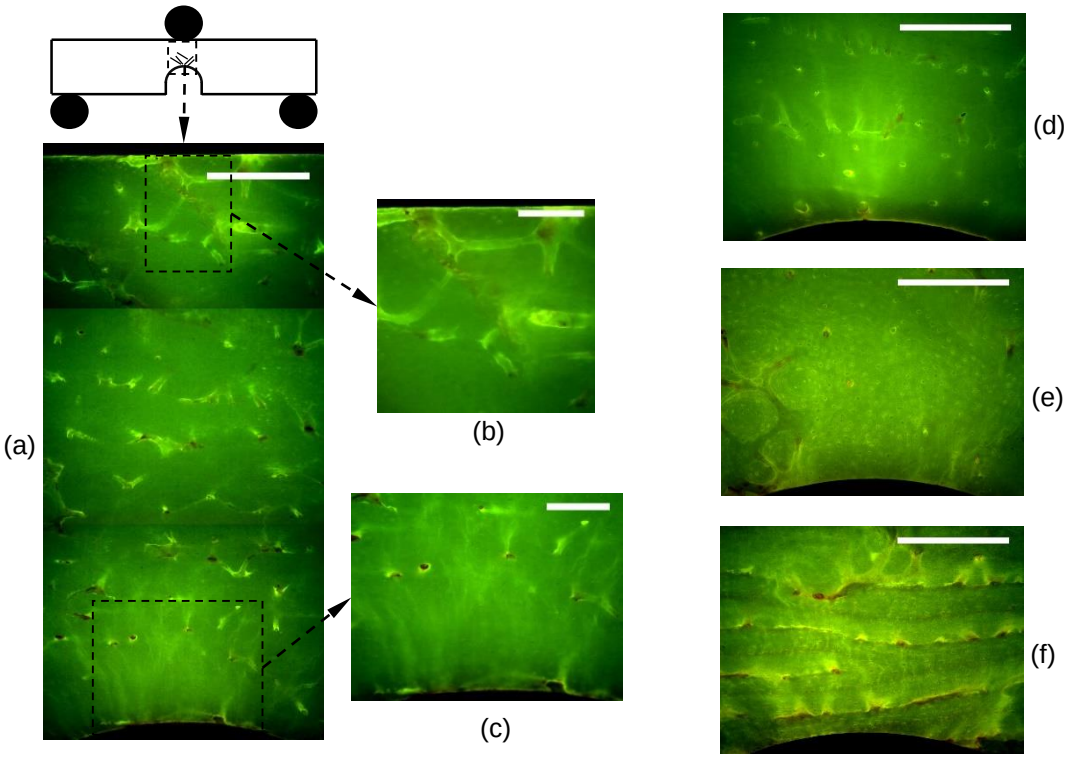

Figure 5.3: (a) Full cross section of tensile fatigue specimen. (b) Close up view of the damage at the far edge and (c) damage at the circular notch. (d)-(f) show the distribution of damage in several different specimens. Scale bar for (a), (d)-(f) is 500µm and scale bars for (b) and (c) are 200µm.

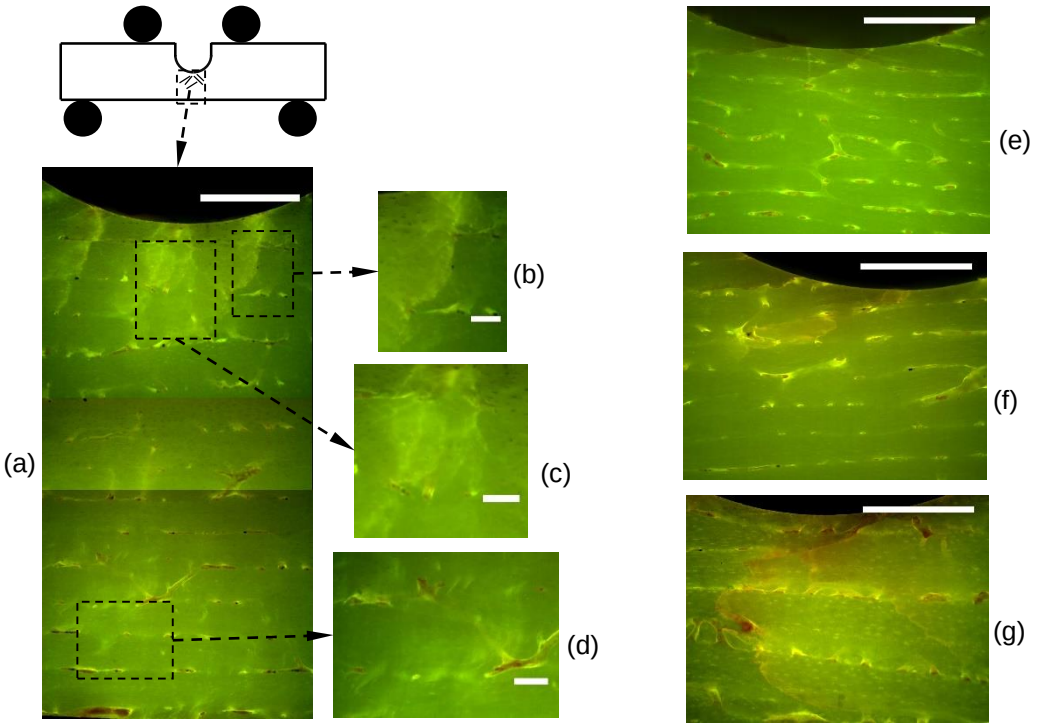

Figure 5.4: (a) Image of fatigue damage pattern of a compressive fatigue damage specimen. (b) to (d) close up views of fatigue microdamage. (e)-(g) show the distribution of damage in several different specimens. Scale bar for (a), (e)-(g) is 500µm and scale bars for (b)-(d) are 100µm.

For the tensile and compressive damaged specimens shown in Figure 5.3 and Figure 5.4 respectively, it can be seen that the intensity of the stain decreases further from the notch. This indicates that the fatigue damage density decreases with increasing distance away from the region of stress concentration. Therefore, the damage zone size was measured for both the tensile and compressive fatigue damage groups. This was done by measuring from the base of the circular notch to the furthest edge of the observed fatigue damage in the direction of optimal driving force for crack growth. For the tensile damaged specimens, the damage zone was (0.60 [0.49,0.68]) mm from the base of the circular notch. The compressive damaged specimen had a fatigue damage zone that extended (0.37 [0.32,0.43]) mm radially from of the circular notch. Note that the data is presented here as (median [quartile 1, quartile 3]) to be consistent with the non-parametric analysis used for comparison of the fracture resistance data in the following section. Note that the damage zone size was measured by taking the largest radial distance from the circular notch to the furthest observable fatigue induced damage.

5.3.2 Fracture Resistance Curves

Fracture resistance testing was performed on all specimens in both control groups and both fatigue damaged groups. Normality was tested for each of the variables analysed in this study using the Shapiro-Wilk test. For the fracture initiation toughness data normality could not be assumed and therefore non-parametric statistical tests were used to analyse the data.

Non-parametric rank sum tests were performed to compare the medians of the control and damaged group for the fracture initiation toughness (a test was considered significant if $p < 0.05$). The non-parametric statistical tests used in this study compare the median of the results thus the data is represented as: (median [quartile 1, quartile 3). **Figure 5.5** shows the fracture resistance curves for all twenty specimens in the compressively loaded control group. The scatter observed in the resistance curves for this group is representative of the scatter in the other test groups of this study. The correlation coefficients for all fitted resistance curves from all test groups ranged from $r^2 = 0.84$ to 0.99.

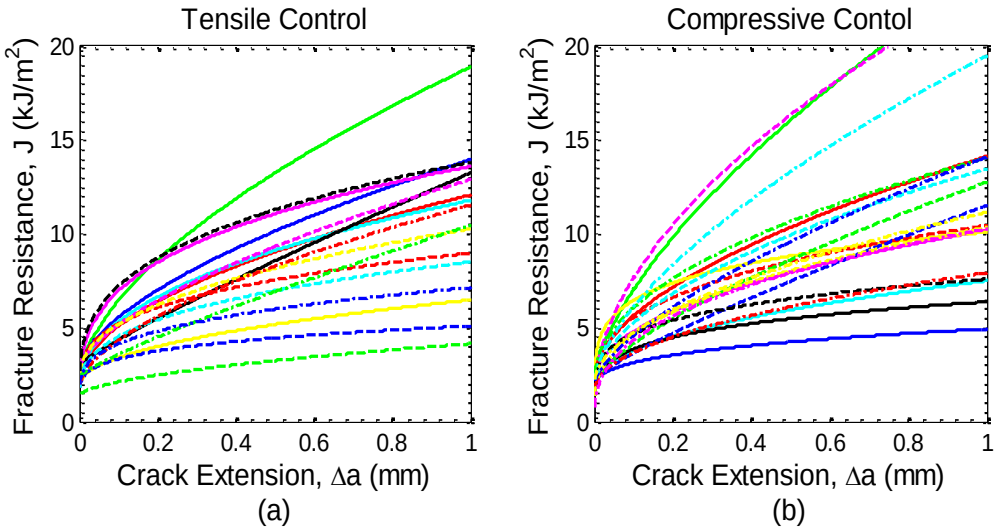

Figure 5.5: (a) All twenty resistance curves for the tensile control group and (b) the compressive control group. The scatter of resistance curves for these groups is representative of the scatter observed in the damaged groups.

Table 5.1 and Table 5.2 summarise the resistance curve data for the tensile fatigue damaged group and compressive fatigue damaged groups respectively. For the tensile control group a_Q was (0.221 [0.217,0.224])mm and (0.220 [0.216,0.223]) mm for the damaged groups. For the compressive fatigue group a_q was (0.221 [0.218,0.226]) mm for the control group and (0.220 [0.217,0.228]) mm for the damaged group. The damage zone for the tensile fatigue group extended approximately 0.60mm from the circular notch hence the average rate of toughening was evaluated within and outside this region of the fracture resistance curve. Similarly, for the compressive fatigue group the damage zone extended 0.38mm. Hence, the average toughening was evaluated within and outside this zone. No statistically significant differences were measured in the rate of toughening for either the tensile or compressive fatigue damaged groups when compared to their respective control group (see Table 5.1 and Table 5.2 for statistical test results for each variable analysed).

Table 5.1: Fracture resistance results for the control and damaged specimens of the tensile fatigue group.

Tensile Fatigue	**J_0 (kJ/m^2)**	**dJ/da, a_Q, ((kJ/m^2)/mm)**	**dJ/da, Δa<0.6mm, ((kJ/m^2)/mm)**	**dJ/da, Δa>0.6mm, ((kJ/m^2)/mm)**
Control	2.34 [2.02.2.65]	10.4 [6.16,11.0]	10.8 [7.92,12.9]	2.85 [1.47,5.75]
Damaged	2.37 [1.99,2.80]	7.85 [5.59,9.70]	9.50 [8.13,11.7]	1.53 [0.29,4.01]
Rank sum (p value)	0.78	0.47	0.78	0.11

Table 5.2: Fracture resistance results for the control and damaged specimens of the compressive fatigue group.'*' denotes a statistically significant difference.

Compressive Fatigue	**J_0 (kJ/m^2)**	**dJ/da, a_Q, ((kJ/m^2)/mm)**	**dJ/da, Δa<0.38mm, ((kJ/m^2)/mm)**	**dJ/da, Δa>0.38mm, ((kJ/m^2)/mm)**
Control	2.09 [1.92,2.29]	9.89 [6.63,12.6]	14.7 [11.5,18.9]	3.08 [1.23,7.30]
Damaged	1.77 [1.53,2.05]	9.83 [7.65,18.0]	16.9 [12.5,22.2]	4.38 [2.23,10.8]
Rank sum (p value)	0.03*	0.52	0.62	0.30

Figure 5.6 (a) and (b) compares the fracture resistance data for both the tensile control and damaged groups. Figure 5.6 (a) shows a comparative box plot of the fracture initiation data. Note that the edges of the box plot indicate the 1st and 3rd quartile while the whiskers indicate the maximum and minimum data values. The notches on the box plots indicate the 95% confidence interval for the median of the data. Figure 5.6 (b) shows the scatter bands for the fracture resistance curves of the tensile control (black line) and damaged (blue line) groups. For the tensile group there is no significant difference (p = 0.78) between the median fracture initiation toughness of the control (2.34 [2.02,2.65]) and the damaged group (2.37 [1.99,2.80]). Analysis of the scatter bands for the overall fracture resistance curves shows significant overlap. This indicates similar crack growth toughening behaviour between the tensile control and damaged groups.

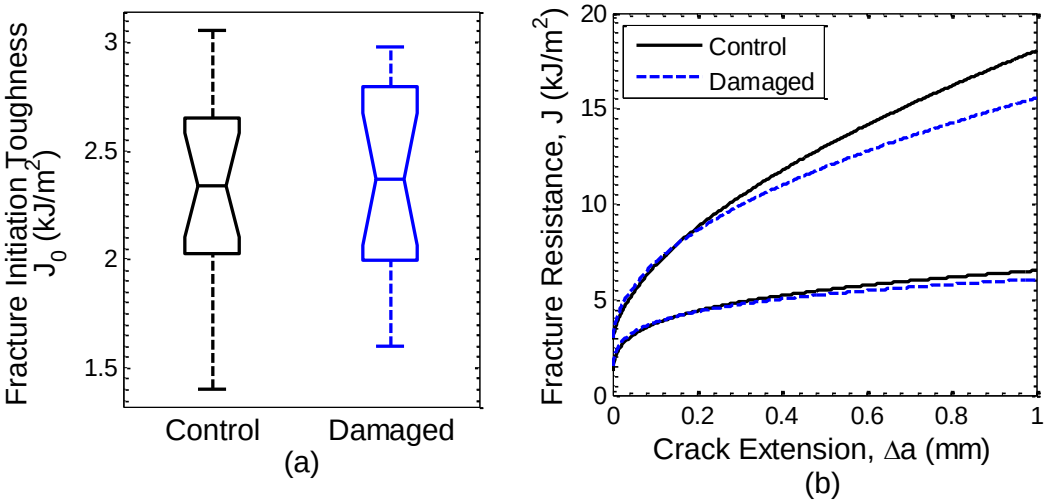

Figure 5.6: Comparison of the fracture resistance behaviour of the tensile fatigue control (black) and damaged (blue) groups. (a) Comparison of the fracture initiation toughness for the tensile control and damaged groups. (b) Scatter bands for the fracture resistance curves of control and damaged groups.

Figure 5.7 (a) and (b) compares the fracture resistance data for both the compressive control and damaged groups. Figure 5.7 (a) shows a comparative box plot of the fracture initiation data and Figure 5.7 (b) shows the scatter bands for the fracture resistance curves of the compressive control (black line) and damaged (blue line) groups. The median fracture initiation toughness of the compressive fatigue damaged group (1.77 [1.53,2.05]) is significantly lower (p = 0.03) than the control group (2.09 [1.92,2.29]). However, there is large amount of overlap for the scatter bands of the fracture resistance curves after the fracture initiation point (see Figure 5.7 (b)). This indicates similar overall toughening behaviour during crack propagation but decreased fracture initiation toughness.

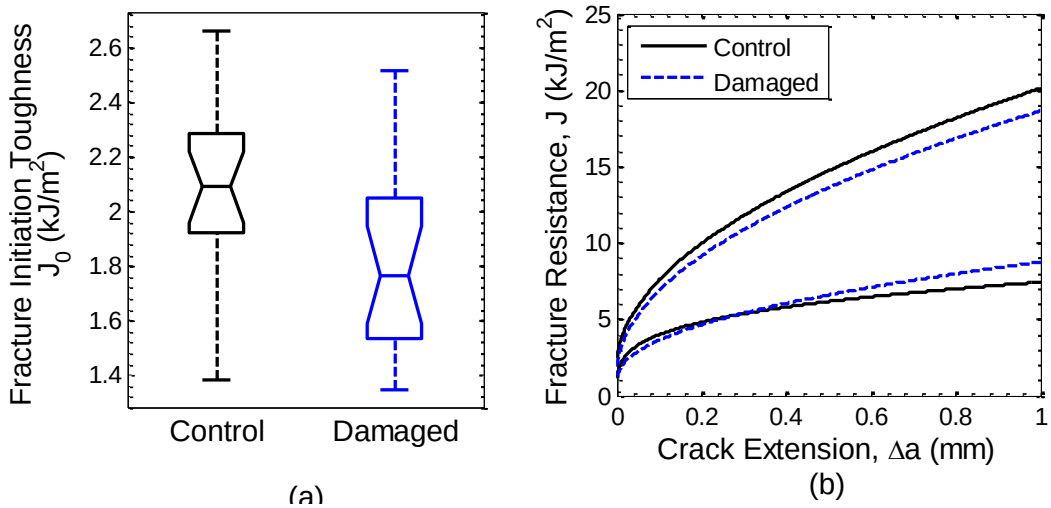

Figure 5.7: Comparison of the fracture resistance behaviour of the compressive fatigue control (black) and damaged (blue) groups. (a) Comparison of the fracture initiation toughness. (b) Scatter bands for the fracture resistance curves of control and damaged groups.

Further analysis was conducted to compare the contributions of the elastic and plastic components of the J-integral. Figure 5.8 compares the scatter bands for the elastic component of the J-integral for the tensile and compressive fatigue groups. Similarly, Figure 5.9 compares the scatter bands for the plastic component of the J-integral. For the tensile damaged group both the elastic and plastic components of the J-integral show significant overlap with the control groups. This is also the case for the compressive fatigue group, indicating that the components of the resistance curve after the initiation point are unchanged by fatigue induced damaged.

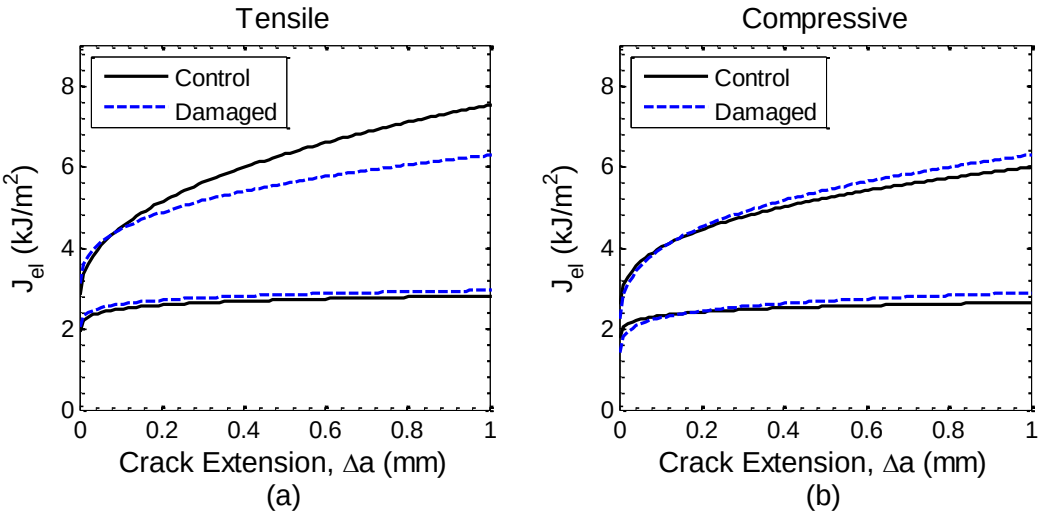

Figure 5.8: Comparison of the scatter bands for the elastic component of the J-integral. (a) Tensile control and damaged group comparison and (b) compressive control and damaged group comparison.

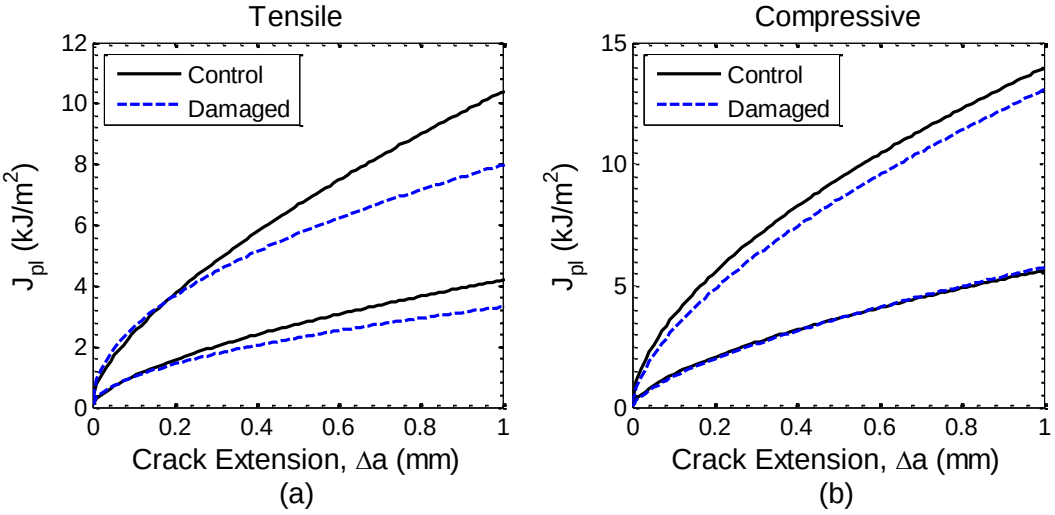

Figure 5.9: Comparison of the scatter bands for the plastic component of the J-integral. (a) Tensile control and damaged group comparison and (b) compressive control and damaged group comparison.

5.3.3 Crack Path Imaging and Interaction

For all test groups the crack path was imaged using fluorescence microscopy. This allowed for visualisation of the toughening mechanisms and crack-path behaviour responsible for the resistance curves of each specimen. Figure 5.10 shows the crack path for a typical control specimen from the tensile group (a) and a typical control specimen from the compressive group (b). The specimens in all test groups usually exhibit a 'stair step' crack deflection path that mostly follows the pores in the 'brick like' microstructure of bovine bone. This characteristic 'stair step' crack deflection pattern is shown in Figure 5.10 (a) and (b). The crack path toughening behaviour observed in the tensile damaged specimens is very similar to the tensile control group.

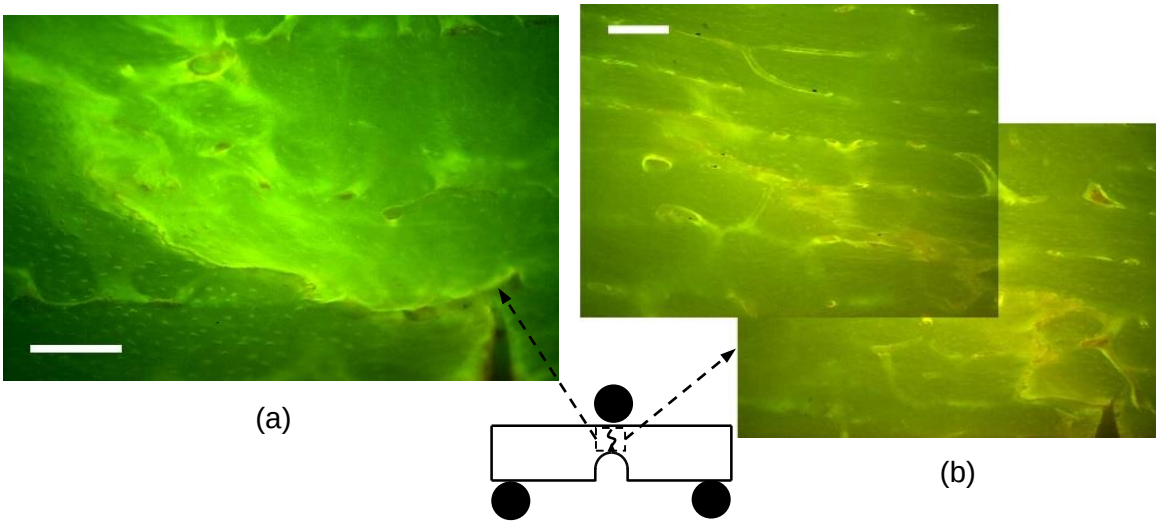

Figure 5.10: (a) Crack path images for control specimens from the tensile and (b) compressive groups. Typical control specimens exhibited a 'stair step' deflection pattern similar to (a) and (b). Scale bars for (a) and (b) are 200µm.

Figure 5.11 shows the crack path for a typical compressive bend specimen (note that this is the same specimen as shown in Figure 5.4). The overall crack path of the specimen in Figure 5.11 (a) shows that the crack deflects along the 'brick like' arrangement of pores in the microstructure. Comparing Figure 5.4 and Figure 5.11 it can be seen that for this specimen the fatigue induced damage has caused the initiation of multiple macrocracks that have linked with the main crack propagating from the starter notch as shown in Figure 5.11 (c). The macrocrack initiating from a fatigue damage site shown in Figure 5.11 (c) links with the main crack at a junction in the 'brick like' arrangement of pores in the microstructure.

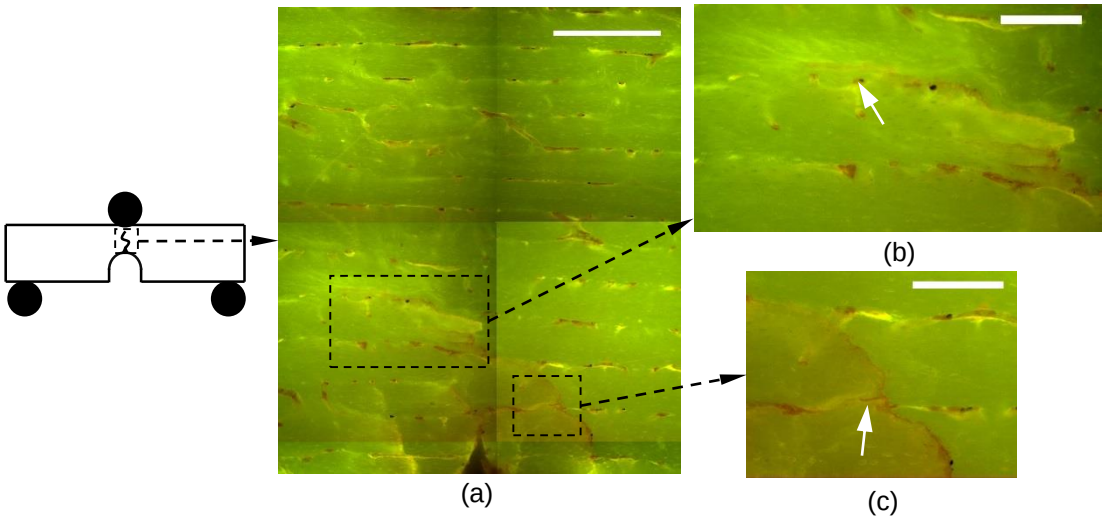

Figure 5.11: (a) Crack path images for the compressive damage specimen shown in Figure 5.4. Note that several of the fatigue microdamage sites have initiated macrocracks that link with the main crack as shown in inset (c). Inset (b) shows microdamage around the crack tip. Scale bar for (a) is 500µm for (b) and (c) it is 200µm.

Both groups showed microdamage formation following fracture resistance testing (i.e. microdamage formation during macrocrack growth). The crack growth damage morphology was similar for both the tensile and compressive groups near the final crack tip zone (see Figure 5.10 and Figure 5.11). This crack tip damage morphology was mostly diffuse damage forming along the main crack path and ahead of the crack tip across microstructural boundaries. The main difference in crack path microdamage morphology is in the area near the notch. This results from interaction between the existing fatigue microdamage and the microdamage formed during crack growth. Specifically, the tensile damage group showed no observable difference when compared to its control group while the compressive damage specimens showed sites of multiple macrocrack initiations and branching (see Figure 5.11).

5.4 Discussion

5.4.1 Fatigue Fracture Interaction Mechanisms in the Transverse Direction

Comparison of the fracture resistance data for the tensile control and damaged groups showed that there are no statistically significant differences in the median fracture initiation toughness. There is also significant overlap of the scatter bands of the overall fracture resistance curves of the tensile control and damaged groups. Similarly, there was significant overlap for the scatter bands of the elastic and plastic components of the J-integral for the tensile damaged group. This suggests that tensile fatigue damage in the form of diffuse damage does not significantly alter the transverse toughening behaviour of cortical bone.

A possible explanation for this result is that the dominant toughening mechanism for transverse crack growth in cortical bone is crack deflection due to the orientation of the weak interfaces in the microstructure (Behiri and Bonfield, 1989; Koester et al., 2011, 2008; Zimmermann et al., 2010). In comparison, for crack initiation toughness the dominant contribution comes from the local material resistance to crack growth or initiation at weak interfaces in the microstructure. In essence, diffuse damage does not create weaker regions of material than the existing interfaces in the microstructure. Hence the toughening behaviour dependent on weak interfaces in the microstructure remains unchanged. The deflection mechanism is not affected by the presence of diffuse damage as the diffuse damage does not alter the weak microstructural boundaries. Crack deflection toughening is highly dependent on weak interfaces in the microstructure such as boundaries between osteons or lamellar sheets, which are misaligned with the optimal direction of crack propagation (Koester et al., 2011; Zimmermann et al., 2011, 2010).

The main crack interacts with these boundaries and will tend to deflect along these weak interfaces. This absorbs energy that would otherwise propagate the main crack (reducing the non-plastic component of the J-integral). Crack deflection also reduces the driving force for crack growth by causing the crack to grow a non-optimal path for maximum driving force (reducing the elastic component of the J-integral).

Typical crack deflection behaviour is evident when analysing the crack path images observed in this study such as Figure 5.10 and Figure 5.11. The diffuse damage observed in this study does not interact with these microstructural interfaces. This is shown by the radial pattern of diffuse damage across microstructural boundaries observed in the tensile damaged specimens, such as the specimen in Figure 5.3. Therefore as the diffuse damage does not interact with the weak interfaces in the microstructure it is unlikely to affect the crack deflection toughening mechanism. Further to this, areas of diffuse damage are composed of small 1-3 μm cracks (Parsamian and Norman, 2001; Vashishth, 2007a). As these are several orders of magnitude smaller than the main crack it is unlikely that they will alter the toughening mechanisms along the crack path. Overall, tensile fatigue damage in the form of diffuse damage did not alter the transverse fracture resistance behaviour of cortical bone in this study. The results of this study show that diffuse damage does not interact significantly with the weak interfaces in the microstructure of cortical bone. These weak interfaces are responsible for the crack deflection toughening mechanism as well as defining the overall crack path. Therefore no significant difference was observed in fracture resistance behaviour.

When the fracture resistance data for the compressive control and damaged groups is compared the fracture initiation toughness was found to be significantly lower for the damaged group. However, there was considerable overlap in the scatter bands for the fracture resistance curves after the fracture initiation point. There was also significant overlap for the elastic and plastic components of the J-integral for the compressive group. This suggests that fracture initiation is reduced in the presence of microcracks but this does not alter the subsequent fracture toughening mechanisms as the crack grows (i.e. the whole resistance curve).

The decreased fracture initiation toughness is probably due to interaction of the existing fatigue microcracks with crack initiation sites in the microstructure. Crack initiation in cortical bone is dependent on the local stress field, microstructure near the initiation point and the local material resistance to crack initiation. It is therefore likely that fatigue induced damage alters the local stress field or the local material resistance to fracture initiation resulting in an overall decrease in fracture initiation toughness. The reason for this is that compressive fatigue microcracks form at the weak microstructural interfaces in bone such

as between lamellar sheets, which are the same sites that can lead to crack initiation (O'Brien et al., 2007). Also, if there is fatigue induced damage near the initiation point, this fatigue damage will occupy the existing weak interfaces in the microstructure thus inhibiting the formation of new microdamage during crack initiation and growth. This will lead to overall reduced plasticity and microdamage formation at the point of crack initiation leading to reduced toughness. The lower fracture initiation toughness of the compressive damaged group may be summarised as follows: Fatigue induced microcracks tend to form at the weak interfaces in the microstructure, which has two main effects on the fracture initiation toughness, 1) Changes in the local stress field and reduction in the local material resistance to crack initiation; and 2) If there are already microcracks at these weak interfaces they inhibit the development of new microdamage during macrocrack initiation reducing plasticity and hence fracture initiation toughness. Despite the reduction in fracture initiation toughness no difference was observed in the rate of toughening for the control or damage compressive fatigue group specimens.

The overall fracture resistance behaviour after the initiation point was similar for the compressive control and damaged groups. The increasing fracture resistance behaviour of cortical bone is a consequence of the fracture toughening mechanisms along the crack path including: microdamage formation, uncracked ligament bridging and crack deflection. For the transverse crack propagation direction, crack deflection is the dominant toughening mechanism due to the orientation of the microstructure with respect to the direction of maximum driving force. For the control and damaged specimens in the tensile group the crack path toughening mechanisms are similar with both showing evidence of significant crack deflection typical of transverse fracture in bone, as seen in Figure 5.10 and Figure 5.11.

Even though there is evidence of crack deflection there are some notable differences in the crack paths of the control and damaged specimens; that is, the damaged specimens show initiation of further cracks from the fatigue induced microcracks that form branches from the main fracture. This multiple site initiation and crack path branching was characteristic of the fatigue damage specimens. The presence of fatigue induced microdamage inhibits the formation of new microdamage during crack growth as shown by the results of this study and the first experiment. The results of this study show that for the transverse crack growth mechanisms fatigue induced microdamage can also provide initiation sites for separate crack growth paths. Each of these crack growth paths can consume energy leading to increased toughening. The propagation of these fatigue induced cracks during propagation of the main fracture will absorb energy that would otherwise cause the main fracture to propagate further. Therefore it is possible that the

fracture energy consumed by propagating the fatigue induced cracks offsets the decrease in toughening due to the saturation of fatigue damage. This potentially explains why no significant difference was observed in the fracture resistance curves after the initiation point for the compressive test groups.

An alternative explanation for there being no observed difference in the overall fracture resistance curves would be that the fatigue damage was concentrated near the notch. Hence, it would provide initiation sites for crack growth but would not affect the crack propagation behaviour as the crack quickly grows away from the fatigue damage zone. While this explanation is a possibility it is unlikely as crack path analysis shows that further cracks initiate from the fatigue microdamage sites and link with the main fracture as shown in Figure 5.11. Further to this, the damage zone size (measured as the length in the direction of optimal driving for crack growth) for each of the test groups was comparable to, or larger than, the damage zone size observed in the first experimental study when analysed as a ratio of damage zone size to crack length. Therefore it is more likely that the fatigue damage itself does not significantly alter the overall fracture resistance curve because it does not interfere with the crack deflection toughening mechanism. Another aspect of fracture in bone is the contribution of the overall microstructure to the fracture behaviour. Therefore a brief discussion of the effects of the ‘brick like’ microstructure of bovine bone will be given below.

The bovine bone used in this study has a different microstructural arrangement to human bone. Specifically: human bone exhibits a secondary osteonal structure with the characteristic feature of the circular osteon. In contrast to this, bovine bone has a ‘brick like’ microstructure. This ‘brick like’ microstructure in bovine bone leads to differences in the magnitude of the fracture resistance when compared to human cortical bone. As the toughening mechanisms present in human and bovine bone are similar the mechanisms of fatigue fracture interaction will also be similar. However, the relative magnitudes of these effects may be different. While it is true that bovine bone does have a different nano-structural composition to human bone in terms of mineral composition this will have a minimal effect on the toughness of bone i.e. post yield properties (however it will lead to a significantly different modulus i.e. pre-yield properties). This is especially evident when considering studies on the fracture toughness of irradiated bone (a process which damages collagen but leaves the mineral intact) (Akkus and Rimnac, 2001; Barth et al., 2011, 2010; Currey et al., 1997). These studies show that damaging the collagen significantly reduces toughness but leaves the stiffness properties unchanged. Hence, it is expected that the difference in mineral composition will have a negligible effect on the fracture behaviour whereas the microstructure configuration will.

Overall, the results of this study show that tensile fatigue damage in the form of diffuse damage does not alter the fracture resistance behaviour of cortical bone. However, compressive fatigue damage in the form of linear microcracks causes a decrease in the transverse fracture initiation toughness but no difference in the subsequent fracture resistance curve. It is interesting to contrast this result with the effects of fatigue damage on the longitudinal fracture resistance observed in the first experimental study (see chapter 3 or Fletcher et al., 2014). In this study it was found that tensile fatigue damage in the form of diffuse damage and linear microcracks significantly decreased the longitudinal fracture initiation toughness and growth toughness (slope of the resistance curve) within the fatigue damage zone. As the current study showed no effect of diffuse damage on the fracture resistance curve it is likely that the decreased fracture resistance result of the first experimental study can be attributed to the linear microcracks alone. As previously mentioned the size scale of the diffuse damage compared to the crack lengths in this study provide further evidence. Note that this does not rule out an important role for diffuse damage in sub-microscale fracture initiation and growth. The difference between the current experiment and the first experimental study in terms of the overall fracture resistance curve is likely to be a result of the different crack path toughening mechanisms present in the longitudinal and transverse fracture directions.

5.4.2 Comparison to Fracture in Aged Bone

The fracture initiation toughness of cortical bone is dependent on both the local material resistance to crack growth and the stress field at the initiation point. For aged human bone there is a significant decrease in the fracture initiation toughness with age for both the longitudinal and transverse fracture directions (Ager et al., 2006; Currey et al., 1996; Koester et al., 2011; Nalla et al., 2006). The decrease in fracture initiation toughness with age has been mainly attributed to changes in the local material resistance to crack growth. This decrease in material resistance has been attributed to a decrease in plasticity of collagen fibrils via increases in cross linking (Wang et al., 2002; Zimmermann et al., 2011). A further contribution to the decreased longitudinal and transverse fracture initiation toughness comes from increased porosity. Increased porosity with age has been shown to lead to a decrease in fracture toughness (Ammann and Rizzoli, 2003; Granke et al., 2015; Zioupos, 2001b). This can be partially attributed to the porosity in the structure interfering with the stress field at the crack tip leading to an overall decrease in initiation toughness. Microstructural changes with age also lead to decreases in the crack growth resistance behaviour of cortical bone.

Longitudinal fracture resistance testing of cortical bone has shown that the dominant toughening mechanism for longitudinal cracking is the formation of uncracked ligament bridges (Nalla et al., 2004b). Subsequently it has been suggested that the formation of microcracks during crack growth in the longitudinal direction provides initiation sites for the formation of uncracked ligament bridges and crack deflection (Zimmermann et al., 2011). In contrast to this, the fracture resistance of cortical bone in the transverse direction is more dependent on the crack deflection toughening mechanism, which is a direct result of the orientation of the underlying microstructure (Koester et al., 2011, 2008; Zimmermann et al., 2009). Crack deflection in the transverse direction results from the crack deflecting along the weak interfaces in the microstructure such as the interfaces in lamellar sheets and the boundaries of osteons, which are generally orientated almost perpendicular to the optimal direction of crack propagation. Both of these primary crack growth orientations and their dominant toughening mechanisms are affected differently by the microstructural changes due to aging.

The overall effect of aging on the microstructure of cortical bone is increased remodelling activity leading to an increased osteonal density (Kennedy et al., 2008; Schaffler, 2003; Zimmermann et al., 2011). The increase in osteonal density leads to increased porosity and a decrease in the spacing of weak microstructural boundaries such as the cement lines of osteons. The decrease in spacing of weak microstructural interfaces causes ligament bridges formed during longitudinal crack growth to be smaller. Thus, there is an overall reduction in the effectiveness of the ligament bridge toughening mechanism with increasing age (Koester et al., 2011; Nalla et al., 2004a). For transverse crack growth the decrease in the spacing of the weak microstructural interfaces leads to a decrease in the efficacy of the crack deflection toughening mechanism (Koester et al., 2011). The decrease in spacing of weak interfaces means that there is less material between microstructural boundaries. Consequently, it requires less energy for the crack to break across these barriers and reinitiate in the direction of optimal driving force leading to many small deflections. The net effect of these many small deflections is an overall crack path that propagates (mostly) in the direction of maximum driving force (Koester et al., 2011; Zimmermann et al., 2011). As the crack deflection mechanism is much less effective for transverse crack growth in aged human bone it is probable that other toughening mechanisms such as ligament bridging and microcrack formation are more significant for this crack growth direction.

There are significant microstructural changes with age that lead to decreases in the overall fracture resistance of cortical bone. In addition to these microstructural changes cortical bone accumulates fatigue damage with age (Schaffler et al., 1995). Thus, combining the

analysis of decreased toughness in aged bone presented above with the experimental data presented in this thesis provides further explanation for the age related decrease in cortical bone toughness.

For both the longitudinal and transverse crack growth directions fatigue damage in the form of linear microcracks was shown to decrease the fracture initiation toughness (results from Experiment 1 and Experiment 3). This can be attributed to two mechanisms: 1) fatigue induced microcracks prevent the formation of new microcracks that would normally form before dominant crack initiation and 2) fatigue induced microcracks interfere with the stress field around the crack tip causing a reduction in toughness (similar to the effect of increased porosity). These mechanisms of fatigue fracture interaction show that in addition to nanoscale changes in plasticity (i.e. changes in collagen structure and cross linking), fatigue damage accumulated with age also reduces the fracture initiation toughness of cortical bone for both transverse and longitudinal crack initiation. The results from experiment presented in this thesis suggest that accumulated fatigue damage reduces the fracture initiation toughness of cortical bone independently of nanoscale changes in the collagen matrix. Therefore, the accumulation of fatigue microcracks is contributing factor to the age related decrease in cortical bone fracture initiation toughness.

The overall fracture resistance behaviour of cortical bone is decreased by fatigue induced microcracks for longitudinal crack growth (Experiment 1) but not for transverse crack growth (Experiment 3). The decrease in growth toughness for the longitudinal crack growth direction was mainly attributed to the fatigue induced microcracks inhibiting the formation of new microcracks during dominant crack growth. Microcrack formation during crack growth is responsible for the formation of ligament bridges along the crack path. Thus, a reduction in the number of ligament bridges was also observed within the damaged region. This reduction in ligament as a consequence of inhibited microcrack formation leads to an overall decrease in the crack growth resistance for the longitudinal direction. As the cortical bone specimens used in this study were relatively young bovine bone there was little if any remodelling observed in the microstructure. Therefore, it is possible that the combination of accumulated fatigue microcracks and the decrease in microstructural spacing are both responsible for the decrease in the effectiveness of the ligament bridge toughening mechanism with age.

For transverse crack growth the overall fracture resistance was not effected by fatigue induced microcracks. However, changes in the microstructure of aged bone (i.e. increases in osteonal density) lead to significantly different crack growth behaviour (Koester et al., 2011; Zimmermann et al., 2011). Specifically, aged bone has reduced crack growth

resistance due to a reduction in crack deflection. Therefore it is possible that the toughening mechanisms for transverse crack propagation in aged bone are more similar to the toughening mechanisms for longitudinal crack propagation. This would imply that toughening mechanisms such as ligament bridging and hence microcracking may be more important in the toughening of aged bone (but potentially less effective than the suppressed crack deflection mechanism). The efficacy of the microcracking and ligament bridging toughening mechanisms is significantly affected by fatigue induced microcracks, as shown by the results of Experiment 1. If ligament bridging and microcracking contribute significantly to the transverse crack growth resistance of aged bone then it is possible that fatigue induced microcracks would reduce the transverse growth toughness in aged bone.

The bones used in this study and the previous work on longitudinal fatigue fracture interaction were young bovine specimens (approximately 12-18 months). Therefore further evidence would need to be provided to support this conjecture, specifically including the use of young and aged human bone specimens for further fatigue fracture interaction studies. However, the proposed conjecture is an interesting hypothesis that may further elucidate the role of fatigue damage in the reduced toughening behaviour of aged human cortical bone.

5.5 Conclusion

This study investigated the effects of tensile and compressive fatigue damage on the transverse fracture behaviour of cortical bone. The fatigue loading protocol used in this study successfully created fatigue damage characteristic of both tensile and compressive loading.

The fracture resistance results of this study show that tensile fatigue damage in the form of diffuse damage does not significantly alter the transverse fracture behaviour of cortical bone. The proposed reason for this is that the fracture resistance of cortical bone in the transverse direction is highly dependent on orientation of the microstructure. For crack initiation the diffuse damage did not affect the local stress field or local material resistance to crack initiation. For crack growth in the transverse direction the crack deflection mechanism is dependent on weak interfaces in the microstructure of cortical bone such as boundaries of osteons and lamellar sheets. These interfaces are unaffected by the formation of diffuse damage and therefore there was no difference in the crack deflection toughening mechanism. Hence, the fracture resistance curve was unchanged by fatigue induced diffuse damage.

In contrast to this compressive fatigue damage does reduce the transverse fracture initiation toughness of cortical bone, but it does not significantly alter the fracture resistance curve after the initiation point. The reduction in fracture initiation toughness was attributed to a decrease in the local material resistance to crack initiation by the fatigue induced microcracks. Specifically, the fatigue induced microcracks provide initiation sites along the weak interfaces in the microstructure allowing the main crack to bypass the normal material resistance as it does not have to break across the collagen fibres to initiate. However, for crack growth the compressive microcracks did not alter the rate of toughening. The reason for this is that the compressive microcracks did not interfere with the weak interfaces responsible for the crack deflection mechanism.

5.6 Limitations and Future Work

A limitation of the present work is that only a single femur was used for each test condition. This raises the possibility that the differences between groups are the result of biological differences in the individual femurs rather than a fatigue-fracture interaction effect. However, as the microstructures and crack path toughening mechanisms observed in the control groups are similar to those in Chapter 4 the differences are unlikely to be significant. Future work for this study will include using specimens from multiple donors to remove this effect. As previously mentioned bovine bone has a different microstructure to human bone so it would be desirable to use human bone for future studies.

An assumption of this study was that the blunt circular notch in the SEN(B) specimen would not alter the comparison of the fracture resistance results. The use of a blunt circular notch in the SEN(B) specimen configuration changes the stress field at the notch (compared to an ideally sharp crack) and hence the fracture resistance calculated near the notch. Therefore the compliance relationships for the standard specimen geometry used to calculate the fracture resistance in terms of ‘J’ may not be accurate near the circular notch as they are derived with an ideally sharp notch. This will introduce a systematic error to the calculated resistance curves of all groups creating an offset in the resistance curves near the circular notch. However, as all specimens were machined with the circular notch geometry (i.e. control and damaged) comparison of the groups is still valid as both test groups had the same offset in fracture resistance near the circular notch.

The following chapter will use finite element modelling techniques to verify the assumption that the circular notch does not alter the comparison of the control and damaged groups for the study described above. This is done by modelling the circular notch geometry and deriving compliance equations that can be used to reprocess the experimental data. The reprocessed data with the corrected equations will then be statistically compared to verify the assumption of this study.

Chapter 6: Finite Element Modelling 1

Verification of Compliance Equations for Circular Notched Specimens

6 Finite Element Modelling 1: Verification of Compliance Equations

6.1 Introduction

The first and third experimental studies presented in this thesis (Chapters 3 and 5 respectively) utilised an altered fracture specimen geometry. Specifically, all specimens in these studies included a blunt circular notch geometry for the purpose of causing the accumulation of a region of fatigue damage without macrocrack initiation. For these studies it was assumed that the circular starter notch would not alter the comparison between control and damaged groups as the geometry used for each group was consistent. The aim of this study was to verify that that this assumption was valid using finite element modelling techniques. In order to achieve this aim it was necessary to derive new equations for the calculation of the stress intensity factor (SIF) that account for the presence of the circular notch and then compared these to the results calculated using the equations for the standard specimen geometry. If the results of this study showed that the comparison between test groups was still valid future studies utilising circular notched geometry would not need to derive new equations for each individual notch geometry and the standard equations could be used.

In order to analyse the effect of the circular notch on the fracture resistance curves from experiments 1 and 3 it was necessary to derive new equations for calculating the fracture resistance curve for the non-standard specimen geometry. Therefore the series of equations for calculating the stress intensity factor from standard specimen geometry (as given in ASTM E1820) are be briefly outlined here for both the Compact Tension ‘C(T)’ (experiment 1 – Chapter 3) and Singled Edge Notched Bend ‘SEN(B)’ (experiment 3 – Chapter 5) specimens. The fracture resistance data from experiment 1 was processed using the optical crack length measured from the *in-situ* stereo microscope (using the procedure and equations outlined in ASTM standard E1820). The stress intensity factor ‘K’ for the C(T) specimens was calculated at the measured crack length of ‘a’ and applied load of ‘P’ using:

$$K = \left[\frac{P}{B\sqrt{W}}\right] f(a/W) \tag{6.1}$$

where ‘B’ is the specimen thickness, ‘W’ is the characteristic length of the specimen and the function:

$$f(a/W) = \left[(2 + a/W)/(1 - a/W)^{3/2}\right][0.886 + 4.64(a/W) - 13.32(a/W)^2 + 14.72(a/W)^3 - 5.6(a/W)^4] \quad (6.2)$$

Similarly, for a SEN(B) specimen the stress intensity factor 'K' at a crack length of 'a' is given by the following relationship:

$$K = \left[\frac{PS}{BW\sqrt{W}}\right] f(a/W) \quad (6.3)$$

where 'B' is the specimen thickness, 'W' is the characteristic length of the specimen, 'S' is the outer support span and the function:

$$f(a/W) = \left[(3(a/W)^{1/2})/(2(1 + 2\,a/W)(1 - a/W)^{3/2})\right][1.99 - (a/W)(1 - a/W)(2.15 - 3.93(a/W) + 2.7(a/W)^2)] \quad (6.4)$$

The fracture resistance data from experiment 3 was processed using the unloading compliance method. The reason for this is that the tortuous crack path for transverse SEN(B) specimens makes accurate optical measurements of the crack length extremely difficult (Koester et al., 2011). Therefore an effective crack length is inferred using the load-line compliance of the specimen C_{LL} = Δ/P. In order to calculate the effective crack length the elastic modulus of the specimen needs to be known. The elastic modulus of the specimen was inferred using the initial crack length, initial compliance and the following relationship:

$$C_{LL} = \frac{1}{EB}\left(\frac{S}{W-a}\right)^2\left[1.193 - 1.198\left(\frac{a}{W}\right) + 4.478\left(\frac{a}{W}\right)^2 - 4.443\left(\frac{a}{W}\right)^3 + 1.739\left(\frac{a}{W}\right)^4\right] \quad (6.5)$$

Where 'E' is the elastic modulus and the geometric variables, 'S' is the support span, 'B' and 'W' are the same as defined for equation 6.3. The calculated elastic modulus is then used to determine the non-dimensional compliance 'U' for the remaining unload/reload sequences in the unloading compliance test:

$$U = \frac{1}{\sqrt{\frac{BWEC_{LL}}{S/4}} + 1} \quad (6.6)$$

The non-dimensional compliance is used to infer the crack length at each unload/reload step using the following relationship:

$$\frac{a}{W} = 0.99748 - 3.9504U + 2.9821U^2 - 3.21408U^3 + 51.51564U^4 - 113.031U^5 \quad (6.7)$$

Note that the methodology described above focuses on the calculation of the stress intensity factor that is used to calculate the elastic component of the J-integral. The scope of this study was limited to the analysis of the stress intensity factor (i.e. the elastic component of the J-integral). The reason for this is that near the initiation point (i.e. near the circular notch) the elastic part of the J-integral forms a significant proportion of the overall J-integral. Thus, as the effect of the circular notch is localised near the starter notch it has a significant effect on the elastic component of the J-integral.

In order to achieve the aim of this study it was be necessary to derive new equations to calculate the stress intensity factor for both the C(T) and SEN(B) geometries including the effects of a circular notch. For the C(T) geometry a finite element model was developed to derive the non-dimensional crack length function f(a/W) that accounts for the circular notch geometry. For the SEN(B) circular notched geometry three separate functions were derived from the finite element models. These functions included the non-dimensional crack length function f(a/W) and the two equations used to infer the crack length from the specimen compliance (similar to equations 6.5 and 6.7). The functions derived from the finite element models were used to reprocess the experimental fracture resistance data accounting for the effect of the circular notch. The fracture resistance results using the standard equations and the derived equations using the circular notched geometry were then compared to verify that the statistical comparison between control and damaged groups from experiments 1 and 3 was unchanged by the circular notch geometry.

6.2 Method

All finite element modelling was carried out using the ANSYS parametric design language (version 14.5). Post processing of the finite element model output was conducted using Matlab (version r2012b). Two separate finite element models were developed for each of the fracture specimen configurations (C(T) and SEN(B)). The first model for each configuration used notch geometry that conforms to the geometrical guidelines in ASTM E1820, this model was used for verification and a mesh independence study. The second model for each of the configurations included circular notch geometry the same as the specimens used in experiment 1 (for the C(T) configuration) and experiment 3 (for the SEN(B) configuration).

6.2.1 Elements and Material Models

All models used a two dimensional 8-node quadrilateral element for meshing the bulk geometry of the fracture specimen. For the purpose of meshing the curved shapes of the pins and surrounding material of the C(T) specimen two dimensional 6-node triangular elements were used. All two dimensional solid elements used a plane stress assumption. Contact was modelled between the loading pins and the test specimens using 3 node target elements on the pin surface and 3 node contact elements on the specimen surface. The pins were modelled using the material properties of steel; that is, linear elastic isotropic with elastic modulus E = 200GPa and Poisson's ratio v = 0.3. The fracture specimen was modelled using the analogous properties of bovine cortical bone: linear elastic isotropic with elastic modulus E = 21.3GPa and Poisson's ratio v = 0.3 (Broz et al., 1995; Cowin and Sadegh, 1991; Reilly et al., 1974).

6.2.2 Compact Tension Model

Figure 6.1 (a) shows the standard geometry for the C(T) fracture specimens while Figure 6.1 (b) shows the circular notch geometry used in experiment 1. The dimensions of the specimen were set such that the characteristic length W = 12 mm. Note that the remaining dimensions of the C(T) specimen geometry are based on the characteristic length 'W'. For the circular notched specimen the diameter of the circular notch d = 2 mm. The finite element model and mesh for both the conventional geometry and the circular notched geometry are shown in Figure 6.2 (a), (b) and Figure 6.2 (c), (d) respectively. Both specimens are uniform through thickness so a two dimensional model was used. The element size was set to 0.2 mm before refinement at the crack tip. Further to this, only half of the specimen was modelled about the symmetry line of the crack path.

All nodes on the top pin area were constrained such that they could not translate horizontally. A vertical displacement of 0.1 mm was then applied to the central node of the pin. A symmetry boundary condition was applied to all nodes ahead of the crack line. When the C(T) specimens were machined for experiment 1 the hole was machined using a jig that ensured that the circular notch was located in the same position. Thus, the end of the circular notch (or wedge notch) for the finite element model was fixed at a/W = 0.49. This initial notch length allows for the crack tip to be located at a/W = 0.5, which accounts for the length of the scalpel notch that was carved into the specimen before fracture testing. The crack length was initially set such that the ratio of crack length to characteristic length was a/W = 0.5, the crack length was then incremented in steps of a/W = 0.01 up to a maximum crack length of a/W = 0.75. The model was re-meshed and solved for each crack length step with the region of mesh concentration centred on the crack tip (as shown in Figure 6.2).

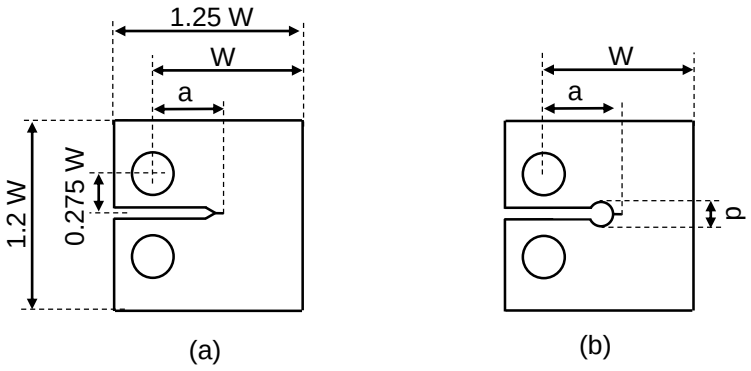

Figure 6.1: (a) Standard geometry of a C(T) specimen showing the key dimensions of the crack length 'a' and characteristic length 'W'. (b) Circular notch C(T) specimen geometry.

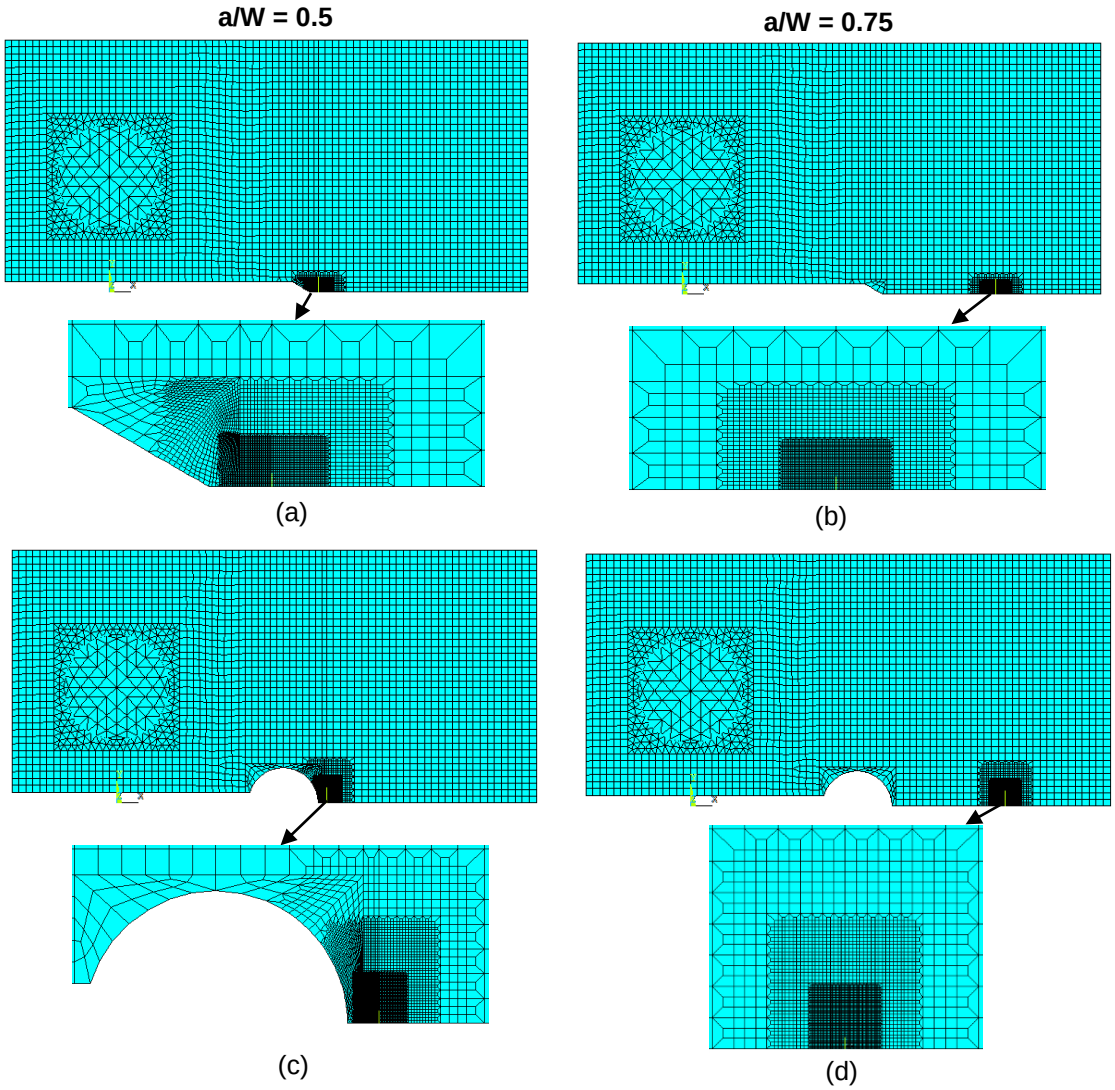

Figure 6.2: (a),(b) Finite element mesh for the standard geometry C(T) specimen and (c),(d) finite element mesh for the circular notch C(T) specimen. Inset images show the mesh concentration at the crack tip. Images on the left show the shortest crack length a/W = 0.5 and images on the right show the longest crack length a/W = 0.75.

6.2.3 Single Edge Notched Bend Model

Figure 6.3 (a) shows the standard geometry for a SEN(B) specimen and Figure 6.3 (b) shows the circular notched configuration used in experiment 3. The dimensions of the specimen were chosen to be the same as the geometry machined for experiment 3 with the characteristic length W = 4.5mm and circular notch diameter of d = 3mm. The finite element model and mesh for both the conventional geometry and the circular notched geometry are shown in Figure 6.4 (a), (b) and Figure 6.4 (c), (d) respectively. As the specimen is symmetric about the crack path only half the specimen was modelled. The specimen geometry is uniform through thickness. Therefore a two dimensional model was used with element size set to 0.1 mm before refinement at the crack tip.

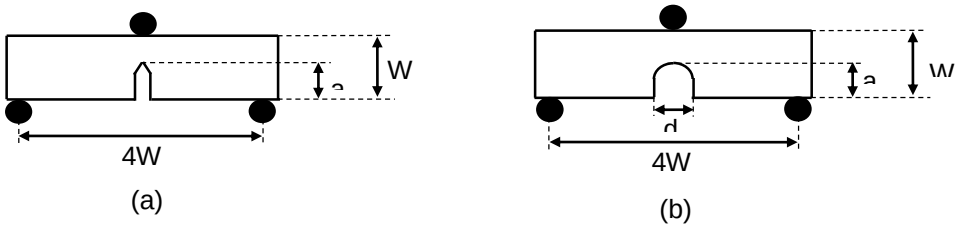

Figure 6.3: (a) Standard geometry of a SEN(B) specimen and (b) the circular notched geometry used in experiment 3.

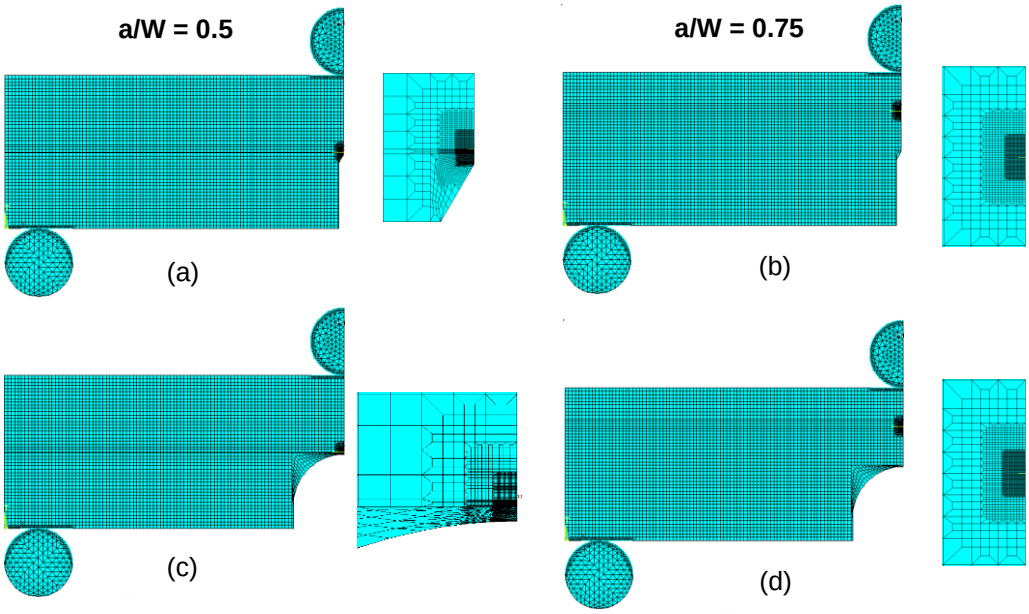

Figure 6.4: (a),(b) Finite element mesh for the standard SEN(B) model and (c),(d) circular notched SEN(B) model. Inset images show the mesh concentration region at the crack tip. Images on the left show a crack length of a/W = 0.5 while images on the right show the longest crack length a/W = 0.75.

All nodes on the bottom pin had all displacement and rotation degrees of freedom constrained. The nodes on the top half pin were constrained to prevent translation in the horizontal direction and a vertical displacement of 0.1 mm downward was applied to the central node of the top pin. A symmetry boundary condition was applied to all nodes along the crack face. The circular notch for the fracture specimens in experiment 3 was machined using a bench top mill. Because of this the location of the circular notch varied between a/W = 0.45 to a/W = 0.55. Therefore the finite element models were used to derive a series of non-dimensional crack length and compliance equations for notch lengths between these values with the notch length incremented in steps of a/W = 0.005. The derived equations were then interpolated to use the measured circular notch length for each specimen. The crack length was initially set such that the ratio of crack length to characteristic length was a/W = 0.04 ahead of the notch length to account for the scalpel starter notch carved into the specimen before fracture testing. The crack length was then incremented in steps of a/W = 0.01 up to a maximum crack length of a/W = 0.75. The model was re-meshed and solved for each crack length step with the region of mesh concentration centred on the crack tip (as shown in Figure 6.4).

6.3 Results and Discussion

6.3.1 Verification and Mesh Independence

For both the C(T) and SEN(B) configurations a mesh independence study was conducted using the standard fracture specimen geometry. For the purpose of the mesh independence study the circular notched geometry was used including a contact model between the pins and the specimen. The mesh near the crack tip region was progressively refined for three different crack lengths a/W = 0.5, 0.6, 0.7 and 0.75. Convergence was analysed for the reaction load at the displaced pin and the J-integral measured at the crack tip. Figure 6.5 shows the results for the C(T) specimen while Figure 6.6 show the results for the SEN(B) specimen configuration.

Even at the most coarse mesh size the reaction load for both models is within 1.5% of the finest mesh value. For both models the reaction load converges within two iterations of mesh refinement. However, as the J-integral is derived from the mesh strain values, it converges slower than the reaction load. Based on the mesh independence results shown in Figure 6.5 and Figure 6.6 a refined crack tip mesh size of 7.4μm was chosen for the C(T) model and 3.7 μm for the SEN(B) model.

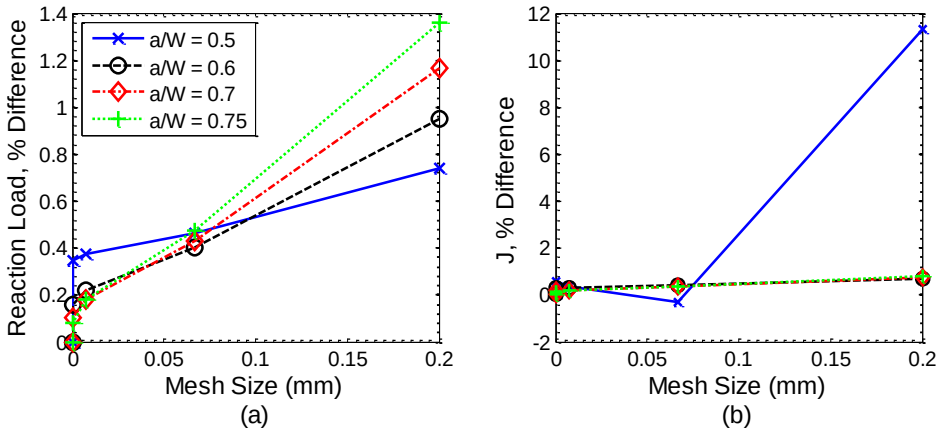

Figure 6.5: Mesh independence results for the C(T) model showing the percentage difference to the minimum mesh size for (a) the reaction load and (b) the J-integral measured at the crack tip.

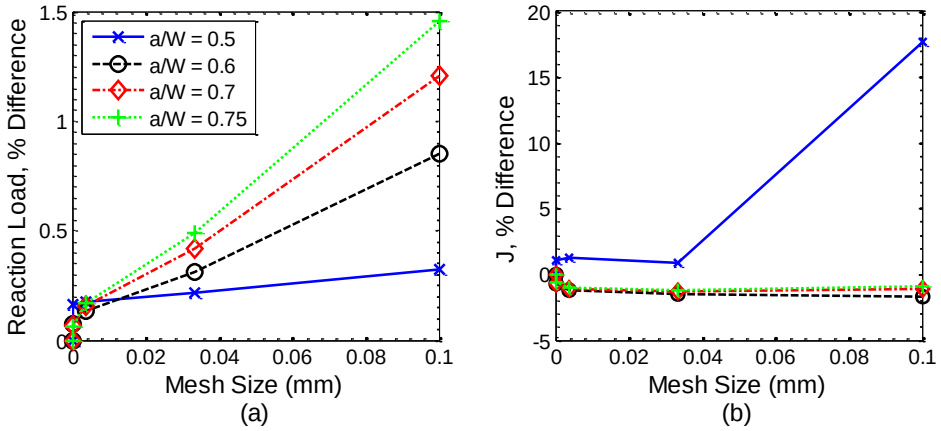

Figure 6.6: Mesh independence results for the SEN(B) model showing the percentage difference to the minimum mesh size for the (a) reaction load and (b) the J-integral measured at the crack tip.

For both the C(T) and SEN(B) models a verification model was compared with results calculated from the stress intensity factor equations in ASTM standard E1820. These verification models, for both the C(T) and the SEN(B) configurations, used simplified point displacement constraints as boundary conditions and did not model contact between the pins and the specimen. Further to this the verification models used an ideally sharp notch. The crack tip mesh was refined based on the results of the mesh independence studies (7.4 µm for the C(T) model and 3.7µm for the SEN(B) model). To verify the model against the equations outlined in ASTM E1820 the stress intensity factor was calculated using equations 6.1 to 6.4 and the nodal reaction force at the displaced node. This was then compared to the stress intensity factor calculated at the crack tip using the J-integral. The results for the verification model are shown in Table 6.1. Both models are within ~1% of the stress intensity factor calculated using the ASTM equations.

Table 6.1: Verification results for the both the C(T) and SEN(B) models. K(P) specifies the stress intensity factor calculated using the nodal reaction at the displaced node and the standard equation in ASTM E1820. K(J) denotes the stress intensity factor calculated using the J-integral value at the crack tip and equation 6.5.

	Compact Tension			**Single Edge Notched Bend**		
a/W	*K(P) (MPa√m)*	*K(J) (MPa√m)*	*% Difference*	*K(P) (MPa√m)*	*K(J) (MPa√m)*	*% Difference*
0.5	8.8478	8.7580	1.015	6.1341	6.0899	0.72
0.6	7.9554	7.9430	0.153	5.6626	5.6268	0.63
0.7	6.8915	6.8951	-0.0531	4.9540	4.9453	0.17
0.75	6.2583	6.2585	-0.0038	4.5167	4.5230	-0.14

6.3.2 Comparison of Non-Dimensional Functions

Figure 6.7 shows the non-dimensional crack length function, 'f(a/W)' for (a) the C(T) and (b) the SEN(B) model. The non-dimensional crack length functions show a decrease near the circular notch which indicates a decrease in the stress intensity factor when compared to the wedge notched model or the ASTM E1820 equations. The circular notch is smaller for the C(T) specimen than the SEN(B) specimens. Therefore the effect of the notch is only significant up to a/W ~ 0.55 for the circular notched C(T) geometry (as shown in Figure 6.7 (b)). The larger circular notch of the SEN(B) specimen causes a significant difference in the stress intensity factor up to a/W ~ 0.6 (as shown in Figure 6.7 (b)). Both the circular notch and wedge notched models show a vertical offset with respect to the standard equations. It is likely that this offset is due to the models including contact between the pins and the specimen whereas the standard equations use ideal 'point' boundary conditions. Using a contact condition with the pins will cause the applied load to be distributed over a larger area for both models. This will cause the effective moment arm over which the force is applied to be reduced leading to a decrease in the apparent applied load. Note that with ideal point boundary conditions both models show excellent agreement with the ASTM E1820 equations as shown in Table 6.1.

For both the C(T) and SEN(B) models the non-dimensional crack length data was fitted with a 6^{th} order polynomial to facilitate the reprocessing of the experimental fracture resistance data. The polynomial curve fit for both the C(T) and SEN(B) models are shown in Figure 6.8 (a) and (b) respectively. Note that for the SEN(B) specimen multiple notch lengths were also analysed. The curve shown in Figure 6.8 is for a notch length of a/W = 0.48. The curve fits for both models showed correlation coefficients of $r^2 > 0.999$.

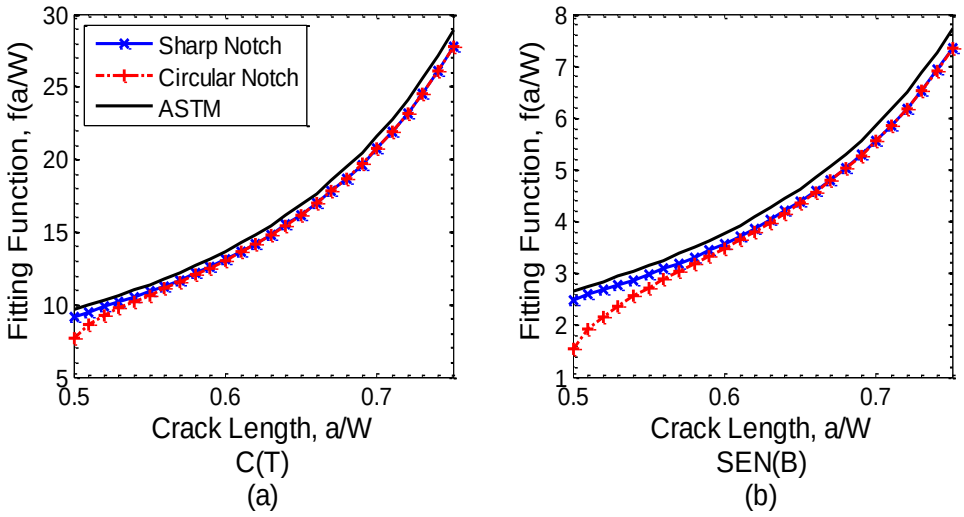

Figure 6.7: (a) Non-dimensional crack length function for calculation of the stress intensity factor for the C(T) model and (b) the SEN(B) model.

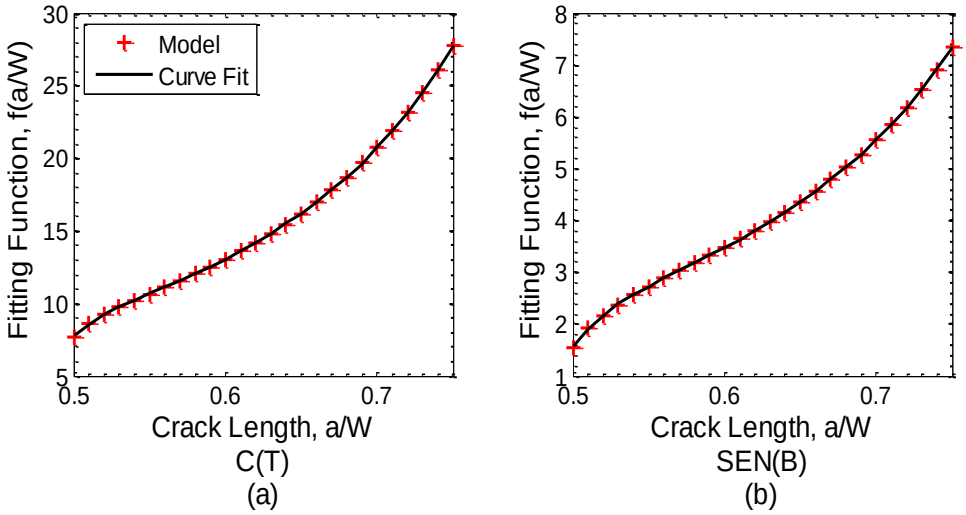

Figure 6.8: (a) Polynomial curve fits for the non-dimensional crack length function 'f(a/W)' for the C(T) model and (b) the SEN(B) model.

For the SEN(B) geometry two further equations were derived in order to infer the crack length from the measured compliance. Figure 6.9 (a) shows the non-dimensional compliance equation used to calculate the initial elastic modulus (similar to equation 6.5). Figure 6.9 (b) shows the non-dimensional compliance equations used to infer the crack length (similar to equation 6.7). Figure 6.9 (a) and (b) show the fitted curve with a solid line at the minimum (Notch Length = 0.45 a/W) and maximum notch lengths (Notch Length = 0.55 a/W).

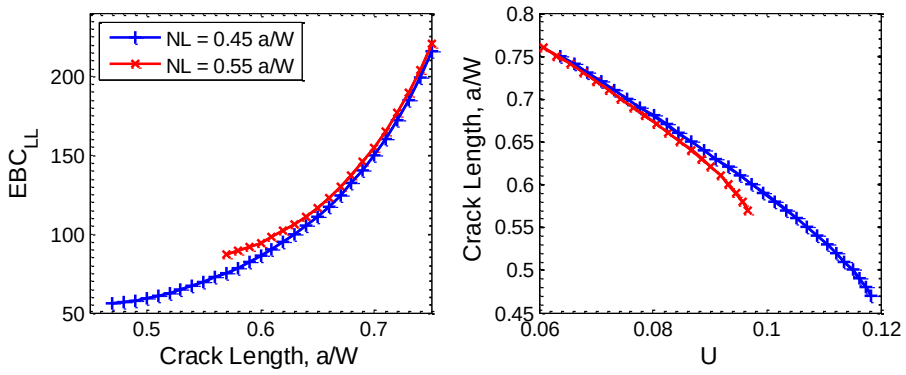

Figure 6.9: (a) Non-dimensional curve showing the compliance as a function of crack length used to infer the elastic modulus. (b) Non-dimensional function used to infer the crack length from the compliance. Both the minimum (NL = 0.45 a/W) and maximum (NL = 0.55 a/W) notch lengths are shown.

6.3.3 Recalculation of Results from Experiments 1 and 3

All fracture resistance curve data from experiments 1 and 3 was reprocessed using the non-dimensional crack length functions derived from the finite element models. Figure 6.10 shows the original resistance curve data for a typical specimen compared to the data processed using the newly derived equations for the C(T) and SEN(B) geometry. For the C(T) specimen shown in Figure 6.10 (a) the newly derived equations translate the points near the starter notch below the standard geometry data while further from the notch the points are translated above the standard geometry data. While for the SEN(B) specimen the reduction in fracture resistance near the notch is more pronounced. This result is expected as the circular notch for the SEN(B) specimen was larger than the C(T) specimen relative to the characteristic length of the specimen. Thus, the 'blunting' effect of the notch will be more prevalent for the SEN(B) specimen.

The results of all reprocessed fracture resistance data were compared with the previous experimental results in order to verify that the circular notch geometry did not change the comparison of experimental groups. Table 6.2 to Table 6.4 show the fracture resistance curve data comparison of the results from experiments 1 and 3 processed using the standard equations and the equations derived from the finite element models. Table 6.2 shows that the results of all statistical tests for the fracture initiation toughness 'J_0' remain unchanged by the use of the equations from the finite element model. The reduction in average fracture initiation toughness is larger for the SEN(B) specimens when compared to the C(T) specimens. This difference is expected as the size of the circular notch relative to the specimen characteristic length is much larger for the SEN(B) (d/W = 0.667) specimens compared to the C(T) specimens (d/W = 0.167).

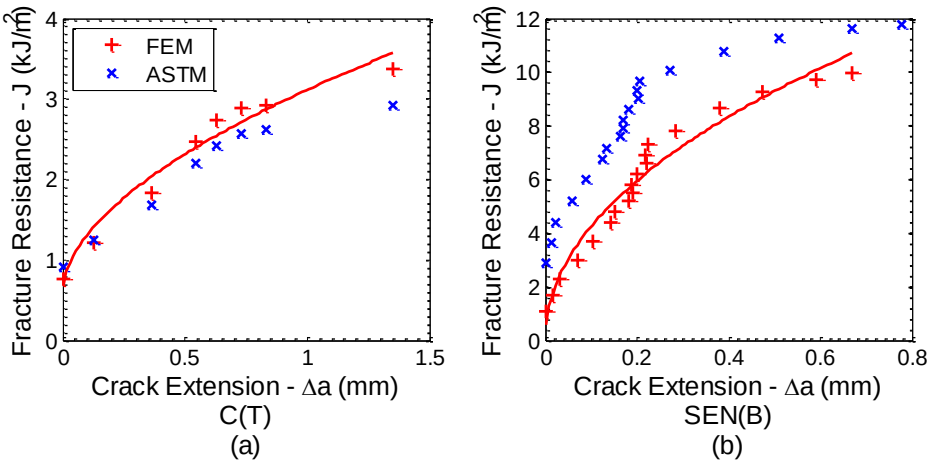

Figure 6.10: (a) Reprocessed resistance curve data for the C(T) and (b) the SEN(B) shown as red '+'. Original data using the standard equations is shown with blue '+'. The solid red line shows the new resistance curve fitted to the reprocessed data.

The results in Table 6.3 shows how the point at which the growth toughness is evaluated 'a_Q' was changed by utilising the new equations that account for the circular notch. For the case of the compact tensions the difference in 'a_Q' was minimal whereas the change in 'a_Q' for the SEN(B) specimens was ~15% for all groups. Table 6.4 shows that the comparison of the growth toughness 'dJ/da'. For this case, it is interesting to note that the percentage change in the growth toughness is more significant for the C(T) specimen geometry than the SEN(B). The observed differences for both 'a_Q' and dJ/da for different specimen geometries is a result of the method used to process the experimental data. For the C(T) geometry the crack extension data is taken directly from the optical measurements during the test. Whereas the crack length is inferred from compliance equations for the transverse SEN(B) specimens.

Table 6.2: Comparison of fracture initiation toughness results from experiment 1 and experiment 3 processed with the standard equations or the finite element model data.

	Experiment 1: C(T)		**Experiment 3: SEN(B) Tensile**		**Experiment 3: SEN(B) Compressive**	
J_0, kJ/m²	*Control*	*Damaged*	*Control*	*Damaged*	*Control*	*Damaged*
Standard	1.23±0.21	0.96±0.29	2.34 [2.02,2.65]	2.37 [1.99,2.80]	2.19 [2.03,2.29]	1.77 [1.53,2.05]
P value (Standard)		0.031*		0.78		>0.01*
FEM	1.09±0.19	0.85±0.29	1.04 [0.83,1.11]	1.02 [0.88,1.18]	0.95 [0.83,1.06]	0.82 [0.72,0.92]
P value (FEM)		0.043*		1.00		0.01*
% Change	-11.4%	-11.5%	-55.6%	-57.7%	-56.6%	-53.6%

Table 6.3: Comparison of a_Q results from experiment 1 and experiment 3 processed using either the standard equations or the finite element model data.

	Experiment 1: C(T)		**Experiment 3: SEN(B) Tensile**		**Experiment 3: SEN(B) Compressive**	
a_Q (mm)	*Control*	*Damaged*	*Control*	*Damaged*	*Control*	*Damaged*
Standard	0.222± 0.003	0.224± 0.022	0.221 [0.217,0.224]	0.220 [0.216,0.223]	0.221 [0.218,0.226]	0.220 [0.217,0.228]
FEM	0.223± 0.003	0.219± 0.008	0.257 [0.242,0.279]	0.250 [0.239,0.264]	0.263 [0.248,0.279]	0.259 [0.247,0.289]
% Change	0.45%	-2.23%	16.3%	13.6%	19.0%	17.7%

Table 6.4: Comparison of dJ/da results from experiment 1 and experiment 3 processed using either the standard equations or the finite element model data.

	Experiment 1: C(T)		**Experiment 3: SEN(B) Tensile**		**Experiment 3: SEN(B) Compressive**	
dJ/da (a_Q) ($kJ/m^2/mm$)	*Control*	*Damaged*	*Control*	*Damaged*	*Control*	*Damaged*
Standard	1.18±0.49	0.85±0.38	10.4 [6.16,11.0]	7.85 [5.59,9.70]	9.89 [6.63,12.6]	9.83 [7.65,18.0]
P value (Standard)		0.16		0.47		0.52
FEM	1.83±0.62	1.37±0.52	10.3 [6.71,11.7]	9.09 [6.93,10.1]	10.2 [7.13,13.1]	9.87 [7.36,17.2]
P value (FEM)		0.09		0.79		0.71
% Change	55.1%	61.2%	-0.96%	15.8%	3.13%	0.41%

6.4 Conclusion

The purpose of this study was to verify the assumption that the use of circular notch geometry did not alter the comparison of resistance curve data. This study utilised a finite element modelling approach to derive new compliance equations for a circular notched fracture specimen representative of those used in experiments 1 and 3 (Chapters 3 and 5 respectively). The results of this study showed that the circular notch does not alter the statistical comparison of the fracture resistance results from experiments 1 and 3. Therefore the standard equations from ASTM E1820 can be used for circular notch geometries in future experiments without the need for further finite element studies and the derivation of new equations.

The results of this study are beneficial as future studies utilising circular notch geometry for comparison of resistance curve behaviour will not need the time and effort required to derive new equations for a specific geometry. Overall, the results of this study show that use of the standard equations for the circular notch geometry changes the magnitude of the fracture initiation toughness and overall fracture resistance curve but it does not change the statistical comparison between groups with consistent geometry.

Chapter 7: Finite Element Modelling 2

Fracture Mechanisms in Cortical Bone

7 Finite Element Modelling 2: Fracture Mechanisms in Cortical Bone

7.1 Introduction

In Chapters 3 and 5 several mechanisms of fatigue fracture interaction were proposed to explain the effect that fatigue damage has on the fracture toughening behaviour of cortical bone. These mechanisms of fatigue fracture interaction described how the fatigue induced damage interacted with the normal toughening behaviour present in bone (e.g. ligament bridging, crack deflection, microcrack formation during crack growth and the local material resistance to fracture). Previously published fracture testing of cortical bone has also provided evidence for the various toughening mechanisms present in normal bone (i.e. not fatigue damaged), and has suggested that the most prevalent mechanisms are ligament bridging or longitudinal cracking (Nalla et al., 2004b) and crack deflection for transverse cracking (Koester et al., 2011). Using experimental techniques it is extremely difficult to decouple and analyse the individual contribution of each of the toughening mechanisms in cortical bone. Therefore the use of a numerical or analytical modelling technique is required, such as finite element modelling. This analysis would be highly beneficial for the overall explanation of experimental results presented in this thesis. Thus, the purpose of this study is to analyse the relative effectiveness of the various toughening mechanisms in cortical bone (i.e. crack deflection, ligament bridging and microcracking) using a finite element modelling approach.

Observation of the crack paths from experimental testing can provide insight into the different mechanisms responsible for the fracture toughening behaviour in cortical bone. However, it is difficult to separate out the individual mechanisms to understand their relative contribution to the overall fracture resistance curve. The main drawback of optical crack path analysis is that it can only suggest what mechanisms are most prevalent along the crack path. The visual analysis does not quantify or give any indication of relative magnitude that each mechanism contributes to the fracture resistance curve. From the analysis of crack path images it is also unclear how other material behaviour effects (such as plastic slip, microcracking and orthotropic material properties) contribute to the overall toughening of cortical bone. An alternative method of analysing fracture toughening mechanisms in cortical bone includes numerical modelling using Finite Element Analysis (FEA) techniques. FEA has been used extensively in previous research to analyse fracture mechanisms in engineering materials and therefore a brief review of the literature on the FEA of fracture mechanics is presented here.

There is a large body of engineering literature that focuses on analytical and numerical analysis of cracks and crack growth in materials. See Tada et al. (1985) for a compilation of analytical and numerical solutions for various cracked geometries or Kuna (2013) for a detailed analysis of the use of FEA for fracture mechanics. As the literature on FEA for fracture mechanics is extensive only a brief outline will be provided here followed. This will then be following by a further outline of the use of FEA to analyse fracture in bone.

Finite element analysis has been used to investigate fracture in engineering materials such as metals (Jha and Narasimhan, 1992; Nishioka and Atluri, 1982; Takuda et al., 2000) ceramics (Jayaraman et al., 1997; Yutaka and Daigora, 1992) and various composites (Goto and Kagawa, 1994; Jha and Charalambides, 1998; Shaw and Miracle, 1996; Xia et al., 2001). Early finite element analysis of cracked bodies focused on the calculation of the stress intensity factor or strain energy release rate for stationary cracks of various simple geometries (e.g. through thickness cracks in a plate and elliptical cracks in a three dimensional plate) (Alwar and Nambissan, 1983; Byskov, 1970; deLorenzi, 1982; Tracey, 1974). More recent work has focused on the modelling of crack growth in various materials, the most common methods include the cohesive zone model (CZM) (Roe and Siegmund, 2003; Siegmund, 2004), the virtual crack closure technique (VCCT) (Agrawal and Karlsson, 2006; Chow and Atluri, 1995; Fawaz, 1998) and the extended finite element method (XFEM) (Liu et al., 2012; Xu and Yuan, 2009).

Previous studies using FEA to analyse the crack growth behaviour of cortical bone have focused on the use of CZMs (Mischinski and Ural, 2013, 2011; Ural et al., 2011; Ural and Vashishth, 2007, 2006) and XFEM (Abdel-Wahab et al., 2012; Budyn et al., 2008). CZMs have been extensively used for the analysis of engineering fibre composites, which exhibit similar toughening mechanisms to bone such as ligament bridging and deflection at interfaces in the microstructure. Initial finite element based fracture studies in cortical bone used the CZM approach to model the stress intensity factor based resistance curve for young and aged human bone (Ural and Vashishth, 2007, 2006). Later studies have been successful in modelling the growth of cracks at the micro scale (Abdel-Wahab et al., 2012; Donaldson et al., 2014; Mischinski and Ural, 2013) along with the combination of microstructural models with macro scale fracture specimens (Ural and Mischinski, 2013a). While CZMs and XFEM have been successful for the analysis of crack growth in cortical bone they combine all of the fracture processes into a zone about the crack tip. This combines all of the toughening phenomena into a single cohesive zone and therefore the contributions of the individual toughening mechanisms cannot be assessed.

The aim of this study is to investigate the relative contribution of various toughening mechanisms to the overall fracture toughening behaviour of cortical bone. As the various crack growth simulation techniques such as CZM and XFEM cannot decouple the multiple toughening mechanisms present in bone this study cannot use these techniques, instead the toughening mechanisms will be directly modelled and parametrically analysed based on crack path imaging from experimental data. The toughening mechanisms that will be modelled as part of this study include: (1) orthotropic material behaviour, (2) uncracked ligament bridging, (3) crack deflection and (4) microcracking. Overall, the results of this study will provide further insight into the relative contribution of each of the main toughening mechanisms present in cortical bone. This will have significant impact on the analysis of fracture toughening mechanisms in cortical bone and may provide further insight into the mechanisms of fatigue fracture interaction proposed in this thesis.

7.2 Method

7.2.1 Overview of Fracture Mechanism Models

All finite element modelling was carried out using the ANSYS parametric design language (version 14.5). Post processing of the finite element model output was conducted using Matlab (version r2012b). All finite element models in the study were based on the general compact tension specimen model describe in section 7.2.2. For each toughening mechanisms modelled in this study modifications were made to the general compact tension specimen model to account for physical effect of each toughening mechanism. Several of the toughening mechanism models were divided into several separate test cases to analyse the limiting conditions for each toughening mechanism. All toughening mechanism finite element model and their relevant test cases are listed here, each model is described in more detail in its respective section of the method:

1. **Material Models - 7.2.3**
    - Case 1: Isotropic material properties
    - Case 2: Orthotropic material properties
    - Case 3: Orthotropic material properties
2. **Ligament Bridging Model - 7.2.4**
    - Case 1: Single ligament bridge along the crack path
3. **Crack Deflection Models - 7.2.5**
    - Case 1: Single 90° deflection
    - Case 2: Single 90° deflection with a region of straight crack growth
    - Case 3: Arbitrary angle of deflection
    - Case 4: Arbitrary angle of deflection with a region of straight crack growth

4. Microcracking Models - 7.2.6

- Case 1: Single microcrack aligned with the crack plane
- Case 2: Single microcrack offset from the crack plane
- Case 3: Array of microcracks aligned with and ahead of the main crack
- Case 4: Array of microcracks offset from and ahead of the main crack
- Case 5: Array of microcracks ahead and behind the main crack tip

The different material models were analysed over a range of crack lengths in the absence of other toughening mechanisms. For most of the toughening mechanisms models; that is, the ligament bridging, crack deflection and microcracking models fixed crack length was used and the toughening mechanism was parametrically analysed. For example: the crack deflection model was analysed with the length of the deflection relative to the crack length and the angle of deflection from the normal plane of crack growth as parameters. The reason for this is that analysis of single long crack length (similar to the crack length at the end of an experiment) shows how the toughening mechanism affects the fracture behaviour over the whole test. Further to this, pilot finite element models showed that the fracture toughening trends were similar for different crack lengths.

7.2.2 General Compact Tension Model

The standard geometry for a compact tension (C(T))specimen is shown in Figure 7.1 (a) (ASTM standard E1820, 2011). For this model the characteristic length ‘W’ was set at 12mm. As the specimen is uniform through thickness the specimen was modelled in two dimensions. The mesh for the bulk geometry of the compact tension specimen is shown in Figure 7.1 (b) and the concentrated mesh at the crack tip is shown in (c). More detailed images for the crack path mesh for the various toughening mechanism models are shown in their respective sections. Note that for the purpose of modelling asymmetric toughening behaviour the whole compact tension specimen was modelled. The C(T) specimen was mapped meshed with two dimensional 8-node quadrilateral elements. The curved shapes of the pins and surrounding curved material of the C(T) specimen were meshed with two dimensional 6-node triangular elements were used. All two dimensional solid elements used a plane stress assumption. Contact was modelled between the loading pins and the test specimens using 3 node target elements on the pin surface and 3 node contact elements on the specimen surface. The pins were modelled using the material properties of steel; that is, linear elastic and isotropic with elastic modulus E = 200GPa and Poisson’s ratio v = 0.3. All displacement degrees of freedom were constrained on the nodes on the bottom pin of the model. All nodes on the top pin area were constrained such that they could not translate horizontally. A vertical displacement of 0.1mm was then applied to the central node of the top pin.

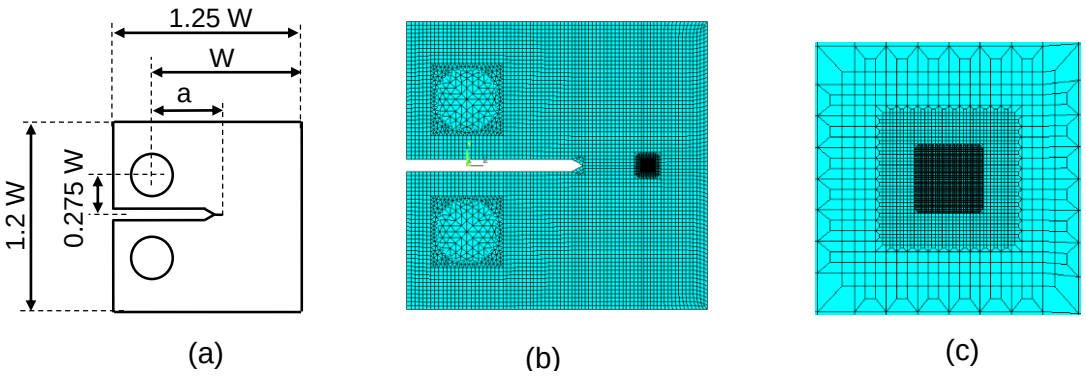

Figure 7.1: (a) General compact tension specimen geometry, (b) whole finite element model mesh and (c) the concentrated mesh at the crack tip.

For all toughening mechanism models the material properties were set to be linear elastic isotropic bone. The reason for only analysing isotropic material behaviour is that by combining both orthotropic and the effects of a toughening mechanism (e.g. crack deflection or ligament bridging) it will not be possible to determine what factor has caused the net change in toughening behaviour when compared to the ideal case. Note that subsequent data processing will utilise the reaction load measured at the pin to determine the ideal SIF, as would be performed experimentally. Utilisation of isotropic material properties allows for the comparison of the ideal value calculated using the equations for the standard specimen geometry and the reaction load to the J-integral taken from the stress field at the crack tip (Note that this is discussed further in section 7.2.7).

7.2.3 Material Models

Following verification two different material models were tested as analogues of the properties of bovine cortical bone. The first model was linear elastic isotropic with: elastic modulus E = 23.1GPa and Poisson's ratio v = 0.3. The second model was linear elastic orthotropic with: elastic modulus: $E_1 = E_2 = 10.4$ GPa, $E_3 = 23.1$GPa, Poisson's ratio: $v_{12} = v_{12} = 0.29$, $v_{12} = 0.51$ and shear modulus: $G_{12} = G_{13} = G_{23} = 3.6$GPa (Burstein et al., 1972a; Reilly et al., 1974). The subscript indices 1, 2 and 3 represent the radial, circumferential and axial directions with respect to the whole bone. For the orthotropic material models the orientation of the modulus was specified to represent either longitudinal (E_3 aligned in the crack growth direction) or transverse cracking (E_3 aligned perpendicular to the crack growth direction). For each material model tested the mesh used was the same as that shown in Figure 7.1 (b) and (c) with the concentrated region of the mesh being located at the crack tip. Various crack lengths were analysed in the range $0.5<a/W<0.75$ in increments of a/W = 0.01. Both the J-integral from the reaction load at the pin and the J-integral at the crack tip were calculated at each crack length.

7.2.4 Ligament Bridge Models

The ligament bridge model used a straight crack path with spring elements applied across the crack face to simulate the toughening effect (Figure 7.2 (b)). This model was tested at a fixed crack extension of a/W = 0.2 (total crack length of a/W = 0.7). The parameters that were investigated as part of this model included: the position of the ligament bridge along the crack path 'P'; the stiffness of the individual spring elements 'k' and the length of the ligament bridge 'L_{lb}'. The crack path for a ligament bridge model is shown schematically in Figure 7.2 (b) with the specified parameters. The mesh for this model was concentrated along the whole crack path and around the crack tip such that the spacing of the spring elements was the same for each position along the crack path. As the mesh spacing is constant along the crack path the ligament bridge parameter 'L_{lb}' indicates the number of spring elements used for each bridge. Hence, the total effective bridge stiffness can be inferred by analysing trends for the ligament bridge length. Note that both the position 'P' and ligament bridge length 'L_{lb}' were expressed non-dimensionally as a ratio of the total crack extension (e.g. L_{lb} = 0.1, P = 0.3 indicates a ligament bridge with a length of 10% of the total crack extension located at 30% of the total crack extension from the starter notch).

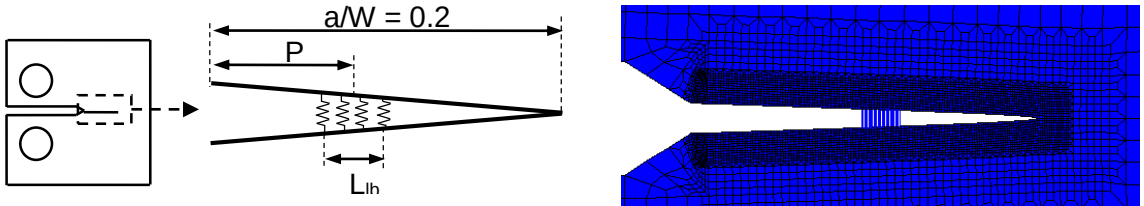

(a) k = spring stiffness

(b)

Figure 7.2: (a) Definition of model parameters for the ligament bridge model and (b) the crack path mesh for this model.

7.2.5 Crack Deflection Models

Four different geometries of crack deflection models were analysed. The first two models analysed the case of a 90 degree deflection along the crack path. The first model in this group is shown in Figure 7.3 (a) with the corresponding crack path mesh shown in Figure 7.3 (b). For this model the deflection position 'P' was parametrically analysed along with the deflection height 'H'. In order to remain consistent with the other toughening mechanism models the position 'P was expressed as a ratio of the maximum crack extension (i.e. as a ratio of 0.2 a/W). The second model in this group analysed the case of a 90 degree deflection followed by another portion of straight crack growth. The second model is shown in Figure 7.3 (c) with the corresponding crack path mesh shown in Figure 7.3 (d). For this model the crack extension was fixed at 0.2 a/W and the deflection position

along the crack path ‘P’ was expressed as a ratio of the total crack extension (e.g. P = 0.2 indicates that the deflection occurs 20% of the crack extension from the starter notch). For both 90 degree deflection models the deflection height ‘H’ was expressed as a ratio of half the specimen width (i.e. the deflection height from the centreline that would just break through the far edge of the specimen).

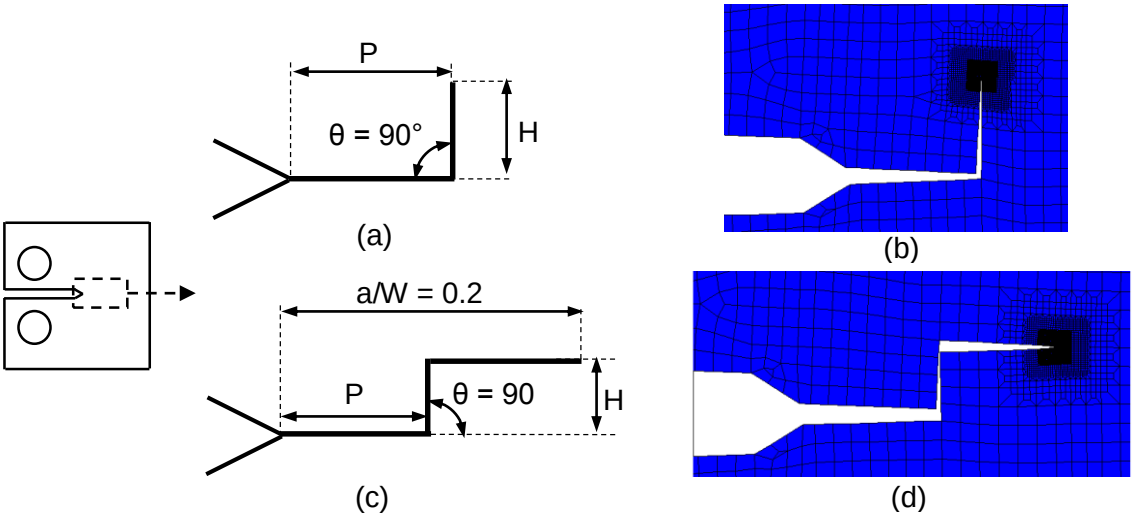

Figure 7.3: (a) Definition of the crack path variables for the 90 degree angle crack deflection models. (a) The first model includes a single deflection and (b) shows the crack path mesh for this model. (c) The second model includes a single deflection followed by region of straight crack growth and (d) shows the crack path mesh for this model.

The second two crack deflection models analysed the more generalised case of an arbitrary deflection angle over a specified portion of the crack path. The first model in this group included a variable length of straight crack growth followed by a single deflection as shown in Figure 7.4 (a). The crack path mesh for the first model is shown in Figure 7.4 (b). The parameters analysed for the first model include: the point at which the deflection begins ‘P’ and the angle of deflection ‘θ’. The second model was similar to the first model with another region of straight crack growth after the deflection (Figure 7.3 (c)). The mesh for the crack path of the second model is shown in Figure 7.4 (d). The parameters analysed for this model included: the point at which the deflection begins ‘P’; the length of the deflection ‘L_d’ and the angle of deflection ‘θ’. For both of these models the total crack extension was fixed at 0.2 a/W and the parameters ‘P’ and ‘L_d’ were expressed as a ratio of the total crack extension. Note that for both of these models the deflection height was not explicitly specified but was calculated from the deflection length and deflection angle.

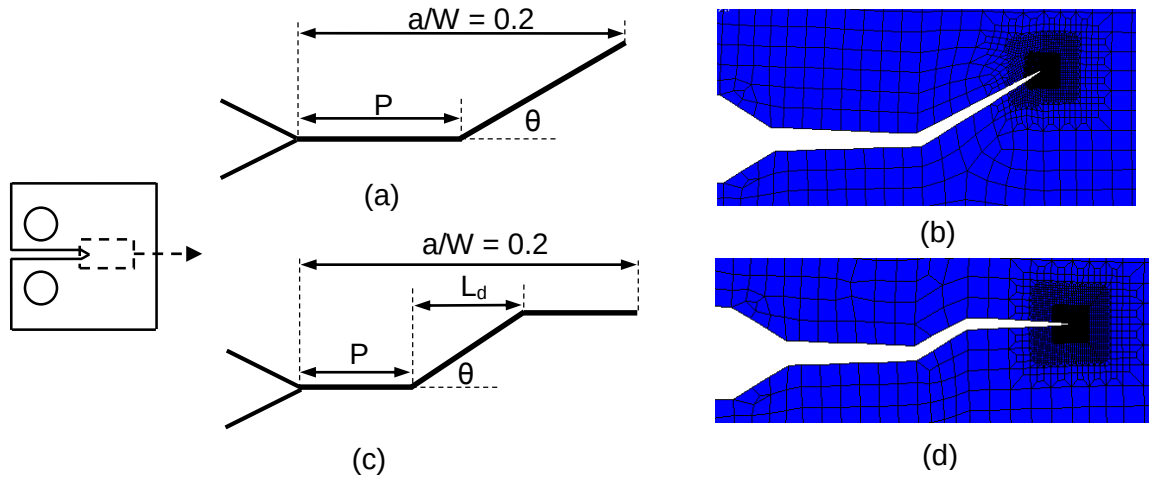

Figure 7.4: (a) Definition of the crack path variables for the arbitrary angle crack deflection models. (a) The first model includes a single deflection and (b) shows the crack path mesh for this model. (c) The second model includes a single deflection followed by region of straight crack growth and (d) shows the crack path mesh for this model.

7.2.6 Microcracking Models

Two separate microcracking models were analysed, the first model analysed a single microcrack and the second model analysed an array of microcracks around the crack tip. For the single microcrack model two different cases were analysed: (1) a single microcrack ahead of and aligned with the crack tip (shown in Figure 7.5 (a)) and (2) a single microcrack offset from the crack tip (shown in Figure 7.5 (c)). For the first case (single aligned microcrack) two parameters were analysed: the horizontal displacement from the main crack tip to the microcrack 'X' and the length of the microcrack 'L_{mc}' (see Figure 7.5 (a)). For the second case (single offset microcrack) the vertical displacement 'Y' was also analysed. Note that for the second case negative values of 'X' (behind the crack tip) were also analysed.

For the microcrack array model three different cases were analysed: (1) uniform pattern ahead of the crack tip with the microcracks closest to the crack tip aligned (shown in Figure 7.6 (a)); (2) uniform pattern of microcracks with the microcracks closest to the crack offset (shown in Figure 7.6 (c)) and (3) same as (1) with microcracks also located behind the crack tip (as shown in Figure 7.6 (e)). For each of these different cases several parameters were analysed including: the length of the microcracks 'L_{mc}' (60, 90 and 120 micron), the spacing of the microcracks in the vertical 's_y' and horizontal directions 's_x' (set equal at 60 to 150 micron) and the length 'R_x' and height 'R_y' of the region in which the microcracks were generated (600 and 1200 micron ahead and/or behind the crack tip). These parameters are shown in the schematics in Figure 7.6 (a). The main crack extension for this model was set at 0.2 a/W (total crack length of 0.7 a/W).

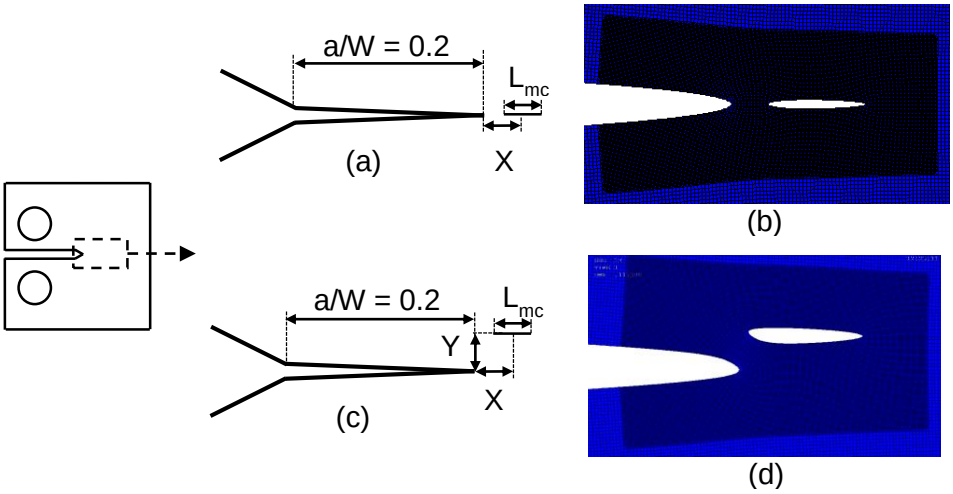

Figure 7.5: Single microcrack model schematic and crack tip mesh images. (a) Shows Case 1 includes a single microcrack aligned with the main crack and (b) shows the crack tip mesh for this model. (c) Shows case 2 which includes a single microcrack offset from the main crack and (d) shows the corresponding crack tip mesh.

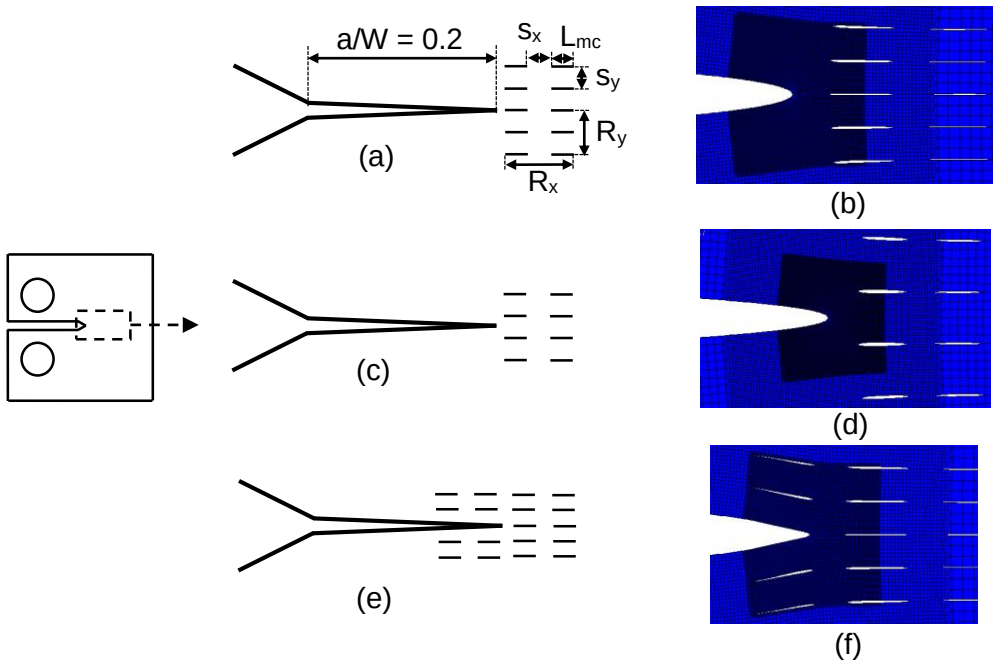

Figure 7.6: Three different cases analysed for the microcrack model: (a),(b) uniform pattern ahead of and aligned with the main crack, (c),(d) uniform pattern ahead of and misaligned with the main crack and (e),(f) uniform pattern ahead of and behind the main crack.

7.2.7 Post Processing

All post processing was performed using custom Matlab programs (version r2012b). For each model the J-integral was taken at the crack tip 'J_{ct}' using the function 'CINT' built into the ANSYS software (version r14.5). The reaction load was taken at the centre of the top pin of the C(T) model where the vertical displacement was applied. The reaction load was then used to calculate the J-integral 'J_{ideal}' using the equations given in ASTM standard E1820 (2011). Note that this study is limited to the analysis of the elastic component of the J-integral

All results are presented as the ratio of the J-integral taken from the crack tip to the J-integral calculated using the ASTM E1820 equations, J_{ct} /J_{ideal}. This normalisation allows for comparison of the J-integral taken from the stress field at the crack tip and the J-integral that would be measured during a fracture resistance test. In general, if the crack path mechanism leads to an increase in the apparent or measured toughness then the crack tip J-integral will be lower than the ideal J-integral calculated using the ASTM standard; that is, J_{ct} /J_{ideal} < 1. In text the ratio 'J_{ct}/J_{ideal}', will be referred to as the 'normalised J-integral'. Note that the apparent or measured toughness will be utilised when comparing the various toughening mechanisms. This is to distinguish the measured toughness from the true material toughness. The measured toughness includes effects from toughening mechanisms along the crack path whereas the material toughness is only the value that the crack tip J-integral (not the value predicted by the remotely applied loading) must reach in order for the crack to grow.

For the crack deflection model the crack orientation with respect to the applied loading will cause mixed mode loading on the main crack (i.e. combined mode I, tensile opening and mode II, shear). Note that the J-integral measured from the strain field at the crack tip for this case includes contributions from both mode I and mode II as follows:

$$J_{ct} = \frac{{K_I}^2}{E} + \frac{{K_{II}}^2}{E} \tag{7.1}$$

Where K_I is the mode I stress intensity factor, K_{II} is the mode II stress intensity factor and E is the elastic modulus It is advantageous to use the J-integral to assess the apparent toughening effects for all models as it combines mode I and mode I crack loading effects into a single parameter. As such, all models in this study use the normalised J-integral to assess the apparent toughening effects of each mechanism. For the deflection model the crack tip J-integral is normalised by the J-integral for the ideal straight crack case.

7.3 Results

7.3.1 Mesh independence Study

For the general C(T) specimen model a mesh independence study was conducted to analyse convergence of the reaction load and J-integral measured at the crack tip. Figure 7.7 (a) shows the results for the reaction load and Figure 7.6 (b) shows the J-integral at the crack tip for crack lengths of a/W = 0.5, 0.6, 0.7 and 0.75. Note that Figure 7.7 is the percentage difference of the reaction load and the J-integral relative to the finest mesh size.

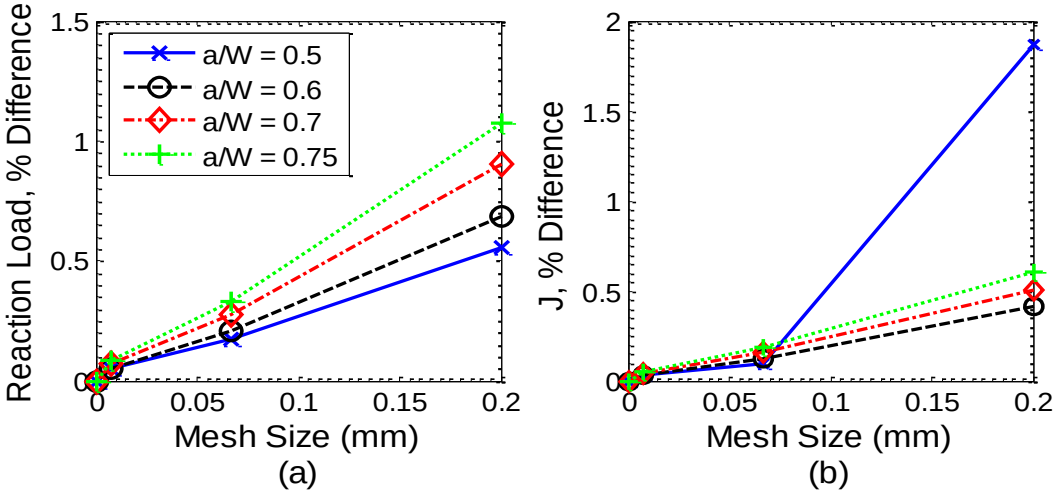

Figure 7.7: (a) Mesh independence results for the reaction load at the top pin and (b) the J-integral at the crack tip.

The results in Figure 7.7 show that within a single mesh refinement step the values have converged to within 0.5% of the finest mesh size for both the reaction load and the J-integral for all crack lengths. As computational time was not deemed to be an issue a crack tip mesh size of 7.4μm was chosen. Using the chosen refined mesh value the model was verified against the equations given in ASTM standard E1820 (2011) for the compact tension specimen geometry. Table 7.1 compares the results from the ASTM equations with the J-integral calculated at the crack tip. The relatively large difference observed near the starter notch (1.1%) is due to the wedge shape geometry of the starter notch being modelled whereas the ASTM equations assume an ideally sharp notch. Most of The toughening mechanism models in this study use a crack length of a/W = 0.7 (crack extension of 0.2 a/W). From the results shown in Table 7.1 this length shows extremely good agreement with the ASTM equations.

Table 7.1: Verification results for the standard compact tension specimen

a/W	K (ASTM) (MPa√m)	K (Model) (MPa√m)	% Difference
0.5	5.1860	5.1281	1.112
0.6	4.3894	4.3803	0.208
0.7	3.6327	3.6241	-0.0407
0.75	3.2418	3.2419	-0.0029

7.3.2 Material Model Results

Figure 7.8 shows the normalised J-integral plotted against the normalised crack length for the three material models. The isotropic material model agrees with the ideal solution taken from the standard equations (J_{ct}/J_{ideal} ~1), apart from the region near the starter notch. This difference is due to the wedge shaped starter notch being included in the present model whereas the standard equations assume an ideally sharp notch. The orthotropic material model for longitudinal direction shows an increase in apparent toughness when compared to the isotropic case ($J_{ct}/J_{ideal} < 1$) while the orthotropic material model for transverse direction shows a decrease in apparent toughness when compared to the isotropic case.

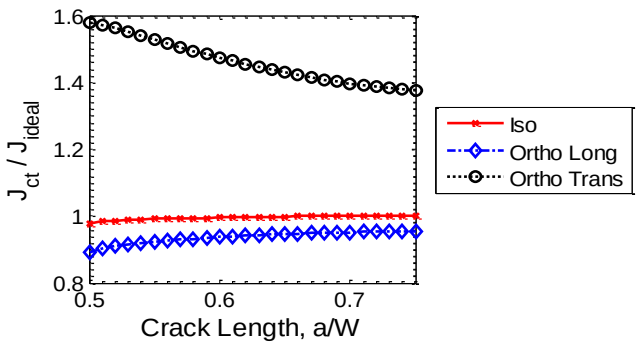

Figure 7.8: Normalised J-integral plotted against crack length for the isotropic and orthotropic material models.

7.3.3 Ligament Bridge Model Results

Figure 7.9 and Figure 7.10 show the normalised J-integral results for the ligament bridge model plotted against the three parameters analysed: ligament bridge length 'L_{lb}', ligament bridge position 'P' and bridge spring stiffness 'k'. Note that as the mesh density along the crack path was constant the ligament bridge length 'L_{lb}' indicates the total number of spring elements used and hence the total bridge stiffness. The limiting case for the individual spring stiffness (i.e. the maximum value) was chosen such that the stiffness of an individual spring was similar to the stiffness of the whole compact tension specimen measured in Experiment 1.

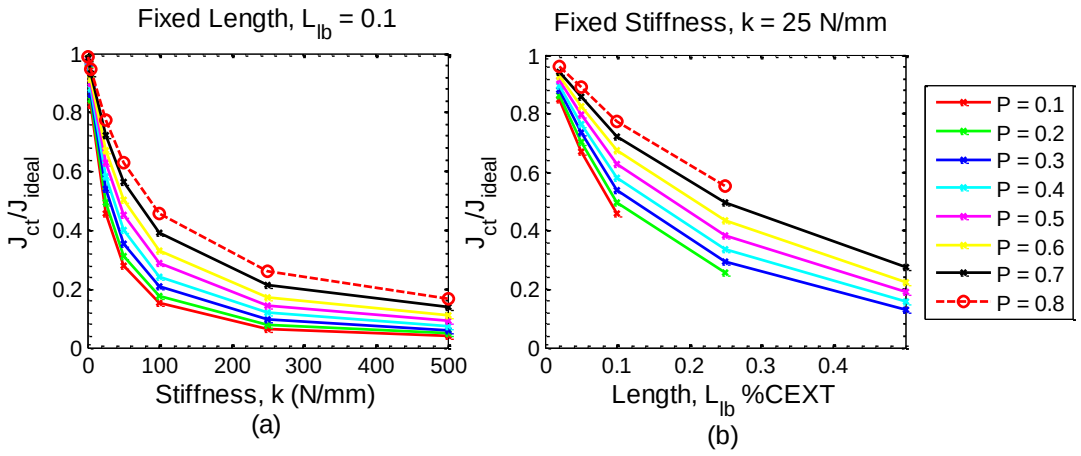

Figure 7.9: (a) Normalised J-integral plotted against ligament bridge spring stiffness 'k' with the ligament bridge length 'L' fixed at 10% of the crack extension.(b) Normalised J-integral plotted against ligament bridge length 'L' with the ligament bridge spring stiffness 'k' fixed at 25 N/mm. 'P' represents the position of the ligament bridge as a fraction of overall crack length.

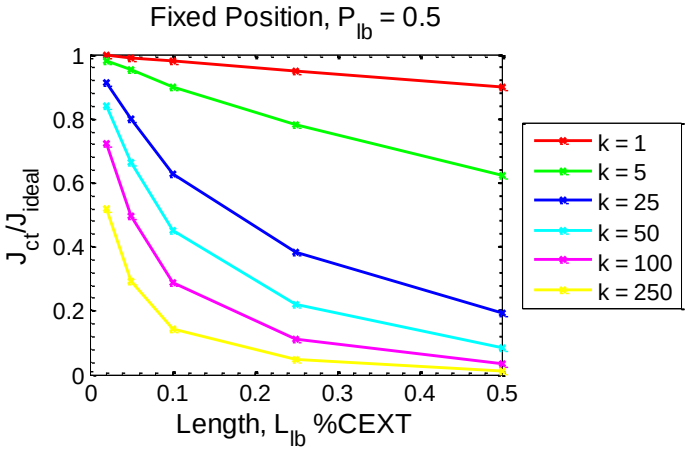

Figure 7.10: Normalised J-integral plotted against ligament bridge length 'L', the ligament position 'L' is fixed at the midpoint of the crack extension. Individual lines show different spring stiffness 'k' values in N/mm.

In Figure 7.9 (b) some of the individual lines (various positions along the crack extension) have fewer points than others. The reason for this is that certain ligament bridge lengths are not valid for specific positions along the crack length as the spring elements that would form the bridge would overlap with the notch or would be formed ahead of the crack tip. The results from the ligament bridge model shown in Figure 7.9 and Figure 7.10 exhibit general trends for each of the analysed parameters. An increase in the ligament bridge stiffness 'k' leads to an exponential increase in the apparent toughness (decrease in the normalised J-integral) as shown in Figure 7.9 (a). Similarly, an increase in the ligament bridge length leads to an exponential increase in toughening, see Figure 7.9 (b). Finally, as the ligament bridge is moved towards the starter notch (away from the crack tip) this causes an approximately linear increase in toughening.

7.3.4 Crack Deflection Model

Figure 7.11 shows the normalised J-integral results for the first 90 degree deflection model. The results for this model show that a small deflection results in a large increase in the apparent toughness with each position (i.e. crack length) approaching an apparent toughness of J_{ct}/J_{ideal} ~ 0.4. Note that this is the same result as that obtained for the semi-infinite case obtained by analytical methods (Cotterell and Rice, 1980; Karihaloo et al., 1981). As the height of the deflection increases the apparent toughening effect remains steady at J_{ct}/J_{ideal} ~ 0.4 until the deflection height increases beyond 20% of the specimen half width. At this point the apparent toughening effect is reduced. It is possible that part of this effect is due to the finite geometry of the model used; that is, as the deflection height is increased it approaches the limits of the specimen geometry. However, there is also likely a contribution from the relative size of the deflection with respect to the total crack size. This effect will be analysed further in the discussion section for the deflection models.

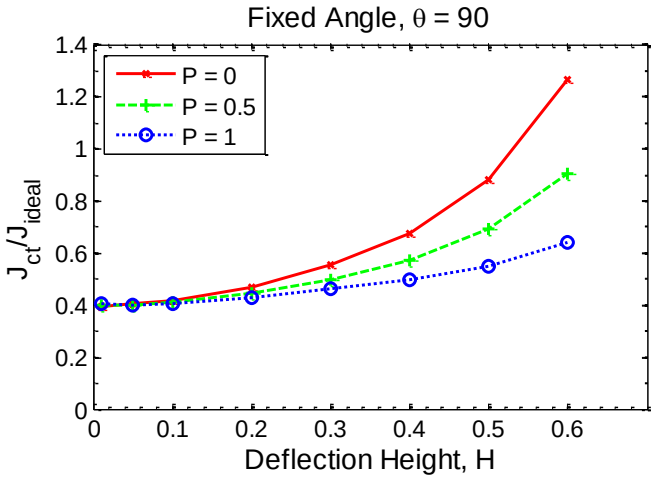

Figure 7.11: Results for the first (single) 90 degree deflection model. Normalised J-integral plotted against deflection height 'H' (as a ratio of half the specimen width) with the separate lines indicating the position 'P' of the deflection (as a ratio of max crack extension, 0.2 a/W).

Figure 7.12 (a) and (b) shows the results for the second 90 degree deflection model. The geometry of this model included another region of straight crack growth following the deflection. Comparison of these results to the first deflection model shows that a straight region of crack growth after a deflection reduces the apparent toughening effect from the deflection. As the straight region becomes larger the apparent toughening effect decreases in an exponential manner. Note that there are likely to be finite geometry effects included in these results similar to the first model.

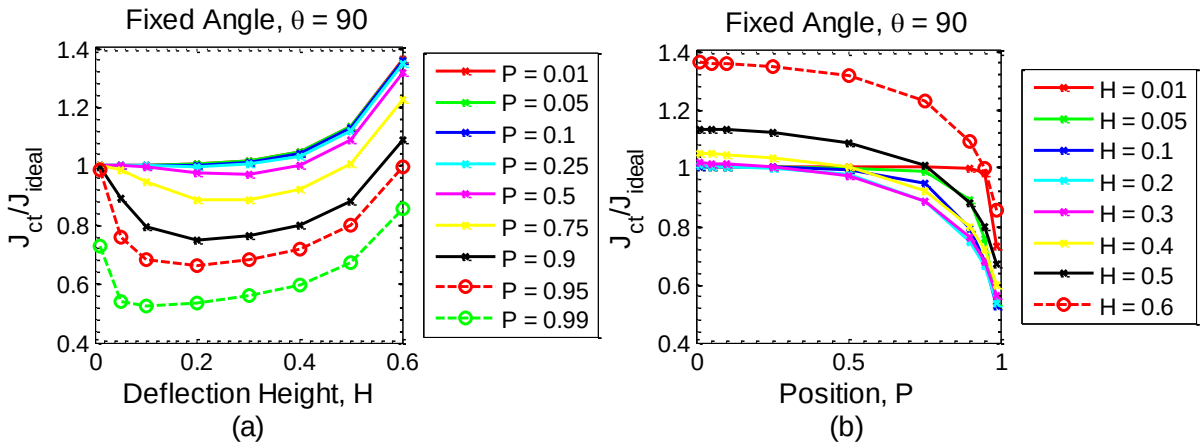

Figure 7.12: Results for the second 90 degree deflection model including a region of straight crack growth after the deflection. (a) Normalised J-integral plotted against deflection height 'H'. (b) Normalised J-integral plotted against deflection position 'P'.

Figure 7.13 shows the normalised J-integral results for the first arbitrary deflection model (single deflection as shown in Figure 7.4 (a)). The results for this model show that the apparent toughening due to crack deflection is strongly dependent on the deflection angle and increases exponentially with increased deflection angle (see Figure 7.13 (a)). This model shows that as the deflection angle increases the apparent toughening effect approaches the limiting case of a 90° deflection. The limiting case of a 90° deflection would theoretically cause the apparent toughening to approach J_{ct}/J_{ideal} ~ 0.4. Note that the increase in normalised J-integral shown for high deflection angles in Figure 7.13 is likely to be due to a finite specimen geometry effect. This is partially due to the model formulation in that the deflection length 'L_d' and angle 'θ' were specified in the model with the deflection height being calculated from this. Therefore large angles of deflection can lead to a significant deflection height, which can approach the edge of the finite compact tension specimen.

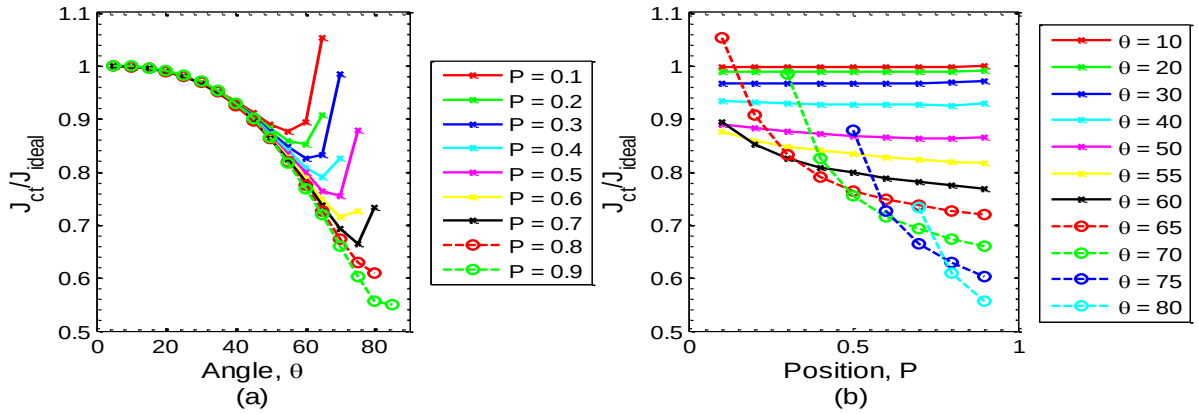

Figure 7.13: (a) Normalised J-integral plotted against deflection angle 'θ', individual lines showing the point at which the deflection starts 'P' as a percentage of the crack extension. (b) Normalised J-integral plotted position 'P'. Individual lines show the deflection angle 'θ'.

Figure 7.14 shows the results for the second arbitrary angle crack deflection model (geometry as shown in Figure 7.4 (b)). The results for the second arbitrary crack deflection model show that the apparent toughening effect due to deflection for this model is significantly dependent on the position of the deflection along the crack path (see Figure 7.14 (a)). Specifically, if the deflected region is far from the crack tip it has a minimal toughening effect, then as the deflected region is moved towards the crack tip the toughening effect increases. The results for the second deflection model also show that the toughening effect due to crack deflection is exponentially dependent on the length of the deflection along the crack path and the deflection angle (see Figure 7.14 (b)). Overall, this model shows similar results to the 90 degree case followed by another straight region of crack growth. In effect, the results of this model show that even a small portion of straight crack growth following a deflection reduces the apparent toughening effect.

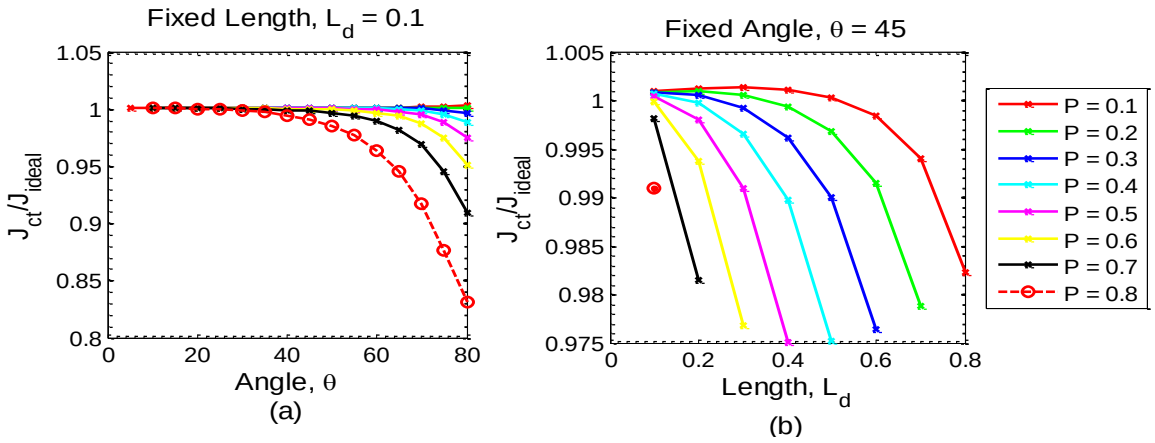

Figure 7.14: (a) Normalised J-integral plotted against deflection angle 'θ' for a fixed deflection length L_d = 0.1. (b) Normalised J-integral plotted against deflection length 'L_d' for a fixed deflection angle of θ = 45°. Separate lines are the position of the deflection as a fraction of crack extension.

7.3.5 Microcracking Model Results

The normalised J-integral results for the aligned single microcrack model (see Figure 7.4 (a)) are shown in Figure 7.15. The results for this model show an overall decrease in apparent toughness. This decrease in apparent toughness is more severe if the microcrack length is increased (see Figure 7.15 (a)) and is less severe if the microcrack is located further away from the crack tip (see Figure 7.15 (b)). Note that for these models the J-integral was analysed at the main crack tip not a microcrack tip.

The results for the single offset microcrack model (Figure 7.4 (b)) are shown in Figure 7.16. When the offset microcrack is located ahead of the main crack it can lead to a decrease in apparent toughness similar to the aligned single microcrack model. However, if the centre of the microcrack is aligned with the crack tip (X position = 0) or slightly behind

the crack tip; the J-integral is greatly reduced at the main crack tip leading to an increase in apparent toughness. Both of these effects decrease as the microcrack is located further from the crack tip in the vertical (Y) and horizontal (X) direction and increase as the microcrack increases in length. In general, the results of the single microcrack models show that microcracks located completely ahead of the main crack lead to a decrease in apparent toughness whereas microcracks located aligned with or behind the main crack lead to an increase in apparent toughness.

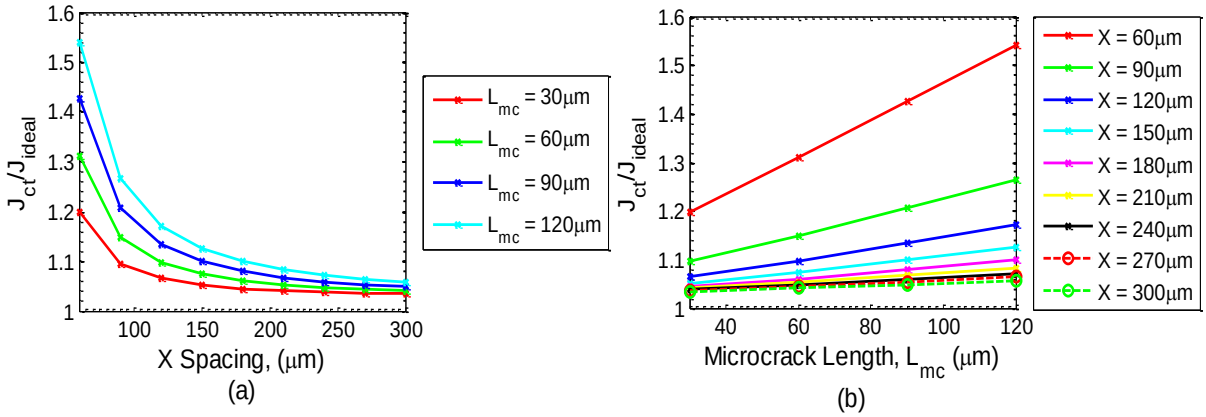

Figure 7.15: (a) Results for single aligned microcrack model. Normalised J-integral plotted against spacing ahead of the main crack. (b) Normalised J-integral plotted against microcrack length.

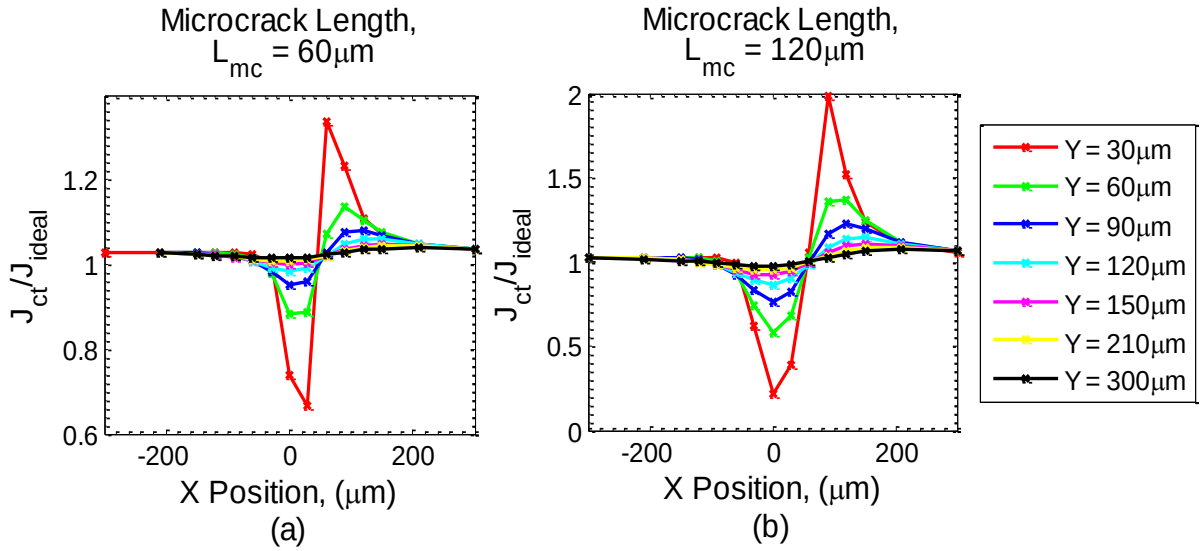

Figure 7.16: (a) Normalised J-integral plotted against microcrack position along the crack path for a single microcrack of length 60μm (note that negative values are located behind the crack tip). (b) Normalised J-integral plotted against microcrack position along the crack path for a single microcrack of length 120μm

The results for the microcrack array model with microcracks ahead of and aligned with the main crack (Figure 7.5) are shown in Figure 7.17 while the results for the microcrack array model with microcracks ahead of and offset with the main crack are shown in Figure 7.18. Both of these models show that microcracks ahead of the main crack decrease toughness, with the decrease in toughness becoming more severe with longer microcracks. This finding is the same as for the single microcrack models. The results for the array models also show that the spacing of the microcracks ahead of the main crack and between each other has a minimal effect on the toughness. An increase in the size of the region that the microcracks where generated in (increase in R_x, R_y) did however cause the decrease in toughening to be more severe.

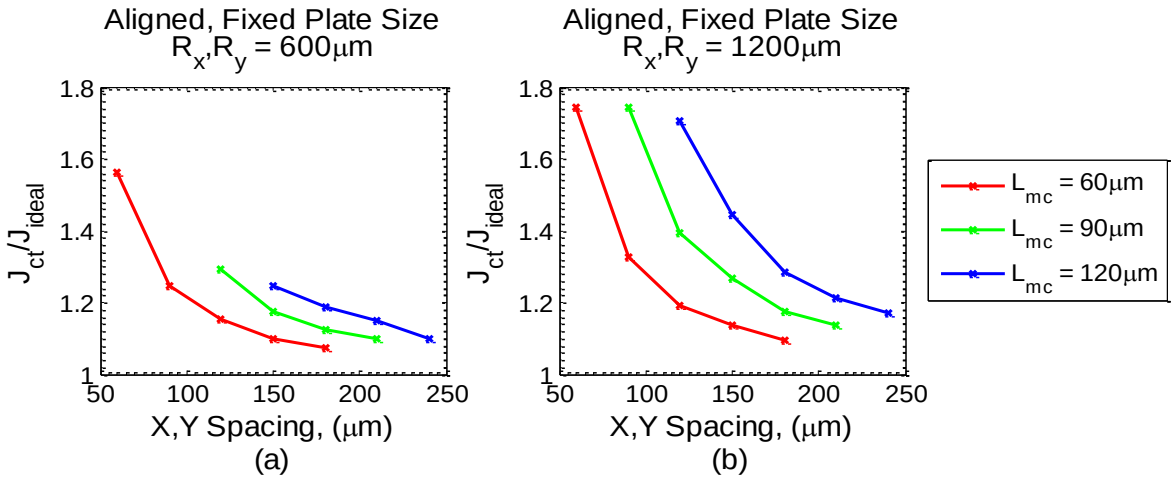

Figure 7.17: Results for the aligned array of microcracks ahead of the main crack tip. (a) Normalised J-integral plotted against microcrack spacing for a fixed region 600μm ahead of the crack tip. (b) Normalised J-integral plotted against microcrack spacing for a fixed region 1200μm ahead of the crack tip.

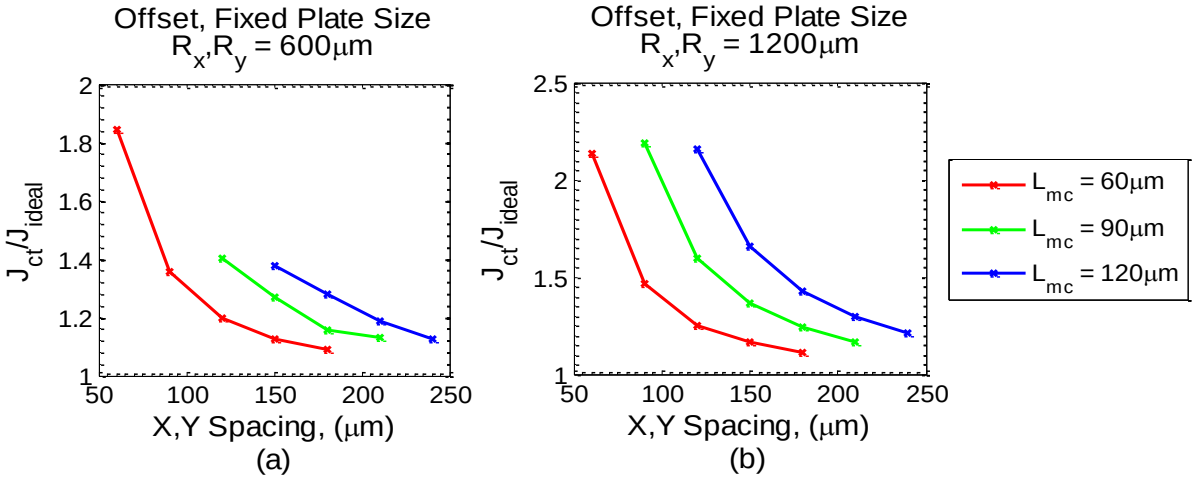

Figure 7.18: Results for the offset array of microcracks ahead of the main crack tip. (a) Normalised J-integral plotted against microcrack spacing for a fixed region 600μm ahead of the crack tip. (b) Normalised J-integral plotted against microcrack spacing for a fixed region 1200μm ahead of the crack tip.

The results for the array microcrack model with microcracks ahead of and behind the main crack (Figure 7.6) are shown in Figure 7.19. For all cases the model shows a decrease in apparent toughness. This result suggests that for microcracks spaced equally ahead and behind the main crack the overall effect is a net decrease in apparent toughness. This suggest that the beneficial effect of microcracks behind the main crack is offset by the detrimental effect of microcracks ahead of the main crack. However, if all microcracks are located in the crack wake the net effect would be a significant increase in apparent toughness.

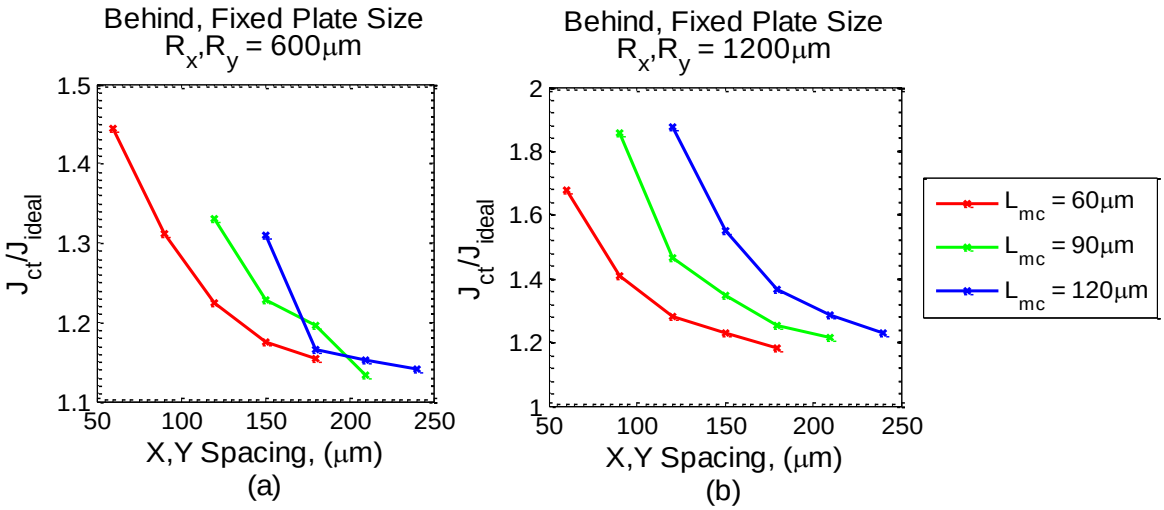

Figure 7.19: Results for the microcrack array spaced equally ahead of and behind the crack tip. (a) Normalised J-integral plotted against microcrack spacing for a fixed region rectangular 600μm about the crack tip. (b) Normalised J-integral plotted against microcrack spacing for a fixed region rectangular 1200μm about the crack tip.

7.4 Discussion

The purpose of this finite element study was to analyse the individual contribution of toughening mechanisms to the elastic component 'J_{el}' of the fracture resistance of cortical bone. The specific material effects analysed in this study included: orthotropic modulus behaviour, ligament bridging, crack deflection and microcracking. Each of these mechanisms was parametrically analysed using finite element modelling techniques. The following discussion will analyse the results for each of the toughening mechanisms modelled and relate the results from the finite element models to the experimental work presented in this thesis and experimental work published by others. This section concludes with an overall discussion of the results of the finite element models of the result of all finite element models.

7.4.1 Material Models Discussion

The set of first finite element models analysed in this study considered the effects of isotropic and orthotropic modulus behaviour. The isotropic model showed excellent agreement with the ideal case as described by the standard equations in ASTM E1820. Thus, for the isotropic model the normalised J-integral tended towards unity, except for the region near the wedge shape starter notch. The decrease in normalised J-integral can be attributed to the non-ideally sharp wedge starter notch interfering with the stress field around the crack tip when the crack length is small. Note that the standard equations for the compact tension geometry assume an ideally sharp crack hence this difference is expected.

Both the longitudinal and transverse orthotropic material models showed significantly different J-integral values when compared to the isotropic case. Cortical bone is an orthotropic material (Burstein et al., 1972a; Currey, 1975; Reilly et al., 1974; Reilly and Burstein, 1975). This orthotropic material behaviour will lead to changes in the stress field around the crack tip when compared to the same geometry with an isotropic material behaviour. This results in a different value measured for the crack tip J-integral. Note that for the pure mode I case analysed here the J-integral is directly proportional to the mode I stress intensity factor K_I. This mode I stress intensity factor is a function of the stress field at the crack tip and perpendicular to the crack path. Thus, any differences in the crack tip J-integral due to using an orthotropic material model are a direct result of changes in the local stress field. For the case of a longitudinally orientated specimen the J-integral at the crack tip was found to be lower than the isotropic case for the same applied load. While for the case of the transverse orientation the J-integral at the crack tip was significantly higher than the isotropic case. The difference in the local crack tip stress field (and therefore the crack tip SIF) is due to the differing levels of elastic constraint in the crack path direction for each of the two cases

Overall, the results of this model show that for the longitudinal case the crack tip J-integral is lower than that calculated using the isotropic model while the crack tip J-integral is higher for the transverse case. Note that the experimental fracture resistance techniques used in this thesis apply the isotropic equations to calculate the elastic component of the J-integral (as do many past studies Barth et al., 2011; Koester et al., 2011; Kulin et al., 2011a; Nalla et al., 2004a; Vashishth et al., 1997; Zimmermann et al., 2011). Therefore it is possible that the true longitudinal fracture resistance is lower than the values calculated using the isotropic equations while the true transverse fracture resistance is probably higher than the values calculated using the isotropic equations.

7.4.2 Ligament Bridge Model Discussion

The second set of finite element models analysed the effects of ligament bridging on the toughness of cortical bone. For the purpose of this model ligament bridges were represented as spring elements along the crack path. The results of this model showed that the toughening effect of the ligament bridge increased with increasing ligament bridge size and ligament bridge stiffness. The ligament bridge toughening mechanism works by reducing the stresses at the crack tip as the applied load is carried directly across the crack faces by the bridge. The reduced stress at the tip means a lower stress intensity factor (or J-integral). Both increasing the ligament bridge size (i.e. adding more spring elements increases total bridge stiffness) and increasing the spring element stiffness leads to an increase in the total bridge stiffness. If a ligament bridge becomes stiffer it will support a larger proportion of the load applied to open the crack faces. Thus for a ligament bridge with a higher total stiffness, less of the applied load will be transmitted to the crack tip leading to an increased toughening effect.

The toughening effect of the ligament bridge was also increased if the ligament bridge was located closer to the starter notch (i.e. further away from the crack tip). The increased toughening as the ligament bridge is positioned closer to the starter notch is due to the bridge being closer to the applied load points. This provides a more direct path for load transfer and hence the ligament bridge supports a larger portion of the applied load. The portion of applied loading that is supported by the ligament bridge is not transferred to the crack tip. This leads to an increase in apparent toughness. However, it is possible that the toughening effect from the ligament bridge position may be exaggerated compared to real ligament bridges in cortical bone. The reason for this is that the finite element model analysed here is purely linear and does not allow for bridge weakening or yielding. It is possible that in bone bridges near the notch (i.e. far from the crack tip) will experience large displacements causing them to yield, weaken and eventually break. For future work this could be modelled by reducing the stiffness of the spring elements as the bridge is located closer to the starter notch or as the bridges experience large displacement.

The finite element model was run for a wide range of ligament bridge conditions (e.g. stiffness and position). Therefore it is necessary to consider these results against the range of ligament bridge parameters that would be realistic for cortical bone. The results from experimental work needs to be analysed to determine the feasible range of the parameters in the model and the subsequent toughening effect. Previous experimental work by Nalla et al. (2005) investigated the effect of ligament bridges on the stress intensity factor at the crack tip for longitudinal compact tension specimens by sequentially cutting the bridges out of the crack path and continuously measuring the specimen

compliance (note that the compliance is the inverse of the specimen stiffness measured in mm/N). A fracture specimen with a bridged crack will be less compliant than a specimen with an ideal crack path as the bridges will act to support some of the load that is applied to open the crack faces. The study by Nalla et al. (2005) found that a bridged crack had a compliance of 0.003 mm/N while the same crack with bridges removed by machining had a compliance of 0.006 mm/N giving a ~50% decrease in compliance due to bridging along the crack path. Overall, the specimens presented in the study by Nalla et al. (2005) showed a decrease in the stress intensity factor at the main crack tip of 1.9-2.4 MPa√m. The bridged stress intensity factor was calculated by Nalla et al. (2005) using:

$$K_{br} = K_{app} - K_{ct} \tag{7.1}$$

where K_{app} is the apparent stress intensity factor calculated from the crack geometry and remote loading; K_{br} is the contribution of bridging to the apparent stress intensity factor and K_{ct} is the true stress intensity factor at the crack tip. Assuming E = 11GPa for longitudinal cracking in human bone and equation 2.8, this gives a range of J_{br} = 0.32-0.52kJ/m^2 due to bridges along the crack path. Note that the process of machining out the crack path to remove the bridges may also remove any crack deflection or microcracking so it is probable that the results from Nalla et al. (2005) over estimate the contribution of ligament bridging to the overall toughening behaviour. In addition, the data from Nalla et al. (2005) included only three compact tension specimens and may not represent the full range of data for bridged cracks in cortical bone. The bridged stress intensity factor does however give an indication of the upper limit of the contribution of ligament bridges to the overall toughening behaviour in the longitudinal direction.

In order to compare the finite element model in this study to the bridged J-integral given above the data needs to be converted to a 'bridge' J-integral value for each test run (rather than the normalised J-integral). This can be done by substituting the relationship between the stress intensity factor 'K' and the J-integral 'J' from equation 2.8, into equation 7.1:

$$J_{br} = \sqrt{{J_{app}}^2 - {J_{ct}}^2} \tag{7.2}$$

where 'J_{br}' is the bridge J-integral, 'J_{app}' is calculated from the reaction load data taken from the finite element model and 'J_{ct}' is the crack tip J-integral taken from the finite element model. The bridged J-integral was calculated for each and compared to the average bridged J-integral calculated from the data in Nalla et al. (2005) (i.e. a limit of J_{br} = 0.42kJ/m^2). The data was then limited to only include the cases where the bridged

J-integral was below the given limit. The limits for each parameter of the ligament bridge model were then found from this data set, with the results shown in Table 7.2. Note that the parameters were analysed based on the maximum toughening observed (i.e. minimum J_{ct}/J_{ideal}). Thus, the results from the ligament bridge finite element model gives toughening due to bridging up to $J_{ct}/J_{ideal} = 0.37$ for the case where, k = 500 N/m, L = 0.05 and P = 0.9.

Table 7.2: Limits for ligament bridge parameters based on maximum toughening observed within the bounds of the experimental data given by Nalla et al. (2005)

Maximised Variable	**Other Variables**		**Apparent Toughness**
K (N/mm)	L (% CEXT)	P (% CEXT)	Jct/Jideal
500	0.05	0.9	0.37
L (% CEXT)	K (N/mm)	P (% CEXT)	Jct/Jideal
0.5	5	0.3	0.53
P (% CEXT)	K (N/mm)	L (% CEXT)	Jct/Jideal
0.1	25	0.1	0.47

For real longitudinal cortical bone fracture specimens ligament bridges will occur along a larger portion of the crack than the 5% given for the maximum toughening case. Ligament bridges in cortical bone can take up a large proportion of the crack path as shown from the images given in Nalla et al. (2005) and the crack path images taken in the first experimental study (see Figure 3.7 and Figure 3.8). Therefore the estimate given for the bridges covering 50% of the crack path is likely to be a more accurate estimate of the toughening due to bridging at $J_{ct}/J_{ideal} = 0.532$.

The finite element model analysed in this study only considered a single ligament bridge along the crack path whereas the data taken from Nalla et al. (2005) may have included multiple bridges present along the crack length of the specimen. For the longitudinal specimens analysed in the experimental work of this thesis multiple ligament bridges were observed (see Figure 3.7). Thus, for future work it would interesting to analyse the effects of multiple bridges along the crack path and compare this to further sequential cutting experiments. It would also be beneficial to examine the stress distribution along the crack faces due to bridging. These models could also incorporate a softening effect for bridges that reach a certain displacement limit near the starter notch.

Overall, the results from the ligament bridge finite element model show that ligament bridging contributes significantly to the fracture toughening behaviour of cortical bone and that this toughening behaviour can be modelled using spring elements across the crack faces.

7.4.3 Crack Deflection Model Discussion

The third set of finite element models analysed the effects of crack deflection on the toughening behaviour of cortical bone. The first two crack deflection models (Figure 7.3) analysed the case of 90 degree deflection while the second two crack deflection models (Figure 7.4) analysed the case of an arbitrary angle deflection. In general these models showed that the apparent toughening effect of crack deflection increases with increasing deflection angle up to the limiting case of a 90 degree deflection where the increase in apparent toughness is maximised. The following discussion will briefly analyse the results of each of the crack deflection models and then relate this back to the experimentally observed crack paths from experiments 1-3.

The first 90 degree crack deflection model (Figure 7.3 (a)) showed the limit of the apparent toughening effect for this case is J_{ct}/J_{ideal} ~ 0.4. This model also showed that the toughening effect of a 90 degree deflection is only maximised if the deflection height is small relative to the overall crack length. The second 90 degree deflection model showed that a portion of straight crack growth following the deflection reduced the apparent toughening effect. This result can be expressed in two different ways: 1) for a crack of a particular total length the greatest toughening effect occurs when the deflected region is nearest to the crack tip or 2) as the crack continues to grow from a deflected region the toughening effect reduces back to unity (i.e. the pre-deflected value). However, if the deflection offset is large then this can lead to an interaction effect with the finite specimen geometry leading to an increase in the crack tip J-integral.

The first and second arbitrary angle crack deflection models show that the apparent toughening effect due to crack deflection increases with increasing deflection angle. This effect is maximised for the case of a 90 degree deflection as shown in the first two deflection models. Similar to the second 90 degree crack deflection model the second arbitrary angle crack deflection model also showed that the apparent toughening effect was reduced with a straight portion of crack growth following the deflected region. It is interesting to note that the magnitude of the toughening due to crack deflection for the case of deflection up to an angle of 45 degrees ($J_{ct}/J_{ideal} > 0.9$) is small when compared to ligament bridging ($J_{ct}/J_{ideal} > 0.5$). For longitudinal fracture the deflection angle rarely exceeds 45 degrees and the deflection length is only a short proportion of the crack path (see crack path images from experiment 1, Figure 3.7 and experiment 2, Figure 3.8).

Specifically, for the longitudinal crack growth many small crack deflections are observed along the crack path with each of these deflected regions returning to straight crack growth following the small deflected region. The second arbitrary crack deflection model further supports this argument by showing that a return to straight crack growth following a deflected region quickly eliminates the apparent toughening effect of crack deflection. Thus, for longitudinal cracking it is expected that crack deflection will have diminished significance when compared to ligament bridging. The combination of results from the ligament bridge and crack deflection models support the hypothesis that ligament bridging is the dominant toughening mechanism for longitudinal crack growth in cortical bone.

The deflection finite element models also show that significant toughening (J_{ct}/J_{ideal} ~ 0.4) due to crack deflection is possible if the deflection angle is greater than 70 degrees and the deflection occurs over only a small portion of the crack length (with the limit being the semi-infinite case with apparent toughening of J_{ct}/J_{ideal} ~ 0.4). For transverse fracture specimens it is not uncommon for crack deflections of 80-90 degrees to occur over very small portions of crack extension in the direction of optimal mode I driving force. See for example the crack path images from experiments 2 and 3 (Figure 4.9 and Figure 5.10) or the crack path images for human specimens in Koester et al. (2008) and Zimmerman et al. (2009). For longitudinal fracture in bone, ligament bridging is the predominant toughening mechanism and for this mechanism to be effective a large proportion of the crack path must be occupied by bridges that form as the crack grows in the direction of optimal driving force (R. . Nalla et al., 2005; Nalla et al., 2004b). While for transverse fracture toughening can occur over very small portions of crack extension due to large deflections from the direction of optimal driving force. This result explains why toughening in the transverse direction for bone occurs at a much higher rate than the longitudinal direction.

For all of the deflection finite element models the limiting case is a 90 degree deflection from the main crack path, in this case the apparent toughening effect from crack deflection approaches the ideal value of J_{ct}/J_{ideal} ~ 0.4. It should be noted that this toughening effect is only maximised if the deflection height is small relative to the crack length. The reason for this maximisation of the toughening effect is related to the J-integral including both mode I and mode II components as shown in equation 7.1. If the deflection height increases the overall toughening effect is reduced as mode II crack growth behaviour begins to dominate over the initial mode I crack. Therefore, to maximise the effectiveness of the crack deflection mechanism it would be beneficial if the main crack arrested after a small portion of growth at 90 degrees and then has to break across the fibres in mode I before initiating another 90 degree deflection. This optimal toughening behaviour is

evident in the ‘stair step’ like pattern of crack growth observed in experiments 2 and 3 for transverse crack growth in bovine bone. In addition to this, for the crack to deflect back across the collagen fibres it would be necessary for the driving force of crack growth to overcome the strength of the fibres. This fibre breakage mechanism is likely to be a plastic phenomenon and it is probable that this would have a significant effect on the plastic component of the J-integral. It should also be noted that even if a crack is arrested and deflects back across the collagen fibre the driving force for crack growth is quickly consumed and the crack will subsequently encounter another weak interface in the structure causing further crack deflection. As crack deflection is the dominant toughening mechanisms for transverse mode I cracking it would be expected that not only would there be a significant increase in toughening for the elastic component of the J-integral but there may also be significant toughening for the plastic component of the J-integral.

Previous analytical modelling of crack deflection shows similar trends to those observed in the single deflection models of this study. (Cotterell and Rice, 1980; Erdogan and Sih, 1963; Williams and Ewing, 1972) It should be noted that these analytical models analyse the case for which the crack has finite length and the deflection region is infinitesimally small compared to the crack length. It is also interesting to note that the results of the crack deflection finite element models are similar to crack deflection toughening in engineering fibre composites. It has been shown in engineering composites that crack deflection along a perpendicular weak interface can provide significant toughening, but only if the crack does not then propagate across the stronger material in the direction of optimal mode I driving force (Liu and Yang, 2014). This was shown in the crack deflection models that included a region of straight crack growth after the deflected region. The models presented in this study showed that the crack deflection mechanism greatly reduces its effectiveness when the crack straightens and continues to grow.

In summary, the results of the crack deflection finite element models provide significant insight into the overall contribution of crack deflection to the fracture resistance behaviour of cortical bone. The limiting case for an increase in apparent toughness is for a 90 degree deflection with a small height compared to the overall crack length giving $J_{ct}/J_{ideal} \sim 0.4$. As large angle (>80°) deflections are common for transverse crack growth in cortical bone it is likely that the crack deflection mechanism is responsible for the rate of toughening observed for this case. For longitudinal crack growth in cortical bone the results from the finite element models show that the contribution of crack deflection to the overall toughness is minimal for two reasons: 1) the deflection angles are small, $\theta < 45$ giving $J_{ct}/J_{ideal} > 0.9$ and 2) the crack deflects back to a straight path following only a small deflection region.

7.4.4 Microcracking Model Discussion

The fourth set of finite element models analysed the effects of individual microcracks and arrays of microcracks on the apparent toughness of cortical bone. The general trend for results from both the single and array microcrack models showed that microcracks ahead of the main crack tip decreased the apparent toughness of bone while microcracks aligned with or behind the main crack caused an increase in apparent toughness. The increase or decrease in apparent toughness from both of these models became more significant if the microcrack was located near the main crack tip or if the length of the microcrack was increased. The final array model showed that if there are microcracks both ahead and behind the main crack tip this causes a net decrease in apparent toughening. Thus, the detrimental effect of microcracks ahead of the main crack tip is dominant over the toughening due to microcracks behind the main crack tip.

The results from the microcrack finite element model agree with the results of analytical and numerical models of microcrack process zones in brittle engineering materials. These models showed that microcracks in the zone ahead of the main crack acted to amplify the main crack stress intensity factor while microcracks behind the crack tip acted to shield the main crack (Kachanov, 1987; Meguid et al., 1991a). Similar studies in engineering materials also showed that for random arrays of microcracks both behind and ahead of the main crack the net effect was a decrease in toughness (Kachanov et al., 1990; Meguid et al., 1991b). In general, for a toughening effect to be observed due to an array of microcracks around the crack tip the distribution of microcracks needs to be skewed such that the microcracks behind the crack tip are closer to the main crack tip than the microcracks ahead of the main crack tip or there needs to more microcrack located behind the crack tip. For fracture in cortical bone further analysis of microcrack distributions will be needed to determine if the microcracks are biased towards configurations that will cause toughening; this would be an interesting area for future work combining experiments and finite element modelling.

While the presence of a randomly distributed array of microcracks is detrimental for a stationary crack in an elastic medium this does not rule out toughening due to the formation of microcracks during crack growth (Meguid et al., 1991a). Specifically, the formation of microcracks during crack growth can consume energy that would otherwise be used to propagate the main fracture. Further, the results of the microcracking finite element in this study suggest that microcracks ahead of and offset from the main crack may provide initiation sites for other toughening mechanisms such as ligament bridging and crack deflection (this is discussed in the next paragraph).

For the single offset microcrack model a significant decrease in the J-integral at the main crack tip was observed when an offset (in the vertical 'Y' direction) microcrack was aligned with or behind the main crack (in the horizontal 'X' direction). The significant decrease in the main crack J-integral suggests that the microcrack is shielding the main crack and potentially has a higher J-integral than the main crack. If this is the case the microcrack would grow instead of the main crack. Therefore further analysis was conducted to analyse the J-integral at the microcrack tip and then compare this with the J-integral at the main crack tip. Figure 7.20 shows the ratio of the J-integral at the microcrack tip 'J_{mc}' to the J-integral at the main crack tip 'J_{ct}' plotted against position in the X direction with the separate lines showing the position in the Y direction. Note that the microcrack tip J-integral 'J_{mc}' was measured from the farthest tip in the positive 'X' direction. When the microcrack J-integral ratio is greater than one 'J_{mc}/J_{ct} >1' this indicates that either the microcrack will grow or both the microcrack and main crack will grow (it is also possible for both the main crack and the microcrack to grow if both of the main crack J-integral and microcrack tip J-integral exceed the material toughness).

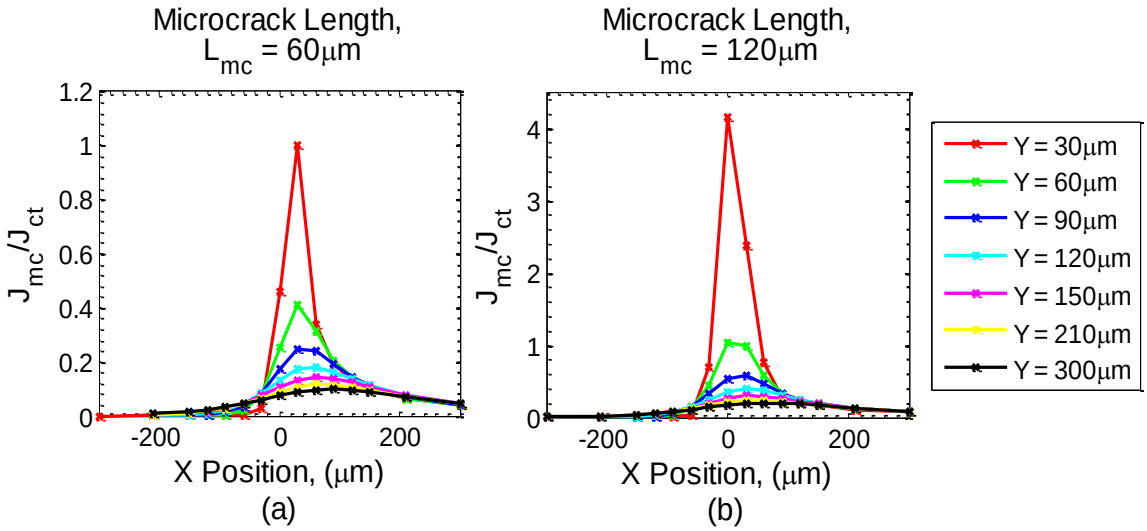

Figure 7.20: Ratio of the J-integral at the microcrack tip to the J-integral at the main crack tip 'J_{mc}/J_{ct}' plotted against the X and Y position with respect to the crack tip. Note that a negative X value is locates the centre of the microcrack behind the main crack tip. (a) Shows results for a microcrack 60μm in length and (b) shows result for a microcrack 120μm in length.

Additional analysis was conducted for the limiting cases; when the microcrack is positioned such that the main crack J-integral is maximised and when it is minimised (i.e. the maximum and minimum points shown in Figure 7.16). Contour plots for the von Mises stress and crack tip shapes are given in Figure 7.21 (a) for the case where the main crack tip J-integral is maximised and Figure 7.21 (b) for the case where the main crack tip J-integral is minimised. Note that the von Mises stresses are presented for visual purposes

as the relative magnitude of the von Mises stress distribution around a crack tip gives a rough indication of the severity of the stress singularity at this point. For the case shown in Figure 7.21 (a), the main crack tip J-integral is J_{ct} = 1.03 kJ/m^2 while the microcrack tip J-integral is J_{mc} = 0.27 kJ/m^2. For the case in Figure 7.21 (b) the main crack tip J-integral is J_{ct} = 0.12 kJ/m^2 while the microcrack tip J-integral is J_{mc} = 0.48 kJ/m^2. In the case of Figure 7.21 (a) the higher main crack tip J-integral would cause the main crack to continue its growth alongside the microcrack. As the main crack grows alongside the microcrack this would then reduce the main crack driving force, leading to a similar situation to that shown in Figure 7.21 (b) in which the main crack arrests and an uncracked ligament bridge is formed. This result suggests that microcracks offset from and near to the main crack path will most likely lead to the formation of uncracked ligament bridges. In practice this suggests that microcracks formed in the process zone of a growing macro crack in bone are therefore most likely to be the sites of ligament bridge formation.

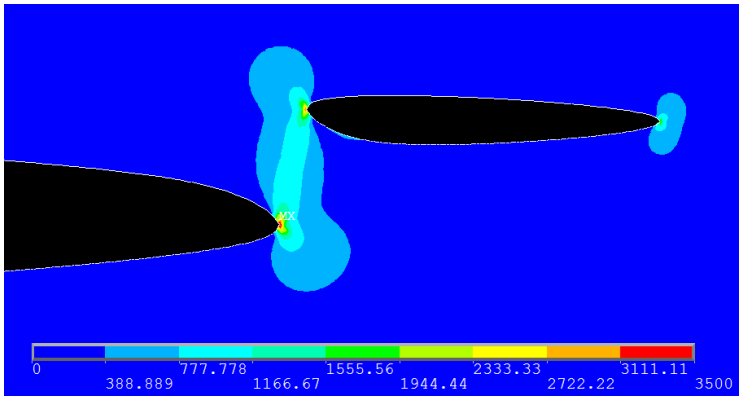

(a)

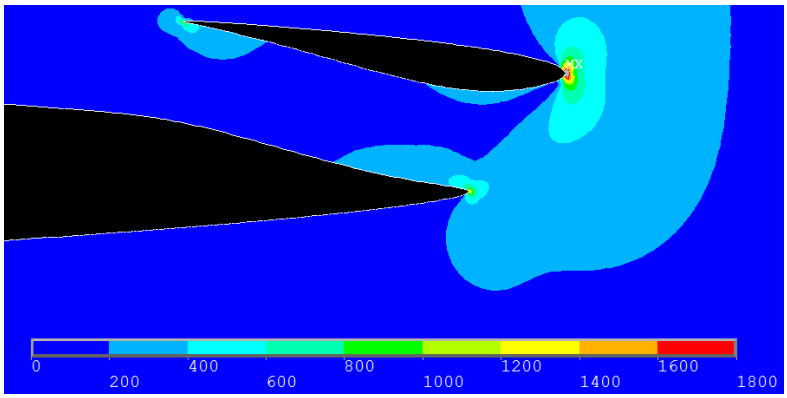

(b)

Figure 7.21: Contour plot of von mises equivalent stress (MPa) overlaid on the deformed shape of the offset microcrack model. (a) Maximum main crack tip J-integral case and (b) minimum main crack tip J-integral. For both cases the microcrack shown is 120µm long.

This analysis of ligament bridge formation from microcracks does not include the effects of microstructural interfaces on the formation of ligament bridges. It is probable that larger ligament bridges can be formed if the main crack encounters a barrier in the microstructure that acts to arrest the main crack. If there is then a microcrack located in a weak interface of the microstructure in a location far from the crack tip this may still initiate a ligament bridge if the driving force required to initiate the microcracks growth is lower than that required for the main crack to break through the microstructural barrier.

7.5 Conclusion

The purpose of this finite element study was to decouple and investigate the relative contributions of different fracture toughening mechanisms to the fracture resistance of cortical bone. This was achieved by modelling the individual toughening mechanisms then relating each of the finite element models to experimental work presented in this thesis and the experimental work of others. The toughening mechanisms investigated were microcracking, ligament bridging, and crack deflection. The major findings for each of the finite element models analysed is summarised below:

1. Ligament bridging can contribute significantly to the apparent toughness increase for the elastic component of the J-integral up to a magnitude of $J_{ct}/J_{ideal} \sim 0.5$.
2. Crack deflection leads to significant increase in apparent toughness ($J_{ct}/J_{ideal} \sim 0.4$) for the limiting case of a 90 degree deflection with a small height relative to the main crack length
3. The apparent toughening effect of crack deflection is reduced if the crack straightens after the deflected region, then as the straight portion continues to grow the toughening effect reduces to the pre-deflected value
4. Compared to ligament bridging, crack deflection does not significantly contribute to the longitudinal fracture resistance
5. Crack deflection contributes significantly to the elastic component of the transverse fracture resistance as transverse crack growth shows large angle deflections ($\theta > 80°$)
6. For microcracks to alter the main crack tip J-integral they need to be located near the crack tip (within a distance of double the microcracks length).
7. Microcracks ahead of the main crack tip act to amplify the elastic component of the main crack tip J-integral and reduce apparent toughness.
8. Microcracks behind the crack tip act to shield the crack tip from the applied loading leading to an increase in apparent toughness.
9. Offset microcracks can shield the main crack tip from the applied load and lead to the formation of other toughening mechanisms such as crack deflection and ligament bridging.

7.6 Limitations and Future Work

The results of the finite element models presented in this study provide further insight into the toughening mechanisms and fatigue fracture interaction mechanisms in cortical bone however, it is also useful to analyse limitations of these models as they can suggest directions for future work. All finite element models in this study analysed the fracture behaviour of cortical bone in two dimensions. Thus, it is assumed that all toughening phenomena occur through thickness. For the case of ligament bridging and crack deflection, experimental data shows that these crack path toughening mechanisms do occur through thickness (Nalla et al., 2005; Zimmermann et al., 2011). In the case of crack deflection it is also possible that the crack can twist in the through thickness direction as has been shown by micro-CT scans of crack paths in bone (see for example: Koester et al. (2011)). Fracture phenomena such as microcracking and plastic deformation about the crack tip are also three dimensional in nature. Single fatigue or fracture microcracks do not generally occur completely through the thickness of a bone specimen, but it is likely that a zone of microcracks occurs through the thickness of the fracture specimen. However, it is not known how the distribution of microcracks varies through the thickness for either fatigue or fracture specimens of cortical bone during crack growth. The three dimensional distribution of microcracks for crack propagation in cortical bone would be an interesting area of future work that would provide further insight into the mechanisms of fatigue fracture interaction. Knowledge of the three dimensional distribution of microcracks around a crack tip in cortical bone would also allow the finite element models developed in this research to be extended to analyse three dimensional arrays of microcracks around a main crack tip. The three dimensional distribution of microcracks may also provide further insight into crack path toughening mechanisms such as crack twist as it may be possible that the effect of an array of microcracks on the stress field in three dimensions results in the occurrence of crack twist.

Another limitation of this work is that it only analysed the effects of the various toughening mechanisms on the linear elastic fracture behaviour of cortical bone; that is, J_{el}. Thus, there is potential future work to analyse the contribution of each of these mechanisms to the plastic component of the J-integral, 'J_{pl}'. However, this analysis is complicated by the fact that plasticity in bone occurs over multiple length scales (unlike metals where plasticity occurs mainly at the nanoscale due to dislocation motion). Specifically, plasticity in bone occurs at the nano-scale by slip of collagen fibres/fibrils while plasticity at the micro-scale occurs in the form of microcracking and diffuse damage (Boyce et al., 1998; Burstein et al., 1972b; Vashishth et al., 2003). Thus, a macroscale tensile test will give results that include the contribution of both microcracking and plastic slip to the non-linear (or "plastic")

region of the stress strain curve. Implementing this behaviour as a bi-linear plasticity model in the finite element analysis is possible. However, if the microcracks are then directly modelled the contribution of the microcracks will be accounted for multiple times, once by the bi-linear plastic material model and once by the directly modelled microcracks. At this time there is no simple solution to this problem. However, it is possible that the solution lies in the use of multiscale finite element models. This type of model combines a microstructural model of a region of interest with a bulk material of a bone and/or specimen, an example of this type of model is given in Ural and Mischinski (2013b). The comparison of these multiscale models with experimental fracture data and direct modelling of fracture toughening mechanisms is an interesting area for future research.

Chapter 8: Discussion and Conclusion

8 General Discussion and Conclusion

8.1 Summary of Previous Findings

The global aim of the research presented in this thesis was to investigate the effects of fatigue induced microdamage on the fracture resistance behaviour of cortical bone. This aim was achieved by combining the results of fracture resistance experiments and finite element modelling to analyse the mechanisms by which fatigue damage alters the fracture toughening behaviour of cortical bone. Three separate experiments were conducted to analyse the effects of fatigue induced damage on both the longitudinal and transverse fracture resistance of cortical bone. These were:

- Experiment 1: Longitudinal Fatigue Fracture Interaction in Cortical Bone
- Experiment 2: Longitudinal and Transverse Fatigue Fracture Interaction in Cortical Bone
- Experiment 3: Fatigue Fracture Interaction in Cortical Bone for Different Fatigue Damage Morphologies

From the results of each of these experiments the fracture resistance curves and optical crack path analysis was combined to propose mechanisms of fatigue fracture interaction. Following the experimental work presented in this thesis, further analysis of the fracture toughening mechanisms in cortical bone was conducted using a finite element modelling approach. This finite element modelling involved directly modelling each of the major toughening mechanisms in cortical bone (i.e. crack deflection, ligament bridging and microcracking). The results from the finite element models were then considered in light of the experimental studies to provide further understanding of the mechanisms of fatigue fracture interaction. The purpose of the following summary is to briefly revise each of the experimental and modelling components presented in this thesis. After the summary presented in this section. The following two sections will aim to synthesise the experimental and modelling work to produce a model of toughening in cortical bone.

The first experimental study (Chapter 3) presented in this thesis analysed the effects of fatigue microdamage on longitudinal fracture resistance of cortical bone. The fracture resistance curves and analysis of the crack paths of both the fatigue damaged and control groups were used to propose mechanisms by which the fatigue damage interacted with both crack initiation and crack growth. The results of this study showed that the fracture initiation toughness and the growth toughness were significantly reduced by fatigue induced damage. The reduction in fracture initiation toughness was attributed to a microcrack saturation mechanism, where the fatigue induced microcracks occupied the existing weak interfaces in the microstructure inhibiting the formation of new microcracks

that would normally absorb energy during crack growth. The results from this experiment also showed that the growth toughness was reduced due to fatigue induced damage. Three mechanisms of fatigue fracture interaction were proposed in this study to explain the reduced growth toughness. These were: 1) fatigue induced microcracks inhibiting the formation new microcracks, 2) aligned microcracks linking with the main crack, and 3) offset microcracks that can form ligament bridges or crack deflection. Subsequent crack path analysis showed that the first mechanism is the most prevalent and is therefore most likely to be responsible for the decrease in growth toughness in longitudinal specimens.

The second experimental study (Chapter 4) analysed the effects of fatigue damage on uniform beam specimens that were subsequently notched and fracture tested. This study also attempted to analyse the effects of fatigue damage on the longitudinal and transverse fracture resistance of cortical bone. The results of this study showed no significant difference between the fracture resistance curves for the longitudinal or transverse fracture specimens when compared to their respective control groups. Subsequent analysis of the fatigue damage zones and crack paths showed that the fatigue damage was concentrated on the edges of the fracture specimen away from the fracture initiation and crack growth region. Therefore, as the fatigue damage was not interacting with the main crack path no effect was observed on the fracture resistance. While this experiment was not successful in analysing fatigue fracture interaction mechanisms it demonstrated that fatigue damage needed to directly interact with the crack path or the stress field around the crack tip to alter the fracture resistance behaviour. The results from this study also showed the contrast between the fracture toughening mechanisms that are responsible for the overall fracture resistance in both the longitudinal and transverse directions. Specifically, for longitudinal crack growth ligament bridging is the most prevalent toughening mechanism while for transverse crack growth the most prevalent toughening mechanism is crack deflection.

The third experimental study (Chapter 5) analysed the effects of both tensile diffuse damage and compressive fatigue microcracks on the transverse fracture resistance of cortical bone. Analysis of the fracture resistance curves for the tensile diffuse damaged specimens showed no difference in fracture behaviour. The reason for this is that the diffuse damage did not interact with the microstructural interfaces that are responsible for toughness in the transverse direction. The fracture resistance curve and crack path analysis for the compressive microcrack group show that while compressive microcracks did reduce the fracture initiation toughness they did not alter the growth toughness. The reduction in fracture initiation toughness for compressive microcracks was attributed to a microcrack saturation mechanism similar to the first study. It was also shown that the

microcracks provided weak sites in the microstructure at which the crack could initiate at lower energy cost (i.e. a reduction in local material strength). While there was a significant difference in the fracture initiation toughness for the compressive fatigue group there was no significant difference in growth toughness. For the compressive fatigue group crack path analysis showed that both control and damaged specimens had significant amounts of crack deflection. Hence, there was no observed effect on the transverse rate of toughening after the crack had initiated as the crack deflection mechanism was not altered by the presence of the fatigue damage.

Following the experimental studies two finite element modelling studies were conducted. The first finite element modelling study aimed to analyse the effects of the circular notched fracture specimen geometry on the fracture resistance curves while the second experimental study analysed the contribution of individual crack path toughening mechanisms to the overall fracture resistance curve. The first and third experimental studies utilised a circular notched fracture specimen geometry, for these studies it was assumed that this would not alter the statistical comparison of fracture resistance behaviour between groups. The purpose of the first finite element study was to verify that this assumption was valid with the added benefit that future studies using this geometry would be able to use standard equations for statistical comparison. This study verified the assumption and it was found that the presence of the circular notch only caused a translation of the fracture resistance curve for both the circular notched compact tension specimen and the circular notched single edge notched bend specimens. Consequently, the comparison of control and damaged groups for experiments 1 and 3 remained unchanged by the effects of the circular notch. Thus, future experiments using a circular notch geometry can still use the equations outlined in ASTM standard E1820 without having to derive new equations for each individual geometry as the comparison between fracture variable is still valid.

The second finite element study directly modelled various toughening mechanisms in cortical bone in order to determine the contribution of each of the mechanisms to overall fracture resistance. This study analysed the following toughening mechanisms: ligament bridging, crack deflection and microcracking. When the results of the ligament bridging model were considered with respect to other published work it was found that the apparent toughening due to ligament bridging is significant in the longitudinal direction. The crack deflection model showed that for small angle deflections over a small portion of the crack path the apparent toughening effect is minimal. These small angle deflections are similar to those observed for longitudinal fracture and show that for this fracture orientation ligament bridging has a much more significant contribution to the overall fracture

resistance. However, for large angle deflection over short portions of crack extension the apparent toughening effect due to crack deflection was significant. This type of large angle crack deflection was typical of crack paths observed in the experimental studies for transverse fracture specimens. Hence, the fracture resistance in the transverse direction can be largely attributed to the large angle deflections that occur along the crack path. The microcrack finite element model showed that microcracks either shield or amplify the J-integral at the main crack. Specifically, microcracks ahead of the main crack acted to amplify the main crack J-integral while microcracks behind the crack tip act to shield the main crack J-integral. For the case where the microcracks are arrayed equally behind and ahead of the crack the detrimental effect of the cracks in front of the main crack is dominant resulting in and overall decrease in apparent toughness. Despite this decrease in apparent toughness due to the presence of microcracks ahead of the crack tip it was shown that offset microcracks can lead to the formation of other toughening mechanisms along the crack path such as ligament bridging or crack deflection.

8.2 Model of Fracture Mechanisms in Cortical Bone

The combination of experimental and numerical results presented in this thesis provides support for a model of toughening behaviour in cortical bone (shown in Figure 8.1). Ultimately the toughening mechanisms observed in cortical bone are a result of crack path interaction with the microstructure of cortical bone. Thus, as the first element of this model is the microstructure, as toughening phenomena are a result of crack path interaction with the microstructure of cortical bone. The second element of this model involves microstructural orientation, specifically transverse or longitudinal to the collagen fibres as the microstructural orientation determines the predominant toughening mechanisms. This section will discuss the model and the specific toughening behaviour observed for each of the dominant crack growth directions.

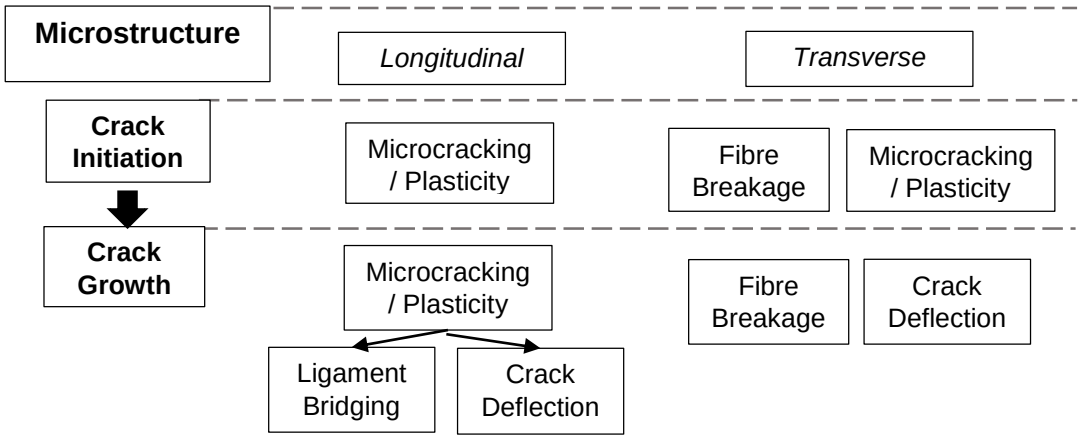

Figure 8.1: Model of toughening mechanisms in cortical bone for longitudinal and transverse fracture. All toughening mechanisms are dependent on crack interaction with the microstructure.

For longitudinal crack initiation the predominant toughening mechanism is microcracking and plasticity. The occurrence of the plastic zone (due to slip of collagen fibres/fibrils) at the crack tip acts to blunt the main crack leading to increased toughness. Microcracks will then form in the weak interfaces of the microstructure in the plastic zone. The formation of these microcracks acts to consume energy that would otherwise be used to initiate the main crack. For longitudinal crack growth the predominant toughening mechanism is ligament bridging. The formation of ligament bridges is driven by the main crack interacting with microstructural boundaries or microcracks along the crack path, which provide sites at which the main crack can arrest and can continue growth from another weaker location in the material. This leaves a region of uncracked material and forms a ligament bridge in the wake of the crack. Crack growth in the longitudinal direction also has a relatively small toughening effect (compared to ligament bridging) from crack deflection as a result of misaligned microstructural boundaries or microcracks along the main crack path.

For transverse crack initiation the predominant toughening mechanisms are microcracking/plasticity and fibre breakage. The microcracking/plasticity mechanism is similar to the longitudinal mechanism described above for fracture initiation. The fibre breakage mechanism results from crack initiation in the direction of maximum driving force requiring the crack to break across the collagen fibres. This requires significantly more energy than breaking the weak interfaces between the fibres hence leading to an increased apparent toughness in the transverse direction. For transverse crack growth the predominant toughening mechanism is crack deflection. In this case the crack deflection is a direct result of the weak interfaces in the microstructure being orientated perpendicular to the direction of maximum driving force for crack growth. These weak interfaces cause the main crack to deflect leading to a reduced driving force for mode I crack growth and contributing to an increase in apparent toughness. Further toughening for transverse crack growth is provided by the fibre breakage mechanism in conjunction with the crack deflection mechanism. For transverse crack growth the crack will deflect along the weak axis perpendicular to the direction of the maximum driving force, this deflection effectively blunts the crack tip in the direction of the maximum driving force. For the crack to grow in the direction of the maximum driving force it will need to re-initiate a sharp crack tip by breaking across the collagen fibrils consuming a significant amount of fracture energy thus leading to a significant increase in apparent toughening.

8.3 Synthesis of Longitudinal Fatigue Fracture Interaction and the Model of Fracture Mechanisms

The experiments and finite element models presented in this thesis aimed to determine the effects of accumulated fatigue damage on the fracture toughening behaviour of cortical bone (referred to as fatigue fracture interaction mechanisms). Using the model in Figure 8.1, fatigue induced damage would need to interact with the microstructure of cortical bone to alter the effectiveness of the toughening mechanisms that are dominant in each crack growth direction. The explanations for the fatigue fracture interaction mechanisms derived in experiments 1 and 3 relied on both fracture resistance results and crack path analysis. The crack path analysis was used to explain the numerical fracture data in terms of the toughening mechanisms along the crack path. Thus, the results from each of the three experiments presented in this thesis will be considered with respect to the toughening model presented above, specifically in terms of how each of the proposed mechanisms relate back to the microstructure, which is responsible for the overall fracture behaviour in cortical bone

The first experiment analysed the effects of fatigue induced microcracks on the longitudinal toughness of cortical bone. For this experiment it was found that fatigue induced microcracks significantly inhibit the fracture initiation toughness and growth toughness of cortical bone. For the fracture initiation toughness in the longitudinal direction the fatigue induced damage interacts with the microcracking toughening mechanism. Specifically, the fatigue induced microcracks occupy the weak interfaces in the microstructure that would normally form microcracks during the process of crack initiation, this inhibits the formation of new microcracks during crack initiation and reduces the overall fracture initiation toughness. The decreased fracture initiation toughness observed in experiment 1 is further supported by the finite element modelling of the microcrack toughening mechanism. The results from the microcrack finite element models show that microcracks ahead of the main crack tip interacts with the stress field of the main crack causing a decrease in toughness. Note that the finite element model only considered the case of a static array of microcracks ahead of the crack tip and it does not account for energy consumed in microcrack formation. However, this result is still instructive as it replicates the case of accumulated fatigue damage inhibiting the formation of new microdamage during dominant crack growth.

The results of both the experimental data and the finite element models agree well with the model of fracture mechanisms in cortical bone. The model shows that toughening behaviour is direct result of crack path interaction with the microstructure. Fatigue induced damage interacts with microstructural features (i.e. weak interfaces) would normally

initiate toughening mechanisms such as microcracking. If these microstructural sites are already fatigue damaged they cannot form new microdamage during crack initiation. The results of experiment 1 also showed that the growth toughness was decreased by accumulated fatigue damage in the longitudinal direction. For this case it was found that the fatigue induced microcracks interfere with both the microcracking toughening mechanism and the ligament bridging mechanism. The first mechanism of fatigue fracture interaction for the growth toughness is similar to the microcrack saturation mechanism proposed for the fracture initiation toughness. The model shows that the microcrack toughening mechanism is a direct results of the stress field of the main crack interacting with the weak interfaces in the microstructure. The model also links the microcracking mechanism to further toughening behaviour such as ligament bridging. Therefore, any change in microcracking for longitudinal crack growth would be expected to alter the subsequent toughening behaviour; that is, fatigue induced microcracks inhibit the formation of new microcracks therefore they would be expected to inhibit the formation of ligament bridges. This is indeed the case for the results from experiment 1 which showed a decreased growth toughness partially attributed to a decrease in the effectiveness of the ligament bridging mechanism.

From the results of the first experiment a further two mechanisms of fatigue fracture interaction were proposed. Unlike the first mechanism of microcrack saturation the second two mechanisms included microcrack directly interacting with the main crack path and linking with the main crack. The second mechanism analysed the case of a fatigue induced microcrack directly aligned with the crack path while the third mechanism involved the analysis of a microcrack that was offset or misaligned from the main crack path. Each of these mechanisms involve a microcrack interacting with a microstructural feature near the crack path and either encouraging toughening behaviour or inhibiting it. The microcrack finite element models also provide further support for these fatigue fracture interaction mechanisms. Specifically, the microcrack models showed that the presence of an aligned microcrack ahead of the main crack causes an increase in the elastic component of the J-integral at the crack tip. This increase will cause the main crack to grow towards and link with the existing microcrack. Thus, not only does the microcrack allow the main crack to link and advance through the already cracked material at a lower energy cost, the very presence of a microcrack ahead of and aligned with the main crack tip reduces measured toughness due to the stress field effect. The results of the microcrack finite element models also show that microcracks can be responsible for the formation of other toughening mechanisms such as ligament bridges and crack deflection

The third mechanism of fatigue fracture interaction from the first experiment analysed the case of a microcrack offset from the main crack. For this case it was hypothesised that the microcrack could cause the formation of crack deflection or ligament bridging. Analysis of the single offset microcrack finite element model shows that a microcrack ahead of and offset from the main crack amplifies the elastic crack tip J-integral causing the main crack to grow towards this microcrack. If the microcrack is close enough to the main crack tip it can act to shield the main crack from the applied loading. This shielding effect can then cause the main crack to arrest and if the J-integral at the microcrack tip is higher than the main crack the microcrack will continue to grow leaving a region of uncracked material, forming a ligament bridge. As part of the third mechanism of fatigue fracture interaction it was also proposed that offset microcracks could lead to crack deflection. For this to be the case the microcrack would need to be at an angle relative to the propagation direction of the main crack or there would need to be a path of weak material from the main crack tip to the far end of the microcrack. Thus, future work for the microcrack finite element model would involve the analysis of microcracks that are not parallel to the crack propagation direction of the main crack to determine if these would lead to crack deflection.

It can be hypothesised that the results for angled microcracks would be similar to the parallel microcrack case as the microcrack ‘discontinuity’ in the material would have a similar effect on the stress field at the crack tip and hence the J-integral at the crack tip. The major difference between angled and parallel microcracks would be that angled microcracks can cause crack deflection even if they are directly aligned with the main crack path whereas parallel cracks will allow the main crack to link and advance through the already cracked material with an overall reduction in toughening. Further analysis would be needed to determine if the detrimental effect of an angled microcrack ahead of the main crack is offset by the toughening effect of crack deflection. Note that for an offset angled microcrack it is possible that both a ligament bridge and crack deflection can occur however, further analysis would be required to determine the dominant toughening effect in this case.

In the first experimental study, only a small number of the fatigue induced cracks were located along the main crack path after the fracture resistance test. Therefore, it is more likely that the first mechanism (array of fatigue microcracks) will occur and these microcracks will interact with the stress field of the main crack acting to reduce the measured toughness. It is possible that even if these fatigue microcracks are not located close enough to directly interact with the stress field of the main crack they may be close enough to interact with the new microcracks that form during fracture. This may alter

where the new microcracks form during crack growth, which could lead to the microcrack arrays at the crack tip being biased towards configurations that decrease the overall toughness or arrays that lead to an overall increase in toughness.

Overall, the model of fracture mechanisms shows excellent agreement with the results for longitudinal fatigue fracture interaction in cortical bone. The model shows that the fracture initiation toughness for longitudinal direction is linked to microcrack toughening mechanism. The microcrack toughening mechanism is inhibited by the fatigue microdamage and therefore a reduction in initiation toughness results. For the growth toughness the model links the microcrack toughening mechanism to the formation of ligament bridges and crack deflection as demonstrated by the microcrack finite element models. Fatigue induced microcracks were shown to inhibit the formation of new microcracks during crack growth and hence reduced the effectiveness of ligament bridging toughening mechanism. Thus, the combination of the finite element models and the experimental results shows that accumulated fatigue microcracks significantly decrease the longitudinal fracture resistance of cortical bone.

8.4 Synthesis of Transverse Fatigue Fracture Interaction and the Model of Fracture Mechanisms

The third experiment presented in this thesis analysed the effects of tensile diffuse fatigue damage and compressive fatigue microcracks on the transverse fracture resistance of cortical bone. In this experiment it was found that diffuse damage did not have any significant effect on the fracture resistance of cortical bone in the transverse direction. The reason for this is that the diffuse damage did not interact with microstructural boundaries of cortical bone and hence the toughening mechanisms that are a result of the crack interacting with microstructural features (e.g. crack deflection) were unaffected by diffuse fatigue damage. However, compressive fatigue microcracks were found to reduce the transverse fracture initiation toughness but not the transverse growth toughness. The reduction in fracture initiation toughness in the presence of fatigue induced microcracks can be attributed to a similar microcrack saturation mechanism as that proposed for the longitudinal specimens in experiment 1. For this case fatigue microcracks act to occupy the weak interfaces in the microstructure that would normally form microcracks during crack initiation. As these weak interfaces already contain fatigue microcracks the formation of new microcracks is inhibited and the energy that would be used to create the microcracks is used to initiate the main crack, thus reducing toughness. Further to this, having microcracks located ahead of the main crack interacts with the stress field around the main crack and acts to amplify the J-integral at the crack tip reducing the measured fracture initiation toughness of the material (as shown by the microcrack finite element

model). The reduced fracture initiation toughness for the transverse direction can also be attributed to a decrease in local material resistance. This is due to the fatigue induced microcracks providing sites that allow the main crack to initiate at lower local material resistance and partially bypass the fibre breakage mechanism described in the model of fracture mechanisms. While the fatigue microcracks provided weak sites for crack initiation once the crack began to grow the normal rate of toughening was restored as the main crack would deflect along the weak microstructural boundaries.

While compressive fatigue microcracks did reduce the fracture initiation toughness they did not reduce the growth toughness in the transverse direction. As described in the model of fracture mechanisms, the growth toughness (i.e. rate of toughening) in the transverse direction is predominantly caused by crack deflection. This crack deflection mechanism is a result of the weak interfaces in the microstructure being orientated at an angle that reduces the overall driving force for crack growth. Compressive fatigue microcracks tend to form along these weak interfaces in the microstructure and therefore do not inhibit the crack deflection toughening mechanism. If compressive fatigue microcracks provided a weaker path through which the main crack could grow across the fibres, then compressive fatigue damage would greatly reduce the growth toughness in the transverse direction by inhibiting the fibre breakage mechanism. Fortunately, in cortical bone compressive fatigue microcracks form along the weak interfaces in the microstructure which are parallel to the collagen fibrils and do not provide paths across the fibres. Thus, the presence of fatigue microcracks does not alter the crack deflection toughening mechanism for transverse crack growth and hence does not alter the growth toughness. Overall, the results of both the experimental and finite element modelling research presented in this thesis show that accumulated fatigue damage reduces the transverse fracture initiation toughness but not the transverse growth toughness.

8.5 Fatigue Fracture Interaction in Aged Bone

The results of the experimental work in this thesis show that fatigue microcracks inhibit the longitudinal initiation/growth toughness and the initiation toughness for transverse crack growth. This has significant consequences for the fracture behaviour of aged bone due to the increase in accumulated fatigue damage with age (Burr et al., 1997; Diab and Vashishth, 2007; Schaffler et al., 1995). Note that fatigue fracture interaction in aged bone was discussed in detail in section 5.4.2. However, for the sake of completeness the discussion of fatigue fracture interaction in aged bone will be briefly summarised here.

In addition to the accumulation of fatigue damage it has also been shown that there are significant changes in the microstructure of cortical bone with age due to the process of remodelling (Schaffler, 2003; Schaffler et al., 1995; Seeman, 2003; Vashishth, 2007b).

The model of toughening mechanisms presented in Figure 8.1 links all toughening behaviour to the microstructure. Therefore, any microstructural change with age would be expected to alter the toughening mechanisms that result from the microstructure. This is evident when considering the results of fracture resistance experiments conducted on aged bone (Koester et al., 2011; Nalla et al., 2004a; Zimmermann et al., 2011). For aged human bone there is a significant decrease in the fracture initiation toughness with age for both the longitudinal and transverse fracture directions (Ager et al., 2006; Currey et al., 1996; Koester et al., 2011; Nalla et al., 2006). The decrease in fracture initiation toughness with age has been mainly attributed to changes in the local material resistance to crack growth and increases in cortical bone porosity (Ammann and Rizzoli, 2003; Granke et al., 2015; Wang et al., 2002; Zimmermann et al., 2011; Zioupos, 2001b).

Microstructural changes with age also lead to decreases in the crack growth resistance behaviour of cortical bone. The primary crack growth orientations (i.e. longitudinal and transverse) and their dominant toughening mechanisms are affected differently by the microstructural changes due to aging. The increase in osteonal density with age leads a decrease in the spacing of weak microstructural boundaries such as the cement lines of osteons. This decrease in spacing of weak microstructural interfaces causes ligament bridges formed during longitudinal crack growth to be smaller. Thus, there is an overall reduction in the effectiveness of the ligament bridge toughening mechanism with increasing age (Koester et al., 2011; Nalla et al., 2004a). For transverse crack growth the decrease in the spacing of the weak microstructural interfaces leads to a decrease in the efficacy of the crack deflection toughening mechanism (Koester et al., 2011). The decrease in spacing of weak interfaces means that there is less material between microstructural boundaries. Therefore, the main crack requires less energy to break across strong microstructural boundaries and reinitiate in the direction of optimal driving force leading to many small deflections. The net effect of these many small deflections is less tortuous crack path (Koester et al., 2011; Zimmermann et al., 2011). These results have excellent agreement with the model of toughening mechanisms provided in this thesis. The toughening mechanism model links all crack growth toughening behaviour to the microstructure of cortical bone. Therefore, changes in the microstructure with age would be expected to cause significant changes in toughening behaviour as evidenced by the experimental work of others (Koester et al., 2011; Zimmermann et al., 2011).

For the longitudinal and transverse crack growth directions accumulated fatigue microcracks were shown to decrease the fracture initiation toughness. This was attributed to two mechanisms: 1) microcrack saturation and 2) microcrack interfering with the stress field of the crack tip. These mechanisms of fatigue fracture interaction show that in

addition to nanoscale changes in plasticity (i.e. changes in collagen structure and cross linking), fatigue damage accumulated with age also reduces the fracture initiation toughness of cortical bone for both transverse and longitudinal crack initiation. Therefore, the data presented in this thesis shows that accumulation of fatigue microcracks is contributing factor to the age related decrease in cortical bone fracture initiation toughness.

The experimental results in this thesis show that the crack growth resistance of cortical bone is decreased by fatigue induced microcracks in the longitudinal direction but not in the transverse direction. The decrease in growth toughness for the longitudinal crack growth direction was a result of the fatigue induced damage inhibiting the formation of new microcracks during crack growth. As microcrack formation was inhibited this lead to a decrease in the effectiveness of the ligament bridge toughening mechanism. It is possible that the effect of accumulated fatigue damage combined with the decrease in microstructural spacing are both contributing factors to the decrease in the effectiveness of the ligament bridge toughening mechanism with age.

The experimental data presented in this thesis showed that for the transverse direction the crack growth resistance was not effected by fatigue induced microcracks. However, changes in the microstructure of aged bone lead to significantly different crack growth behaviour that may have a different interaction with accumulated fatigue damage. Specifically, the crack deflection mechanism is significantly inhibited with age leading to straighter overall crack path. This suggests that longitudinal toughening mechanisms such as microcracking and ligament bridging may be more important for the transverse toughness of aged bone. If this is the case, then the fatigue fracture interaction mechanisms proposed for the longitudinal direction would apply for the transverse crack growth direction in aged bone. Therefore, it can be hypothesised that accumulated fatigue damage would be detrimental to both the fracture initiation toughness and transverse growth toughness in cortical bone. However, a future study would be needed to provide support for this conjecture.

Clinical fractures in the elderly are usually the result of complex mixed mode loading on bones. While the experiments presented in this thesis have focused on mode I crack growth as it is normally the case of the maximum driving force for crack growth it is also important to consider the implication of the experimental results in light of mixed mode fracture. A previous study by Zimmerman et al. (2010) has shown that for mixed mode loading in cortical bone mode II loading shows similar toughening behaviour to longitudinal mode I loading; that is, shear loading acting to slide the collagen fibres across each other causes microcracking and ligament bridging to become the dominant toughening

mechanisms. For the case of mode II loading it can be hypothesised that fatigue induced microcracks will be detrimental to both the fracture initiation toughness and growth toughness for mode II crack growth in cortical bone. This conjecture would need to be verified with future experiments, which would also allow the assessment of fatigue damage on combined mode I and mode II cases.

8.6 Future Work

The results of both the experimental and finite element modelling presented in this thesis suggest many directions in which this work can be extended in the future. Some of these future studies and extensions on the current work have been mentioned in their respective chapters. However, a summary of the three major areas that could extend this work will be presented below.

The first area in which this work could be extended would be the area of mixed-mode fracture and different microstructural orientations. Loading of bones *in vivo* leads to complex mixed-mode loading. Therefore, it can be expected that *in vivo* fracture is also a result of mixed-mode loading on cracks that form in the bone. The work presented in this thesis provides the basis for fatigue fracture interaction mechanisms for mode I cracking in both the longitudinal and transverse direction in cortical bone. A logical extension of the work presented in this thesis would be to analyse the effects of fatigue induced microdamage on the mode II fracture resistance of cortical bone or at various levels of combined mode I and mode II loading. This could be done using an offset four point bending method such as that used by Zimmerman et al. (2009). Another extension of the current work would be to analyse mode I fracture for different microstructural angles. The studies presented in this thesis analysed longitudinal (parallel to the weak interfaces in the microstructure) and transverse (perpendicular to the weak interfaces in the microstructure) fracture however, it would also be possible to look at different microstructural angles between these two extremes to determine the point at which crack deflection becomes a more dominant toughening mechanism when compared to ligament bridging.

The second area that would extend this work would be the analysis of high loading rate fracture. Fracture mechanisms at higher loading rates have become an area of increasing research as the loading rate for *in-vivo* failures can vary significantly from low loading rate fragility fractures to higher loading rate events (Johnson et al., 2010; Kulin et al., 2008, 2011a; Ural et al., 2011). The fracture mechanisms in bone change significantly at high loading rates for transverse fracture. Specifically, at high loading rates microdamage formation during crack growth is significantly reduced and the crack deflection mechanism becomes less effective (Kulin et al., 2011b). As the microcrack toughening mechanism is

suppressed at high loading rates it is expected that the fatigue fracture interaction mechanism of microcrack saturation would be less prevalent. However, this does not rule out the effects of fatigue induced microcracks interacting with the stress field around the crack tip reducing the fracture initiation toughness. Further fatigue fracture interaction experiments at a range of loading rates would be required to fully characterise the effects of loading rate on the toughening mechanisms of cortical bone.

The third area that would extend this work would be the analysis of fatigue fracture interaction in aged or diseased human bones. It has been shown that bones form fatigue damage with normal use and that the amount of fatigue damage increases with age (Burr et al., 1985; Schaffler et al., 1995). Aged and diseased human bones also show significant microstructural differences when compared to healthy bones and therefore can be expected to have different fatigue damage formation and fracture behaviour. Both of these factors (i.e. fatigue microdamage and microstructural changes) will interact and lead to an overall decrease in the fracture resistance of aged bone. Previous work by Koester et al. (2011) shows that aged human bone has reduced fracture resistance when compared to younger bone. In the study by Koester et al. (2011) the reduction in fracture resistance was attributed to microstructural changes that caused the crack deflection mechanism to be suppressed in aged bone. Combining this result with the experimental results presented in this thesis suggests that transverse fracture in aged bone may be more similar to longitudinal fracture. This is due to the microstructural changes with age allowing more weak paths in the microstructure to be more closely aligned with the direction of the optimal driving force. Thus, it could be reasoned that for both longitudinal and transverse fracture in aged bone microcracking and ligament bridging are important toughening mechanisms. The results from the experimental work in this thesis show that both of these toughening mechanisms (i.e. microcracking and ligament bridging) are inhibited by the presence of fatigue induced microdamage. Therefore, it may be possible that the detrimental effect of fatigue damage on the fracture resistance of aged bone is more significant than in young bone. However, future studies on fatigue fracture interaction in aged bone would be required to confirm this hypothesis.

8.7 Conclusion

Overall, the body of experimental and finite element modelling work presented in this thesis has provided a valuable contribution to the knowledge of fatigue fracture interaction mechanisms in cortical bone. The results from the body of research presented in this thesis show that fatigue microdamage is detrimental to the fracture resistance of cortical bone. Specifically, fatigue induced microdamage reduces both the fracture initiation

toughness and the growth toughness for cracking in the longitudinal direction and reduces the fracture initiation toughness for cracking in the transverse direction. The results of both the experimental studies and the finite element modelling studies were combined with existing literature on the fracture behaviour of cortical bone to propose a model of toughening in cortical bone. This model proposed that all toughening mechanisms in cortical bone are a result of the crack path interaction with microstructural features. The model further divided the fracture toughening mechanisms by microstructural orientation with respect to the crack growth direction. For the longitudinal crack growth direction, the dominant toughening mechanism is ligament bridging as a result of microcracking ahead of the main crack tip while for the transverse direction the dominant toughening mechanism is crack deflection due to misalignment of the direction of optimal driving force and the weak interfaces in the microstructure.

This model was then applied to the results from the fatigue fracture interaction experiments to clarify the proposed mechanisms of fatigue fracture interaction. For longitudinal crack initiation the formation of new microcracks acts to absorb energy that would normally be used to initiate the main crack. The presence of fatigue damage acts to inhibit the formation of new microcracks during crack growth reducing the fracture initiation toughness. Fatigue microcracks also interact with the stress field around the main crack and reduces apparent toughness. For longitudinal crack growth the dominant toughening mechanism is ligament bridging as a result of microcracks forming ahead of the main crack path. Fatigue microdamage inhibits the formation of new microcracks during crack growth reducing the formation of ligament bridges hence, the overall reduction in the crack growth toughness.

For transverse crack initiation the toughness of cortical bone is a result of the collagen fibre strength and the formation of microcracks before crack initiation. Similar to longitudinal fracture initiation the presence of fatigue damage inhibits the formation of new microcracks before crack initiation. Further, fatigue cracks reduce the local material strength and allow the crack to break across the collagen fibres at a lower energy cost reducing fracture initiation toughness. For transverse crack growth the dominant toughening mechanism is crack deflection along the weak interfaces of the microstructure. While fatigue microcracks reduce the fracture initiation toughness they do not alter the orientation of the weak paths in the microstructure and hence the crack deflection toughening mechanism. Therefore, fatigue microcracks do not alter the growth toughness in the transverse direction. Thus, once a crack has initiated in the transverse direction it will then propagate along the perpendicular weak interfaces causing significant toughening.

Finally, the results from this work also suggest that the detrimental effect of fatigue microdamage may be further amplified in aged bone due to the microstructural changes that occur with age. Specifically, transverse fracture in aged bone is more similar to the longitudinal case as the crack deflection mechanism is suppressed. This would imply that toughening mechanisms such as microcracking and ligament bridging are more important for transverse crack growth in aged bone. If this is the case then it is probable that the fatigue fracture interaction mechanisms for the longitudinal direction become significant in aged bone, even for transverse crack growth. Thus, it is probable that fatigue microdamage decreases both the fracture initiation toughness and growth toughness in aged bone regardless of fracture orientation.

References

Abdel-Wahab, A.A., Maligno, A.R., Silberschmidt, V.V., 2012. Micro-scale modelling of bovine cortical bone fracture: Analysis of crack propagation and microstructure using X-FEM. Comput. Mater. Sci. 52, 128–135. doi:10.1016/j.commatsci.2011.01.021

Ager, J. w., Balooch, G., Ritchie, R. o., 2006. Fracture, Aging, and Disease in Bone. J. Mater. Res. 21, 1878–1892. doi:10.1557/jmr.2006.0242

Agrawal, A., Karlsson, A.M., 2006. Obtaining mode mixity for a bimaterial interface crack using the virtual crack closure technique. Int. J. Fract. 141, 75–98. doi:10.1007/s10704-006-0069-4

Alwar, R.S., Nambissan, K.N.R., 1983. Three-dimensional finite element analysis of cracked thick plates in bending. Int. J. Numer. Methods Eng. 19, 293–303. doi:10.1002/nme.1620190210

Ammann, P., Rizzoli, R., 2003. Bone strength and its determinants. Osteoporos. Int. 14, 13–18. doi:10.1007/s00198-002-1345-4

An, B., Liu, Y., Arola, D., Zhang, D., 2011. Fracture toughening mechanism of cortical bone: An experimental and numerical approach. J. Mech. Behav. Biomed. Mater. 4, 983–992. doi:10.1016/j.jmbbm.2011.02.012

Anderson, T.L., 2005. Fracture Mechanics: Fundamentals and Applications. Taylor & Francis.

ASTM Standard E1820, 2011. Test Method for Measurement of Fracture Toughness. ASTM International.

Barth, H.D., Launey, M.E., MacDowell, A.A., Ager III, J.W., Ritchie, R.O., 2010. On the effect of X-ray irradiation on the deformation and fracture behavior of human cortical bone. Bone 46, 1475–1485. doi:10.1016/j.bone.2010.02.025

Barth, H.D., Zimmermann, E.A., Schaible, E., Tang, S.Y., Alliston, T., Ritchie, R.O., 2011. Characterization of the effects of x-ray irradiation on the hierarchical structure and mechanical properties of human cortical bone. Biomaterials 32, 8892–8904. doi:10.1016/j.biomaterials.2011.08.013

Basquin, O.H., 1910. The exponential law of endurance tests. Am. Soc. Test. Mater. 10, 625–630.

Bayoumi, M.R., Abdellatif, A.K., 1995. Effect of surface finish on fatigue strength. Eng. Fract. Mech. 51, 861–870. doi:10.1016/0013-7944(94)00297-U

Behiri, J.C., Bonfield, W., 1989. Orientation dependence of the fracture mechanics of cortical bone. J. Biomech. 22, 863–872. doi:10.1016/0021-9290(89)90070-5

Behiri, J.C., Bonfield, W., 1984. Fracture mechanics of bone--the effects of density, specimen thickness and crack velocity on longitudinal fracture. J. Biomech. 17, 25–34.

Boyce, T.M., Fyhrie, D.P., Glotkowski, M.C., Radin, E.L., Schaffler, M.B., 1998. Damage type and strain mode associations in human compact bone bending fatigue. J. Orthop. Res. 16, 322–329. doi:10.1002/jor.1100160308

Broz, J.J., Simske, S.J., Greenberg, A.R., 1995. Material and compositional properties of selectively demineralized cortical bone. J. Biomech. 28, 1357–1368. doi:10.1016/0021-9290(94)00184-6

Bruce Martin, R., Burr, D.B., 1982. A hypothetical mechanism for the stimulation of osteonal remodelling by fatigue damage. J. Biomech. 15, 137–139. doi:10.1016/S0021-9290(82)80001-8

Budyn, E., Hoc, T., Jonvaux, J., 2008. Fracture strength assessment and aging signs detection in human cortical bone using an X-FEM multiple scale approach. Comput. Mech. 42, 579–591. doi:10.1007/s00466-008-0283-1

Burr, D., 2003. Microdamage and bone strength. Osteoporos. Int. 14, 67–72. doi:10.1007/s00198-003-1476-2

Burr, D.B., 1997. Bone, exercise, and stress fractures. Exerc. Sport Sci. Rev. 25, 171–194.

Burr, D.B., 1993. Remodeling and the repair of fatigue damage. Calcif. Tissue Int. 53, S75–S81. doi:10.1007/BF01673407
Burr, D.B., Forwood, M.R., Fyhrie, D.P., Martin, R.B., Schaffler, M.B., Turner, C.H., 1997. Bone Microdamage and Skeletal Fragility in Osteoporotic and Stress Fractures. J. Bone Miner. Res. 12, 6–15. doi:10.1359/jbmr.1997.12.1.6
Burr, D.B., Martin, R.B., Schaffler, M.B., Radin, E.L., 1985. Bone remodeling in response to in vivo fatigue microdamage. J. Biomech. 18, 189–200. doi:10.1016/0021-9290(85)90204-0
Burr, D.B., Milgrom, C., Boyd, R.D., Higgins, W.L., Robin, G., Radin, E.L., 1990. Experimental stress fractures of the tibia. Biological and mechanical aetiology in rabbits. J. Bone Joint Surg. Br. 72-B, 370–375.
Burr, D.B., Turner, C.H., Naick, P., Forwood, M.R., Ambrosius, W., Sayeed Hasan, M., Pidaparti, R., 1998. Does microdamage accumulation affect the mechanical properties of bone? J. Biomech. 31, 337–345. doi:10.1016/S0021-9290(98)00016-5
Burstein, A.H., Currey, J.D., Frankel, V.H., Reilly, D.T., 1972a. The ultimate properties of bone tissue: The effects of yielding. J. Biomech. 5, 35–44. doi:10.1016/0021-9290(72)90017-6
Burstein, A.H., Currey, J.D., Frankel, V.H., Reilly, D.T., 1972b. The ultimate properties of bone tissue: The effects of yielding. J. Biomech. 5, 35–44. doi:10.1016/0021-9290(72)90017-6
Byskov, E., 1970. The calculation of stress intensity factors using the finite element method with cracked elements. Int. J. Fract. Mech. 6, 159–167. doi:10.1007/BF00189823
Caler, W.E., Carter, D.R., 1989. Bone creep-fatigue damage accumulation. J. Biomech. 22, 625–635. doi:10.1016/0021-9290(89)90013-4
Carter, D.R., Caler, W.E., 1985. A cumulative damage model for bone fracture. J. Orthop. Res. Off. Publ. Orthop. Res. Soc. 3, 84–90. doi:10.1002/jor.1100030110
Carter, D.R., Hayes, W.C., 1977. Compact bone fatigue damage—I. Residual strength and stiffness. J. Biomech. 10, 325–337. doi:10.1016/0021-9290(77)90005-7
Carter, D.R., Hayes, W.C., 1976. Fatigue life of compact bone—I effects of stress amplitude, temperature and density. J. Biomech. 9, 27–34. doi:10.1016/0021-9290(76)90136-6
Carter, D.R., Hayes, W.C., Schurman, D.J., 1976. Fatigue life of compact bone—II. Effects of microstructure and density. J. Biomech. 9, 211–218. doi:10.1016/0021-9290(76)90006-3
Cezayirlioglu, H., Bahniuk, E., Davy, D.T., Heiple, K.G., 1985. Anisotropic yield behavior of bone under combined axial force and torque. J. Biomech. 18, 61–69. doi:10.1016/0021-9290(85)90045-4
Chong, A.C.M., Miller, F., Buxton, M., Friis, E.A., 2007. Fracture Toughness and Fatigue Crack Propagation Rate of Short Fiber Reinforced Epoxy Composites for Analogue Cortical Bone. J. Biomech. Eng. 129, 487–493. doi:10.1115/1.2746369
Chow, W.T., Atluri, S.N., 1995. Finite element calculation of stress intensity factors for interfacial crack using virtual crack closure integral. Comput. Mech. 16, 417–425. doi:10.1007/BF00370563
Cotterell, B., Rice, J.R., 1980. Slightly curved or kinked cracks. Int. J. Fract. 16, 155–169. doi:10.1007/BF00012619
Cowin, S.C., Sadegh, A.M., 1991. Non-interacting modes for stress, strain and energy in anisotropic hard tissue. J. Biomech. 24, 859–867. doi:10.1016/0021-9290(91)90311-A
Currey, J.D., 1975. The effects of strain rate, reconstruction and mineral content on some mechanical properties of bovine bone. J. Biomech. 8, 81–86. doi:10.1016/0021-9290(75)90046-9
Currey, J.D., 1960. Differences in the Blood-Supply of Bone of Different Histological Types. J. Cell Sci. s3-101, 351–370.

Currey, J.D., 1959. Differences in the tensile strength of bone of different histological types. J. Anat. 93, 87–95.
Currey, J.D., Brear, K., Zioupos, P., 1996. The effects of ageing and changes in mineral content in degrading the toughness of human femora. J. Biomech. 29, 257–260. doi:10.1016/0021-9290(95)00048-8
Danova, N.., Colopy, S.., Radtke, C.., Kalscheur, V.., Markel, M.., Vanderby Jr., R., McCabe, R.., Escarcega, A.., Muir, P., 2003. Degradation of bone structural properties by accumulation and coalescence of microcracks. Bone 33, 197–205. doi:10.1016/S8756-3282(03)00155-8
deLorenzi, H.G., 1982. On the energy release rate and the J-integral for 3-D crack configurations. Int. J. Fract. 19, 183–193. doi:10.1007/BF00017129
Diab, T., Condon, K.W., Burr, D.B., Vashishth, D., 2006. Age-related change in the damage morphology of human cortical bone and its role in bone fragility. Bone 38, 427–431. doi:10.1016/j.bone.2005.09.002
Diab, T., Vashishth, D., 2007. Morphology, localization and accumulation of in vivo microdamage in human cortical bone. Bone 40, 612–618. doi:10.1016/j.bone.2006.09.027
Diab, T., Vashishth, D., 2005. Effects of damage morphology on cortical bone fragility. Bone 37, 96–102. doi:10.1016/j.bone.2005.03.014
Donaldson, F., Ruffoni, D., Schneider, P., Levchuk, A., Zwahlen, A., Pankaj, P., Müller, R., 2014. Modeling microdamage behavior of cortical bone. Biomech. Model. Mechanobiol. 13, 1227–1242. doi:10.1007/s10237-014-0568-6
Enlow, D.H., 1962. A Study of the Post-Natal Growth and Remodeling of Bone. Am. J. Anat. 110, 79–101. doi:10.1002/aja.1001100202
Erdogan, F., Sih, G.C., 1963. On the Crack Extension in Plates Under Plane Loading and Transverse Shear. J. Basic Eng. 85, 519–525. doi:10.1115/1.3656897
Fawaz, S.A., 1998. Application of the virtual crack closure technique to calculate stress intensity factors for through cracks with an elliptical crack front. Eng. Fract. Mech. 59, 327–342. doi:10.1016/S0013-7944(97)00126-4
Finestone, A.S., Milgrom, C., 2012. Diagnosis and Treatment of Stress Fractures, in: Doral, M.N. (Ed.), Sports Injuries. Springer Berlin Heidelberg, pp. 775–785.
Fleck, C., Eifler, D., 2003. Deformation behaviour and damage accumulation of cortical bone specimens from the equine tibia under cyclic loading. J. Biomech. 36, 179–189. doi:10.1016/S0021-9290(02)00364-0
Fletcher, L.C., Codrington, J.D., Parkinson, I.H., 2015. Methods for assessing the effects of accumulated fatigue damage on the fracture resistance of cortical bone, in: Proceedings: The 8th Australasian Conference of Applied Mechanics. Presented at the 8th Australasian Conference of Applied Mechanics, Melbourne, Australia.
Fletcher, L., Codrington, J., Parkinson, I., 2014. Effects of fatigue induced damage on the longitudinal fracture resistance of cortical bone. J. Mater. Sci. Mater. Med. 25, 1661–1670. doi:10.1007/s10856-014-5213-5
Fletcher, L., Codrington, J., Parkinson, I., 2012. Effects of irradiation and non-enzymatic glycation on the fracture resistance of bovine cortical bone. Proc. 7th Australas. Congr. Appl. Mech. ACAM 7 9-12 Dec. 2012 Univ. Adel. North Terrace Campus Natl. Comm. Appl. Mech. Eng. Aust. 322.
Forwood, M.R., Burr, D.B., 1993. Physical activity and bone mass: exercises in futility? Bone Miner. 21, 89–112.
Frost, H.M., 1969. Tetracycline-based histological analysis of bone remodeling. Calcif. Tissue Res. 3, 211–237. doi:10.1007/BF02058664
Frost, H.M., 1960. Presence of microscopic cracks in vivo in bone. Henry Ford Hosp. Med. Bull. 8, 35.
George, W.T., Vashishth, D., 2005. Damage mechanisms and failure modes of cortical bone under components of physiological loading. J. Orthop. Res. 23, 1047–1053. doi:10.1016/j.orthres.2005.02.008
Giladi, M., Milgrom, C., Simkin, A., Danon, Y., 1991. Stress fractures. Identifiable risk factors. Am. J. Sports Med. 19, 647–652.

Goto, K., Kagawa, Y., 1994. Crack-fiber interaction and interfacial failure models in fiber-reinforced ceramics. Mater. Sci. Eng. A 176, 357–361. doi:10.1016/0921-5093(94)90999-7

Granke, M., Makowski, A.J., Uppuganti, S., Does, M.D., Nyman, J.S., 2015. Identifying Novel Clinical Surrogates to Assess Human Bone Fracture Toughness. J. Bone Miner. Res. 30, 1290–1300. doi:10.1002/jbmr.2452

Harris, B., Morley, J., Phillips, D.C., 1975. Fracture mechanisms in glass-reinforced plastics. J. Mater. Sci. 10, 2050–2061. doi:10.1007/BF00557483

Hertzberg, R.W., Manson, J.A., Skibo, M., 1975. Frequency sensitivity of fatigue processes in polymeric solids. Polym. Eng. Sci. 15, 252–260. doi:10.1002/pen.760150404

Hiller, L.P., Stover, S.M., Gibson, V.A., Gibeling, J.C., Prater, C.S., Hazelwood, S.J., Yeh, O.C., Martin, R.B., 2003. Osteon pullout in the equine third metacarpal bone: Effects of ex vivo fatigue. J. Orthop. Res. 21, 481–488. doi:10.1016/S0736-0266(02)00232-2

Hoc, T., Henry, L., Verdier, M., Aubry, D., Sedel, L., Meunier, A., 2006. Effect of microstructure on the mechanical properties of Haversian cortical bone. Bone 38, 466–474. doi:10.1016/j.bone.2005.09.017

Itoga, H., Tokaji, K., Nakajima, M., Ko, H.-N., 2003. Effect of surface roughness on step-wise S–N characteristics in high strength steel. Int. J. Fatigue 25, 379–385. doi:10.1016/S0142-1123(02)00166-4

Iwamoto, J., Takeda, T., 2003. Stress fractures in athletes: review of 196 cases. J. Orthop. Sci. Off. J. Jpn. Orthop. Assoc. 8, 273–278. doi:10.1007/s10776-002-0632-5

Jacobsen, T.K., Sørensen, B.F., 2001. Mode I intra-laminar crack growth in composites — modelling of R-curves from measured bridging laws. Compos. Part Appl. Sci. Manuf. 32, 1–11. doi:10.1016/S1359-835X(00)00139-1

Janssen, M., Zuidema, J., Wanhill, R.J.H., 2004. Fracture Mechanics. Taylor & Francis.

Jayaraman, S., Sadeghipour, K., Baran, G., 1997. Finite element analysis of horizontal and branched subsurface cracks in brittle materials. Wear 208, 237–242. doi:10.1016/S0043-1648(96)07498-4

Jha, M., Charalambides, P.G., 1998. A finite element analysis of fracture initiation in ductile/brittle periodically layered composites. Int. J. Fract. 90, 299–323. doi:10.1023/A:1007488927130

Jha, M., Narasimhan, R., 1992. A finite element analysis of dynamic fracture initiation by ductile failure mechanisms in a 4340 steel. Int. J. Fract. 56, 209–231. doi:10.1007/BF00012328

Johnson, T.P.M., Socrate, S., Boyce, M.C., 2010. A viscoelastic, viscoplastic model of cortical bone valid at low and high strain rates. Acta Biomater. 6, 4073–4080. doi:10.1016/j.actbio.2010.04.017

Jonvaux, J., Hoc, T., Budyn, É., 2012. Analysis of micro fracture in human Haversian cortical bone under compression. Int. J. Numer. Methods Biomed. Eng. 28, 974–998. doi:10.1002/cnm.2478

Kachanov, M., 1987. Elastic solids with many cracks: A simple method of analysis. Int. J. Solids Struct. 23, 23–43. doi:10.1016/0020-7683(87)90030-8

Kachanov, M., Montagut, E.L.E., Laures, J.P., 1990. Mechanics of crack—microcrack interactions. Mech. Mater. 10, 59–71. doi:10.1016/0167-6636(90)90017-A

Karihaloo, B.L., Keer, L.M., Nemat-Nasser, S., Oranratnachai, A., 1981. Approximate Description of Crack Kinking and Curving. J. Appl. Mech. 48, 515–519. doi:10.1115/1.3157665

Kennedy, O.D., Brennan, O., Mauer, P., Rackard, S.M., O'Brien, F.J., Taylor, D., Lee, T.C., 2008. The effects of increased intracortical remodeling on microcrack behaviour in compact bone. Bone 43, 889–893. doi:10.1016/j.bone.2008.07.235

Koester, K.J., Ager, J.W., Ritchie, R.O., 2008. The true toughness of human cortical bone measured with realistically short cracks. Nat. Mater. 7, 672. doi:10.1038/nmat2221

Koester, K.J., Barth, H.D., Ritchie, R.O., 2011. Effect of aging on the transverse toughness of human cortical bone: Evaluation by R-curves. J. Mech. Behav. Biomed. Mater. 4, 1504–1513. doi:10.1016/j.jmbbm.2011.05.020

Kulin, R., Jiang, F., Vecchio, K., 2008. Aging and loading rate effects on the mechanical behavior of equine bone. JOM J. Miner. Met. Mater. Soc. 60, 39–44. doi:10.1007/s11837-008-0069-0

Kulin, R.M., Jiang, F., Vecchio, K.S., 2011a. Loading rate effects on the R-curve behavior of cortical bone. Acta Biomater. 7, 724–732. doi:10.1016/j.actbio.2010.09.027

Kulin, R.M., Jiang, F., Vecchio, K.S., 2011b. Effects of age and loading rate on equine cortical bone failure. J. Mech. Behav. Biomed. Mater. 4, 57–75. doi:10.1016/j.jmbbm.2010.09.006

Kuna, M., 2013. Finite Elements in Fracture Mechanics: Theory - Numerics - Applications. Springer Netherlands.

Lankford, J., Kusenberger, F.N., 1973. Initiation of fatigue cracks in 4340 steel. Metall. Trans. 4, 553–559. doi:10.1007/BF02648709

Lee, T.C., O'Brien, F.J., Taylor, D., 2000. The nature of fatigue damage in bone. Int. J. Fatigue 22, 847–853. doi:10.1016/S0142-1123(00)00054-2

Lee, T., Rammohan, A.V., Chan, A., Beng Chye Tan, V., Das De, S., Link, T.M., Eckstein, F., Schafer, B.W., 2012. The susceptibility of the femoral neck to fracture: An assessment incorporating the effects of age-remodeling and stress reduction. J. Biomech. 45, 931–937. doi:10.1016/j.jbiomech.2012.01.021

Lipson, S.F., Katz, J.L., 1984. The relationship between elastic properties and microstructure of bovine cortical bone. J. Biomech. 17, 231–240. doi:10.1016/0021-9290(84)90134-9

Liu, P.F., Yang, Y.H., 2014. Finite Element Analysis of the Competition Between Crack Deflection and Penetration of Fiber-Reinforced Composites Using Virtual Crack Closure Technique. Appl. Compos. Mater. 21, 759–771. doi:10.1007/s10443-013-9375-y

Liu, P.F., Zhang, B.J., Zheng, J.Y., 2012. Finite Element Analysis of Plastic Collapse and Crack Behavior of Steel Pressure Vessels and Piping Using XFEM. J. Fail. Anal. Prev. 12, 707–718. doi:10.1007/s11668-012-9623-8

Malik, C.L., Stover, S.M., Martin, R.B., Gibeling, J.C., 2003. Equine cortical bone exhibits rising R-curve fracture mechanics. J. Biomech. 36, 191–198. doi:10.1016/S0021-9290(02)00362-7

Martin, B., 1992. A theory of fatigue damage accumulation and repair in cortical bone. J. Orthop. Res. 10, 818–825. doi:10.1002/jor.1100100611

Martin, R.B., 2003. Fatigue Microdamage as an Essential Element of Bone Mechanics and Biology. Calcif. Tissue Int. 73, 101–107. doi:10.1007/s00223-002-1059-9

Martin, R.B., Burr, D.B., 1989. Structure, function, and adaptation of compact bone. Raven Press.

Martin, R.B., Gibson, V.A., Stover, S.M., Gibeling, J.C., Griffin, L.V., 1997. Residual strength of equine bone is not reduced by intense fatigue loading: Implications for stress fracture. J. Biomech. 30, 109–114. doi:10.1016/S0021-9290(96)00113-3

Meguid, S.A., Gaultier, P.E., Gong, S.X., 1991a. A comparison between analytical and finite element analysis of main crack-microcrack interaction. Eng. Fract. Mech. 38, 451–465. doi:10.1016/0013-7944(91)90095-I

Meguid, S.A., Gong, S.X., Gaultier, P.E., 1991b. Main crack-microcrack interaction under mode I, II and III loadings: Shielding and amplification. Int. J. Mech. Sci. 33, 351–359. doi:10.1016/0020-7403(91)90074-D

Milgrom, C., Giladi, M., Stein, M., Kashtan, H., Margulies, J.Y., Chisin, R., Steinberg, R., Aharonson, Z., 1985. Stress fractures in military recruits. A prospective study showing an unusually high incidence. J. Bone Joint Surg. Br. 67-B, 732–735.

Miller, K.J., 1993. Materials science perspective of metal fatigue resistance. Mater. Sci. Technol. 9, 453–462. doi:10.1179/mst.1993.9.6.453

Mischinski, S., Ural, A., 2013. Interaction of microstructure and microcrack growth in cortical bone: a finite element study. Comput. Methods Biomech. Biomed. Engin. 16, 81–94. doi:10.1080/10255842.2011.607444
Mischinski, S., Ural, A., 2011. Finite Element Modeling of Microcrack Growth in Cortical Bone. J. Appl. Mech. 78, 041016. doi:10.1115/1.4003754
Mizutani, Y., Nagashima, K., Takemoto, M., Ono, K., 2000. Fracture mechanism characterization of cross-ply carbon-fiber composites using acoustic emission analysis. NDT E Int. 33, 101–110. doi:10.1016/S0963-8695(99)00030-4
Mohsin, S., O'Brien, F.J., Lee, T.C., 2006. Osteonal crack barriers in ovine compact bone. J. Anat. 208, 81–89. doi:10.1111/j.1469-7580.2006.00509.x
Mori, S., Burr, D.B., 1993. Increased intracortical remodeling following fatigue damage. Bone 14, 103–109. doi:10.1016/8756-3282(93)90235-3
Nalla, R.K., Kruzic, J.J., Kinney, J.H., Balooch, M., Ager III, J.W., Ritchie, R.O., 2006. Role of microstructure in the aging-related deterioration of the toughness of human cortical bone. Mater. Sci. Eng. C 26, 1251–1260. doi:10.1016/j.msec.2005.08.021
Nalla, R.K., Kruzic, J.J., Kinney, J.H., Ritchie, R.O., 2004a. Effect of aging on the toughness of human cortical bone: evaluation by R-curves. Bone 35, 1240–1246. doi:10.1016/j.bone.2004.07.016
Nalla, R.K., Kruzic, J.J., Ritchie, R.O., 2004b. On the origin of the toughness of mineralized tissue: microcracking or crack bridging? Bone 34, 790–798. doi:10.1016/j.bone.2004.02.001
Nalla, R.K., Kruzic, J., Kinney, J., Ritchie, R., 2005. Aspects of in vitro fatigue in human cortical bone: time and cycle dependent crack growth. Biomaterials 26, 2183–2195. doi:10.1016/j.biomaterials.2004.05.024
Nalla, R.., Kruzic, J.., Kinney, J.., Ritchie, R.., 2005. Mechanistic aspects of fracture and R-curve behavior in human cortical bone. Biomaterials 26, 217–231. doi:10.1016/j.biomaterials.2004.02.017
Nishioka, T., Atluri, S.N., 1982. Finite element simulation of fast fracture in steel DCB specimen. Eng. Fract. Mech. 16, 157–175. doi:10.1016/0013-7944(82)90148-5
Norman, T.L., Yeni, Y.N., Brown, C.U., Wang, Z., 1998. Influence of microdamage on fracture toughness of the human femur and tibia. Bone 23, 303–306. doi:10.1016/S8756-3282(98)00103-3
Norman, T., Vashishth, D., Burr, D., 1995a. Fracture toughness of human bone under tension. J. Biomech. 28, 309–320. doi:10.1016/0021-9290(94)00069-G
Norman, T., Vashishth, D., Burr, D., 1995b. Fracture toughness of human bone under tension. J. Biomech. 28, 309–320. doi:10.1016/0021-9290(94)00069-G
O'Brien, F.J., Hardiman, D.A., Hazenberg, J.G., Mercy, M.V., Mohsin, S., Taylor, D., Lee, T.C., 2005a. The behaviour of microcracks in compact bone. Eur. J. Morphol. 42, 71–79. doi:10.1080/09243860500096131
O'Brien, F.J., Taylor, D., Clive Lee, T., 2007. Bone as a composite material: The role of osteons as barriers to crack growth in compact bone. Int. J. Fatigue 29, 1051–1056. doi:10.1016/j.ijfatigue.2006.09.017
O'Brien, F.J., Taylor, D., Clive Lee, T., 2005b. The effect of bone microstructure on the initiation and growth of microcracks. J. Orthop. Res. 23, 475–480. doi:10.1016/j.orthres.2004.08.005
O'Brien, F.J., Taylor, D., Lee, T.C., 2003. Microcrack accumulation at different intervals during fatigue testing of compact bone. J. Biomech. 36, 973–980. doi:10.1016/S0021-9290(03)00066-6
Paris, P.C., Gomez, M.P., Anderson, W.P., 1961. A Rational Analytic Theory of Fatigue. Trend Eng. 13, 9–14.
Parsamian, G.P., Norman, T.L., 2001. Diffuse damage accumulation in the fracture process zone of human cortical bone specimens and its influence on fracture toughness. J. Mater. Sci. Mater. Med. 12, 779–783. doi:10.1023/A:1017916800421

Paschalis, E.P., Shane, E., Lyritis, G., Skarantavos, G., Mendelsohn, R., Boskey, A.L., 2004. Bone Fragility and Collagen Cross-Links. J. Bone Miner. Res. 19, 2000–2004. doi:10.1359/jbmr.040820

Pegoretti, A., Accorsi, M.L., Dibenedetto, A.T., 1996. Fracture toughness of the fibre-matrix interface in glass-epoxy composites. J. Mater. Sci. 31, 6145–6153. doi:10.1007/BF00354431

Poundarik, A.A., Diab, T., Sroga, G.E., Ural, A., Boskey, A.L., Gundberg, C.M., Vashishth, D., 2012. Dilatational band formation in bone. Proc. Natl. Acad. Sci. doi:10.1073/pnas.1201513109

Radon, J.C., Culver, L.E., 1975. Effect of temperature and frequency in fatigue of polymers. Polymer 16, 539–544. doi:10.1016/0032-3861(75)90014-2

Reilly, D.T., Burstein, A.H., 1975. The elastic and ultimate properties of compact bone tissue. J. Biomech. 8, 393–405.

Reilly, D.T., Burstein, A.H., Frankel, V.H., 1974. The elastic modulus for bone. J. Biomech. 7, 271–275. doi:10.1016/0021-9290(74)90018-9

Rho, J.-Y., Kuhn-Spearing, L., Zioupos, P., 1998. Mechanical properties and the hierarchical structure of bone. Med. Eng. Phys. 20, 92–102. doi:10.1016/S1350-4533(98)00007-1

Rice, J.R., 1968. A Path Independent Integral and the Approximate Analysis of Strain Concentration by Notches and Cracks. J. Appl. Mech. 35, 379–386. doi:10.1115/1.3601206

Ritchie, R.O., 1999. Mechanisms of fatigue-crack propagation in ductile and brittle solids. Int. J. Fract. 100, 55–83. doi:10.1023/A:1018655917051

Ritchie, R.O., Buehler, M.J., Hansma, P., 2009. Plasticity and toughness in bone. Phys. Today 62, 41–47.

Roe, K.L., Siegmund, T., 2003. An irreversible cohesive zone model for interface fatigue crack growth simulation. Eng. Fract. Mech. 70, 209–232. doi:10.1016/S0013-7944(02)00034-6

Rosenfield, A.R., Shetty, D.K., 1983. Cleavage fracture of steel in the upper ductile-brittle transition region. Eng. Fract. Mech. 17, 461–470. doi:10.1016/0013-7944(83)90042-5

Sauer, J.A., Richardson, G.C., 1980. Fatigue of polymers. Int. J. Fract. 16, 499–532. doi:10.1007/BF02265215

Schaffler, M.B., 2003. Role of bone turnover in microdamage. Osteoporos. Int. 14, 73–80. doi:10.1007/s00198-003-1477-1

Schaffler, M.B., Choi, K., Milgrom, C., 1995. Aging and matrix microdamage accumulation in human compact bone. Bone 17, 521–525. doi:10.1016/8756-3282(95)00370-3

Schwartz, A., Sellmeyer, D., 2007. Diabetes, fracture, and bone fragility. Curr. Osteoporos. Rep. 5, 105–111. doi:10.1007/s11914-007-0025-x

Seeman, E., 2003. Reduced bone formation and increased bone resorption: rational targets for the treatment of osteoporosis. Osteoporos. Int. J. Establ. Result Coop. Eur. Found. Osteoporos. Natl. Osteoporos. Found. USA 14 Suppl 3, S2–8. doi:10.1007/s00198-002-1340-9

Shaw, L.L., Miracle, D.B., 1996. Effects of an interfacial region on the transverse behavior of metal-matrix composites—A finite element analysis. Acta Mater. 44, 2043–2055. doi:10.1016/1359-6454(95)00270-7

Shelton, D.R., Martin, R.B., Stover, S.M., Gibeling, J.C., 2003. Transverse fatigue crack propagation behavior in equine cortical bone. J. Mater. Sci. 38, 3501–3508. doi:10.1023/A:1025165221258

Siegmund, T., 2004. A numerical study of transient fatigue crack growth by use of an irreversible cohesive zone model. Int. J. Fatigue 26, 929–939. doi:10.1016/j.ijfatigue.2004.02.002

Sinclair, R., Preuss, M., Maire, E., Buffiere, J.-Y., Bowen, P., Withers, P.., 2004. The effect of fibre fractures in the bridging zone of fatigue cracked Ti–6Al–4V/SiC fibre composites. Acta Mater. 52, 1423–1438. doi:10.1016/j.actamat.2003.11.024

Spitz, D.J., Newberg, A.H., 2002. Imaging of stress fractures in the athlete. Radiol. Clin. North Am. 40, 313–331.
Suresh, S., 1998. Fatigue of Materials. Cambridge University Press.
Tada, H., Paris, P.C., Irwin, G.R., 1985. The stress analysis of cracks handbook: by Hiroshi Tada, with the cooperation of Paul C. Paris and George R. Irwin. Paris Productions & (Del Research Corp.).
Takuda, H., Mori, K., Takakura, N., Yamaguchi, K., 2000. Finite element analysis of limit strains in biaxial stretching of sheet metals allowing for ductile fracture. Int. J. Mech. Sci. 42, 785–798. doi:10.1016/S0020-7403(99)00018-1
Tanaka, K., Mura, T., 1981. A Dislocation Model for Fatigue Crack Initiation. J. Appl. Mech. 48, 97–103. doi:10.1115/1.3157599
Tang, S.Y., Vashishth, D., 2011. The relative contributions of non-enzymatic glycation and cortical porosity on the fracture toughness of aging bone. J. Biomech. 44, 330–336. doi:10.1016/j.jbiomech.2010.10.016
Taylor, D., 1998. Fatigue of bone and bones: An analysis based on stressed volume. J. Orthop. Res. 16, 163–169. doi:10.1002/jor.1100160203
Taylor, D., Kuiper, J.H., 2001. The prediction of stress fractures using a “stressed volume” concept. J. Orthop. Res. Off. Publ. Orthop. Res. Soc. 19, 919–926. doi:10.1016/S0736-0266(01)00009-2
Taylor, D., Lee, T.C., 2003. Microdamage and mechanical behaviour: predicting failure and remodelling in compact bone. J. Anat. 203, 203–211. doi:10.1046/j.1469-7580.2003.00194.x
Taylor, D., O’Brien, F., Prina-Mello, A., Ryan, C., O’Reilly, P., Lee, T.C., 1999. Compression data on bovine bone confirms that a “stressed volume” principle explains the variability of fatigue strength results. J. Biomech. 32, 1199–1203. doi:10.1016/S0021-9290(99)00112-8
Taylor, D., O’Reilly, P., Vallet, L., Lee, T.C., 2003. The fatigue strength of compact bone in torsion. J. Biomech. 36, 1103–1109. doi:10.1016/S0021-9290(03)00104-0
Tortora, G.J., Derrickson, B.H., 2008. Principles of Anatomy and Physiology. John Wiley & Sons.
Tracey, D.M., 1974. Finite elements for three-dimensional elastic crack analysis. Nucl. Eng. Des. 26, 282–290. doi:10.1016/0029-5493(74)90063-6
Tracey, D.M., 1971. Finite elements for determination of crack tip elastic stress intensity factors. Eng. Fract. Mech. 3, 255–265. doi:10.1016/0013-7944(71)90036-1
Turner, C.H., Wang, T., Burr, D.B., 2001. Shear Strength and Fatigue Properties of Human Cortical Bone Determined from Pure Shear Tests. Calcif. Tissue Int. 69, 373–378. doi:10.1007/s00223-001-1006-1
Ural, A., Mischinski, S., 2013a. Multiscale modeling of bone fracture using cohesive finite elements. Eng. Fract. Mech., Advances in Failure Assessment Using Fracture and Damage Mechanics. 103, 141–152. doi:10.1016/j.engfracmech.2012.05.008
Ural, A., Mischinski, S., 2013b. Multiscale modeling of bone fracture using cohesive finite elements. Eng. Fract. Mech., Advances in Failure Assessment Using Fracture and Damage Mechanics. 103, 141–152. doi:10.1016/j.engfracmech.2012.05.008
Ural, A., Vashishth, D., 2007. Anisotropy of age-related toughness loss in human cortical bone: A finite element study. J. Biomech. 40, 1606–1614. doi:10.1016/j.jbiomech.2006.07.023
Ural, A., Vashishth, D., 2006. Cohesive finite element modeling of age-related toughness loss in human cortical bone. J. Biomech. 39, 2974–2982. doi:10.1016/j.jbiomech.2005.10.018
Ural, A., Zioupos, P., Buchanan, D., Vashishth, D., 2011. The effect of strain rate on fracture toughness of human cortical bone: A finite element study. J. Mech. Behav. Biomed. Mater. 4, 1021–1032. doi:10.1016/j.jmbbm.2011.03.011
Vashishth, D., 2007a. Hierarchy of bone microdamage at multiple length scales. Int. J. Fatigue 29, 1024–1033. doi:10.1016/j.ijfatigue.2006.09.010
Vashishth, D., 2007b. The role of the collagen matrix in skeletal fragility. Curr. Osteoporos. Rep. 5, 62–66. doi:10.1007/s11914-007-0004-2

Vashishth, D., 2004. Rising crack-growth-resistance behavior in cortical bone:: implications for toughness measurements. J. Biomech. 37, 943–946. doi:10.1016/j.jbiomech.2003.11.003
Vashishth, D., Behiri, J.C., Bonfield, W., 1997. Crack growth resistance in cortical bone: Concept of microcrack toughening. J. Biomech. 30, 763–769. doi:10.1016/S0021-9290(97)00029-8
Vashishth, D., Tanner, K.., Bonfield, W., 2003. Experimental validation of a microcracking-based toughening mechanism for cortical bone. J. Biomech. 36, 121–124. doi:10.1016/S0021-9290(02)00319-6
Vashishth, D., Tanner, K.E., Bonfield, W., 2001. Fatigue of cortical bone under combined axial-torsional loading. J. Orthop. Res. 19, 414–420. doi:10.1016/S0736-0266(00)00036-X
Wang, X., Shen, X., Li, X., Mauli Agrawal, C., 2002. Age-related changes in the collagen network and toughness of bone. Bone 31, 1–7. doi:10.1016/S8756-3282(01)00697-4
Williams, J.G., Ewing, P.D., 1972. Fracture under complex stress — The angled crack problem. Int. J. Fract. Mech. 8, 441–446. doi:10.1007/BF00191106
Xia, Z., Curtin, W.A., Peters, P.W.M., 2001. Multiscale modeling of failure in metal matrix composites. Acta Mater. 49, 273–287. doi:10.1016/S1359-6454(00)00317-7
Xu, Y., Yuan, H., 2009. On damage accumulations in the cyclic cohesive zone model for XFEM analysis of mixed-mode fatigue crack growth. Comput. Mater. Sci. 46, 579–585. doi:10.1016/j.commatsci.2009.04.029
Yang, Q.D., Cox, B.N., Nalla, R.K., Ritchie, R.O., 2006a. Re-evaluating the toughness of human cortical bone. Bone 38, 878–887. doi:10.1016/j.bone.2005.10.014
Yang, Q.D., Cox, B.N., Nalla, R.K., Ritchie, R.O., 2006b. Fracture length scales in human cortical bone: The necessity of nonlinear fracture models. Biomaterials 27, 2095–2113. doi:10.1016/j.biomaterials.2005.09.040
Yan, J., Mecholsky Jr., J.J., Clifton, K.B., 2007. How tough is bone? Application of elastic–plastic fracture mechanics to bone. Bone 40, 479–484. doi:10.1016/j.bone.2006.08.013
Yeni, Y.., Fyhrie, D.., 2002. Fatigue damage-fracture mechanics interaction in cortical bone. Bone 30, 509–514. doi:10.1016/S8756-3282(01)00696-2
Yeni, Y.N., Brown, C.U., Wang, Z., Norman, T.L., 1997. The influence of bone morphology on fracture toughness of the human femur and tibia. Bone 21, 453–459. doi:10.1016/S8756-3282(97)00173-7
Yeni, Y.N., Norman, T.L., 2000. Fracture toughness of human femoral neck: effect of microstructure, composition, and age. Bone 26, 499–504. doi:10.1016/S8756-3282(00)00258-1
Yutaka, T., Daigora, I., 1992. Static and dynamic finite element analysis of transformation toughening in ceramic materials. Eng. Fract. Mech. 42, 911–924. doi:10.1016/0013-7944(92)90132-X
Zimmermann, E.A., Launey, M.E., Barth, H.D., Ritchie, R.O., 2009. Mixed-mode fracture of human cortical bone. Biomaterials 30, 5877–5884. doi:10.1016/j.biomaterials.2009.06.017
Zimmermann, E.A., Launey, M.E., Ritchie, R.O., 2010. The significance of crack-resistance curves to the mixed-mode fracture toughness of human cortical bone. Biomaterials 31, 5297–5305. doi:10.1016/j.biomaterials.2010.03.056
Zimmermann, E.A., Schaible, E., Bale, H., Barth, H.D., Tang, S.Y., Reichert, P., Busse, B., Alliston, T., Ager, J.W., Ritchie, R.O., 2011. Age-Related Changes in the Plasticity and Toughness of Human Cortical Bone at Multiple Length Scales. Proc. Natl. Acad. Sci. 108, 14416–14421. doi:10.1073/pnas.1107966108
Zioupos, P., 2001a. Accumulation of in-vivo fatigue microdamage and its relation to biomechanical properties in ageing human cortical bone. J. Microsc. 201, 270–278. doi:10.1046/j.1365-2818.2001.00783.x

Zioupos, P., 2001b. Ageing Human Bone: Factors Affecting Its Biomechanical Properties and the Role of Collagen. J. Biomater. Appl. 15, 187–229. doi:10.1106/5JUJ-TFJ3-JVVA-3RJ0

Zioupos, P., Currey, J.., 1998. Changes in the Stiffness, Strength, and Toughness of Human Cortical Bone With Age. Bone 22, 57–66. doi:10.1016/S8756-3282(97)00228-7

Zioupos, P., Currey, J.D., 1994. The extent of microcracking and the morphology of microcracks in damaged bone. J. Mater. Sci. 29, 978–986. doi:10.1007/BF00351420

Zioupos, P., Currey, J.D., Casinos, A., 2001. Tensile Fatigue in Bone: Are Cycles-, or Time to Failure, or Both, Important? J. Theor. Biol. 210, 389–399. doi:10.1006/jtbi.2001.2316

Zioupos, P., Wang, X., Currey, J., 1996. The accumulation of fatigue microdamage in human cortical bone of two different ages in vitro. Clin. Biomech. 11, 365–375. doi:10.1016/0268-0033(96)00010-1